Solid-State Potassium Metal Batteries – a Polymer Electrolyte Approach

Zur Erlangung des akademischen Grades eines
DOKTORS DER NATURWISSENSCHAFTEN
(Dr. rer. nat.)
von der KIT-Fakultät für Chemie und Biowissenschaften
des Karlsruher Instituts für Technologie (KIT)

genehmigte
DISSERTATION
von
M. Sc. Anna Khudyshkina

1. Referent: Prof. Dr. Helmut Ehrenberg
2. Referent: Prof. Dr. Patrick Théato
Tag der mündlichen Prüfung: 07.05.2025

Selbständigkeitserklärung

Hiermit versichere ich, dass ich die vorliegende Arbeit selbstständig verfasst habe, dass ich keine anderen als die angegebenen Quellen und Hilfsmittel benutzt habe, dass ich die wörtlich oder inhaltlich übernommenen Stellen als solche gekennzeichnet habe und dass ich die Satzung des KIT zur Sicherung guter wissenschaftlicher Praxis in der jeweils gültigen Fassung beachtet habe.

Karlsruhe, den

Anna Khudyshkina

Abstract

The diversification of battery technologies is driving post-lithium systems such as potassium-ion batteries (KIBs) – a sustainable, low-cost alternative due to abundant potassium resources. However, a key challenge in KIBs is the electrolyte, which must provide stable electrode/electrolyte interfaces, high ionic conductivity, and mechanical strength. Liquid electrolytes (LEs) pose safety risks due to flammability and reactivity, causing severe side reactions, especially with potassium metal, resulting in rapid capacity degradation and eventual cell failure. In contrast, solid polymer electrolytes (SPEs) offer intrinsic chemical stability, thermal tolerance, mechanical integrity and high cathodic stability, making them promising candidates for long-term potassium metal batteries. While ion transport in Li^+- and Na^+-batteries has been well studied, further investigation is needed for K^+-based systems.

In this thesis, material selection began with the most prominent example of SPE applications, poly(ethylene oxide) (PEO), mixed with potassium bis(trifluoromethanesulfonyl)imide (KTFSI), to evaluate rheological and ion transport properties. The analyses of the PEO-KTFSI electrolytes revealed a loss of mechanical integrity when approaching high ionic conductivities, highlighting the need for structural modifications. To address this, two strategies adapted from lithium-based systems were applied to PEO-KTFSI SPEs: the composite approach and the block copolymer strategy.

Both approaches showed that the physical properties of K^+-containing electrolytes were strongly dependent on the structure of polyether-based materials. The incorporation of inorganic nanofillers (Al_2O_3 and SiO_2) enhanced the mechanical stability through nanoparticle-ion-polymer Lewis acid-base interactions, transforming the materials from a liquid-like to a solid-like state. Additionally, a microphase-separated poly(vinyl benzyl methoxy poly(ethylene oxide) ether)-*block*-polystyrene (PVBmPEO-*b*-PS) copolymer served as a host material, effectively eliminating crystalline domains in PEO and allowing rapid K^+ diffusion while maintaining the solid-like properties of the electrolytes. Furthermore, this thesis introduces for the first time the potential of carbonyl-containing polymer host materials for K^+ conduction.

This thesis approaches the understanding of electrode/SPE interfacial chemistry using a combination of electrochemical techniques. While all tested SPEs exhibited high interfacial resistances in symmetrical K-metal cells, the benefits of the modified electrolytes were demonstrated by galvanostatic cycling in K-metal/SPE/$K_2Fe[Fe(CN)_6]$ cells, where significantly improved capacity retention (up to 99 %) and Coulombic efficiencies (CE) (>98 %) were observed over 100 cycles. These results highlight the potential of optimized SPEs for stable, high performance KIBs, advancing all-solid-state potassium metal technologies.

Kurzfassung

Die Diversifizierung der Batterietechnologien treibt die Entwicklung von Post-Lithium-Systemen wie Kalium-Ionen-Batterien (KIBs) voran – eine nachhaltige, kostengünstige Alternative, da Kalium im Überfluss vorhanden ist. Eine zentrale Herausforderung bei KIBs ist jedoch der Elektrolyt, der stabile Elektroden/Elektrolyt-Grenzflächen, hohe Ionenleitfähigkeit und mechanische Festigkeit bieten muss. Flüssige Elektrolyte (LEs) stellen aufgrund ihrer Entflammbarkeit und Reaktivität ein Sicherheitsrisiko dar und verursachen schwere Nebenreaktionen, insbesondere mit Kaliummetall, was zu einem schnellen Kapazitätsverlust und insgesamt zu einer verkürzten Batterielebensdauer führt. Im Gegensatz dazu bieten feste Polymerelektrolyte (Solid Polymer Electrolytes, SPEs) eine intrinsische chemische Stabilität, thermische Toleranz, mechanische Integrität und hohe kathodische Stabilität, was sie zu vielversprechenden Kandidaten für langfristige Kaliummetallbatterien macht. Während der Ionentransport in Li^+- und Na^+-Batterien gut untersucht wurde, sind für K^+-basierte Systeme weitere Untersuchungen erforderlich.

In dieser Arbeit begann die Materialauswahl mit dem bekanntesten Beispiel für SPE-Anwendungen, Poly(ethylenoxid) (PEO), gemischt mit Kaliumbis(trifluormethansulfonyl)imid (KTFSI), um die rheologischen und Ionentransporteigenschaften zu bewerten. Die Analysen der PEO-KTFSI-Elektrolyte ergaben einen Verlust an mechanischer Integrität bei Annäherung an hohe Ionenleitfähigkeiten, was die Notwendigkeit struktureller Änderungen deutlich macht. Um dieses Problem anzugehen, wurden zwei Strategien, die von lithiumbasierten Systemen übernommen wurden, auf PEO-KTFSI SPEs angewandt: ein Kompositansatz und eine Blockcopolymer-Strategie.

Beide Ansätze zeigten, dass die physikalischen Eigenschaften von K^+-haltigen Elektrolyten stark von der strukturellen Architektur des PEO abhängig sind. Die Einbindung anorganischer Nanofüllstoffe (Al_2O_3 und SiO_2) verbesserte die mechanische Stabilität durch Lewis-Säure-Base-Wechselwirkungen zwischen Nanopartikeln, Ionen und Polymeren, wodurch die Materialien von einem flüssigkeitsähnlichen in einen feststoffähnlichen Zustand überführt wurden. Darüber hinaus diente ein mikrophasengetrenntes Poly(vinyl benzyl methoxy poly(ethyleneoxid) ether)-*Block*-Polystyrol (PVBmPEO-*b*-PS) Copolymer als Wirtsmaterial, das kristalline Domänen in PEO effektiv eliminierte und eine schnelle K^+-Diffusion ermöglichte, während die festkörperähnlichen Eigenschaften der Elektrolyte erhalten blieben. Darüber hinaus wird in dieser Arbeit zum ersten Mal das Potenzial carbonylhaltiger Polymer-Wirtsmaterialien für die K^+-Leitung vorgestellt.

Diese Arbeit nähert sich dem Verständnis der Elektroden/SPE-Grenzflächenchemie durch eine Kombination elektrochemischer Techniken. Während alle getesteten SPEs in symmetrischen K-Metall-Zellen hohe Grenzflächenwiderstände aufwiesen, wurden die Vorteile der modifizierten Elektrolyte durch galvanostatische Zyklen in K-Metall/SPE/$K_2Fe[Fe(CN)_6]$-Zellen demonstriert, bei denen eine signifikant verbesserte Kapazitätserhaltung (bis zu 99 %) und coulombische Effizienzen (CE) (>98 %) über 100 Zyklen beobachtet wurden. Diese Ergebnisse unterstreichen das Potenzial optimierter SPEs für stabile, leistungsstarke KIBs, die die Festkörper-Kaliummetalltechnologien voranbringen.

Table of Contents

List of Abbreviations

ΔH_m – melting enthalpy

σ – ionic conductivity

X_C – crystallinity degree

A^+ – alkali metal cation

AlOx – aluminum oxide

An^- – anion

ASR – area specific resistance

BO – 1,2-butylene oxide

BPE – block copolymer electrolyte

C_g – geometric capacitance

CE – Coulombic efficiency

COF – covalent organic framework

CP – constant potential

CV – cyclic voltammetry

DFT – density functional theory

DSC – differential scanning calorimetry

EC – ethylene carbonate

EIS – electrochemical impedance spectroscopy

E_{sp} – specific energy

ESW – electrochemical stability window

FEC – fluoroethylene carbonate

G' – storage modulus

G'' – loss modulus

GCPL – galvanostatic cycling with potential limitation

GPE – gel polymer electrolyte

HOMO – highest occupied molecular orbital

ICP-OES – inductively coupled plasma-optical emission spectroscopy

j – current density

K_2PC – potassium 2,5-pyridinedicarboxylate

K_2TP – potassium terephthalate

KFF – potassium iron hexacyanoferrate

KFSI – potassium bis(fluorosulfonyl)imide

KIB – potassium-ion battery

KO_2 – potassium superoxide

KPF_6 – potassium hexafluorophosphate

KTFSI – potassium bis(trifluoromethanesulfonyl)imide

LE – liquid electrolyte

LIB – lithium-ion battery

LSV – linear sweep voltammetry

LUMO – lowest occupied molecular orbital

M – transition metal

M_n – number average molecular weight

MOF – metal organic framework

Mw – weight average molecular weight

Mv – viscosity average molecular weight

NIB – sodium-ion battery

PAQS – poly(anthraquinonyl sulfide)

PBA – prussian blue analogues

PC – propylene carbonate

PCL – poly(ε-caprolactone)

PEO – poly(ethylene oxide)

PFG-NMR – pulsed field gradient nuclear magnetic resonance

PISE – polymer in salt electrolyte

PO – propylene oxide

PPMTC – poly(propylene monothiocarbonate)

PS – polystyrene

PTMC – poly(trimethylene carbonate)

PVA – polyvinyl alcohol

PVBmPEO-*b*-PS – poly(vinyl benzyl methoxy poly(ethylene oxide) ether)-*block*-polystyrene

$Q_{cat/an}$ – specific capacity of cathode/anode

$Q_{ch/disch}$ – specific charge/discharge capacity

Q_{dl} – constant phase element capacitance (double layer)

RAFT – reversible addition-fragmentation chain transfer polymerization

R_b – bulk electrolyte resistance

R_u – uncompensated resistance

SAOS – small amplitude oscillatory shear

SEI – solid electrolyte interphase

SEC – size exclusion chromatography

SiOx – silicon oxide

SPE – solid polymer electrolyte

Sym- – symmetrical

T_A^+ – cation transference number

TGA – thermogravimetric analysis

T_g – glass transition temperature

T_m – melting temperature

TO – methyl ether triethylene glycol glycidyl ether

VFT – Vogel-Fulcher-Tammann equation

Acknowledgements

First and foremost, I would like to express my sincere gratitude to Prof. Dr. *Helmut Ehrenberg*, the head of our IAM-ESS, for the invaluable opportunities provided during my PhD journey. The supportive environment and resources provided under his leadership have played a crucial role in the successful completion of this thesis.

I am deeply grateful to my PhD supervisor, Dr. *Fabian Jeschull*, for introducing me to the fascinating world of electrochemical analysis in batteries. His continuous support, insightful guidance, and encouragement have been instrumental in shaping my research and scientific development. His expertise and patience have not only helped me overcome challenges but also inspired me to push the boundaries of my knowledge. Beyond his scientific mentorship, Dr. *Jeschull´s* enthusiasm for research and his ability to foster an environment of curiosity and critical thinking have profoundly influenced my approach to problem solving.

I would also like to extend my thanks to my second advisor, Prof. Dr. *Patrick Théato*, for his valuable input on all polymer science-related aspects of my research. His expertise and constructive feedback have significantly contributed to the depth and quality of this thesis.

Sincere thanks are extended to Prof. Dr. *Stanislav Fedotov* and Dr. *Polina Morozova* for their mentorship during my internship at the Center for Energy Science and Technology at Skoltech, as well as for sharing their valuable expertise on cathode materials for potassium-ion batteries.

I am also grateful to Prof. Dr. *Daniel Brandell*, Prof. Dr. *Jonas Mindemark* and Dr. *Isabell L. Johansson* for their warm welcome during my internship at the Ångström Laboratory at Uppsala University and for generously sharing their knowledge on polycarbonate-based polymer electrolytes.

Special thanks go to *Liuda Mereacre* for providing essential technical support throughout my PhD time, and to *Luis Martin Sanchez Neudeck* for IT support.

Beyond the academic and technical aspects, I am truly grateful to my friends and colleagues for their companionship and support throughout this journey. Special thanks go to (ex)members of IAM-ESS: *Jasmine, Lydia, Ahmad, Marina, Jessica, Hang, Ung-Hsuan, Jiali, Philip, Christian, Chris, Laura, Leonie, Eugen, Ulf, Celine, Iurii, Ramon, Cedric, Tim, Sasha*; and other great people: *Alina, Vladimir, Katya, Masha, Opel.* Their encouragement, laughter, and shared experiences have made this challenging process much more manageable and enjoyable.

Last but certainly not least, I owe my deepest gratitude to my family for their unconditional love, belief, and support. To my partner, *Mikhail*, for his patience, understanding, and great support that have been my rock throughout this journey. From celebrating the small victories to lifting me up during the most difficult moments, his belief in me never wavered, and for that,

I am endlessly grateful. To my beautiful daughter, *Eva*, who has been my greatest source of joy and inspiration (not always but most of the time). To my dear parents, *Natalia and Denis*, for instilling in me the values of resilience, hard work, and determination. Without my family, none of this would have been possible.

List of Publications

Xing, S.; Khudyshkina, A.; Rauska, U.-C.; Butzelaar, A. J.; Voll, D.; Theato, P.; Tübke, J.; Jeschull, F. Degradation of Styrene-Poly(Ethylene Oxide)-Based Block Copolymer Electrolytes at the Na and K Negative Electrode Studied by Microcalorimetry and Impedance Spectroscopy. *J. Electrochem. Soc.* **2024**, *171* (4), 040516. https://doi.org/10.1149/1945-7111/AD3B72.

Khudyshkina, A. D.; Rauska, U.-C.; Butzelaar, A. J.; Hoffmann, M.; Wilhelm, M.; Theato, P.; Jeschull, F. Impact of Nano-Sized Inorganic Fillers on PEO-Based Electrolytes for Potassium Batteries. **2023**. https://doi.org/10.1002/batt.202300404.

Khudyshkina, A. D.; Butzelaar, A. J.; Guo, Y.; Hoffmann, M.; Bergfeldt, T.; Schaller, M.; Indris, S.; Wilhelm, M.; Théato, P.; Jeschull, F. From Lithium to Potassium: Comparison of Cations in Poly(Ethylene Oxide)-Based Block Copolymer Electrolytes for Solid-State Alkali Metal Batteries. *Electrochim. Acta* **2023**, *454*, 142421. https://doi.org/10.1016/J.ELECTACTA.2023.142421.

Khudyshkina, A. D.; Morozova, P. A.; Butzelaar, A. J.; Hoffmann, M.; Wilhelm, M.; Theato, P.; Fedotov, S. S.; Jeschull, F. Poly(Ethylene Oxide)-Based Electrolytes for Solid-State Potassium Metal Batteries with a Prussian Blue Positive Electrode. *ACS Appl. Polym. Mater.* **2022**, *4* (4), 2734–2746. https://doi.org/https://doi.org/10.1021/acsapm.2c00014.

Contributions of Co-authors and Other Researchers

Parts of **Chapter 6** and the corresponding parts in the experimental section (**Section 4**) were extracted from the publications[1–3] and adapted with permission of the author (Anna Khudyshkina).

Conceiving the idea of these studies, developed methodology, organisation of the work and all included electrochemical results were done by Anna Khudyshkina and supervised by Fabian Jeschull. Anna Khudyshkina visualized the presented data and wrote the manuscripts. Block copolymer PVBmPEO-*b*-PS was synthesized by Andreas Butzelaar. Andreas Butzelaar also conducted all DSC measurements. SAOS measurements were done by Maxi Hoffmann. Preparation and examination of the BPE-based SPEs were carried out with help of Yiran Guo during her «Masterarbeit». Ulf C. Rauska contributed into preparation the filler-containing electrolytes and collecting the experimental data during his «Vertiefer» internship.

1. Introduction

Over the past few decades, lithium-ion batteries (LIBs) have become the dominant technology for portable and large-scale stationary energy storage, owing to their high-energy and power densities, as well as their long cycle life.[4–6] However, the rapid expansion of the energy storage market has raised concerns regarding cost and resource limitations due to the finite supply of lithium.[7–10] As a result, increasing efforts are being directed towards the development of rechargeable battery systems based on more abundant and cost-effective materials to ensure the long-term sustainability of energy storage technologies. Among these alternatives, potassium-ion batteries, KIBs, have emerged as a promising complementary technology, with the potential to achieve specific energies comparable to some modest LIBs (e.g., in the graphite/electrolyte/$LiCoO_2$ or /$LiFePO_4$ configurations).[11,12] Although the larger atomic mass and ionic radius of potassium negatively impact volumetric and gravimetric capacities, these drawbacks can be offset by the higher electrode potentials of commonly used cathode materials[13,14,15,16] with the potential to achieve cell voltages exceeding 4 V.[17,18] However, currently developed KIBs, like their lithium-based counterparts, rely predominantly on liquid electrolytes, which present significant safety challenges due to their high volatility, toxicity, and reactivity, and are more prone to component degradation in the potassium environment.[19,20,21] Furthermore, the lack of mechanical stiffness exacerbates the issue of uncontrollable dendrite growth, often leading to premature cell failure.

To address these limitations, solid polymer electrolytes have been proposed as a promising alternative, offering enhanced electrochemical and mechanical stability due to their inherent chemical inertness and thermal tolerance.[22,23,24,25] Research on SPEs dates back to the 1970s, when Wright *et al*. first reported ionic conductivity in poly(ethylene oxide) (PEO) doped with Na^+ and K^+ salts.[26] This breakthrough laid the foundation for the development of polymer-based electrolytes, demonstrating both fundamental importance and practical viability. A milestone in the commercialization of SPEs was reached in 2006, when the Bolloré Group introduced the first all-solid-state battery in an electric vehicle (Bluecar), with a lithium metal anode, a $LiFePO_4$ cathode, and a Li^+-conducting PEO-based electrolyte.[27] This development underlined the feasibility of polymer electrolytes in real-world applications and highlighted their potential for the next-generation of energy storage systems.

Nearly two decades after SPEs commercialization, PEO remains the most widely used and extensively studied polymer host material for SPE applications. This continued interest is largely due to its promising electrochemical properties, in particular its relatively high cathodic stability,[28,29] which is essential when combined with reactive metal anodes. In addition, PEO

has a low glass transition temperature (T_g) of around -60 °C,[25] indicating a potential for fast ion transport due to the increased chains mobility and polymer free volume.[30] As ion transport occurs predominantly within the amorphous phase, the primary drawback of PEO-based electrolytes is their semi-crystalline nature, which significantly suppress ionic conductivity at temperatures below the melting point of the polymer (T_m). To address this challenge, several approaches have been explored to suppress PEO crystallinity, including the incorporation of plasticizers,[31,32,33] blending with low T_g polymers,[34,35] and graft copolymerization.[36–38] These strategies effectively yield highly amorphous (co)polymers with reduced T_g values, improving ionic conductivity at near-ambient temperatures. However, this improvement comes at the expense of mechanical integrity, as the increased segmental mobility results in a liquid-like state. As a result, such materials lack the mechanical stiffness highly required for SPE applications for mitigation of dendrites formation, making them unsuitable as separators within electrochemical cells.[39,40]

Alternative strategies for modifying PEO have proven more effective in enhancing ionic conductivity while preserving a solid-like state. One such strategy involves the incorporation of nano-sized active[41,42,43,44] and passive[45–49,54–56] fillers into Li- and Na-SPEs. These fillers serve to suppress the crystallinity of the polymer host material,[50] simultaneously facilitating ion transport through particle-polymer and particle-ion Lewis-acid-base interactions.[51,52,53,54] In case of filler-polymer interactions confinement effect along the particle interface would be expected that restrict polymer chain mobility,[55,56] which is reflected in elevated T_g. Simultaneously, ion mobility can increase in such particle-polymer interface regions through formation of conducting pathways and restricted chain movement, but strongly depends on the dominating interactions between the individual components, as well as factors such as fillers size, its distribution and concentration.[22,52,54,57] Another effective strategy for mitigating high crystallinity while preserving the structural integrity of PEO-based electrolytes is block copolymerization with a high T_g polymer. This approach leverages the formation of a microphase-separated structure,[58–60,61] wherein the ion-conducting PEO-based block facilitates efficient transport, while the non-polar rigid block provides mechanical stability over a broad temperature range, extending above the melting point of PEO and below the T_g of the reinforcing phase, such as polystyrene. This polymeric architecture enables the simultaneous optimization of both ion transport and mechanical properties, addressing the key bottleneck of conventional PEO-based SPEs.

What is important to emphasise, cationic conductivity in polymer electrolytes is strongly dependent on the coordination strength between cations and the polymer matrix. From this

perspective, carbonyl-containing polycarbonates and polyesters represent a promising alternative to PEO-based SPEs. Unlike PEO, which exhibits strong coordination between alkali metal ions (A^+) and ether oxygen, polycarbonates and polyesters demonstrate weaker cation-polymer interactions due to reduced electrostatic strength between A^+ and carbonyl oxygen.[62–64,65] This weaker coordination is expected to facilitate ion transport, making these materials attractive candidates for SPEs.

The advantages and challenges of the strategies discussed above were studied for Li- and Na-based systems, while only a few works report on solid-state potassium batteries. Therefore, revisiting and validating previous findings in the context of K-metal batteries is particularly timely. This work provides pathway to addressing several key challenges of the development of high-energy potassium metal batteries: (1) overcoming the limited ion transport in PEO, which arises from its high crystallinity and strong cation coordination; (2) advancing beyond PEO-based electrolytes by exploring novel polymer architectures and alternative host materials; (3) addressing the issue of unstable electrode/electrolyte interface through the implementation of mechanically and electrochemically stable electrolyte systems. Overcoming these challenges is critical to enabling the practical application of potassium metal batteries as a viable alternative for next-generation energy storage.

2. Theoretical Background

2.1. Working Principles of Potassium Ion Batteries

Potassium-ion batteries, KIBs, operate on the same fundamental principles as LIBs and sodium-ion batteries (NIBs), involving the transfer of alkali metal cations, A^+, between electrodes during charge and discharge cycles.[66] However, significant differences exist between potassium and its alkali metal counterparts, primarily due to variations in the electrochemical properties of these charge carrier ions. One key distinction is that, unlike lithium, potassium does not form alloys with aluminum. This property makes aluminum a viable candidate for use as a negative electrode current collector in KIBs.[67,68] Additionally, potassium is significantly more abundant in the Earth crust compared to lithium and is on par with sodium, with concentrations of 20.9 g kg^{-1} for K, 23.6 g kg^{-1} for Na, and only 0.02 g kg^{-1} for Li, as shown in **Table 1**.[9] This higher abundance of potassium, along with its compatibility with aluminum, contributes to the potential for reduced costs in KIB technology.

When evaluating the performance of batteries, specific energy (Wh kg^{-1}) and energy density (Wh L^{-1}) are crucial metrics, representing the amount of energy that can be stored per unit of weight or volume. Equally important is the power density, which reflects the rate at which energy can be delivered per unit of weight or volume (W kg^{-1} or W L^{-1}). Both energy and power densities characteristics play a central role in evaluating the suitability of KIBs for various applications.

Such parameters as specific capacity of cathode and anode ($Q_{cat/an}$, Ah kg^{-1}), and average cell voltage U (V) contribute into specific energy, E_{sp}:

$$E_{sp} = \frac{(Q_{cat} \times Q_{an}) \times U}{Q_{cat} + Q_{an}} \qquad \textbf{Equation 1}$$

Although Li, Na, K feature the same number of electrons available for transfer, neither potassium nor sodium can compete with lithium in terms of specific capacity, as their higher atomic masses reduce the specific capacities (**Table 1**). However, this disadvantage may be mitigated by KIBs potential to operate at higher voltages over a broader voltage range compared to NIBs. This is attributed to the low redox potential of K^+/K in organic electrolytes.[10,69,70] While the standard reduction potentials (relative to the standard hydrogen electrode, SHE) reduce in the raw Na^+/Na (-2.71 V) > K^+/K (-2.93 V) > Li^+/Li (-3.04 V), experimental studies and theoretical calculations have shown a shift in this hierarchy in organic solvents such as propylene carbonate (PC). In PC environment, the potentials change to Na^+/Na (-2.56 V) > Li^+/Li (-2.79 V) > K^+/K (-2.88 V).[69,70] This shift enables KIBs to exploit a wider electrochemical voltage window when potassium metal is used, potentially leading to higher operating voltages and contributing to increased E_{sp}. Although cathode materials for KIBs may

offer high working potentials, the energy density achieved remains below those of current LIBs and NIBs. Exemplary, a KIB with a graphite anode and a Prussian blue analogue (PBA)-based $K_2Fe[Fe(CN)_6]$ cathode achieves a gravimetric energy density of 378 Wh kg^{-1}.[68] This value is comparable to that of an LIB with a graphite anode and a $LiCoO_2$ cathode (387 Wh kg^{-1}), which is the example of a LIB with modest E_{sp} among high energy density lithium batteries.[12] Thus, the wider voltage window and higher operating voltage of KIBs represent a pathway to stay on track by offsetting their lower specific capacities.

Furthermore, K^+ is expected to exhibit the fastest ion diffusion in both aqueous and organic solutions when compared Li^+ and Na^+. Despite having the largest ionic radius among the three, K^+ displays the smallest Stokes radius in aqueous and PC solutions (**Table 1**). This behaviour arises from the weaker Lewis acidity of K^+, which leads to reduced cation-solvent molecule interactions in solution. Consequently, this weaker interaction enhances ionic mobility and results in higher ionic conductivity. Assuming the same degree of ion association and anion mobility for salts based on Li^+, Na^+ and K^+, potassium cations provide a higher cationic transference number. This characteristic is particularly advantageous for high-power battery applications, as it facilitates more efficient ion transport and reduces polarization within the electrolyte.[67]

Table 1. Comparison of the characteristics of Li, Na and K. As published in the references.[9,68]

Characteristic	Li	Na	K
Abundance in Earth crust, g kg^{-1}	0.02	23.60	20.90
Atomic mass, u	6.94	23.00	39.10
Specific capacity, Ah g^{-1}	3.86	1.16	0.68
E^0 (A/A^+_{aq}), V vs.SHE	-3.04	-2.71	-2.93
E^0 (A/A^+_{PC}), V vs. Li/Li^+_{PC}	0	0.23	-0.09
Shannon's ionic radius, Å	0.76	1.02	1.38
Stokes radius in water, Å	2.38	1.84	1.25
Stokes radius in PC, Å	4.8	4.6	3.6

The working principle of a KIB is analogous to that of LIB or NIB and is schematically illustrated in **Figure 1**. Two configurations are depicted: **(a)** a typical KIB comprising a graphite anode and a $K_2Fe[Fe(CN)_6]$ cathode enabled by an organic LE, and **(b)** a solid-state potassium-metal battery featuring a K-metal anode and a $K_2Fe[Fe(CN)_6]$ cathode enabled by a SPE. In electrochemical terms, the anode is the electrode where oxidation (loss of electrons) occurs, while reduction (gain of electrons) takes place at the cathode. Since the primary function of a battery is to return the stored energy (to be discharged), the terminology for the electrodes is based on their function during this phase: graphite/K-metal undergoes oxidation and therefore

serves as an anode, while $K_2Fe[Fe(CN)_6]$ is reduced (cathode). During charging, potassium atoms in $K_2Fe[Fe(CN)_6]$ are converted to K^+, accompanied by the release of electrons into the external circuit. The K^+ migrate through the electrolyte layer (either liquid- or solid-state) toward the anode, where they are intercalated or deposited. Simultaneously, the electrons travel through the external circuit to the anode. During discharge, the K^+ stored in the anode are extracted and conducted back to the cathode. At the same time, the electrons flow in the reverse direction, from the anode to the cathode *via* the external circuit. These processes are governed by oxidation and reduction reactions occurring at the respective electrode materials. Thus, the energy storage and release mechanism in KIBs is fundamentally based on the reversible shuttling of K^+ ions between the electrodes and the corresponding flow of electrons through the external circuit.

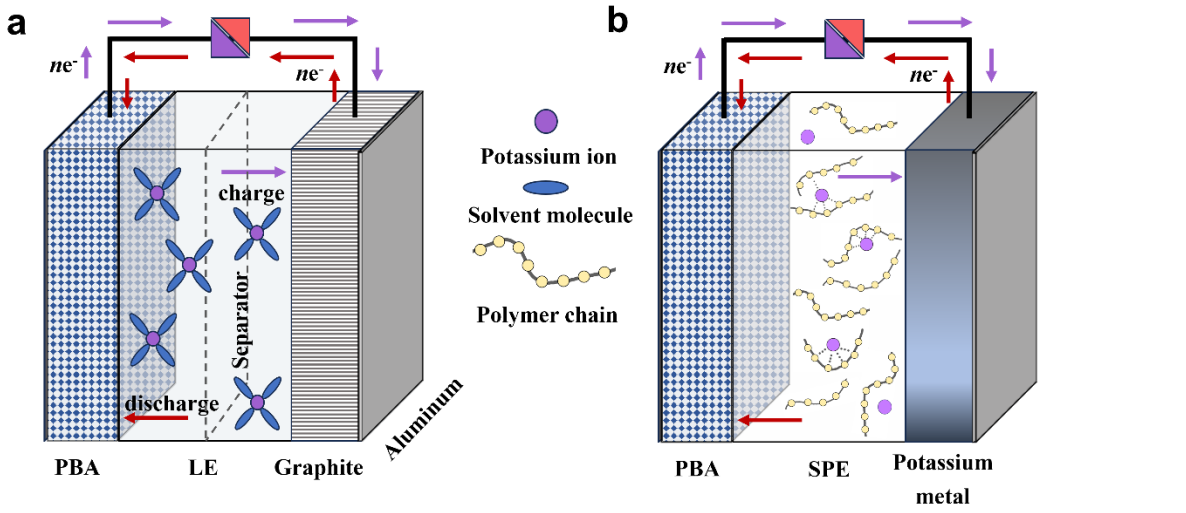

Anode: $nK_xC_8 \rightleftarrows 8nC + xnK^+ + xne^-$

Cathode: $nK_2Fe[Fe(CN)_6] \rightleftarrows 2nK^+ + nFe[Fe(CN)_6] + 2ne^-$

Full cell: $nK_2Fe[Fe(CN)_6] + 8nC \rightleftarrows nFe[Fe(CN)_6] + nK_xC_8$

Anode: $nK_x \rightleftarrows xnK^+ + xne^-$

Cathode: $nK_2Fe[Fe(CN)_6] \rightleftarrows 2nK^+ + nFe[Fe(CN)_6] + 2ne^-$

Full cell: $nK_2Fe[Fe(CN)_6] \rightleftarrows nFe[Fe(CN)_6] + nK_x$

Figure 1. A schematic illustration of a potassium battery comprising **(a)** a graphite anode, a $K_2Fe[Fe(CN)_6]$ (PBA) cathode, and an organic liquid electrolyte (LE); **(b)** a K-metal anode, a PBA cathode, and a solid polymer electrolyte (SPE).

As shown in **Figure 1**, configuration **(a)** represents a full cell, while configuration **(b)** corresponds to a half cell, which features an unlimited source of potassium. In LIBs, CE can approach nearly 100 %.[71,72] In comparison, the highest CE reported for KIBs is 90 %.[11] The use of a metallic potassium anode, which provides an unlimited source of potassium, offers the potential to enhance CE and enable higher operating voltages. However, the practical use of metallic potassium anodes is associated with safety concerns due to the highly reactive nature

of potassium metal. This safety challenge can be mitigated by employing solid polymer electrolytes. A more detailed discussion of this approach is presented in the following subsections (**2.1.2** and **2.1.3**).

2.1.1. Commonly Used Positive Electrode Materials

***Layered transition metal oxides*.** Layered transition metal oxides are the predominant cathode materials in commercial LIBs and SIBs, owing to their high-energy density, excellent stability, and low cost.[73–75] These materials possess a layered structure K_xMO_2, in which transition metal (M) and alkali ions are arranged in alternating slabs, forming two-dimensional frameworks that enable efficient ion migration, even for the larger K^+.[76] During the charge and discharge processes, K^+ reversibly intercalate and deintercalate within the framework, typically occupying octahedral (O) or prismatic (P) sites, accompanied by structural phase transformations.

K_xCoO_2, the potassium analogue of $LiCoO_2$, has been studied as a potential cathode material for potassium-ion batteries, inspired by the stability and high-energy density demonstrated by its lithium-based counterpart. However, the large ionic radius of K^+ poses challenges for reversible intercalation, resulting in rapid capacity fading and pronounced structural degradation.[77] The restricted intercalation range is often reflected in stepwise voltage curves, where the voltage jumps correspond to the formation of thermodynamically stable phases within narrow K^+ concentration ranges.[78,79] For instance, P2-K_xCoO_2 typically displays five distinct voltage steps between 1.5 and 3.9 V in half cell configuration.[80] In contrast, multimetallic K_xMO_2 systems improve electrochemical performance by leveraging the synergistic effects of multiple metals, leading to smoother voltage profiles, higher average operating potentials, and enhanced structural stability. For example, Mai *et al*. reported a full cell KIB employing $K_{0.7}Fe_{0.5}Mn_{0.5}O_2$ nanowires as the cathode material and a soft carbon anode that operated at 0.5-3.5 V vs. K^+/K voltage range. This system demonstrated a high discharge capacity of 178 mAh g^{-1} with 76 % capacity retention over 250 cycles.[81] In a separate study, the K-ion full cell operating at a voltage window of 0.5-3-5 V vs. K^+/K using P2-$K_{0.44}Ni_{0.22}Mn_{0.78}O_2$ cathode and soft carbon anode delivers impressive electrochemical performance with a high discharge capacity of 70 mAh g^{-1} at 50 mA g^{-1} and high capacity retention of up to 90 % after 500 cycles.[82]

Despite the potential of K_xMO_2 materials for cost-effective energy storage, achieving both higher specific capacity and higher average operating potential remains a critical challenge for their practical application in KIBs (see overview in **Figure 2**).

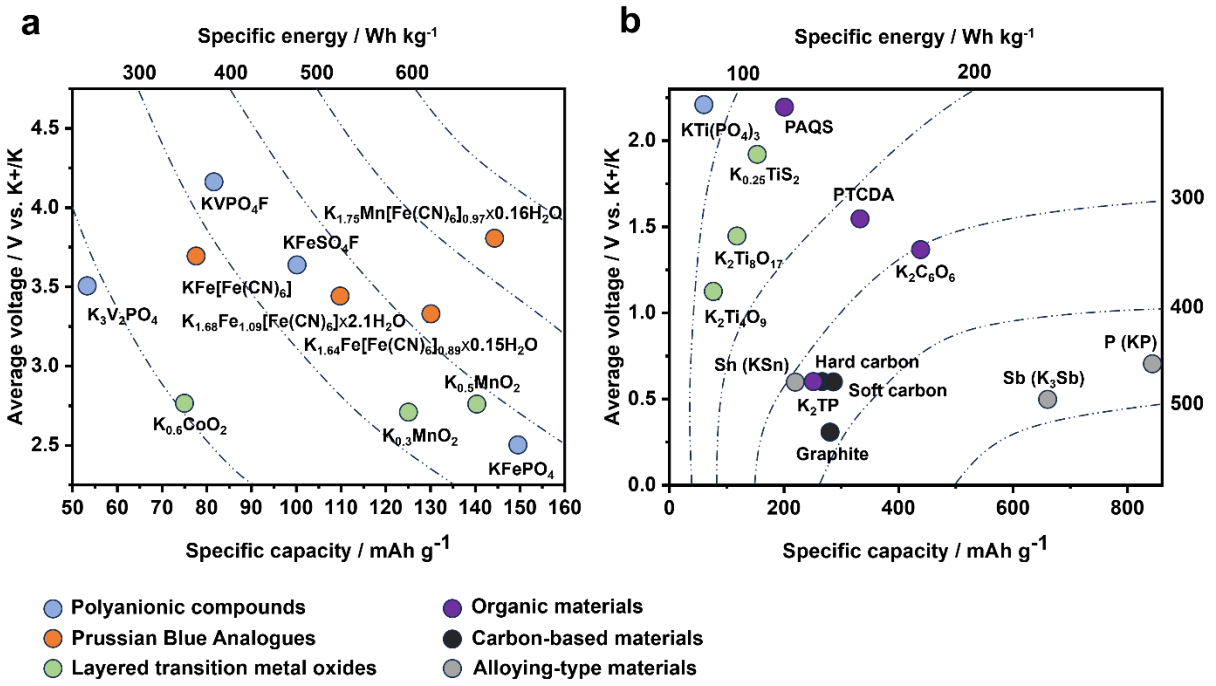

Figure 2. Materials overview for selected **(a)** cathode and **(b)** anode for KIBs. The materials can be reported as either cathodes or anodes depending on their electrochemical function in a battery. Adapted from the reference.[83]

***Organic materials*.** As stated above, the insertion of large K^+ into inorganic host materials often induces structural changes that lead to electrochemical instability, resulting in fast capacity fade. As a result, research efforts have shifted toward organic electrode materials, which offer intrinsically flexible frameworks and large primary interlayer spacing. These structural characteristics enable organic materials to accommodate K^+ without structural collapse, making them promising candidates for KIBs.[14,84,85] For electrochemical performance as electrodes, organic materials are expected to feature functional groups that are electrochemically active in either oxidation or reduction reactions. Generally, organic electrodes can be classified into N-type and P-type materials, depending on their charge storage mechanism. N-type materials undergo redox reactions involving cations, while P-type materials interact electrochemically with anions.[86–88]

Several organic compounds have demonstrated high capacities and long cycle life as cathode materials for KIBs, 3,4,9,10-perylene-tetracarboxylicacid-dianhydride (PTCDA),[89,18] copper-tetracyanoquinodimethane,[90] carbonyl-based polyimide and polyquinoneimide[91] and poly(anthraquinonyl sulfide) (PAQS).[92] However, organic electrode materials face challenges related to organic molecules solubility in electrolytes, which leads to capacity fading during cycling. To address this issue, such strategies as surface coating, polymerization, usage of salt

can be employed.[93] However, these approaches often result in increased dead mass within the cathode, thereby reducing energy density.

One of polymeric examples is PAQS, which was investigated as a cathode material for KIBs by Jian *et al*.[92] The PAQS electrode exhibited a high reversible capacity of 190 mAh g^{-1} at a current density of 20 mA g^{-1}, corresponding to 84% of its theoretical capacity, operating within a voltage window of 1.5-3.4 V in a potassium-based half cell configuration. In 2018, Fei *et al*. reported an all-solid-state K-battery with a PTCDA cathode and K-metal anode operating in a voltage window of 1.5-3.5 V vs. K^+/K. The cell exhibited a maximum discharge capacity of 118 mAh g^{-1} at a current density of 20 mA g^{-1} and retained 78 % of the capacity over 40 cycles. The average discharge voltage was 2.3 V, below the threshold required for KIBs.

While organic-based cathode materials hold significant potential for KIB applications, key challenges such as low conductivity, poor energy density and limited average operating voltage must be addressed for their practical implementation.[68]

***Polyanionic compounds*.** Polyanionic compounds have been extensively studied as electrode materials due to their high operating voltage, competitive conductivity, and long cycle life.[94,95] These materials consist of MO_x and $(XO_4)^{n-}$ polyhedra, where M refers to transition metal, and X represents elements such as P, S, As, Si, Mo, or W. The incorporation of polyanionic units leads to an open framework structure, which facilitates alkali metal ion diffusion. Compared to layered transition metal oxides, polyanionic compounds generally exhibit higher operating voltages, primarily due to the inductive effect.[95] This increase in redox potential results from the decreased covalency of M-O bonds, which is influenced by the presence of highly covalent X-O bonds.[96] Therefore, the electronegativity of X is a key factor: when X is highly electronegative, the M-O bond becomes more ionic and less covalent, leading to an increase in redox potential. Additionally, the presence of $(XO_4)^{n-}$ units not only enhances the diffusion kinetics of alkali metal ions but also improves structural stability during prolonged charge/discharge cycling.

In KIBs, polyanionic compounds that have been reported include $KFePO_4$, $K_3V_2(PO)_4$, $KVOPO_4$, $KFeSO_4F$, $KVPO_4F$, etc.[97] In general, these compounds exhibit higher operating voltages than their Na-based counterparts and in some cases are even comparable to some Li-based analogues. In particular, some K-containing materials can be cycled at voltages above 4 V vs. K^+/K (**Figure 2**). Such high potentials are advantageous in compensating for the larger atomic mass of potassium. For example, $KVOPO_4$ and $KVPO_4F$ offer a theoretical capacity of 131 mAh g^{-1} and an average potential of 4.3 V, resulting in a theoretical energy density of about 560 Wh kg^{-1}, which is comparable to that of $LiFePO_4$-based LIBs.[98] In practice, polyanionic

compounds have demonstrated superior capacity retention among KIBs cathode materials. For instance, Liao *et al.*[99] presented a full potassium-ion cell utilizing a $KVPO_4F$ cathode and a VPO_4 anode that achieved a capacity of 101 mAh g^{-1} at an operating voltage of 3.1 V, and remarkable capacity retention of 86.8 % over 2000 cycles.

However, to unlock the full potential of these class of cathode materials, the development of next-generation electrolytes capable of stable operation across a wide voltage range (i.e. up to 5 V) is critical.[13,100] Noteworthy, a particularly significant aspect is the sustainability of vanadium as a key component of polyanionic compounds.[101] Ensuring sustainable extraction and recycling of vanadium is critical for potassium-ion battery technology.

***Prussian Blue Analogues*.** Prussian blue and its analogues, PBAs, belong to the class of metal hexacyanoferrates, generally represented by the chemical formula $A_xM_2[M_1(CN)_6]_{1-y}\times zH_2O$, where A is an alkali metal (Li, Na, K), M_1 and M_2 are transition metals (e.g. Fe, Ni, Co, Mn, Ti); $0 < x < 2$; $y < 1$; and *z* denotes the number of water molecules either occupying interstitial sites (interstitial water) or coordinating to transition metal vacancies (coordinated water).[102,103] The typical PBAs crystallize in a face-centered cubic structure (space group *Fm-3m*) comprising high-spin and low-spin transition metal-based octahedra, bridged by cyanide ligands. This rigid three-dimensional framework forms open ion channels and spacious voids, allowing the intercalation of various cations, including Li^+, Na^+, K^+, Mg^{2+}, Ca^{2+}, Al^{3+}, as well as water crystals.[102,104] Depending on the guest cation or/and molecules, the octahedra rotate, resulting in monoclinic (*P2₁/n*) or rhombohedral (typically *R-3m*) structures.[68]

Among PBAs, KMnFe-PBA and KFeFe-PBA have demonstrated the most promising electrochemical performance as cathode materials for KIBs. Exemplary, KFeFe-PBA undergoes a color change from blue to white when Fe^{3+} is fully reduced to Fe^{2+}, forming its reduced counterpart, Prussian White ($K_2Fe[Fe(CN)_6]$). The partially reduced state corresponds to Prussian Blue ($KFe[Fe(CN)_6]$), while the fully oxidized form is known as Prussian (Berlin) Green ($Fe[Fe(CN)_6]$). KMnFe-PBA exhibits a high average discharge voltage of 3.8-3.9 V vs. K^+/K,[105] attributed to the high redox potential of the Mn^{3+}/Mn^{2+} couple. Meanwhile, KFeFe-PBA offers superior cycling stability, but a lower average discharge voltage (~3.6 V) due to the lower redox potential of the Fe^{3+}/Fe^{2+} redox couple.

In 2017, Goodenough *et al.*[106] first reported the use of $K_{1.89}Mn[Fe(CN)_6]_{0.92}\times 0.75H2O$ as a cathode material for KIBs. This compound featured the redox activity of high-spin Mn^{3+}/Mn^{2+} and low-spin Fe^{3+}/Fe^{2+} pairs, enabling the intercalation of two redox-active K^+ per unit formula. Consequently, the material exhibited a high theoretical discharge capacity of 156 mAh g^{-1}, achieving a practical capacity of 142 mAh g^{-1} with an average voltage of 3.6 V vs. K^+/K.

Extensive research has been conducted to address two key challenges associated with PBAs: $[Fe(CN)_6]^{4-}$ vacancies and water content. The number of vacancies can be controlled through various synthetic strategies, such as chelate-assistance precipitation.[107–109] Additionally, minimizing interstitial water is crucial to maintaining structural integrity and electrochemical performance. Effective drying requires a balance between removing water and preventing decomposition, with an optimal drying temperature of below 200 °C.[16]

2.1.2. Commonly Used Negative Electrode Materials

In LIBs, graphite serves as the primary anode material due to its ability to form a series of reversible graphite intercalation compounds with a final stoichiometry of LiC_6, delivering a high theoretical specific capacity of 372 mAh g^{-1} along with high cycling stability.[110,111] In 2015, Komaba *et al.*[67] demonstrated the successful reversible intercalation of potassium into graphite, leading to the formation of KC_8 with a lower theoretical specific capacity of 279 mAh g^{-1}. Since then, extensive research has been conducted to identify alternative anode materials for KIBs that offer enhanced electrochemical stability and higher energy density.[112] Beyond graphite, various materials have been explored as anodes for KIBs, including non-graphitic carbons (hard carbon, soft carbon), alloys, organic compounds, and potassium metal. Depending on the potassium storage mechanism, anode materials can be classified into three main categories: intercalation-, conversion-, and alloying-type materials. The following section provides a brief overview of the key anode materials reported for KIBs, highlighting their advantages and limitations.

Carbon-based anode materials. Two distinct potassium intercalation mechanisms have been proposed for graphite, resulting in the formation of intercalation compounds with varying potassium-to-carbon atomic ratios, specifically KC_{12n} (n = 1, 2) and KC_{8n} (n = 1, 2, 3).[113–115] Density functional theory (DFT) calculations have indicated that the maximum thermodynamically stable stoichiometry is KC_8, whereas the formation of KC_6, analogous to LiC_6 in LIBs, is not expected at low potentials due to the preferential deposition of metallic potassium.[115] Jian and co-authors investigated potassium insertion and extraction in graphite and reported a practical specific capacity of 273 mAh g^{-1}, closely matching the theoretical value (279 mAh g^{-1}), during the first depotassiation process.[113] However, a significant challenge associated with graphite as an anode material for KIBs is its structural instability, primarily due to the large size of K^+, which induces substantial volume expansion upon intercalation. Unlike lithium intercalation, which results in a 10 % interlayer expansion when forming LiC_6, the formation of KC_8 in KIBs causes an interlayer expansion of 60 %, i.e. six times greater than

that observed in LIBs.[116] This pronounced volume change leads to the degradation of the solid electrolyte interphase (SEI) layer formed during the initial potassiation. The repeated reconstruction of the SEI due to continued electrolyte consumption and decomposition, contributing to unstable cycling performance, rapid capacity fading, and ultimately, battery failure.

Unlike graphite, which consists of well-ordered graphene layers stacked in ABAB (hexagon) or ABCABC (rhombohedron) sequences, hard and soft carbons lack a well-defined crystalline structure and are thus commonly referred to as amorphous carbons. Hard carbon is characterized by small sp^2 carbon domains, a larger interlayer spacing, and micropores within the particles.[110] These structural features enable A^+ to be stored both in the interlayer spaces and within the micropores.[117] Compared to graphite, the expanded interlayer distance in hard carbon accommodates a larger number of K^+ during potassiation while providing greater tolerance to volume expansion. This structural flexibility helps mitigate the mechanical strain associated with K^+ intercalation, reducing the risk of electrode degradation.[118] The electrochemical potassium storage properties of hard carbon were first investigated by Jian *et al.*[119,120] in a potassium half cell at 0.1C (1C rate corresponded to 279 mAh g^{-1}) at voltage window of 0.01-2 V vs. K^+/K. Their study reported initial potassiation and depotassiation capacities of 344 and 260 mAh g^{-1}, respectively, with an initial CE of 76 %. Furthermore, Jian *et al*. also examined the potassium storage behaviour of soft carbon at the same conditions as for the hard carbon. The soft carbon exhibited initial potassiation and depotassiation capacities of 392 and 246 mAh g^{-1}, respectively, though with a lower initial Coulombic efficiency of 63 %.[119] Therefore, improving initial CE and high rate capability of carbon-based anode materials is still one of the most critical challenges to reach practical application.

Alloying-type anode materials. Elements from groups 14 and 15 have been extensively studied as potential anode materials for LIBs, NIBs, and KIBs due to their ability to store alkali metals through alloying reactions.[121–123] The potassiation process in alloying anodes follows the general reaction: $A + nK^+ + ne^- \rightarrow K_nA$ (where A represents alloying element). Compared to carbon-based anodes, alloying-type materials provide a greater number of transferable electrons, leading to higher theoretical capacities. Silicon (Si) – one of the most promising alloying-type anode materials in LIBs – exhibited very low electrochemical activity toward K^+ and is therefore was considered as unsuitable anode material for KIBs.[123] In contrast, tin (Sn), commonly used as an alloying anode in LIBs and NIBs, demonstrated ability to alloy with potassium. However, while providing high theoretical specific capacities of 990 mAh g^{-1} for $Li_{22}Sn_5$ and 847 mAh g^{-1} for $Na_{15}Sn_4$, Sn can alloy with K in a one-to-one ratio to form KSn

with a relatively low theoretical capacity of 226 mAh g^{-1}.[105,124] Among group 15 elements, phosphorus (P) has been extensively investigated due to its ability to form K_3P, which delivers an exceptionally high theoretical capacity of 2596 mAh g^{-1}. However, the formation of more thermodynamically stable compounds such as KP and K_4P_3 provides reduced but still considerable theoretical capacities of 865 and 1154 mAh g^{-1}, respectively.[125,126] Similarly, antimony (Sb) and bismuth (Bi) have emerged as promising alloying anode materials due to their high gravimetric capacities, low operating voltages, and high electrical conductivity.[127,128] However, one of the primary challenges associated with alloying-type anodes is the significant volume expansion during potassiation induced by the large ionic radius of K^+. For instance, the volume expansion observed for KSn, KP, K_3Sb, and K_3Bi corresponded to 180, 232, and >400 %, respectively. This excessive expansion generates severe mechanical strain, leading to particle pulverization, structural degradation, and electrode delamination from the current collector, ultimately compromising the cycling stability and practical viability of these materials.

Organic anode materials. As previously discussed, organic materials have been extensively explored as cathode materials for KIBs. In addition, a variety of organic compounds exhibit redox activity at low potentials, making them suitable candidates for anode applications. Various organic molecules,[77,129,112] metal-organic frameworks (MOFs),[130] covalent organic frameworks (COFs),[131] and polymers[132,133] have been investigated for alkali metal-ion batteries due to their ability to reversibly interact with A^+ through redox-active functional groups. These materials provide an intrinsic structural advantage by accommodating the large ionic radius of K^+, thereby enhancing electrode stability. In 2017, potassium terephthalate (K_2TP) and potassium 2,5-pyridinedicarboxylate (K_2PC) were reported as organic-based anode materials for KIBs.[134] Their energy storage mechanism involved reversible electron transfer between the oxidized and reduced states of para-aromatic dicarboxylates. When cycled in K-based half-cells at a C/5 cycling rate within a voltage window of 0.2-2.0 V vs. K^+/K, K_2TP and K_2PC delivered average specific capacities of 181 and 190 mAh g^{-1}, respectively. However, small-molecule carboxylates suffer from high solubility in liquid organic electrolytes, leading to rapid capacity fading.[105] To address this issue, efforts have focused on developing novel synthesis strategies and optimizing electrode/electrolyte interface engineering. For instance, Zhang *et al.*[135] designed π-conjugated polymer-based KIB anodes with enhanced stability. Using oxidation polymerization, they synthesized polypyrene nanoflowers composed of nanosheets, which exhibited superior electrochemical performance. The polypyrene-based anode delivered a reversible capacity of 302 mAh g^{-1} at 100 mA g^{-1} after 60 cycles, and a reversible capacity of

190 mAh g^{-1} even after 1000 cycles at 500 mA g^{-1} in a K-half cell (0.01-3 V vs. K^+/K). Additionally, the material demonstrated minimal solubility in conventional KIB electrolytes even after 30 days, contributing to its excellent cycle life and relatively high electronic conductivity. Despite flexibility and ability to accommodate large K^+ ions, organic-based anode materials generally suffer from low electronic conductivity and limited energy density, making them less competitive than other anode materials for KIBs applications.

K-metal anodes. As discussed in details in **Section 2.1,** metallic potassium is an attractive candidate among other alkali metals due to its natural abundance, low electrochemical potential in carbonate-based solvents (**Table 1**), and compatibility with lightweight aluminum current collectors. With a high theoretical specific capacity of 687 mAh g^{-1}, K-metal outperforms most KIBs anodes.[136] Despite these advantages, several critical challenges hinder the practical application of K-metal anodes, and these challenges appear to be more severe than those associated with metallic Li- and Na-based anodes. These challenges include high reactivity, which leads to an unstable SEI, substantial volume expansion during cycling due to its hostless nature, and uncontrolled dendrite formation, which can cause internal short circuits.[137] To address these issues, strategies such as host material design,[138–140] artificial SEI formation,[140,141] Na-K alloying,[142,143] and electrolyte optimization[144,145] have been explored. Among these, replacing conventional liquid electrolytes, LEs, with SPEs has shown significant promise. Due to their higher mechanical rigidity, SPEs effectively suppress dendrite growth while providing enhanced electrochemical stability, chemical inertness, and thermal resistance.[22,23,24,25] Fei *et al.*[146] demonstrated improved capacity retention and CE over a liquid electrolyte system of an anode half cell when a solid poly(ethylene oxide)-based electrolyte is employed. The same authors received similar promising results with an organic cathode with an average potential of 2.3 V vs. K^+/K (on discharge)[18]. However, current K-metal full cells remain at the proof-of-concept stage and lack systematic and comprehensive investigation.

2.1.3. Choice of Electrolyte – Solid Polymer Electrolyte (SPE) Approach

As previously discussed, polymer electrolytes have gained significant attention as a viable alternative to conventional organic LEs, offering the potential to overcome the drawbacks associated with the latter.[22,23,24,25] A solid polymer electrolyte, SPE, is commonly defined as an electrolyte salt dissolved in a polymer host material, providing both mechanical stability – sufficient to be considered a solid on a macroscopic scale – and ionic conductivity, thereby fulfilling the primary function of an electrolyte, i.e. facilitating the ionic transport. As follows from this definition, SPEs are «dry» systems, devoid of any liquid component. Noteworthy,

some polymer-based electrolyte systems include a liquid component, making them susceptible to the same stability issues and degradation pathways observed in conventional LEs. It is essential to distinguish between such gel polymer electrolytes (GPEs) and SPEs, as they differ fundamentally in ion transport mechanisms: while GPEs rely on small-molecule-solvated vehicular transport, SPEs facilitate ion conduction through polymer-associated mechanisms (a detailed discussion of ion transport mechanisms in polymers follows in **Section 2.2**). Compared to organic liquid electrolytes and gel-based counterparts, polymer electrolytes generally exhibit lower flammability and greater resistance to rapid decomposition reactions, rendering them inherently safer for battery applications.[147] Moreover, their solid-like properties result in enhanced mechanical strength, effectively mitigating alkali metal dendrite formation and thereby further improving battery safety.[148,149–151] Despite these advantages, the widespread commercialization of SPEs remains hindered primarily by their lower ionic conductivity as compared to liquid electrolytes. While LEs typically achieve ionic conductivities of ~10^{-2} S cm^{-1} at room temperature, SPEs generally fall within the range of 10^{-5}-10^{-6} S cm^{-1}.[152] Another key challenge associated with SPEs is their limited ability to establish extensive interfacial contact with porous electrode structures. In alkali-ion batteries, liquid electrolytes readily infiltrate the porous architecture of electrodes and effectively wet the surfaces of active material particles, thereby facilitating efficient charge transfer. In contrast, polymer electrolytes creep deeper layers of the electrode, eventually achieving a higher degree of contact with the active material particles. This is often reflected in enhancing specific capacity in the initial cycles. To improve ion transport in the electrode layer, a polymer-salt additive can be added in the slurry during electrode preparation.[153–155] Thus, ensuring intimate electrode/electrolyte contact is crucial for optimizing charge transfer kinetics and enhancing the electrochemical performance of solid-state batteries. While polymer electrolytes generally exhibit better interfacial contact with electrodes than ceramic electrolytes, interfacial resistance often remains a significant limiting factor. A summary of the advantages and challenges of SPEs comparatively to LEs is provided in **Figure 3**.

Since the primary function of an electrolyte is to facilitate ion transport, ionic conductivity is a critical parameter when evaluating the performance of SPE materials. However, several additional key aspects are essential for their SPEs application in the batteries. These include high cationic mobility, resulting in a high cation transference number (T_A^+), a low glass transition temperature, T_g, a high fraction of amorphous phase, while maintaining mechanical strength, and electrochemical stability against commonly used electrode materials. Thus, a sufficiently wide electrochemical stability window (ESW), typically in the range of 4-5 V – the

difference between the oxidation and reduction potentials of the electrolyte – is necessary to ensure compatibility with high-voltage electrode materials to achieve high-energy density batteries. A more detailed discussion of these key performance metrics follows in the subsequent sections.

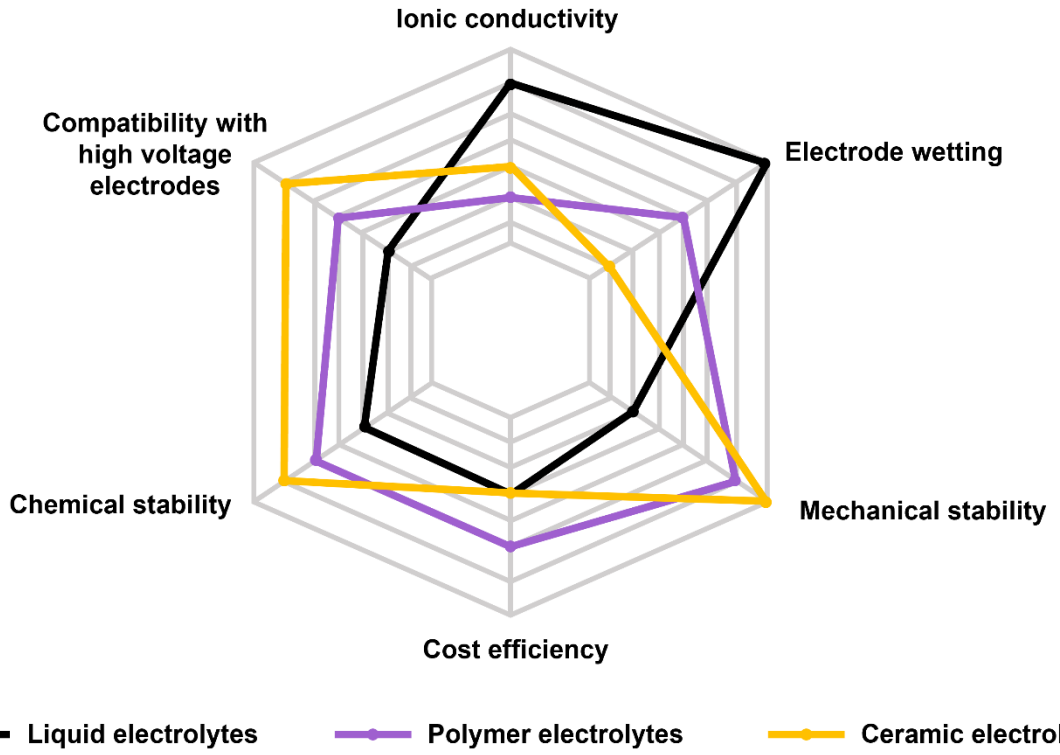

Figure 3. Spider diagram comparatively presenting the advantages and disadvantages of different electrolyte systems: liquid, polymer, and ceramic electrolytes. Adapted from the reference.[147]

2.2. Ion Transport Mechanisms

As stated above, the definition of SPE includes electrolyte salt dissolved in a polymer host matrix. According to acid-base theory, alkali metal ions, A^+, can be seen as typical Lewis acids. Therefore, it is crucial for the polymer host material to contain coordinating groups with electronegative atoms (Lewis bases) to solvate A^+. Moreover, for effective ion solvation in SPEs, the interactions between ions and the polymer chains must be stronger than ion-ion and polymer-polymer interactions. The ion-ion pairing of the salt in a solvent is often related to the dielectric constant of the medium, which governs the shielding of charges from each other. The dielectric constant tends to be comparatively low for many polymer host materials, yet they are good complexing agents for A^+. This is associated with the solvation ability of a solvent that is determined by its Lewis basicity, allowing to achieve favorable ion coordination, and is

commonly described by the donor number.[156] Thus, polymers featuring ether group (-R_1-O-R_2-),[157,25] imide (-NH-),[36,158,159] and thiol (-S-),[160] are candidates for dissolving A^+-containing salts.

In general, the dissolution of alkali salts in the polymer host occurs when the Gibbs free energy of mixing is negative:[147]

$$\Delta G_{mix} = \Delta H_{mix} - T\Delta S_{mix} \quad \textbf{Equation 2}$$

where G_{mix} is the Gibbs free energy, S_{mix} refers to entropy, and H_{mix} is enthalpy of the mixing process.

The mixing process involves multiple simultaneous events, such as ions disordering, the creation of suitable sites in the polymer, and the formation of coordinating ion-polymer bonds, overall contributing to the Gibbs free energy. Therefore, dissolution of salt in polymer host material is facilitated if the dissociation energy of the salt is low.[161,162] Consequently, salts with bulky anions, where the negative charge is delocalized over a large volume, are commonly used. Examples include perchlorate (ClO_4^-), tetrafluoroborate (BF_{4-}), hexafluorophosphate (PF_6^-), bis(fluoromethanesulfonimide) (FSI^-), bis(trifluoromethanesulfonyl)imide ($TFSI^-$).[147] Furthermore, the presence of larger A^+ in the structure of electrolyte salt generally results in lower dissociation energies. In alkali metal (A^+)-polymer complexes, larger cations possess weaker coordination (larger bond lengths with polymer)[163,164,165] and therefore are less tightly bound to the polar group. This can potentially enhance cations transport of K^+ (investigated in this thesis) within the polymer host as compared to smaller cations (Li^+ or Na^+).[161,162]

Initially, it was assumed that ion transport in solid polymer electrolytes takes place *via* a hopping mechanism, similar to that in solid-state ceramic inorganic electrolytes, where the immobile ceramic lattice supports ion hopping through point defects.[166] Although A^+ hopping can occur in polymeric crystals with an ordered structure, this is not the most favorable pathway for ion transport in polymers. Several factors contribute to this: A^+ cations are strongly bonded to the coordinating groups of the polymer and/or the ions free path for hopping is significantly larger compared to that in inorganic electrolytes. For the ion hopping mechanism, the relationship between temperature and ionic conductivity (as a metric of ion transport) can be derived from the Arrhenius equation and expressed as the **Equation 3**:

$$\sigma = \sigma_0 \exp\left(-\frac{E_a}{K_B T}\right) \quad \textbf{Equation 3}$$

where σ represents ionic conductivity, σ_0 is pre-exponential factor, E_a is the activation energy, K_B is the Boltzmann constant, and T is the absolute temperature.

When the temperature dependence of ionic conductivity follows the Arrhenius relationship, the ion transport mechanism can be assigned to that observed in ionic crystals, where ions jump to

the nearest vacant sites independently of the segmental motion of the surrounding environment (*uncoupled* to segmental motion ion transport). Several studies reported Arrhenius behaviour for SPEs based on poly(vinyl pyrrolidone) containing $KClO_4$,[167] poly(vinyl alcohol) (PVA)-$LiClO_4$ and chitosan-PVA-NH_4NO_3 systems.[168,169] Ion hopping was also observed in the crystalline phases of PEO with alkali metal salts, facilitating the transport of Li^+, Na^+, K^+, and Rb^+ cations.[170–173] In these structures, PEO chains form tunnel-like configurations around the cations, creating well-defined ion transport channels, with anions positioned on the outer space. Although it was initially assumed that ion transport in such structures could be highly selective for cations, subsequent studies revealed that in crystalline PEO_8-$NaAsF_6$ electrolytes ion transport was dominated by anions.[173]

Alternatively to the hopping between fixed coordination sites, ion transport in amorphous phase of semi-crystalline SPEs can be described as a continuous ion exchange within the constantly evolving solvation shell of the ion coordinated by the polymer (as illustrated in **Figure 4**), i.e. *coupled* mechanism of ion transport.

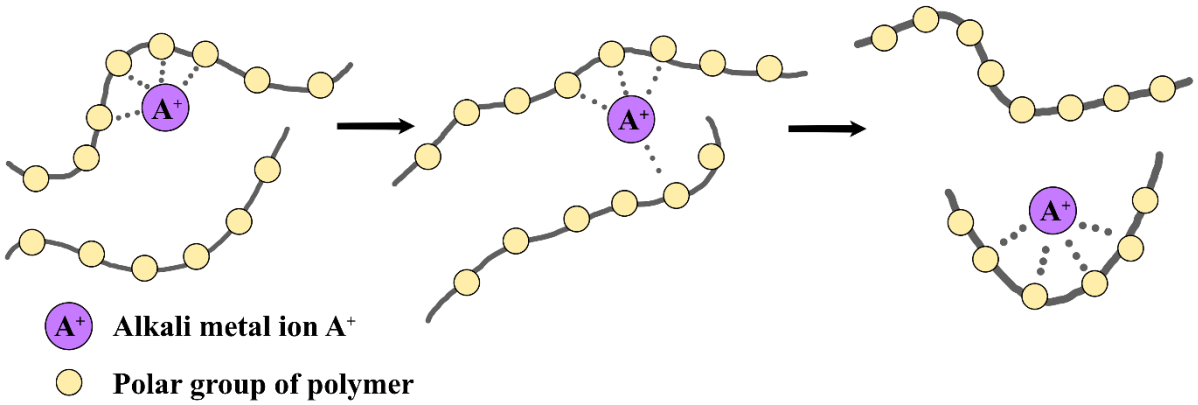

Figure 4. A schematic illustration of the *coupled* ion transport mechanism for alkali metal ions A^+ within a polymer matrix, facilitated by the continuous coordination and re-coordination by polar groups along the polymer chain. Adapted from the reference.[174]

It is important to highlight that *coupled* ion transport in polymer electrolytes differs from the mechanism observed in liquid electrolytes, where ions move along with their solvation shells *via* the *vehicular* mechanism. Due to the large molecular weights of polymers, polymer chains are generally considered macroscopically immobile (non-diffusive) solvents (on a typical experimental timescale).[152] Since A^+ transport is *coupled* to the segmental motion of the polymer, it is strongly dependent on chain dynamics and occurs only at temperatures above the glass transition temperature, T_g. As a result, the temperature dependence of ionic conductivity

does not follow Arrhenius behaviour but can be more accurately described by the Vogel-Fulcher-Tammann (VFT) equation:[175–177]

$$\sigma = \sigma_0 \exp\left(-\frac{B}{T-T_0}\right) \qquad \textbf{Equation 4}$$

where B represents the pseudo-activation energy for conductivity, and T_0 is known as «Vogel temperature» (experimentally established ca. 50 K below T_g of a polymer). T_0 is considered as the temperature at which segmental motion ceases. The VFT model aligns with the free volume theory,[30] postulating that higher ionic conductivity can be achieved when larger degree of free space is available for the chains movements. This theory is supported by data from studies on the total ionic conductivity of PEO-LiTFSI SPEs with varying concentrations of salt.[178] Initially, ionic conductivity enhances along with the increase of number of charge carriers and the addition of a plasticizer (represented by bulky anions) that creates free volume. However, at higher salt concentrations, conductivity typically decreases. This is associated with the formation of large degree of cation-chain coordinative bonds (named ionic cross-linking)[179,180,181] that lower free volume of the system and restrict segmental motion, typically resulting in the increased T_g.

It should be noted that in some cases high salt concentrations can lead to the formation of ionic clusters that act as plasticizers, thereby lowering the T_g. When approaching salt concentration above 50 wt.% (polymer-in-salt electrolyte, PISE, illustrated in **Figure 5**), a *percolation* network[182] can be formed, resembling the properties of a plasticized salt or an ionic liquid.[183,184]

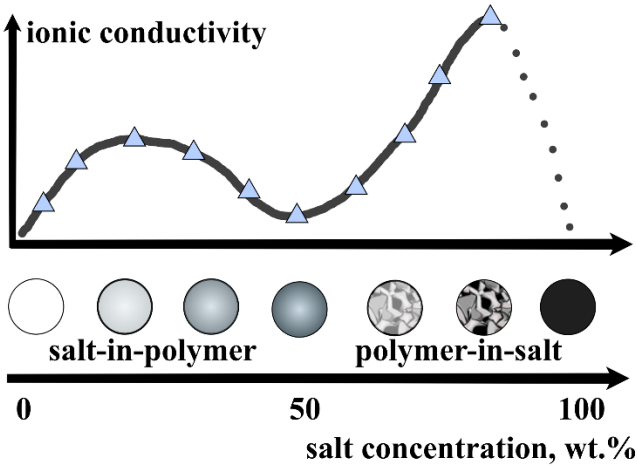

Figure 5. A schematic illustration of ionic conductivity dependency on electrolyte salt concentration for different regimes of polymer/salt concentrations. Adapted from the reference.[25]

In such systems, ion transport likely occurs through ion hopping within the salt clusters that form a continuous *percolation* network throughout the material. Compared to the conventional salt-in-polymer electrolyte regime, this *percolation* transport mechanism can result in significantly higher ionic conductivities. For instance, Mindemark *et al.*[185] reported that PISE PTMC-NaFSI (with 66.3 wt.% of salt) exhibited an ionic conductivity as high as 5×10^{-5} S cm^{-1} at 25 °C, exceeding that of salt-in-polymer electrolytes by ca. three orders of magnitude.

It is important to emphasize that ion transport in SPEs is closely related to the strength of ion coordination. Since ion transport occurs through a series of solvation and desolvation events as ions migrate between different coordination sites, the local coordination environment has a crucial impact on the A^+ transport that is favored in polymeric architectures where the ion binding strength is relatively weak. This concept has been explored and proved in several studies by Andersson and co-authors and will be discussed in detail in the following sections.[64,65,186]

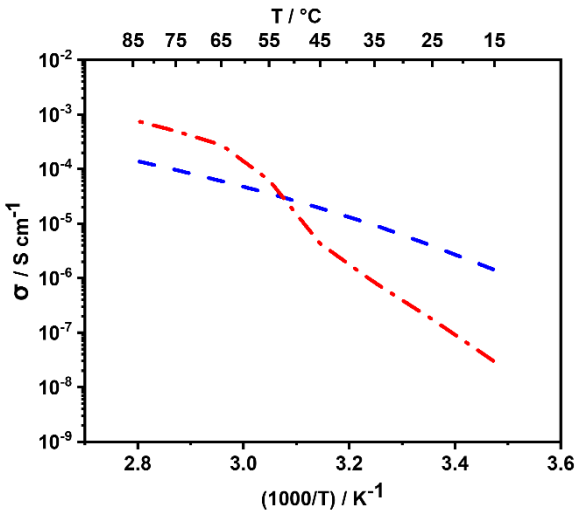

Figure 6. Example of different types of temperature dependence of ionic conductivity of SPEs. Red dash-dot line represents conductivity behaviour of semi-crystalline PEO-KTFSI (with molar ratio of EO:K = 8:1), and blue dash line is the data observed for amorphous poly(vinyl benzyl methoxy poly(ethylene oxide) ether)-*block*-polystyrene mixed with KTFSI (EO:K = 15:1). Representative data is derived from temperature-dependent EIS measurements conducted in the frequency range from 1 MHz to 500 mHz with a voltage amplitude of 10 mV.

To summarize, different mechanisms of ion transport can occur in solid polymers electrolytes, influenced by the structure of polymer, chain dynamics and experimental conditions. As a result, in practice the temperature dependence of ionic conductivity of SPEs is complex, thus

for semi-crystalline polymers a VFT behaviour is typically observed at temperatures above melting (above T_m) of the crystalline phases (red dash-dot line in **Figure 6**).

2.3. Key Metrics of SPEs

2.3.1. Total Ionic Conductivity

The ability to transport ions in an electrochemical system is a crucial characteristic of an electrolyte, and thus its total ionic conductivity, σ, is a key parameter to be determined. It is well known that the main bottleneck of polymer electrolytes is their relatively low ionic conductivity as compared to liquid or solid ceramic electrolytes (10^{-5}-10^{-6} vs. 10^{-2}-10^{-3} S cm^{-1} at room temperature).[152] Numerous research efforts have been focused on addressing this challenge, including such approaches as polymers cross-linking,[187,188] the addition of plasticizers[31,32,33] or nanofillers,[189,190,51,52] or design of polymers with advantageous structures that enable low T_g.[191,192]

Ionic conductivity can be generally described using the equation:

$$\sigma = \sum_i^n n_i q_i u_i \qquad \textbf{Equation 5}$$

where σ represents total ionic conductivity, n_i is the concentration of the charge carrier, u_i stands for their mobility, and q_i is the charge of the carriers. Following this equation, higher ionic conductivity can be achieved when increased number of charge carriers is introduced to the system, possessing high ionic mobility. However, as discussed above (**Section 2.2**), for polymer electrolytes this is not so straightforward as the concentration of charge carriers affects the dynamics of the polymer chains, which is a key parameter of *coupled* ion transport mechanism. According to free volume theory,[30,193] polymers with a lower T_g are considered promising electrolytes in terms of their enhanced ionic conductivity. When larger space is provided for the chains movements, more beneficial chain dynamic can be realized, allowing faster cations transport *via* inter- and intra (re)coordination of A^+ by polar groups of the polymer. From this perspective, developing polymer host materials with the lowest possible T_g can be seen as an approach for enhancing ionic conductivity. However, there are challenges associated with materials that feature low T_g, and these will be discussed in detail in the following subsection (**Subsection 2.3.3**).

On the other hand, a low degree (or even the absence) of crystalline phases in the polymer matrix is preferred to achieve improved ionic conductivity[32,194,195] (not true for certain PISEs, where *percolation* mechanism is realized). Thus, for well-studied PEO-LiTFSI electrolytes, the highest ionic conductivity was found in so called «crystallinity gap», i.e. in the range of EO:Li molar ratios that shows the absence of crystalline phases (6 < EO:Li < 12).[196,197] It was reported

that PEO-KTFSI compositions (studied in this thesis), contrary to their LiTFSI counterparts, remain partly crystalline over a wide range of molar ratios (1.5 < EO:K < 60),[196] and therefore show lower room-temperature ionic conductivity. In attempt to enhance ionic conductivity, semi-crystalline SPEs are typically operated above the melting point of the polymer phase,[25] which leads to a significant loss of their mechanical strength.

In SPEs total ionic conductivity can be measured using electrochemical impedance spectroscopy (EIS). In brief, the fundamental basics of the method as well as the technique description are given in **Section 3**.

2.3.2. Transference Number

Total ionic conductivity is indeed a key metric of electrolytes, however being not a comprehensive parameter without measuring transference number. As stated above, ion-containing $A^+(An)^-$ salt (where A^+ represents alkali metal cation, and $(An)^-$ is its counter anion) should be dissolved in a polymer host material. In an ideal electrolyte, the salt should be completely dissociated into free ions that move *via* diffusion and migration modes of mass transport independently, i.e. without mutual interference. These assumptions can be met in infinitely dilute solutions, where the solvent has a high dielectric constant. In non-ideal solid polymer electrolytes, various equilibrium reactions can coexist in the polymeric media, providing such species as: A^+, $A_2(An)^+$, An^-, $A(An)_2^-$, $A_n(An)_m^{(n-m)}$, etc. In this case, the cation is driven towards the cathode by positively charged species and towards the anode by negatively charged species.[198] In practical electrolytes, the A^+ transference number can be described as:

$$T_A = t_{A^+} + 2t_{A_2(An)^+} - t_{A(An)_2^-} + (n\text{-}m)t_{A_n(An)_m^{(n-m)}} \quad \textbf{Equation 6}$$

Hence, the A^+ transference number, T_{A^+}, is defined as the number of moles of A transferred in one direction by migration per Faraday of charge.[25] It should be noted that T_{A^+} differs from transport number, t_+, which refers to the fraction of the current transferred by specific species. When no ion association occurs, i.e. in ideal electrolytes, transference and transport number can be considered equal.

Since A^+ is involved into electrochemical redox processes, achieving a high T_{A^+} is crucial for an electrolyte as it indicates that total ionic conductivity is primarily due to A^+ mobility. When an electric field is applied, both cations and anions migrate in opposite directions. In a system with anion-blocking electrodes, anions accumulate at the anode and are depleted at the cathode, leading to the formation of a concentration gradient that drives anion diffusion. At steady-state, anion transport is dominated by diffusion ($T_{An^-} = 0$), while only A^+ species contribute into migration ($T_{A^+} = 1$). Consequently, the steady-state current serves as a key parameter in

determining the maximum current that an electrolyte can sustain under anion-blocking conditions.[199] A high T_{A^+} is critical to supporting cell reactions at high charge or discharge rates, preventing unfavorable electrode-electrolyte interfacial processes (such as salt precipitation on the electrode surface under high current), which accelerates capacity fade.[200] Moreover, it was reported that a low transference number promotes dendrites formation.[201,202] Monroe and Newman[202] reported that enhancement of transference number may suppress the dendrite growth by eliminating the concentration gradients across the cell, especially at the dendrite front. Therefore, enhancing T_{A^+} in polymer electrolytes is essential for operating cells with high-energy density and ensuring significant capacity retention. However, for well-studied Li^+-containing salts in PEO, T_{Li^+} is typically below 0.3,[203] and can be improved by such approaches as filler addition.[204]

The most commonly used method for transference number determination is Bruce-Vincent method[205] employed in this thesis and discussed in detail in **Section 3**. However, when evaluating T_{A^+} of solid polymer electrolytes, the accuracy of Bruce-Vincent method becomes questionable due to the large interfacial resistances of SPEs in symmetrical metal cell, which can influence the calculated value for the transference number. This issue is even more pronounced when transitioning from Li^+ to Na^+ or K^+, most likely due to their higher reactivity.[206,207] Alternative methods, such as Watanabe method,[208] Sørensen and Jacobsen approach,[209] pulsed-field gradient nuclear magnetic resonance (PFG-NMR)[210] are also reported. However, it is important to stress that these methods are reliable in ideal electrolytes, when ion-ion interactions are negligible in dilute systems. In concentrated systems, the concentration gradient facilitates the diffusion of ion pairs/associations, which in turn leads to an overestimation of T_{A^+}. Noteworthy, recent experimental advancements have revitalized electrophoretic NMR, enabling the determination of ion mobilities even in highly concentrated A^+-based ion-conducting polymer electrolytes.[65,186]

2.3.3. Ionic Conductivity vs. Mechanical Stability

Mechanical stability is required for SPEs since they function as both: electrolytes and separators between the cathode and anode in the cell configuration, thus suppressing dendrites formation and preventing short circuits.[148,149–151] As previously stated, ion transport in solid polymer electrolytes is typically realized *via coupled* mechanism that is highly dependent on polymer chain dynamics. Thus, the polymers with low T_g values are preferable for SPE applications since these exhibit relatively high ionic conductivities. However, when considering mechanical integrity, a low T_g often appears to be disadvantageous due to the resulting material softness.

In general, mechanical stiffness in SPEs can be provided *via* ion-polymer interactions and/or ensured by crystalline phases, coexisting with amorphous regions in semi-crystalline electrolytes.[147] In both cases, the chain dynamic of the polymer is restricted, posing a challenge to the development of polymer electrolytes that simultaneously offer high ionic conductivity and strong mechanical integrity. Commonly known strategies to improve mechanical integrity of polymer electrolytes include for example the addition of ceramic nanofillers,[189,190,51,52] chemical cross-linking[188,211], or the utilization of multiphase structures as in graft or physical cross linking *via* block copolymeric materials,[58,181,212,213,214] where mechanical stiffness is guaranteed by a high T_g block and ion transport is enabled *via* another block with a low T_g.
Most polymer electrolytes utilized for SPE applications display viscoelastic properties[215] that can be investigated using rheological shearing (small amplitude oscillatory shear test was employed in this thesis, see in **Section 3).** The storage (G') and loss (G'') moduli can be examined and their dependency on frequency reveals whether the material exhibits solid-like (required for SPE) or liquid-like properties.[216,217]

2.3.4. Electrochemical Stability

For the application of polymer-based materials as electrolytes in electrochemical systems, e.g. potassium-ion batteries, it is crucial that PEs not only exhibit high ionic conductivity and mechanical stiffness but also offer electrochemical stability. The electrochemical stability of SPEs is often evaluated through their electrochemical stability window, ESW, which is defined as the potential difference between the oxidation and reduction of the electrolyte. This corresponds to the difference between the lowest unoccupied molecular orbital (LUMO) and the highest occupied molecular orbital (HOMO).[218] It is important to note that HOMO and LUMO are individual molecular properties dependent on the electronic structure of isolated molecules, whereas redox potentials are thermodynamic properties. This means that redox potentials are influenced not only by the molecules themselves but also significantly by the reaction products formed. This distinction often leads to a common misconception in the literature, where the ESWs of polymer electrolytes are misinterpreted as HOMO/LUMO gaps and calculated using DFT,[147,219] resulting in unrealistically large ESW values that weakly correlate with the reduction/oxidation potentials. Estimating the ESW of polymer electrolytes is further complicated by the fact that salt-polymer complexes have their own distinct redox potentials, which differ from the properties of the salt and polymer individually. Therefore, it is recommended to avoid using HOMO and LUMO concept when describing the electrolyte stability. Instead, discussions should focus on the reduction potential of the electrolyte at

negative potentials and the potential of oxidation at positive potentials.[220] Plating and stripping experiments in symmetrical alkali metal cells can be utilized to estimate the practical stability of SPEs at the negative electrode (details provided in **Section 3**). However, these experiments do not offer a complete understanding of stability of electrolytes at low potentials. In practice, techniques such as cyclic voltammetry (CV) and linear sweep voltammetry (LSV) are commonly used to determine the upper and lower potential limits of the ESW. Both methods implement a cell setup comprising a working electrode, an electrolyte, and a counter-reference electrode (typically an alkali metal). The working electrode must be inert within the potential range being investigated, thus copper is often used for low potential ranges, while stainless steel is more suitable for high voltage applications. Cyclic voltammetry provides insights into redox processes by applying a linear potential using a triangular waveform. During the potential sweep, the current generated by electrochemical reactions is measured. An increase in current indicates electrolyte degradation at the working electrode surface and can be seen as an electrochemical stability limit for the electrolyte. Unlike CV, LSV involves only a forward potential scan, without a backward scan. While voltammetry techniques do offer qualitative information about the stability of polymer electrolytes, data interpretation (precise ESWs evaluation) can be challenging.[221,222] Determining thermodynamic redox potentials is straightforward for reversible reactions, but it becomes problematic for irreversible reactions. Additionally, the relatively low ionic conductivity of SPEs can negatively impact the accuracy of these experiments. Thus, the challenges discussed above lead to to a poor correlation between the ESWs reported for SPEs and their electrochemical stability in real electrochemical systems.[223–225]

2.4. Choice of Polymer for SPE

As previously discussed in **Sections 2.2** and **2.3**, a polymer electrolyte is obligated to exhibit a balanced combination of physical and electrochemical properties, such as a low T_g, a high fraction of the amorphous phase, solid-like characteristics, and a favorable trade-off with ionic conductivity and electrochemical stability. These factors are crucial for ensuring the feasibility of applications. This section aims to provide a critical review of the most extensively studied candidates for SPE applications, highlighting their advantages, shortcomings, and strategies to overcome these disadvantages.

2.4.1. The «Standard» Poly(ethylene oxide) (PEO)

Poly(ethylene oxide), PEO, is the most extensively studied semi-crystalline polymer host material that has been discovered 50 years ago[26] (a «grandfather» of the SPEs field). Since its discovery, it has become the most frequently used polymer matrix for alkali metal salts dissolution.[29,178,226–228] It is for a good reason: the electronegative oxygen of the ether unit was proven to be an excellent coordinating species, enabling PEO to dissolve large amounts of electrolyte salts. At temperatures below T_m of crystalline phase of PEO (~60 °C),[229] A^+ can be transferred either along the polymer chain (i.e. intrachain hopping) or between chains (i.e. interchain hopping), illustrated in **Figure 7**.

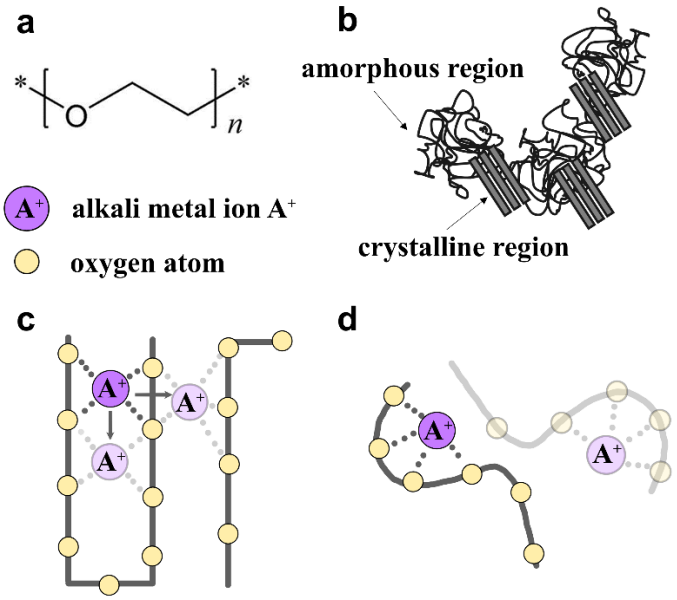

Figure 7. **(a)** Structure of poly(ethylene oxide), PEO. A schematic illustration of **(b)** semi-crystalline nature of PEO consisting of both amorphous and crystalline regions; ion transport in PEO **(c)** *via* intra- and interchain hopping mechanism; **(d)** *via* segmental motion of the polymer chains, *coupled* mechanism.

Although, even in the crystalline state of pure PEO there is an ionic mobility within the crystallites due to jump motions along the helical screw,[230] the favourable mechanism of ion transport is realized *via* the amorphous phase (*coupled* mechanism).[32] An advantage of the amorphous phase of PEO is its low glass transition temperature ($T_g \approx$ -60 °C)[25] that enhances the polymer free volume, chains flexibility, and potentially advances ion transport.

However, PEO is predominantly crystalline, showing the degree of crystallinity of 70-80 wt.% in its pure state (at temperatures below T_m).[231] This adversely impacts ion transport at ambient temperatures, resulting in low values of ionic conductivity (e.g. 10^{-6}-10^{-8} S cm^{-1} when mixed

with A^+-salts).[218] In addition, for the most intensively studied Li^+-PEO complexes, a high-energy of coordination bond leads to a strong interaction between Li^+ and the ether units, hindering ion transport. Earlier researches on the cation coordination of PEO-$A^+(An)^-$ complexes (A^+ = Li, Na, K, Rb; $(An)^-$ = SCN, ClO_4, CF_3SO_3) suggested changes in the coordination number and PEO chain conformation for cations with radii larger than that of Li^+.[163,164,165] Thus, Bruce *et al.*[163] investigated PEO-based complexes incorporating $LiCF_3SO_3$, $NaClO_4$, KSCN, RbSCN salts. The total coordination number increased along with increasing ionic radii of the cations and equaled to 5, 6, and 7 for Li^+, Na^+, and K^+, respectively. Moreover, weaker ion-polymer binding was observed as the coordination number increased due to the polymer adjusting its conformation to accommodate the larger cations.This could potentially benefit faster cation transport in K^+ conductors, compared to Li^+-PEO.[161,164,165,232]

Chandra *et al.*[233] reported ionic conductivities for PEO-KBr SPEs with various content of K^+-salt, fabricated using a solvent-free hot-pressing method. They observed an increase of σ along with the addition of KBr, reaching its maximum for the formulation with 30 wt.% of the salt (~5×10^{-7} S cm^{-1} at 25 °C). This aligns with the common understanding that ionic conductivity raises with an increase of charge carriers and simultaneous decrease of PEO crystallinity. However, as the salt concentration increased further, the authors detected a decline in σ, which can be attributed to reduced polymer free volume caused by K^+-EO cross-linking. Additionally, when the KBr concentration exceeded 50 wt.%, the SPE films became brittle and less flexible (PISE regime). The same authors examined K-SPEs based on PEO-KCl compositions.[234] Similar pattern of ionic conductivity dependency on KCl concentration was reported with the maximum of σ for the sample containing 30 wt.% of the salt (~5×10^{-7} S cm^{-1} at 25 °C). Literature values for a PEO-based electrolyte employing the FSI-salt were recently provided by Fei *et al.*[146] Therein, it was reported that PEO-KFSI (with molar ratio of EO:K = 10:1) possessed the highest ionic conductivity of 1.14×10^{-5} S cm^{-1} at 40 °C. Compared to K^+-containing PEO-based SPEs, Li^+-PEO complexes generally show higher ionic conductivities, such as 3.54×10^{-5} S cm^{-1} at ambient temperature for PEO-LiTFSI system.[235] However, it is crucial to consider the ion transference number when evaluating ion transport. For PEO-ATFSI (A = Li, Na, K) systems, Oteo *et al.*[161] recently reported similar ionic conductivities but a higher Na^+ transference number, T_{Na^+}, than for the Li-system (T_{K^+} was not determined). Using molecular dynamics simulation, Fortuin *et al.* found coordination numbers of 6, 7 and 8 for the PEO-LiTFSI, -NaTFSI, -KTFSI complexes (EO:A = 20:1), respectively. They confirmed a weaker coordination strength (increased coordination distance) for larger cations, which was reflected in their higher cationic mobility.[236]

Among other characteristics, the electrochemical stability of PEO is an important parameter, especially when paired with reactive metallic negative electrode. Although early studies suggested that in SPEs based on solely PEO no degradation processes occur up to the voltage of 4.2 V vs. Li^+/Li,[29,222] further research revealed that this wide ESW was overestimated because of kinetic polarization.[237] Subsequent investigations demonstrated that the oxidation of PEO-SPEs begins around 3.8 V vs. Li^+/Li,[218] which limits their compatibility with high-voltage cathodes.

As discussed in this subchapter, (1) susceptibility of PEO to degradation at high voltages, (2) its partial crystalline nature that results in low ionic conductivities display the major challenges within this material. Although ionic conductivity in the PEO-based SPEs can be adjusted *via* the addition of electrolyte salt, this often comes at the expense of mechanical strength, which is critical for SPE applications. To enhance the amorphous phase and thereby improve the ionic conductivity of PEO, while maintaining its mechanical strength, different approaches can be employed. Such approaches as modifying PEO with inorganic nanofillers,[189,190,51,52] as well as design of copolymeric materials[58,181,212,213,214] will be reviewed in the following subchapters.

2.4.2. PEO with Inorganic Fillers

Filler-modified SPEs can be characterized composite polymer electrolytes composed of inorganic (ceramic) nanofillers distributed in polymer matrices along with incorporated A^+-containing salts. As stated in the previous subsection, the addition of inorganic nanofillers serves as a strategy to enhance the overall performance of SPEs by increasing ionic conductivity, improving mechanical integrity as well as interfacial stability. The nanofillers can be classified as either active or passive fillers based on the presence or absence of corresponding A^+ in their structures, respectively. With the incorporation of active fillers, such as Li_3N,[41,42] $LiAlO_2$,[43] $NaAlO_2$,[44] $Li_{1+x}Al_xGe_{2-x}(PO_4)_3$,[238] $Li_{1+x}Al_xTi_{2-x}(PO_4)_3$,[239,240] $Na_3Zr_2Si_2PO_{12}$,[241] $Li_7La_3Zr_2O_{12}$,[242,243] etc., a strong enhancement of ion transport is expected. This is attributed to the high inherent bulk ionic conductivity of the ceramics, where multiple ions hopping is facilitated by continuous structural defects, resulting in reduced migration energy barriers.[244]

In the case of passive fillers, such as Al_2O_3,[45–49] SiO_2,[47,245–247] TiO_2,[245,248] ZnO,[229,249] ZrO_2,[250,251] the mechanisms behind the enhancement of ionic conductivity are not yet fully understood. However, several theories attempt to explain this phenomenon. The hypothesis involves specific interactions between the surface groups of the ceramic particles and the polymer groups as well as the A^+-salt anions.[51] These interactions are often interpreted through the framework

of Lewis acid-base interactions, suggesting that the ceramic surfaces may act as a Lewis acid, Lewis base or neutral species (**Figure 8**).

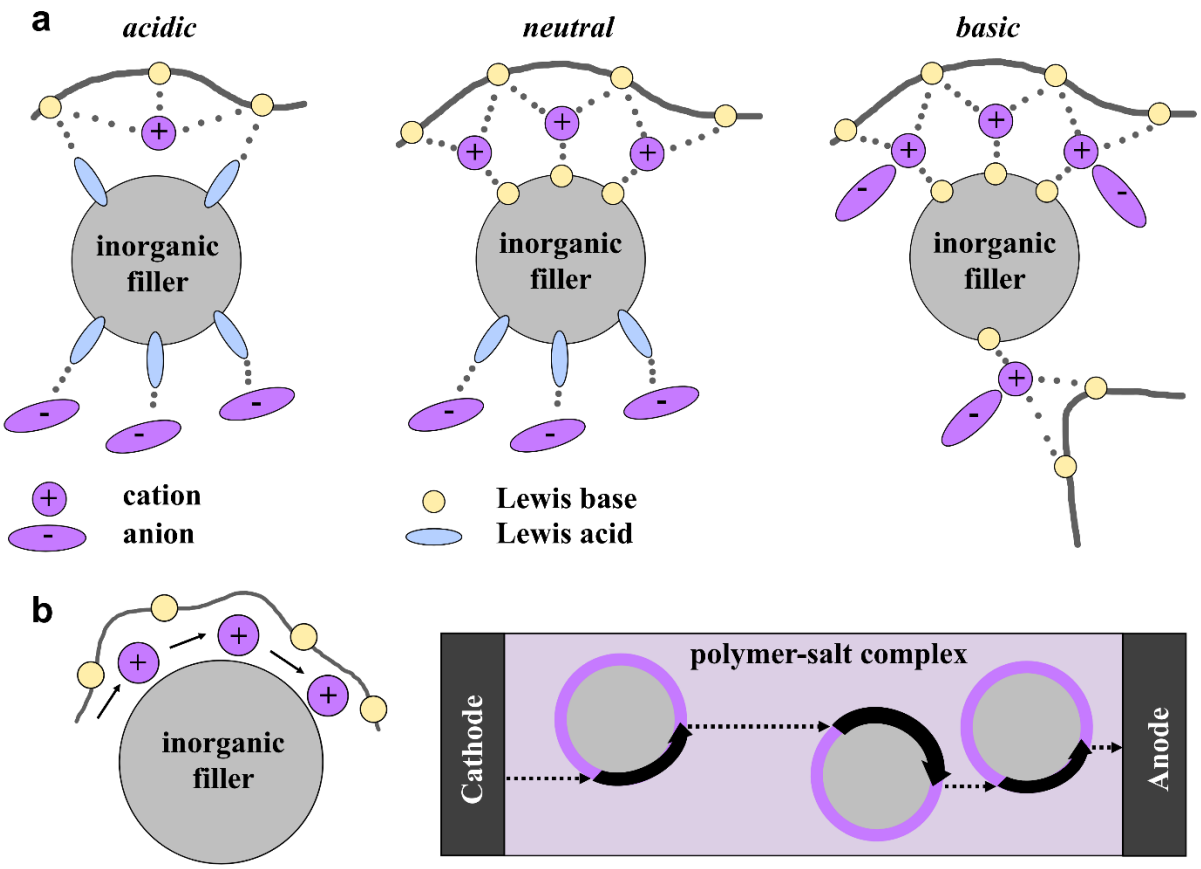

Figure 8. **(a)** A model based on Lewis acid-base interactions between the surface groups of an inorganic filler, polymer and A^+-containing salt. **(b)** A schematic illustration of express channels for A^+ transport formed *via* Lewis acid-base interactions. Adapted from the references.[51,52]

As shown in **Figure 8**, when the filler surface feature an acidic nature, Lewis acid-base interactions can form between the surface and the anion of the A^+-containing salt as well as with the polymer basic segments (e.g. ether units of PEO). In contrast, surfaces with basic properties may compete with A^+ to complex with Lewis basic segments of the polymer chains.[52] In theory, higher transference number T_{A^+} can be achieved when the acidic centres of the ceramic interact with the anions, immobilizing them and thereby lowering ion-ion coupling in the system. Moreover, the ceramic surface can function as a cross-linking centre for the polymer chains, inhibiting polymer recrystallization and promoting the formation of express channels for A^+ transport. Based on this, for the acidic nature of the inorganic filler, structural

modifications are expected to be more beneficial for enhancing ion transport in composite polymer electrolytes (**Figure 8**).

Park *et al*. studied the impact of Al_2O_3 nanoparticles with activated acidic, basic and neutral nature on the PEO-$LiClO_4$ compositions.[46] Their findings indicated that composites containing acidic and neutral Al_2O_3 exhibited enhanced ionic conductivity as well as electrochemical stability. This effect was mainly associated with the hydrogen bonding between the filler surface and ClO_4^-. In a separate study, Huo *et al.*[252] proposed a novel cationic metal-organic framework containing RNH_2 and $R(N)^+CH_3$ within its structure. The incorporation of this additive to PEO-LiTFSI matrix led to several notable outcomes. A high transference number T_{Li}^+ of 0.72 was achieved, in contrast to T_{Li}^+ of 0.28 for a corresponding filler-free PEO-LiTFSI. The Lewis acid groups on the surface of ceramic particles competed with Li^+ to complex with $TFSI^-$, which led to a higher degree of LiTFSI dissociation. This mechanism increased the concentration of free Li^+ available for ion transport. Moreover, for the modified PEO-LiTFSI the electrochemical window was extended up to 4.97 V. The authors associated the effect with the hydrogen bonds formed between ether oxygen of PEO chains and -NH_2 groups, leading to a protected ether oxygen and stable composite structure at high voltages. Croce *et al.*[53] also observed an increase of T_{Li}^+ in the PEO-$LiClO_4$ system upon the incorporation of 10 wt.% of TiO_2. The T_{Li}^+ value reached 0.6 within the temperature range of 45-90 °C, whereas in ceramic-free SPEs this value typically ranged between 0.2 and 0.3. Thus, the increase of T_A^+ can be attributed to enhanced cation mobility through the formation of rapid transport channels facilitated by polymer-ceramic interactions, a reduction in anion mobility due to anion-ceramic interactions, or a combination of both mechanisms. Noteworthy, hydrogen bonding between the polymer chain and ceramics can also be seen as an advanced mechanism, contributing to the improvement of electrochemical stability.[253,254]

Another benefit of incorporating inorganic nanofillers is their impact on glass transition temperature T_g and the crystallinity degree of polymer-based composites. Li *et al.*[255] designed and examined SiO_2-filled composites based on chitosan, PEO and LiTFSI. They reported that T_g dropped by 3 °C as the SiO_2 content increased from 1 to 4 wt.%. These findings are consistent with other studies evaluating the change of T_g upon the incorporation of inorganic fillers into polymeric matrix.[256–258] The decline of T_g is often accompanied by a decrease in the degree of crystallinity of polymeric materials. This can be explained by the polymer-ceramic interactions that reduce intermolecular forces, contributing to disorder of the polymer chains and simultaneous enhance of their mobility. Furthermore, the addition of inorganic fillers can increase the free volume of the polymer as the fillers act as plasticizers. Although the proportion

of the crystalline phase is reduced, the mechanical integrity of the composite polymer electrolytes is maintained through cross-linking interactions between the polymer chains and the ceramic particles.

It is important to emphasize that the impact of inorganic filler incorporation has been primarily studied in Li^+-conducting systems, while specific considerations are required for K^+-containing SPEs. The Lewis acid-base interactions between the ceramic particle surface and the salt can promote salt dissociation. However, the dissociation energies of NaTFSI and KTFSI are lower than that of LiTFSI (~590 kJ mol^{-1} (LiTFSI), ~490 kJ mol^{-1} (NaTFSI) and ~425 kJ mol^{-1} (KTFSI)).[161] As a result, the benefits of such interactions may diminish as the dissociation energies decrease. However, evaluating the impact of nanofiller incorporation in the context of K^+-SPEs is a scientifically relevant task.

2.4.3. Copolymer Approach

An alternative strategy for the development of polymer-based electrolytes with favorable ionic conductivity and mechanical stability is the design of advanced copolymer architectures.[259,260,261] As previously mentioned, crystallinity is a critical parameter that affects the dynamics of polymer chains and, therefore, directly impacts ion transport properties. To address this, an early approach in copolymer synthesis involved the incorporation of a controlled amount of comonomer units into semi-crystalline polymers, such as PEO, to reduce crystallinity or entirely suppress the crystallization process.[38,262,263,264] For this purpose, St-Onge and coworkers[265] recently synthesized a series of statistical PEO-based copolymers incorporating propylene oxide (PO), 1,2-butylene oxide (BO), or methyl ether triethylene glycol glycidyl ether (TO) as comonomers (**Figure 9a**). These copolymers with varying molar concentrations of comonomers were synthesized and further studied in SPEs containing LiTFSI. In particular, the introduction of comonomers reduced the T_ms and crystallinity, resulting in an increased amorphous phase content and decreased T_gs (down to -70 °C for the copolymers). The copolymer-based SPEs with 10 mol.% of comonomers and 18 wt.% of LiTFSI achieved the highest ionic conductivities, up to 1×10^{-5} S cm^{-1} at 25 °C, and enhanced cationic transport. This improvement can indeed be attributed to the increase of the total fraction of amorphous phase in the copolymers. However, it is widely reported that the major drawback of highly amorphous (co)polymers is their loss of dimensional stability at room (and elevated) temperature due to the low T_gs at around -65 °C.[39,40]

Another promising approach for developing materials with both high ionic conductivity and sufficient mechanical integrity involves the synthesis of block copolymer electrolytes with a

microphase-separated architecture.[58–60,61] In these systems, ionic conductivity is achieved through the conductive block(s), while microphase separation ensures mechanical stiffness. For example, Xu *et al*.[59] developed and investigated SPEs based on poly(propylene monothiocarbonate)-*b*-poly(ethylene oxide) (PPMTC-*b*-PEO) (**Figure 9b)** block copolymers with LiTFSI.

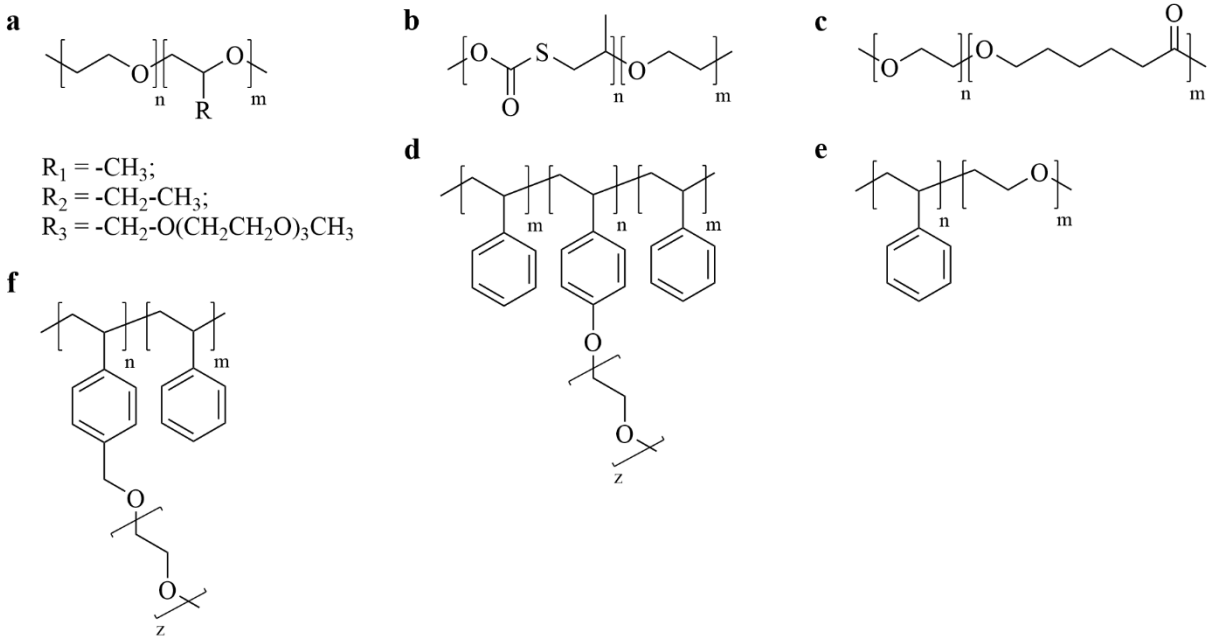

Figure 9. Various structures of copolymers featuring poly(ethylene oxide), PEO, either as a block or as a side chain as published by **(a)** St-Onge *et al*.,[265] **(b)** Xu *et al*.,[59,61] **(c)** Huang *et al*.,[60] **(d)** Wang *et al*.,[266] **(e)** Singh *et al*.,[267] **(f)** Butzelaar *et al*.[58]

This system featured two conductive phases, and the microphase separation was regulated by the ratio of LiTFSI incorporated into the electrolyte composition. At low salt concentrations, microphase separation occurred due to the preferential interaction of Li^+ with the PEO block. A similar microphase separation behaviour was observed in poly(ε-caprolactone)-*b*-PEO (PCL-*b*-PEO) (**Figure 9c)** SPEs doped with various metal salts, including LiCl, $CuCl_2$, and $FeCl_3$.[60] The PPMTC-*b*-PEO-LiTFSI electrolytes containing two conductive phases demonstrated an ionic conductivity of up to 2×10^{-4} S cm^{-1} at 25 °C, which was approximately one order of magnitude higher than that of single-phase copolymer-based electrolytes. Additionally, microphase separation significantly improved the mechanical properties of the material. The storage moduli, G', of PPMTC-*b*-PEO-LiTFSI electrolytes were found to be 1-4 orders of magnitude higher (~10^5 Pa at 30 °C) than that of neat PEO-LiTFSI electrolytes. Nevertheless,

despite this improvement in mechanical strength, the storage modulus values remained below the threshold required for SPE applications.

Kinetic modeling by Monroe *et al*. demonstrated that metallic lithium dendrite growth can be suppressed when the shear modulus of an electrolyte exceeds 7×10^9 Pa.[149] This threshold based on the principle that the shear modulus of an electrolyte should be approximately twice the G'of Li metal (4.2×10^9 Pa). Noteworthy, since K metal has a lower value of G' (1.3×10^9 Pa), it is slightly easier for an electrolyte to meet the requirement. Based on this concept, the incorporation of a polystyrene (PS) block into block copolymer electrolytes is particularly relevant for mitigating dendrite formation,[148,150,151] as PS exhibits high mechanical stiffness (G', G'' of ~1×10^9 Pa)[268] and maintains this property at temperatures up to 100 °C. When PEO is employed as the conductive block in combination with PS, the mechanical strength of the material decreases relative to pure PS. However, these block copolymers are still significantly more robust than conventional homopolymer electrolytes, with elastic moduli approaching 10^9 Pa.[149] Through self-assembly, block copolymers can form microphase-separated structures, wherein ion conduction occurs within the polar PEO domains, while the non-polar PS domains with high T_g provide mechanical stability. When the composition of these domains is properly balanced (optimized molecular weights of the domains and the ratio between them), the result is mechanically solid block copolymer films providing sufficient ionic conductivity. Early work by Wang *et al*.[266] demonstrated that high molecular weight PS-*b*-(PS-*graft*-PEO)-*b*-PS block-graft copolymer (**Figure 9d)** exhibited a high dynamic Young's modulus, E', of 10^8 Pa, while achieving a modest ionic conductivity of 10^{-5} S cm^{-1} at 25 °C. Similarly, a separate study reported high storage and loss moduli of 10^7-10^8 Pa for PS-*b*-PEO copolymer (**Figure 9e)** electrolytes (100.000 g mol^{-1} > M_n of PEO > 25.000 g mol^{-1}, 75.000 g mol^{-1} > M_n of PS > 40.000 g mol^{-1}).[267] More recently, Zhang and co-authors[269] studied polystyrene-*b*-poly(ethylene glycol)-*b*-polystyrene, PS-*b*-PEG-*b*-PS, triblock copolymers with the additional PS block in the macromolecule structure with varying low molecular weights of PS blocks (M_w of 1.000, 2.500, 4.500 g mol^{-1}). Although a high ionic conductivity (up to 1×10^{-4} S cm^{-1} at 25 °C) was observed for triblock copolymers, they exhibited poor membrane forming ability, most likely due to the PS block molecular weight being below its entanglement molecular weight, which reduces the mechanical properties of the polystyrene domains. Therefore, molecular weight is a critical factor to consider, even when incorporating a rigid PS block for mechanical reinforcement.

In 2021, Butzelaar *et al*. reported the synthesis of a side-chain block copolymer named poly(vinyl benzyl methoxy poly(ethylene oxide) ether)-*block*-polystyrene, PVBmPEO-*b*-PS (**Figure 9f)**.[58] This study employed three different lengths of PEO side chains, comprising 8,

22, and 45 ethylene oxide units, which corresponded to molar masses of 400, 1000, and 2000 g mol^{-1}, respectively. When the two blocks were matched to a weight ratio of 50:50, the resulting PVBmPEO-*b*-PS copolymers exhibited total molar masses of 25.000, 29.000, and 38.000 g mol^{-1} for the copolymers with 8, 22, and 45 EO units, respectively. Notably, when comparing samples with the same LiTFSI ratio, the copolymer with the shortest PEO side chain exhibited an increase in T_g, associated with a higher proportion of PS phase that possesses a high T_g. The material of choice, i.e. the copolymer with the longest PEO side chain, demonstrated microphase separation with long-range order, which contributed to enhanced mechanical stability (G', G'' of ~10^6 Pa) and exhibited ionic conductivity of 1×10^{-5} S cm^{-1} at 25 °C. When paired with different electrodes and active materials, the SPE showed a sufficient resistance to oxidation up to 4.75 V vs. Li^+/Li during potentiostatic and galvanostatic techniques, which is promising for high-voltage cathodes application. To this date, detailed studies on the K-systems with copolymer-based SPEs have not been carried.

2.4.4. Polycarbonates and Polyesters

Polymers containing carbonyl-coordinating groups have been proposed as alternatives to traditional polyether-based host materials, inspired by linear alkyl carbonates commonly used as solvents in liquid electrolytes. Examples include polycarbonates, polyesters, and polyketones (not covered in this subsection as they are beyond the scope of this discussion), which contain carbonyl groups capable of coordinating A^+ in a manner similar to that of the ethylene oxide units in PEO. However, unlike polyether-based SPEs, those based on polycarbonates and polyesters exhibit weaker coordination strength between A^+ and the carbonyl oxygen due to reduced electrostatic interactions with the cations.[62–64] Recent work by Andersson *et al.*[64] investigated the coordination strength of Li^+, Na^+ and Mg^{2+} (all paired with the same anion, $TFSI^-$) in polymer electrolytes based on polyether (i.e. PEO), polycarbonate (poly(trimethylene carbonate), PTMC), and polyester (poly(ε-caprolactone), PCL) (the structures are given in **Figure 10**) using NMR and FTIR spectroscopy. The study revealed that PEO exhibited the strongest ion coordination strength for all cations investigated, while PTMC displayed the weakest coordination strength, attributed to weaker electrostatic interactions with the cations. Another study of the same authors on Na^+, K^+, Mg^{2+} systems[65] confirmed that this weaker coordination in polycarbonates is often associated with higher cation transference numbers T^+. For instance, T_{Li^+} values as high as 0.8 have been reported for PTMC-LiTFSI with a molar ratio of [TMC]:Li = 8:1,[62] a result that stands in stark contrast to traditional PEO-based systems and

even surpasses typical values reported for polyester-based systems. Further details on this topic will follow in the current subsection.

Polycarbonates. The simplest representative of polymeric carbonates is poly(ethylene carbonate) (PEC), which contains two methylene groups and a carbonyl group within its repeating unit (as illustrated in **Figure 10**).

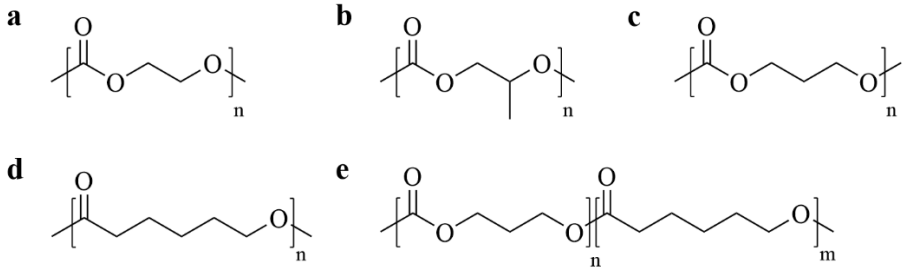

Figure 10. Various structures of polycarbonates: **(a)** poly(ethylene carbonate), PEC, **(b)** poly(propylene carbonate), PPC, **(c)** poly(trimethylene carbonate), PTMC; polyester: **(d)** poly(ε-caprolactone), PCL; copolymer of PTMC and PCL: **(e)** P(CL_m-TMC_n). As published by Brandell *et al*.[147]

The well-controlled synthesis method for polycarbonates, ring-opening polymerization, is not suitable for PEC producing due to the high stability of its five-membered ring.[270] Instead, PEC can be synthesized *via* the copolymerization of carbon dioxide with ethylene oxide, yielding a fully amorphous polymer with a T_g of ca. 9 °C.[271] Notably, this relatively high T_g can be significantly reduced by incorporating Li^+-containing salts in PEC. Tominaga *et al*.[272] reported that while the addition of salts such as $LiCF_3SO_3$ and $LiClO_4$ resulted in PEC-based electrolytes behaving as typical SPEs, salts like $LiBF_4$, LiBETI, LiFSI and LiTFSI demonstrated a plasticizing effect on the polymer. For instance, a PEC-LiTFSI complex with 80 wt.% of salt exhibited a significant T_g reduction down to -62 °C, resulting in $\sigma = 5\times10^{-6}$ S cm^{-1} at 30 °C for this PISE. Similarly, a high ionic conductivity of 4×10^{-4} S cm^{-1} was observed at 40 °C for a PEC-LiFSI complex with a molar ratio of [EC]:Li = 0.53:1.[273] The increase in σ with higher salt concentrations suggests a *percolation*-type ion transport mechanism. However, the conduction mechanism also involves elements of both *percolation* and *coupled* segmental motion mechanisms of ion transport, as the reduced T_g facilitates faster ion mobility. A similar trend of decreasing T_g with increasing salt concentration was observed for poly(propylene carbonate) (PPC) (**Figure 10**).[274] However, the plasticizing effect of electrolyte salts, combined with weak ion-polymer interactions, resulted in a complete loss of mechanical stability in PEC- and PPC-based electrolytes. Moreover, upon contact with lithium metal PPC degraded to

micromolecular segments and depolymerized to propylene carbonate[275], likely due to the high stability of five-membered cyclic carbonates. This behaviour is also assumed to occur in PEC. In contrast to five-membered cyclic carbonates, those containing six-membered undergo well-controlled ring-opening polymerization, resulting in the formation of polycarbonates of the PTMC type. PTMC is typically an amorphous polymer with a T_g of -15 °C at high molecular weights.[147] Noteworthy, the mechanical stability of PTMC-based electrolytes is maintained by their high molecular weights. Unlike PEC-LiTFSI/LiFSI complexes, PTMC-based systems exhibit behaviour similar to polyether-based electrolytes. In 2014, Sun *et al*. investigated the conductivity of PTMC-LiTFSI polymer electrolytes across a wide range of LiTFSI concentrations (2 < [TMC]:Li < 21).[276] A decrease in T_g was observed as the [TMC]:Li molar ratio approached 5:1, followed by an increase at higher salt concentrations. The highest σ was observed for [TMC]:Li molar ratios of 13:1 and 8:1, with values on the order of 10^{-7} S cm^{-1} at 60 °C and 10^{-9} S cm^{-1} at 20 °C. The results indicated that increasing the LiTFSI concentration beyond these ratios did not enhance ionic conductivity, suggesting that PTMC-LiTFSI electrolytes did not offer the *percolation*-type ion transport mechanism. In contrast, Mindemark *et al*. studied PTMC-NaTFSI electrolytes within a molar ratio range of 3 < [TMC]:Na < 60.[277] Their findings showed an almost linear increase in T_g with increasing salt concentration. The highest ionic conductivity was achieved for the [TMC]:Na molar ratio of 3:1, reaching ca. 10^{-8} S cm^{-1} at 20 °C. The combination of good mechanical stability and elevated ionic conductivity at higher temperatures enabled the operation of a solid-state sodium cell comprising a Na-metal anode and a PBA-based $Na_2Fe[Fe(CN)_6]$ cathode, using PTMC-NaTFSI as the SPE. The cell demonstrated stable cycling over 8 cycles at 60 °C and a C/10 rate, retaining 94% of its initial capacity. Additionally, the *percolation* mechanism of ion transport was observed for PTMC-NaFSI electrolytes at high salt concentrations.[185] Notably, σ of 5×10^{-5} S cm^{-1} at 25 °C was achieved for the [TMC]:Na molar ratio of 1:1. However, the most stable battery performance was observed for the [TMC]:Na molar ratio of 5:1, which enabled cycling at a C/5 rate and a temperature as low as 40 °C in a Na-metal/PBA cell. Under these conditions, the cell retained 94 % of its capacity over 80 cycles.

Polyesters. Among polyesters, poly(ε-caprolactone), PCL, is one of the most extensively studied examples (**Figure 10**). PCL is a semi-crystalline polymer characterized by a T_g of -65 °C and T_m of 60 °C, consistent with the thermal properties of many polyesters.[147] Similar to PEO, the semi-crystalline nature of PCL poses a significant limitation to its ion transport capabilities, particularly at temperatures below its T_m. Comparative studies of the coordination strength of Li^+ in PTMC and PCL demonstrated a stronger coordination to CL monomers than

to TMC monomers.[62] Random copolymerization of PCL and TMC was proposed as a strategy to mitigate the drawbacks associated with PCL, including its semi-crystallinity and strong ion binding. Thus, Eriksson *et al*. investigated the impact of carbonate units inclusion on cation dynamics, and reported that for P(CL-TMC) random copolymers (structure is illustrated in **Figure 10**) with LiTFSI salt the T_{Li^+} varied from 0.49 for the pure PCL to 0.83 for pure PTMC as the TMC content increased.[63] Mindemark *et al*. further investigated P(CL_m-TMC_n)-based electrolytes with molar ratios of *m:n* = 90:10, 80:20, and 70:30, across various concentrations of LiTFSI.[192] Their findings identified the 80:20 ratio as the optimal composition for ionic conductivity. For this copolymer, remarkable conductivities were observed, delivering an ionic conductivity of 4×10^{-5} S cm^{-1} at 25 °C for the sample with 36 wt.% of LiTFSI. This high ionic conductivity enabled the operation of a Li/SPE/LFP cell at ambient temperature, achieving > 80 % of the theoretical capacity (150 mAh g^{-1}) at a C/50 rate and maintaining stable performance at rates up to C/10. In a following study of P(CL_m-TMC_n)-NaFSI electrolytes,[278] the 80:20 copolymer with 10 wt.% NaFSI exhibited the highest ionic conductivity of 1.3×10^{-5} S cm^{-1} at 25 °C. However, the T_{Na^+} was lower compared to that for Li^+ (T_{Na^+} of 0.47 at 80 °C vs. T_{Na^+} of 0.66 at 60 °C in the LiTFSI-containing counterpart). These findings were also supported by the quantitative analysis of ion coordination strength,[64] where the strength decreased in the row Na^+, Li^+, Mg^{2+} for the carbonyl coordinating group. However, no data on K^+ mobility in polyesters/polycarbonates has been published so far.

3. Methodology

3.1. Characterization of SPEs

3.1.1. Differential Scanning Calorimetry (DSC)

Differential scanning calorimetry (DSC) is an efficient thermal analysis to examine the thermal behaviour of a material at a chosen temperature range. A DSC calorimeter consists of two cells: a reference cell (typically an empty one) and a cell with the investigated material. In principle, to heat up/cool down both cells with the same heating/cooling rate, a different amount of heat capacitance is required. The working principle is to register the difference of heat flow (W g^{-1}) as a function of temperature and time to observe thermal effects – endo- and exothermic processes. For semi-crystalline and amorphous polymers, melting/crystallization processes as well as glass transition are the characteristics of a great importance. The glass transition temperature T_g can be seen as an indicator of segmental chain mobility to enable an efficient cationic diffusion within a host material. Moreover, an endothermic melting process can be characterized by melting temperature T_m and melting enthalpy (ΔH_m), which can be further used to calculate crystallinity (X_c) according to **Equation 7**:

$$X_C = \left(\frac{\Delta H_m}{\Delta H(\text{Polymer})_m \times (1 - \phi_{add})}\right) \qquad \textbf{Equation 7}$$

where ϕ_{add} represents the total amount of additives (nanoparticles, etc.).[147]

This metric can be used for estimation of ionic transport through the host material as larger content of amorphous phase (preferable for ions hopping) supports higher ionic conductivities in semi-crystalline polymer.

3.1.2. Oscillatory Rheology

Polymer electrolytes typically display viscoelastic properties, i.e. neither an ideal liquid (viscous) nor ideal solid (elastic) behaviour.[215] The primary method for evaluating viscoelastic properties with a rotational rheometer is small amplitude oscillatory shear (SAOS). When conducting oscillation test, a parallel plate system is used, where the sample is placed between the plates with a predetermined gap. The upper plate oscillates back and forth at a specified stress or strain amplitude and frequency (**Figure 11**). This oscillatory motion is typically represented as a sinusoidal wave, with stress or strain amplitude plotted on the y-axis and time on the x-axis. In a controlled stress test, an oscillating torque is applied to the upper plate, and the angular displacement is measured to determine the strain. Conversely, in a controlled strain test, the angular displacement is controlled, and the required torque is measured to calculate the shear stress.

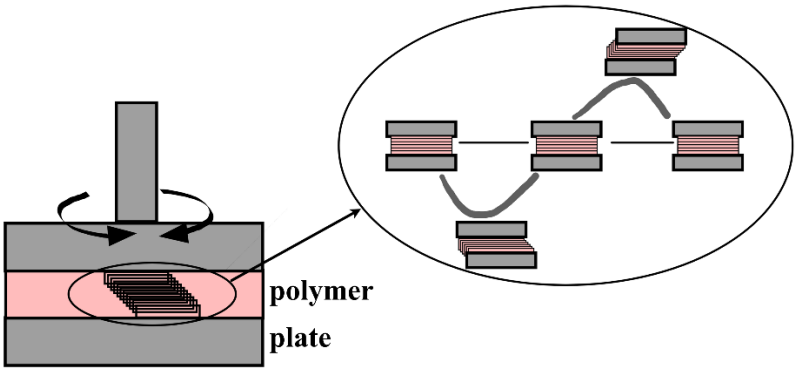

Figure 11. A schematic illustration of a sample positioning in a parallel plate geometry with sinusoidal oscillatory motion.

The complex shear modulus |G| can be described as following equation:

$|G| = G' + iG''$ **Equation 8**

In viscoelastic materials storage modulus G' is ascribed to the elastic portion or solid-state behaviour and loss modulus G'' can be seen as the viscous portion or liquid-like behaviour of the polymer sample.[216,217] Under the influence of shear and/or temperature the value of G'' can exceed the magnitude of G', indicating liquid-like properties of a material. Contrary, when G' > G'', desired for SPEs solid-like properties are guaranteed.

3.1.3. Electrochemical Impedance Spectroscopy (EIS)

The information about total bulk ionic conductivity (σ) of SPEs can be gathered using EIS. The measurement is usually performed in a two-electrode setup, where the electrolyte film is placed between two blocking electrodes. For instance, in this thesis, stainless steel/SPE/stainless steel configuration was used for determination of σ. The impedance spectroscopy can be conducted in potentiostatic mode by applying an AC potential (with a small voltage amplitude of 10-20 mV) V(t), and the current response, I(t), is monitored. Impedance, Z, serves as the AC equivalent of resistance, representing the ability of a circuit to resist the flow of electrical current. The difference is that resistance follows Ohm´s law, which applies to an ideal resistor. In contrast, impedance provides a more realistic interpretation of the electrical properties of materials. Thus, the potential difference, $\Delta V(t)$, changes sinusoidally with time (**Equation 9**), while the corresponding sinusoidal change in $\Delta I(t)$ also includes a phase shift (**Equation 10**):

$\Delta V(t) = \Delta V_0 \times \sin(\omega t)$ **Equation 9**

$\Delta I(t) = \Delta I_0 \times \sin(\omega t + \theta)$ **Equation 10**

where ω is the angular frequency, and θ is the phase shift angle. Then the impedance, |Z|, is a vector quantity expressed in **Equation 11**, and consists of two components: the real part, Z' (**Equation 12**), and the imaginary part, $-Z''$ (**Equation 13**).

$$|Z| = \frac{\Delta V(t)}{\Delta I(t)} \qquad \textbf{Equation 11}$$

$$Z' = |Z| \times \cos\theta \qquad \textbf{Equation 12}$$

$$Z'' = |Z| \times \sin\theta \qquad \textbf{Equation 13}$$

A Nyquist plot ($-Z''$ vs. Z') is a graphical representation of the obtained data (**Figure 12**).

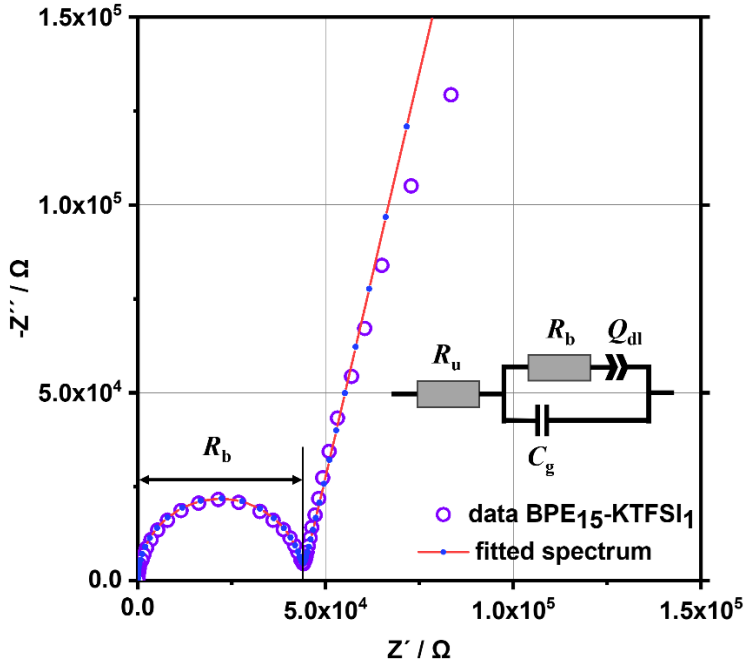

Figure 12. Example of the extraction of the bulk electrolyte resistance (R_b) from EIS measurements at different temperatures. The EIS spectra were fitted using a Debye circuit (R_u is uncompensated resistance, Q_{dl} is constant phase element capacitance of double layer, C_g is geometric capacitance), which in this case corresponds in good approximation to the transition into the low frequency regime at around 4.37×10^4 Ω (fit shown as red line with dark blue symbols). Representative data is gathered from EIS measurement of BPE-KTFSI (EO:K = 15:1) in the frequency range from 1 MHz to 500 mHz with a voltage amplitude of 10 mV at 5 °C.

Each point on the Nyquist plot reflects the complex value of the transfer function at that frequency. The Nyquist plot of SPEs is a semicircle at high frequencies (as a result of the geometric capacitance) followed by a vertical or near-vertical tail at low frequencies. From the Nyquist plot, the bulk electrolyte resistance (R_b) can be extracted as the impedance at the low frequency intersection of the semicircle with the x-axis (Z') or through fitting the data to an

appropriate equivalent circuit (typically a Debye equivalent circuit, see **Figure 12**). Further, the total ionic conductivity can be calculated according to **Equation 14**:

$$\sigma = \frac{1}{R_b} \cdot \frac{l}{A} \qquad \textbf{Equation 14}$$

where l represents the thickness, and A represents the area of a SPE film.

3.1.4. Transference Number Measurements – Bruce-Vincent Method

The transference number T_{A^+} (where A^+ represents alkali metal cation) can be determined electrochemically through the combination of potentiostatic polarization of a symmetric A-metal/SPE/A-metal cell and EIS measurements (before and after polarization). Bruce-Vincent method is the one that is commonly used for measuring T_{Li^+} in Li-containing SPEs systems.[205] Potentiostatic polarization is typically performed at low voltage amplitudes (10-50 mV, so that the potential distribution across the cell could be linearized), and EIS is applied before and after polarization to determine initial and steady-state interfacial resistances, respectively (**Figure 13**).

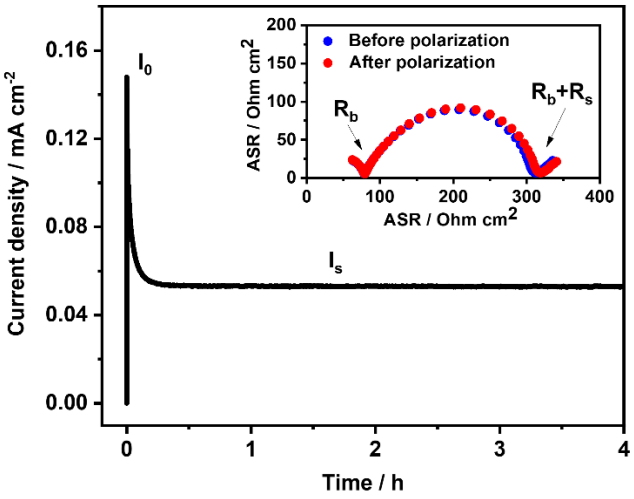

Figure 13. Example of the data interpretation of the transference number T_{A^+} measurement through Bruce-Vincent method. Representative data is gathered from a Li-metal/BPE-LiTFSI/Li-metal cell at 55 °C, at ΔV of 50 mV. EIS spectra were recorded in the frequency range from 1 MHz to 100 mHz with an amplitude of 10 mV.

Furthermore, the transference number T_{A^+} can be calculated using **Equation 15:**

$$T_A^+ = \frac{I_s\,(\Delta V - I_0\,R_0)}{I_0\,(\Delta V - I_s\,R_s)} \qquad \textbf{Equation 15}$$

where I_0 and I_s represent the initial and steady-state current, respectively, ΔV is the polarization voltage, and R_0 and R_s are the initial and steady-state electrode resistance, respectively. The initial current I_0 can be calculated using **Equation 16**:

$$I_0 = \frac{\Delta V}{R_b + R_0} \qquad \textbf{Equation 16}$$

where R_b is the resistance of the polymer electrolyte determined from the Nyquist plot (EIS before polarization). The initial current I_0 calculated according to **Equation 16** should be equal to the experimental value, which can be derived from the polarization plot.

3.2. Electrochemical Analysis of Batteries

In this thesis, polymer electrolytes were electrochemically tested using symmetrical potassium metal cells and a half cell configuration. The symmetrical cell design was employed to evaluate electrochemical processes occurring at the electrode-electrolyte interfaces. In the half cell setup, potassium metal served as both the reference and counter electrode.[279] Unlike a full cell configuration, the half cell allows to study the electrochemistry of either a positive or negative electrode without limited charge carrier inventory. However, the full cell is considered as a closer prototype of a potassium-ion battery due to the limited metal supply and the balanced capacities and voltages of the cathode and anode. It is important to note that the definition of a potassium-ion battery does not exclude the use of potassium metal as the negative electrode. Therefore, in this dissertation the electrochemical data from the half cell experiments can be considered as prototypes for actual potassium batteries.

3.2.1. Plating and Stripping Experiments

When thermodynamically favorable, alkali metal ions (K^+ cations in this thesis) gain electrons and undergo reduction ($K^+ + e^- \rightleftarrows K$), forming metallic potassium that deposits on the electrode surface. A portion of the deposited potassium can then be stripped back from the electrode, leading to the formation of reversible potassium. This process is known as the plating/stripping of metallic potassium. The difference between the equilibrium potential and the actual potential during plating/stripping is known as the overpotential, which is associated with the energy barriers and processes occurring during the electrochemical reaction.[280] By adjusting the (over)potential, the reaction rate can be controlled. Conversely, if the reaction rate (i.e. the applied current) is kept constant, the observed overpotential can serve as an indicator of the energy barriers and the stability of the electrode-electrolyte interface. For metal deposition to occur, several processes are involved, including (1) mass transport, (2) charge transfer, and (3) nucleation, all contributing to the overpotential (**Figure 14**).

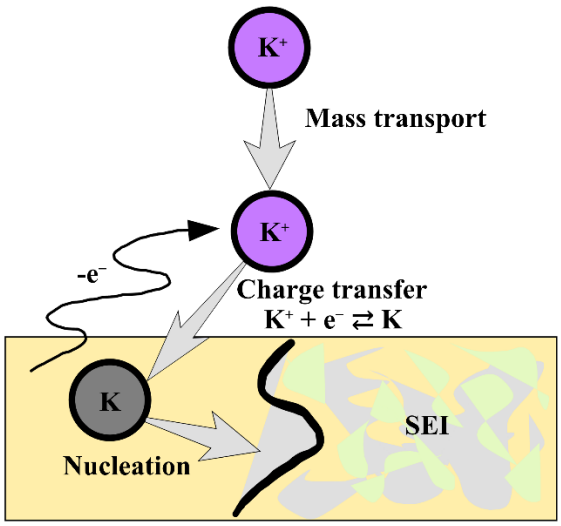

Figure 14. A schematic illustration of potassium metal deposition from electrolyte.

As shown in **Figure 14**, a portion of the deposited potassium cannot be stripped back, leading to the formation of irreversible metal. At the electrode-electrolyte interface, the metallic potassium reacts with the (polymer) electrolyte to form SEI, which encapsulates the metallic potassium. The accumulation of irreversible potassium results in capacity fade due to the loss of K^+ ions.[281]

3.2.2. Galvanostatic Cycling

Galvanostatic cycling is the commonly used technique for studying the behaviour of batteries or their prototypes during cycling. In this thesis, galvanostatic cycling with potential limitation (GCPL) was employed as a standard protocol to avoid irreversible side reactions in highly oxidative or reductive potential regions. The performance of a battery is judged based on its charge and discharge conditions within a chosen potential range and at a specific cycling rate.[279] The cycling rate, or C-rate, is typically expressed as C/*h* (A g^{-1} or mA g^{-1}), where *h* represents the number of hours required for the nominal capacity of the working electrode (or the battery involving both positive and negative electrodes) to pass through. For example, a C-rate of C/15, as used in this thesis, corresponds to a current density that fully charges or discharges the cell in 15 hours, whereas a C-rate of 15C would theoretically allow for full charging or discharging in just 4 minutes. GCPL enables the evaluation of various electrochemical characteristics of cells such as the charge (Q_{ch}) and discharge (Q_{disch}) capacity, the dependence of capacity on the current density (rate capability test), analysis of the capacity-voltage profile, voltage hysteresis, and Coulombic efficiency, CE, which is calculated as the ratio of Q_{disch} to Q_{ch}:

$$CE = \frac{Q_{disch}}{Q_{ch}}$$ **Equation 17**

4. Experimental Section

4.1. Materials

Poly(ethylene oxide), PEO, with an average M_v of 5.000.000 g mol^{-1} (Sigma-Aldrich), potassium bis(trifluoromethanesulfonyl)imide, KTFSI, (99.5 %, Solvionic), γ-Al_2O_3 nano powder (99.97 %, avg. particle size: 20-30 nm, pH 5.0-6.5, Nanostructured & Amorphous Materials, Inc., USA) and SiO_2 nano powder (>99+ %, avg. particle size: 20 nm, pH 5.5-6.5, Nanostructured & Amorphous Materials, Inc., USA) were dried at 110 °C for 12 h under vacuum (10^{-3} mbar) prior to use and transferred to the Ar-filled glovebox, where all following procedures were carried out under inert atmosphere (H_2O < 0.1 ppm, O_2 < 0.1 ppm).

For poly(vinyl benzyl methoxy poly(ethylene oxide) ether)-*block*-polystyrene block copolymer synthesis, sodium hydride (60 wt.% dispersion in mineral oil, Sigma-Aldrich), poly(ethylene oxide) monomethyl ether (mPEO2000 equals to M_n = 2000 g mol^{-1}, TCI), 4-vinylbenzyl chloride (90 wt.%, Sigma-Aldrich), 2-(dodecylthiocarbonothioylthio)-2-methylpropionic acid (98 wt.%, Sigma-Aldrich) were used as received. Styrene (99 wt.%, Acros) was passed through basic alumina oxide prior to use.

For polycarbonates synthesis, trimethylene carbonate (TMC, Obiter Research) was used as received, ε-caprolactone (CL, 99 % Sigma Aldrich) was distilled over reduced pressure over CaH_2, $Sn(Oct)_2$ (95 %, Sigma Aldrich) was prepared as a 1 M solution in toluene (extra dry, over molecular sieves, 99.8 %, AcroSeal®, Acros Organics). All samples were stored, handled, and prepared in an argon-filled glovebox under inert atmosphere (H_2O < 0.1 ppm, O_2 < 0.1 ppm).

For potassium iron hexacyanoferrate $K_{2-x}Fe[Fe(CN)_6]_{1-y}\times zH_2O$ synthesis, $FeSO_4\times 7H_2O$ (99 %, Ruskhim), polyvinylpyrrolidone (M_w = 40.000, Sigma-Aldrich), $Na_3Cit\times 5.5H_2O$ (99.5 %, Ruskhim), $K_4Fe(CN)_6\times 3H_2O$ (99 %, Ruskhim) were used as received.

Carbon black (SuperC, Imerys Graphite & Carbon, Switzerland), poly(vinylidene difluoride) PVdF (HSV900, Arkema), *N*-methyl-2-pyrrolidone (99.5 %, Sigma-Aldrich), anhydrous acetonitrile (99.8 %, Sigma Aldrich) were used as received.

For liquid electrolyte preparation, hexafluorophosphate KPF_6 (99 %, AcrosOrganics) was dried at 110 °C for 12 h under vacuum (10^{-3} mbar) prior to use and transferred to the Ar-filled glovebox, ethylene carbonate (EC) (99 %, Sigma-Aldrich) and propylene carbonate (PC) (99.7 %, Sigma-Aldrich), fluoroethylene carbonate (FEC) (≥ 99 %, Sigma-Aldrich) were used as received in an Ar-glovebox.

Potassium metal (98 % stored in mineral oil, Sigma-Aldrich) was transferred to the Ar-filled glovebox (H_2O < 0.1 ppm, O_2 < 0.1 ppm), washed with hexane and further used under inert atmosphere.

4.2. Polymers Synthesis

4.2.1. Block Copolymer Synthesis

Poly(vinyl benzyl methoxy poly(ethylene oxide) ether)-*block*-polystyrene block copolymer (PVBmPEO-*b*-PS further shortened to BP) was synthesized by reversible addition-fragmentation chain-transfer (RAFT) polymerization, following the described procedure.[58]

4.2.2. Polycarbonates Synthesis

Poly(trimethylene carbonate) PTMC (with an average M_n = 140.000 g mol^{-1}) and poly(ε-caprolactone-*co*-trimethylene carbonate) P(CL_m-TMC_n) with molar ratio *m:n* of 80:20 (with an average M_n = 310.000 g mol^{-1}), were both synthesized through ring-opening polymerization of the respective monomers using a 1 M solution of $Sn(Oct)_2$ as the catalyst , following previously reported synthetic procedures.[276,282]

4.3. SPEs Preparation and Characterization

4.3.1. SPEs Preparation

The predefined amounts of the respective polymer host material and KTFSI corresponding to certain molar ratios of [polymer unit]:K (see in **Table 2**) were homogeneously dissolved in acetonitrile. In the case of Al_2O_3- and SiO_2-containing samples, the predefined amounts of nanofiller, corresponding to a certain mass fraction (relatively to the polymer-salt composition), were weighed in a ball-mill container. The container was transferred to a ball-mill mixer SPEX 8000, and the components were mixed as dry solids for 1 h. Subsequently, acetonitrile was added to the resulting solid mixture, and the slurry was stirred overnight.

The solutions/slurries were casted onto Teflon molds with an inner diameter of 40 mm, followed by the solvent evaporation at 60 °C. The obtained films were dried at 110 °C for 36 h under vacuum (10^{-3} mbar) and transferred to the glovebox (H_2O < 0.1 ppm, O_2 < 0.1 ppm) without further exposure to air or moisture, where all preparations for following measurements were carried out. The derived films with a thickness range of ~100-200 μm (specified further) were used for all measurements.

Table 2. Compositions of solid polymer electrolytes studied in this thesis.

Polymer host material	[Polymer unit]:K molar ratio	Nanofiller	Nanofiller mass fraction, wt.%
PEO	20:1	–	–
	16:1		
	12:1		
	8:1		
	4:1		
PEO	12:1	Al_2O_3	2
			5
			8
			10
			12
			15
PEO	12:1	SiO_2	2
			5
			8
			10
BPE	20:1	–	–
	15:1		
	10:1		
PTMC, $P(CL_{80}\text{-}TMC_{20})$	24:1	–	–
	20:1		
	16:1		
	12:1		
	8:1		
	4:1		
	2:1		
	1:1		

4.3.2. DSC

For DSC measurements, A DSC Q200 (TA Instruments) system was used to register thermograms of the PEO-based SPEs, while the polycarbonate-based SPEs were analysed using a Mettler Toledo DSC 3+ system. For both systems, the samples with the mass of 5-15 mg were sealed in aluminum pans. The samples were cooled from ambient temperature to -70 °C at a cooling rate of 10 K min^{-1} and heated up to 160 °C (for the PEO-SPEs) or to 200 °C (for the polycarbonates-SPEs) at a heating rate of 10 K min^{-1}. Two colling-heating cycles were performed on the samples to remove any thermal history, and the second heating scans are presented and discussed in this thesis.

4.3.3. Oscillatory Rheology

Rheological measurements were performed on a strain-controlled ARES G2 (TA Instruments) rheometer *via* SAOS with shear strains amplitudes γ_0 = 0.1 - 1 %. The tests were conducted on the above prepared SPEs under nitrogen atmosphere in the angular frequency range from 0.1 to

100 rad s^{-1} in the temperature range from 25 to 65 °C in 10 °C steps. The samples with a diameter of 8 mm and a thickness of 0.5 mm were prepared from the films obtained by the SPE preparation.

4.3.4. EIS

Prior to EIS measurements, the cells (**Table 3**) were assembled in an Ar-filled glovebox. To avoid electrode-electrode contact, gasket rings made from Mylar separators were used. Subsequently, the cells were sealed and pre-conditioned at elevated temperature of 60 °C for 12 h in a temperature chamber, followed by cooling to ambient temperature (25 °C). Further, EIS measurements were performed at the chosen conditions listed in **Table 3**. Prior to recording impedance spectra, the temperature of the measurement was maintained constant for at least 40 min.

Further, the bulk electrolyte resistance (R_b) was determined by fitting with a Debye circuit to the data in the Nyquist plot, and the ionic conductivity (σ) was calculated according to **Equation 14**.

Table 3. Chosen conditions of EIS measurements.

SPE-KTFSI	Cell type	Film thickness, μm	Film diameter, mm	Analyzer	Freq. range, Hz	Voltage amplitude, mV	Temp. range, °C
PEO	Swagelok	~200	8	Biologic SP-200	1×10^6-500×10^3	20	15-85
Al_2O_3-/SiO_2-filled PEO	CR2032 coin	~200	12	Biologic VSP	1×10^6-500×10^3	20	15-85
BPE	CR2032 coin	~100	10	Biologic VSP	1×10^6-500×10^3	10	5-85
PTMC/P(CL_{80}-TMC_{20})	CR2025 coin	~100	12	Schlumberger SI 1260 Impedance/ Gain-Phase Analyzer	10×10^6-1	10	25-85

4.4. Electrode Material Synthesis and Characterization

Potassium iron hexacyanoferrate $K_{2-x}Fe[Fe(CN)_6]_{1-y}\times zH_2O$ (KFF) was synthesized *via* co-precipitation method reported elsewhere.[11] Three solutions were prepared: (a) 0.782 g of $FeSO_4\times7H_2O$ (99 %, Ruskhim) and 0.100 g of polyvinylpyrrolidone (M_w = 40.000, Sigma-Aldrich) in 20 ml of deionized water, (b) 0.244 g of $Na_3Cit\times5.5H_2O$ (99.5 %, Ruskhim) in 10 ml of deionized water and (c) 1.268 g of $K_4Fe(CN)_6\times3H_2O$ in 10 ml of deionized. The

solutions were added to the vessel in the order (a), (b) and (c). The resulting suspension was stirred for 36 hours at ambient temperature. Subsequently, the resulting precipitate was centrifuged and washed with the mixture of ethanol and deionized water (1:1 ratio by volume) several times and dried at 110 °C for 12 hours under vacuum (10^{-3} mbar). After drying, the obtained powder was ground using a mortar.

The chemical composition was further determined[2] using a combination of thermogravimetric analysis (TGA) and inductively coupled plasma optical emission spectroscopy (ICP-OES) in order to determine the water content and the K:Fe ratio of the compound $K_{2-x}Fe[Fe(CN)_6]_{1-y}\times zH_2O$, respectively. The resulting stoichiometry of the compound was calculated to $K_{1.90}Fe[Fe(CN)_6]_{0.98}$, from which the water content can be determined to z = 1.0, yielding the total stoichiometry $K_{1.90}Fe[Fe(CN)_6]_{0.98}\times 1.0H_2O$.

4.5. Electrode Preparation and Cell Assembly

4.5.1. Electrode Preparation

For the preparation of positive electrodes for electrochemical tests with the liquid electrolyte, 180.0 mg of the synthesized $K_{1.90}Fe[Fe(CN)_6]_{0.98}$, 90.0 mg of carbon black, 30.0 mg of PVdF (resulting in 60:30:10 ratio by mass) were weighed in a ball-mill container and *N*-methyl-2-pyrrolidone was added. The container was transferred to a ball-mill mixer SPEX 8000 and the slurry was mixed for 1 hour. Subsequently, the slurry was spread onto conductive carbon-coated aluminium foil using an automatic film applicator Zehntner ZAA 2300 with a gap width of 150 µm and dried after a deposition at 60 °C. To uniform thickness and surface, the electrode sheet was roll-pressed to a thickness of ~40 µm with a mass loading of ~1 mg cm^{-2}. Round-shaped electrodes with a diameter of 16 mm were cut out and dried at 110 °C for 12 hours under vacuum (10^{-3} mbar) and transferred in an Ar-filled glovebox without further exposure to air or moisture. Positive electrodes for electrochemical tests with SPEs were prepared according to the same sequence of procedures as described above. In this case, slurries contained 180.0 mg of KFF, 90.0 mg of carbon black, 30.0 mg of PVdF, 30.0 mg of PEO and 14.0 mg of KTFSI (overall electrode composition 52.3: 26.2: 8.7: 8.7: 4.1 ratio by mass, wt.%).

4.5.2. Symmetrical Cell Assembly

For measurements of the transference number T_{K^+} and for plating and stripping experiments, symmetrical K-metal/SPE/K-metal coin cells (CR2032-type cells) were assembled in an Ar-filled glovebox. For the T_{K^+} measurements, the SPEs based on PEO-KTFSI (with a molar ratio of EO:K = 20:1, Sym-PEO-cell) and BPE-KTFSI (EO:K = 15:1, Sym-BPE-cell) were prepared

as previously described in **4.3.1**. Furthermore, for plating and stripping experiments, PEO-KTFSI (EO:K = 12:1) with 8 wt.% of the inorganic nanofiller (Al_2O_3 or SiO_2 further denoted as Sym-AlOx-8-cell or Sym-SiOx-8-cell, respectively) were additionally prepared. The electrolyte discs with a thickness of ~200 µm and a diameter of 8 mm (for Sym-PEO-cell), 16 mm (for Sym-BPE-cell), 16 mm (for Sym-AlOx-8-cell) and 14 mm (for Sym- SiOx-8-cell) were placed between the potassium metal electrodes. Prior to the measurements, the cells were pre-conditioned at a temperature of 55 °C for 1 h.

4.5.3. Half Cell Assembly

For galvanostatic cycling coin cells were assembled in an Ar-filled glovebox. In K/SPE/KFF configuration, K-metal negative electrode, KFF-based positive electrode (prepared as described in **4.4**) and respective SPE (prepared as described in **4.3.1)** were used. The electrolyte discs with a thickness of ~200 µm and a diameter of 16 mm were placed between the electrodes. For the reference cells with liquid electrolyte, glassfiber separators (Whatman GF/B) were dried at 110 °C for 12 hours under vacuum (10^{-3} mbar) and one layer of the separator was soaked with 150 µl of an electrolyte comprising a 0.5 M KPF_6 solution in a mixture of EC:PC (1:1 ratio by volume) with 2 wt.% of FEC. The SPE-based cells were preconditioned in a temperature chamber at 55 °C for 20 hours prior to the following cycling at this temperature. The liquid electrolyte-based cells were preconditioned at ambient temperature (25 °C) for 2 hours prior to the following cycling at this temperature.

4.6. Electrochemical Tests

4.6.1. Plating and Stripping Experiments in Symmetrical Cells

Potassium metal plating and stripping experiments were performed on a VMP-300 potentiostat (BioLogic Science Instruments) at a temperature of 55 °C. For the Sym-PEO- and Sym-BPE-cells, the current densities (j, where $j = I/A$) of 0.01, 0.02, 0.05 and 0.01 mA cm^{-2} were used, and j was increased stepwise every 10 cycles. The last sequence was performed at the decreased current density of 0.01 mA cm^{-2}. Each cycle comprised plating and stripping for 1 h each, for 20 h in total. When switching from plating to stripping (and reverse), an OCV step of 30 min was applied for Sym-PEO-cell. For the Sym-AlOx/SiOx-cells, pre-conditioning step was introduced at OCV at the experimental temperature for 4 h. Then EIS measurements were performed in 4 h intervals in the frequency range between 10 mHz and 200 kHz and a voltage amplitude of 20 mV. The total conditioning time was 42 h and 13 min. The current densities of 0.01, 0.02, 0.05, 0.075 and 0.1 mA cm^{-2} were used. For each j in the range of

0.01-0.075 mA cm^{-2}, the sequence time totalled to 20 h (1 h for plating, 1 h for stripping). At the highest *j* of 0.1 mA cm^{-2}, the cells were cycled for 200 h in total. A rest step of 30 min was applied between plating and stripping steps (and reverse). After each *j* increase, EIS was conducted under the same conditions as for the OCV phase.

4.6.2. Transference Number Measurements – Bruce-Vincent Method

The measurements of the transference number T_{K^+} were performed on a VMP-300 potentiostat (BioLogic Science Instruments) at 55 °C. For the K/PEO-KTFSI/K cell, the impedance data were collected in a frequency range from 200 kHz to 10 mHz with an amplitude of 10 mV. Afterwards, direct current polarization was applied with a polarization voltage of ΔV = 30 mV, while the impedance spectra were recorded before and after the polarization, respectively. Meanwhile, EIS spectra of the K/BPE-KTFSI/K cell were recorded in the frequency range from 1 MHz to 100 mHz with an amplitude of 10 mV. The polarization voltage of ΔV = 50 mV was further applied.

The transference number T_{K^+} was calculated using **Equation 15,** and the initial current I_0 was calculated using **Equation 16**.

4.6.3. Galvanostatic Cycling

As stated in **4.5.3**, the galvanostatic cycling tests were performed in K-metal/electrolyte/KFF cell configuration under following conditions (**Table 4**):

Table 4. Chosen conditions of galvanostatic cycling experiments. 1C = 141 mAh g^{-1} with respect to the theoretical capacity of $K_{1.90}Fe[Fe(CN)_6]\times 1.0H_2O$.

Electrolyte type	Analyzer	Temperature, °C	C-rate	Cut-off limits, V
Liquid electrolyte	Neware BTS4000	25	C/25	2.5-4.3
PEO-KTFSI	Neware BTS4000	55	C/25	2.5-4.3
AlOx/SiOx-PEO-KTFSI	Biologic VMP-300	55	C/15	2.5-4.3
BPE-KTFSI	Biologic VMP-300	55	C/15	2.5-4.3

Additionally, for filler-containing and BPE-based SPEs, a constant potential (CP) step was applied for a maximum of 1 h after each charge/discharge sequence.

4.7. Data Processing

The galvanostatic cycling data was exported to TXT file extension using the EC-Lab software (V11.27) and further processed using the in-house developed «bat2dat» R package that is

available on github.[283] The EIS data for total ionic conductivity measurements was fitted to a Debye equivalent circuit using RelaxIS software.

5. Scope of this Thesis

Potassium-ion batteries became an intensively growing field of research as a complementary post-Li technology. Despite higher atomic mass of potassium, KIBs could be successfully used as stationary energy storage systems especially if high average cell voltages (above 4.0 V) and a high stoichiometric content are achieved.[67,68,157] However, the realisation of efficient and high-performance KIBs is impeded by lack of stable interface chemistries often resulting from the high reactivity of potassium towards electrolyte components, especially in K-metal batteries.[19,127,284,285] This leads to electrolyte degradation and thus rapid increase of the surface layer thickness and cell resistance, as well as fast capacity fade.[284,286] SPEs have recently demonstrated improved capacity retention in half cell configurations compared to conventional LEs, although the low ionic conductivity, insufficient mechanical strength, and interfacial compatibility of the former still remain challenges to be addressed.

Within the scope of this thesis, two classes of polymers – the state-of-the-art, PEO, and the carbonyl-containing homopolymer PTMC and copolymer P(CL_m-TMC_n) – will be examined as host materials for SPE applications in potassium metal batteries. For PEO-based host materials, different strategies will be investigated along the aforementioned key metrics, namely (1) a homopolymer approach, (2) composite strategy involving the incorporation of inorganic nanofillers (Al_2O_3, SiO_2), and (3) block copolymerization to obtain PVBmPEO-*b*-PS copolymer. The impact of these approaches on the temperature-dependent rheological and ion transport properties will be evaluated using SAOS, DSC and EIS techniques. The issue of mechanical stability of PEO while maintaining sufficient ionic conductivity will be addressed through the strategies employed. Structural differences between electrolytes with varied salt and/or additive contents, and/or based on different host materials (homopolymer vs. block copolymer) will be further correlated to the electrochemical behaviour in symmetrical K-metal/SPE/K-metal cells and K-metal/SPE/$K_{2-x}Fe[Fe(CN)_6]$ half cells.

6. PEO-based SPEs for KIBs

In this chapter, a comparative analysis of SPEs based on PEO (as an ion conducting host material) including three different material approaches, namely (1) homopolymer, (2) composite, (3) block copolymer, with varied concentration of KTFSI was made, evaluating their rheological properties, ionic conductivity and electrochemical performance. The findings offer a comprehensive understanding of how to «tune» the SPEs properties by changing the salt content and/or the morphology of the host material.

6.1. Characterization of Thermal and Rheological Properties

In this section, the trends of thermal behaviour of PEO-based SPEs and the impact on their mechanical rigidity were studied, when (1) varying KTFSI concentration in the PEO-KTFSI matrix, (2) adding inorganic nanofillers Al_2O_3 and SiO_2 to the PEO-KTFSI SPEs, (3) utilizing the PEO-based block copolymer as a host material for SPE. Furthermore, comparative discussion of benefits and shortcomings of mechanical parameters of the PEO-based SPEs as well as outlook were given.

6.1.1. PEO-KTFSI Compositions as the Starting Point

***Thermal characterization*.** Thermal properties of the series of PEO_x-$KTFSI_y$ blends, where the ratio of *x*:*y* corresponded to different EO:K molar ratios (20:1, 16:1, 12:1, 8:1, 4:1), and pristine pure PEO were characterized by DSC (**Figure A1a**, summary given in the appendix **Table A1**).

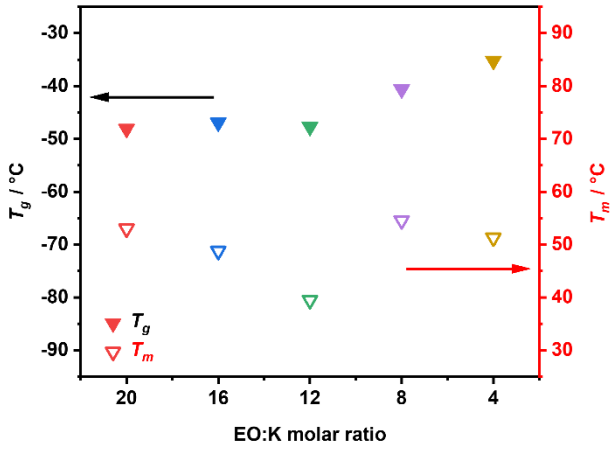

Figure 15. The dependence of glass transition T_g and melting T_m temperatures on EO:K molar ratio in PEO-KTFSI SPEs.

The pristine PEO featured a T_g at -59.8 °C, whereas the PEO-KTFSI SPEs showed a predominant tendency of T_g shift towards higher temperatures with increasing salt content

(**Figure 15**). This trend can be explained by ionic cross-linking[179,180,181] as a result of the coordination of K^+ by different segments of the polymer chains, leading to their physical cross-linking, which reduces the polymer free volume and thereby partially immobilizes and restricts segmental motion.[25] Simultaneously, the melting point T_m decreased from 69.2 °C for pure PEO to melting points below 55 °C for PEO-KTFSI SPEs. As can be clearly seen in **Figure 15**, the polymer blends featured decreasing T_m values as the EO:K ratio changed from 20:1 to 12:1, most likely due to the plasticising effect of the bulky $TFSI^-$ anions.[287] This was reflected in the declining trend of melting enthalpies ΔH_m from pure PEO (196.4 J g^{-1})[34] to the 12:1 blend (11.1 J g^{-1}, given in **Table A1**), corresponding to the substantial reduction in the degree of crystallinity. As the KTFSI content further increased (EO:K = 8:1), both T_m and ΔH_m increased again, which was likely related to the formation of crystalline intermediate compounds.[196] Surpassing the saturation limit of EO:K = 5,[162,196] the concentration regime changed from salt-in-polymer to polymer-in-salt.[288,289] Thus, in **Figure A1a** of PEO_4-$KTFSI_1$, an additional endothermic peak at 135 °C can be clearly observed, corresponding to the phase reported in the literature with the molar ratio of EO:K = 1.5:1.[162] A mixed-phase system was also observed in the case of PEO_{20}-$KTFSI_1$ that manifested an additional phase with a lower melting point (T_m = 37 °C). Contrary to the PEO-LiTFSI blends,[162,196] showing the absence of any crystalline phases in the so called «crystallinity gap», i.e. in the range of EO:Li molar ratios between 6 < EO:Li < 12, no «crystallinity gap» for the investigated EO:K molar ratios was detected. This is in agreement with previously reported phase diagram of the PEO-KTFSI SPEs, where the samples remain partly crystalline over a wide range of molar ratios (1.5 < EO:K < 60).[196]

***Rheological characterization*.** SAOS test was used to evaluate the impact of KTFSI concentration on the rheological properties of the PEO-based electrolytes. The storage and loss (G' and G'', respectively) moduli of PEO-KTFSI SPEs were measured from 0.1 to 100 rad s^{-1} at low shear strains from 0.1 to 1 % in the temperature range from 25 to 65 °C in 10 °C steps (see in the appendix **Figure A2**) to be within the linear regime.

As already stated, maintaining the structural integrity is highly relevant for SPE, acting both as electrolyte and separating layer between anode and cathode, preventing dendrites growth and subsequent short circuits.[148] In general, SPEs can gain the mechanical strength from a rigid crystalline phase of polymer or cross-links due to ion-polymer interactions,[147] restricting the polymer chains motion and contributing to a structural integrity. Herein, the predominant contribution of these effects to the mechanical properties of PEO-based compositions depending on their KTFSI content is discussed. As demonstrated in **Figure A2a-e**, for the PEO_4-$KTFSI_1$, PEO_8-$KTFSI_1$, PEO_{20}-$KTFSI_1$ compositions, as well as for pure PEO, the

storage moduli dominated the loss moduli over the whole temperature range investigated (G' > G'', from 25 to 65 °C), thus providing the desired solid-state behaviour. However, the mechanical strength of these materials was likely governed by different effects: pristine PEO and PEO_{20}-$KTFSI_1$ possessed the highest crystallinity degrees (**Table A1**), while PEO_8-$KTFSI_1$ and PEO_4-$KTFSI_1$ exhibited the highest T_g values due to a large number of ionic cross-links. In **Figure 16** the dependence of the storage and loss moduli is shown for investigated EO:K molar ratios at angular frequency of 0.1 rad s^{-1} and temperatures of 25 and 55 °C.

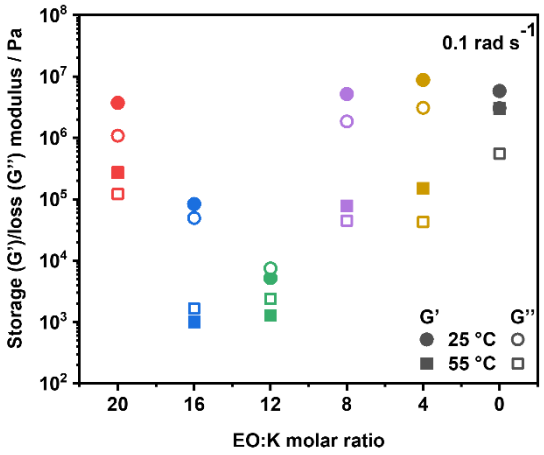

Figure 16. The dependence of storage (G') and loss (G'') modulus on EO:K molar ratio of PEO-KTFSI SPEs at angular frequency of 0.1 rad s^{-1} at 25 and 55 °C.

As seen in **Figure 16**, at temperatures below T_m, PEO_4-$KTFSI_1$ and PEO_8-$KTFSI_1$ demonstrated the highest storage and loss moduli among all blends and pristine polymer, indicating the significant contribution of cross-links to the improvement of structural integrity. Moreover, both PEO_4-$KTFSI_1$ and PEO_8-$KTFSI_1$ maintained the mechanical strength below T_m (25-45 °C, **Figure A2a-c**), and only a negligible decline of their moduli along with the temperature increase was found. Contrary, the PEO_{20}-$KTFSI_1$ blend with the lowest T_g but highest crystallinity exhibited a greater decrease of its moduli in the same temperature range. This correlates with the thermal properties of PEO_{20}-$KTFSI_1$, reflecting the loss of structural integrity of an additional crystalline phase with a lower melting point (T_m = 37 °C, **Table A1**). Surpassing the T_m of PEO_4-$KTFSI_1$ and PEO_8-$KTFSI_1$, the rigid crystalline phases melted and consequently the samples lost their mechanical integrity, which was dramatically reflected in the altered rheological properties (**Figure 16**). In contrast, PEO_{20}-$KTFSI_1$ possessed the highest moduli compared to other blends at temperatures above T_m. This might be attributed to the fact that PEO_{20}-$KTFSI_1$ employed a lower amount of bulky $TFSI^-$ in comparison to other blends,

thus possessing less hindered polymer chains alignment. Therefore, the rheological properties of this blend are expected to be the closest to that of pristine PEO, which had the highest values of G' and G'' above 55 °C. In **Figure A2e**, the significant moduli decline can be seen for the pure polymer, when approaching its T_m (69.2 °C, **Table A1**), however still possessing the highest moduli in comparison to all blends. As discussed above, PEO_{12}-$KTFSI_1$ and PEO_{16}-$KTFSI_1$ exhibited the lowest T_m and crystallinity degrees (**Table A1**). In accordance with their thermal properties, the lowest values of both G' and G'' were found over the investigated temperature range. Moreover, for PEO_{12}-$KTFSI_1$ the trend G'' > G' was observed in the low frequency region, indicating the dominance of liquid-like material properties. With increasing frequency, a cross-over point (G'' = G') was observed, signifying a transition to viscoelastic behaviour. At higher frequencies, G' exceeded G'', suggesting that the material exhibited solid-like properties at given conditions. The frequency of cross-over shifted as expected towards higher values along with the increase of temperature. This can be explained by the simultaneous increase of polymer chains motion in PEO_{12}-$KTFSI_1$. It is noteworthy, that similar tendency was manifested for PEO_{16}-$KTFSI_1$ above its T_m.

6.1.2. Towards Mechanical Stability: Inorganic Nanofillers in PEO-KTFSI

In this subsection, PEO-based composites incorporating nano-sized inorganic fillers, specifically Al_2O_3 and SiO_2 in a PEO_{12}-$KTFSI_1$ matrix, were investigated with respect to their thermal and rheological properties. The PEO_{12}-$KTFSI_1$ was employed as an exemplary composition with a high content of amorphous phase that promises high total ionic conductivities at near-ambient temperatures, but at the same time is unsuitable to serve as a separator in KIBs configurations due to liquid-like rheological properties. Impact of the nanofillers addition to predominantly amorphous PEO-based matrix on thermal parameters, i.e. T_g, T_m, ΔH_m, and mechanical stiffness of the resulting SPEs was thoroughly studied and discussed.

***Thermal characterization*.** DSC measurements were conducted to evaluate the impact of the nanofillers (Al_2O_3, SiO_2) addition on thermal properties of the PEO_{12}-$KTFSI_1$-based SPEs (**Figure A1b & 1c**, summary given in **Table A2**). Both melting T_m and glass transition T_g temperatures are plotted in **Figure 17** (T_m refers to the temperature at the peak maximum).

The SiO_2-containing composites displayed no dependencies between filler content and T_g, within a margin of ±2°C, with respect to the pristine PEO_{12}-$KTFSI_1$ composition (T_g = -47.7 °C, see **Table A1**). Marginally higher T_gs were observed for the Al_2O_3-filled electrolytes with the filler contents of 5, 8 and 12 wt.% (named AlOx-5, AlOx-8 and AlOx-12, respectively), without

a clear trend in glass transition temperature. As will be discussed later, differences between the fillers may arise from different degrees of surface-polymer and surface-ion interactions, which can alter the polymer chains dynamics in the electrolytes.

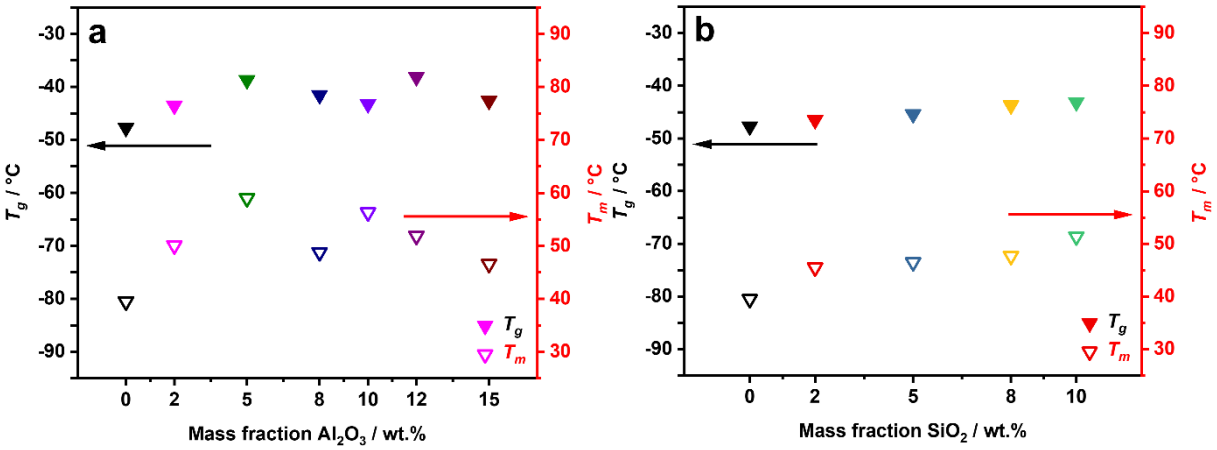

Figure 17. The dependence of glass transition T_g and melting T_m temperatures on the mass fraction of nano-sized **(a)** Al_2O_3 and **(b)** SiO_2 in PEO_{12}-$KTFSI_1$-based SPEs.

As can be seen in DSC scans in **Figure A1b**, the endothermic peaks around the melting temperature comprised of at least two broad overlapping features. Moreover, in the case of AlOx-5, two endothermic peaks were clearly observed, both reported in **Table A2**. In SiO_2 composites (**Figure A1c**), the endothermic peaks appear to overlap stronger but still show a discernible shoulder. This suggests the presence of several crystalline phases (with compositional differences), as described previously for PEO-LiTFSI systems.[290,291] By comparison with the filler-free PEO_{12}-$KTFSI_1$, one component can be attributed to its melting point at T_m = 39.5 °C, which is a substantial reduction in melting point (from 69 °C for pure, linear PEO with a high molecular weight). The melting points of filler-containing samples are clustered around 46.5±2 °C with few compositions exceeding 50 °C. Based on the thermal properties of various PEO_x-$KTFSI_y$ ($4 < x{:}y < 20$) compositions described in the previous subsection, the melting points of the adjacent PEO_{16}-$KTFSI_1$ composition (T_m = 48.8 °C, **Table A1**) and the majority of the filler-containing samples tested herein coincide almost. The formation of a crystalline EO:K = 16:1 phase, or more generally segregation into K-rich PEO phase(s) and K-depleted PEO phase(s), as described by Marzantowicz *et al.*[197] for PEO-LiTFSI electrolytes, can explain the mixed phase thermal behaviour. The local immobilization of PEO chains at the nanoparticle surface may induce crystallisation and phase separation, with the nanofillers acting as nuclei or seeds for nucleation and growth, resulting in an increase in melting enthalpies and degrees of crystallinity (ΔH_m and X_C, respectively, in **Table A2**).

Rheological characterization. Further, rheological properties of the Al_2O_3- and SiO_2-filled PEO_{12}-$KTFSI_1$ samples were investigated by SAOS tests (**Figure A3**). Thus, **Figure A3a & 3b** presents the dependency of the shear moduli on angular frequency of the Al_2O_3-filled PEO_{12}-$KTFSI_1$ with different mass fraction of the filler at 25 and 55 °C, respectively. All modified electrolytes in the investigated range of the filler concentration displayed G' > G''. This corresponds to the solid-like behaviour required for SPEs. In contrast, the filler-free PEO_{12}-$KTFSI_1$ (black circles) showed an opposite behaviour at low angular frequencies, indicating liquid-like properties (G'' > G').

As clearly seen in **Figure 18a**, at 25 °C the AlOx-filled samples exhibited more than one order of magnitude higher G' as compared to the pristine PEO_{12}-$KTFSI_1$ ($1.1\text{-}5.5\times10^5$ vs. 5.0×10^3 Pa at 0.1 rad s^{-1}).

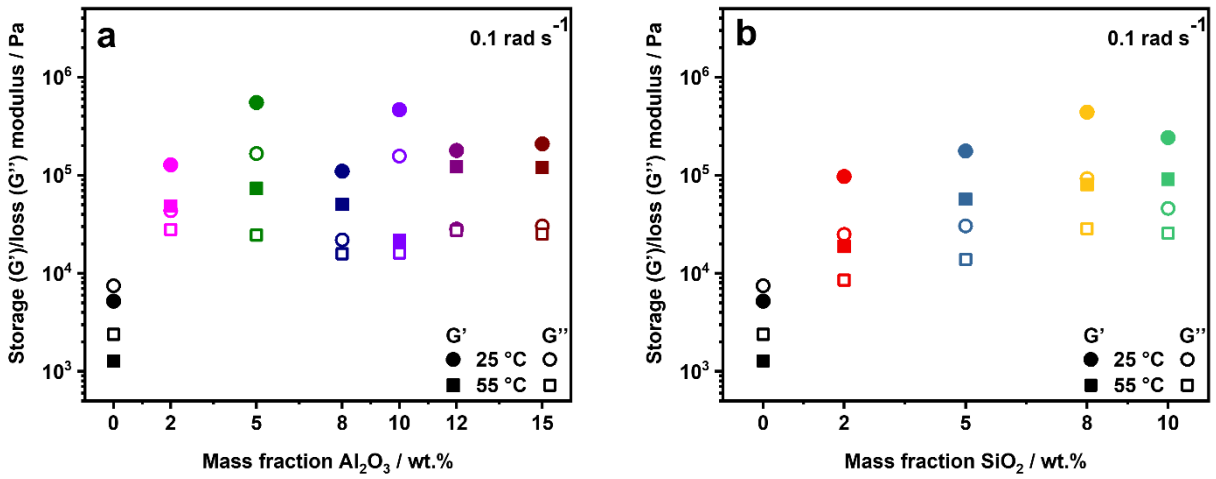

Figure 18. The dependence of storage (G') and loss (G'') moduli on the mass fraction of nano-sized **(a)** Al_2O_3 and **(b)** SiO_2 in PEO_{12}-$KTFSI_1$-based SPEs at angular frequency of 0.1 rad s^{-1} at 25 and 55 °C.

Moreover, the two compositions with higher melting points, i.e. AlOx-5 and AlOx-10, showed a notable shift to higher shear storage and loss moduli (by about half an order of magnitude) compared to the other samples investigated. The desired solid-like behaviour (G' > G'') was manifested for the SPEs at ambient temperature, suggesting possibility to obtain free-standing films for all Al_2O_3-PEO_{12}-$KTFSI_1$ samples in the investigated range of the filler concentration. Contrary to this expectation, in practice the SPEs containing less than 8 wt.% of Al_2O_3 did not yield a good processable, free-standing polymer electrolyte films. At 55 °C, all AlOx-containing compositions exceeded their melting points, which seemed to eliminate major differences between the compositions. In **Figure 18a,** the largest decrease in storage moduli

(by about one order of magnitude) can be seen for AlOx-5 and AlOx-10, while the G' values of AlOx-2 and AlOx-8 decreased by ca. half an order of magnitude and remained almost unchanged for AlOx-12 and AlOx-15. It should be noted that the corresponding shear loss moduli remain by and large in the same range and, more importantly, do not intercept the storage moduli curves in the measured frequency range (i.e. G' > G'' still applies). Noteworthy, at 55 °C AlOx-10 exhibited notably close values of G' and G'' at low angular frequency (**Figure 18a** at 0.1 rad s^{-1}, and **Figure A3** in the range of 0.1-1 rad s^{-1}).

Similar rheological behaviour was observed for the SiO_2-filled PEO_{12}-$KTFSI_1$ electrolytes (**Figure 18b**). At 25 °C, the storage moduli of the samples with SiO_2 were found to be in the range of G' = 9.4×10^4-4.4×10^5 Pa at 0.1 rad s^{-1}, which is more than one order of magnitude higher than G' of the pristine PEO_{12}-$KTFSI_1$ (measured at low angular frequencies). Furthermore, the SiO_2-filled electrolytes manifested solid-like properties (G' > G'') that were preserved even at an elevated temperature of 55 °C (**Figure 18b**). However, the overall shear moduli decreased along with a reduction in the gap between the storage and loss moduli. Although the SiO_2-SPEs (with 2-10 wt.% of the nanofiller) exhibited viscoelastic solid-like rheological behaviour at 25 °C (**Figure A3**) at the investigated angular frequency range, in practice free-standing films from SiOx-2 and SiOx-5 could not be obtained, which is a prerequisite for SPE application in K-metal batteries.

6.1.3. Coming in One Package: «Block Copolymer» Approach

In the following subsection, the poly(vinyl benzyl methoxy poly(ethylene oxide) ether)-*block*-polystyrene copolymer (shorted to PVBmPEO-*b*-PS or BP), was tested as a host polymer for SPEs. Prior to the preparation of the SPEs, BP was synthesized as previously reported (**Scheme 1**).[58] The average length of the mPEO side chain with a molar mass of 2.000 g mol^{-1} was determined using ^{1}H-NMR spectroscopy and calculated to an average number of ~48 EO units per side chain. In addition, the blocks of BP were matched to a weight ratio of around 50:50 to target self-standing films. Overall, the block copolymer with a molar mass (M_n) of 38.300 g mol^{-1} (as determined by size exclusion chromatography, SEC) was obtained.[58] The synthesized BP was further used to prepare the corresponding block copolymer electrolyte (BPE) compositions using KTFSI salt with varying the molar ratio of EO:K (20:1, 15:1, 10:1). Herein, the impact of the block copolymer structure and the salt concentration on thermal and rheological characteristics of the BPE_x-$KTFSI_y$ electrolytes was evaluated.

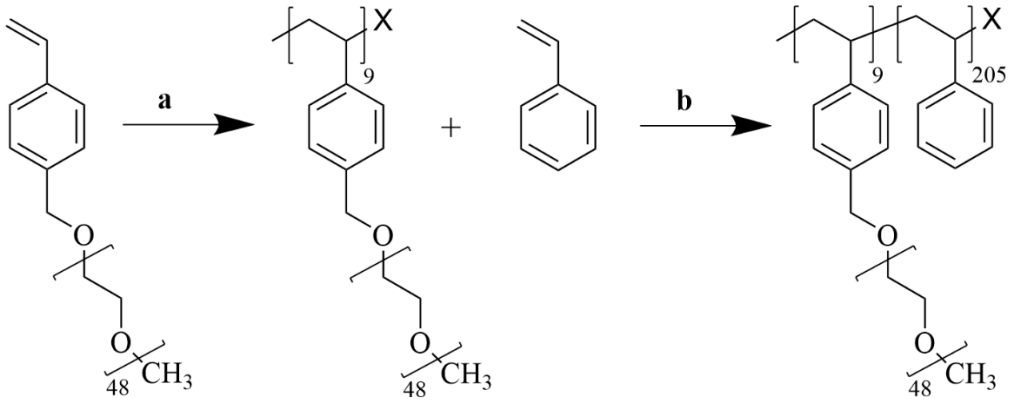

Scheme 1. Block copolymer synthesis by **(a)** polymerizing VBmPEO yielding PVBmPEO as a macro-RAFT agent (X symbolizes the RAFT end group). Subsequently, styrene was used for the chain extension **(b)** yielding PVBmPEO-*b*-PS (BP).

***Thermal characterization*.** Thermal properties of BPE_x-$KTFSI_y$ with different molar ratio of EO:K (*x:y* = 20:1, 15:1, 10:1) were investigated by DSC (**Figure A1d**).

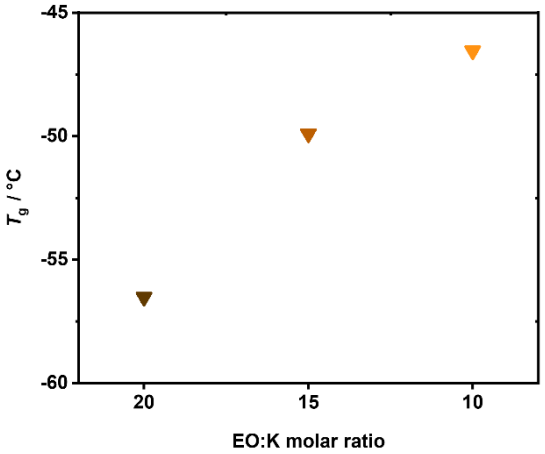

Figure 19. The dependence of glass transition temperature T_g (PEO phase) on the EO:K molar ratio in BPE-KTFSI SPEs.

Notably, all investigated SPEs featured two distinct T_gs: one in the temperature range from -56.5 to -41.3 °C, and another around 100 °C (summary given in **Table A3)**, corresponding to the PEO phase and the PS phase, respectively. Thus, a lamellar microphase-separated morphology is obtained, allowing both ion transport properties and mechanical strength (enabled by PEO and PS blocks, respectively).[58] Hence, BPE-KTFSI SPEs can benefit from structural integrity that would potentially prevent a short circuit, inhibiting metallic dendrite growth.[149–151] The T_g values of the PS phase in all investigated compositions were detected in the temperature range of ~99-103 °C (**Table A3**), showing no significant shift and thus,

indicating the absence of salt concentration influence on the PS phase formation. However, the BPE-KTFSI SPEs showed a notable shift of the PEO phase T_gs, depending on EO:K molar ratio.

The T_g increases with increasing concentration of electrolyte salt (**Figure 19**, given in **Table A3**). This tendency can be explained by the phenomenon of ionic cross-linking,[25,58,179–181] manifested by physical interactions between K^+ and PEO side chains that originates from the coordination of cations. As the number of cationic species in BPEs increased, a larger degree of physical cross-links restricting segmental motion of PEO chains was present, therefore, increasing the T_gs. It is noteworthy that the addition of KTFSI not only influences the T_g of resulting BPEs, but also significantly impacts their crystallinity. For comparison, T_m of the pristine BP was determined to be 47.3 °C and had a corresponding melting enthalpy, ΔH_m, of 52.9 J g^{-1}.[2] However, BPE_{20}-$KTFSI_1$ already demonstrated a decrease of the T_ms and ΔH_ms (**Figure A1d, Table A3**), indicating that the crystallinity was suppressed due to the presence of bulky anions hindering chain alignment.[287] With increasing salt concentration (BPE_{15}-$KTFSI_1$, BPE_{10}-$KTFSI_1$) fully amorphous materials were obtained, indicated by the absence of any endothermic peaks (**Figure A1d**) and two T_gs for both the PEO and PS phases.

Based on the thermal characteristics of the investigated BPE_x-$KTFSI_y$, the most promising composition in terms of ionic conductivity was expected to be the BPE_{15}-$KTFSI_1$, as this not only exhibited a completely amorphous state, but also showed the lowest T_g among the investigated non-crystalline compositions, i.e. compared to BPE_{10}-$KTFSI_1$. Therefore, the BPE_{15}-$KTFSI_1$ was chosen for examination of its rheological properties and further discussion.

***Rheological characterization*.** To examine the rheological properties and therefore evaluate the mechanical integrity of the BPE_{15}-$KTFSI_1$, SAOS measurements were conducted. As shown in **Figure 20**, the frequency dependences of the shear storage G' and loss G'' moduli of the BPE_{15}-$KTFSI_1$ were measured at ambient and elevated temperatures (25 and 55 °C, respectively). Importantly, G' > G'' was observed for the examined composition, indicating its dominating solid-like behaviour[216] at given conditions. At 25 °C, the storage moduli of the BPE_{15}-$KTFSI_1$ composition were found in the range of 3.3-5.3×10^5 Pa, showing a weak dependence on the frequency. As presented in **Figure 20**, the block copolymer-based composition maintained G' > G'', and only slightly lower moduli (2.4-3.5×10^5 Pa), indicating a negligible loss of mechanical stability at 55 °C due to the presence of the rigid PS block.[58,267] Here, the PS block possesses a high mechanical stiffness (G', G'' of ~1 GPa),[268] which is close to the threshold required for the suppression of metallic potassium dendrite growth (~2 GPa, based on theoretical work of Monroe *et al.*).[148,150,151]

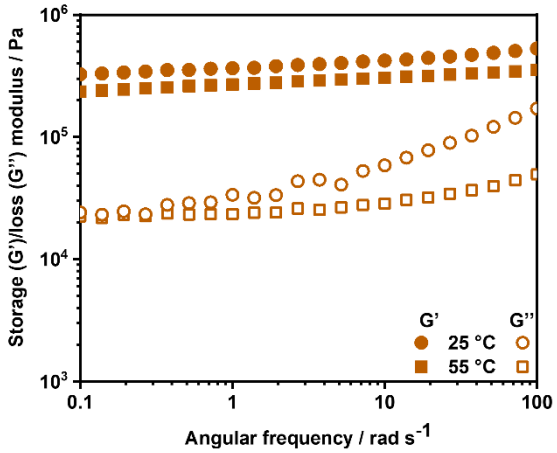

Figure 20. The dependence of storage (G') and loss (G'') moduli of BPE_{15}-$KTFSI_1$-based SPE on angular frequency at 25 ℃ and 55 ℃.

6.1.4. Structure–rheological Properties Relationships in PEO-based SPEs

As presented above, structural adjustments in PEO-based SPEs can lead to a drastic change of their rheological properties. For the examined PEO_x-$KTFSI_y$ (4:1 < *x:y* < 20:1) compositions, varying concentration of the electrolyte salt resulted in their twisted rheological behaviour, i.e. either solid-like (G' > G'') or liquid-like (G'' > G') properties. Noteworthy, rheological characteristics were found to be depended on several competing effects of KTFSI presence: the degree of crystallinity suppression (the result of $TFSI^-$ plasticizing effect), the degree of ion-ion and cation-polymer interactions (cross-links). Based on the obtained results, the PEO_x-$KTFSI_y$ compositions with EO:K = 16:1 and 12:1 were the most promising candidates in terms of their potentially high σ at near-ambient temperatures due to the highest fraction of the amorphous PEO phase. At the same time, the amorphous nature of the PEO_{12}-$KTFSI_1$ and PEO_{16}-$KTFSI_1$ adversely affected their mechanical strength, while blends with a higher number of cross-links and/or a higher degree of crystallinity, i.e. PEO_4-$KTFSI_1$, PEO_8-$KTFSI_1$ and PEO_{20}-$KTFSI_1$, respectively, yielded electrolyte films with higher shear moduli (maintaining G' > G'') and hence better mechanical stability. Although the measured shear moduli were several orders of magnitude lower than the critical threshold required to prevent potassium dendrite growth (~2 GPa),[149] their magnitude remains significant in contributing to dendrite suppression. Thus, in the PEO_x-$KTFSI_y$ mechanical strength was associated with the presence of (1) crystalline structure and/or (2) rigid ion-polymer or ion-ion linked structure. Unfortunately, both crystalline and rigid ion-polymer or ion-ion linked structures generally allow slow *coupled* to segmental motion ion transport due to the lower polymer free volume.

For further comparative discussion the semi-crystalline PEO_{20}-$KTFSI_1$, PEO_{12}-$KTFSI_1$, PEO_{12}-$KTFSI_1$ with 8 wt.% of Al_2O_3 (AlOx-8), and amorphous BPE_{15}-$KTFSI_1$ were chosen as the examples of the impact of structural adjustments on rheological properties, specifically mechanical stiffness that is required for SPE applications.

As seen in **Table 5**, for PEO_{20}-$KTFSI_1$ high storage G' and loss G'' moduli at 25 and 55 °C were ensured by high crystallinity degree, while predominately amorphous PEO_{12}-$KTFSI_1$ presented liquid-like properties, reflected in low values of G' and G'' with G'' > G'.

Table 5. Thermal and rheological characteristics (T_g, ΔH_m and degree of crystallinity X_C, storage G' and loss G'' moduli) of the examined PEO-based SPEs.

SPE	T_g, °C	ΔH_m, J g^{-1}	Crystallinity X_C*, %	G', Pa at 0.1 rad s^{-1} and 25 °C	G'', Pa at 0.1 rad s^{-1} and 25 °C	G', Pa at 0.1 rad s^{-1} and 55 °C	G'', Pa at 0.1 rad s^{-1} and 55 °C
PEO_{20}-$KTFSI_1$	-48.1	68.1	34.7	3.7×10^6	1.1×10^6	2.7×10^5	1.2×10^5
PEO_{12}-$KTFSI_1$	-47.7	11.1	5.7	5.2×10^3	7.5×10^3	1.3×10^3	2.4×10^3
AlOx-8	-41.5	43.6	24.1	1.1×10^5	2.2×10^4	5.0×10^4	1.6×10^4
BPE_{15}-$KTFSI_1$	-49.9	–	–	2.3×10^5	2.2×10^4	3.2×10^5	2.4×10^4

* Crystallinity X_C was calculated according to **Equation 7**.

The difference in rheological behaviour of PEO_{20}-$KTFSI_1$ and PEO_{12}-$KTFSI_1$ can be clearly seen in **Figure 21** showing the dependency of G' and G'' of PEO-based SPEs on oscillation stress at elevated temperature of 55 °C.

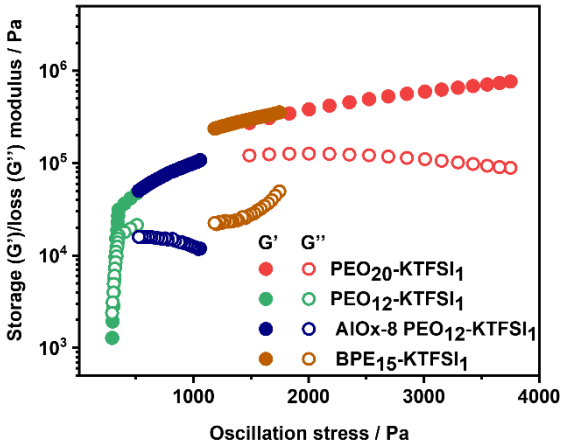

Figure 21. The dependence of storage (G') and loss (G'') moduli of PEO-based SPEs on oscillation stress at 55 °C.

For PEO_{12}-$KTFSI_1$, relatively low values of storage and loss moduli corresponded to low values of oscillation stress (~300-500 Pa), while PEO_{20}-$KTFSI_1$ demonstrated G' and G''

dependencies in the range of higher oscillation stress values (~1500-3800 Pa), thus indicating higher mechanical stability. Moreover, contrary to PEO_{20}-$KTFSI_1$, in the G' and G'' dependencies of PEO_{12}-$KTFSI_1$ the sweep can be seen, revealing the maximum stress of 350 Pa that can be applied before the SPE entered viscous flow behaviour (liquid-like properties) at 55 °C.

Furthermore, rheological properties of the predominantly amorphous PEO-based matrix, i.e. PEO_{12}-$KTFSI_1$, could be structurally adjusted *via* incorporating Al_2O_3 or SiO_2 inorganic nanoparticles. Based on the results shown in **6.1.2,** the Al_2O_3- and SiO_2-filled PEO-based composites demonstrated no tendency of T_g shift towards lower temperatures. This contradicts the general hypothesis in related Li- and Na-systems that nanoparticles act as plasticizers, increasing the amorphous regions due to the creation of free volume, which is typically reflected in the decreased T_g. Nanoparticles also suppress polymer chain ordering and consequently suppress crystalline growth and the formation of larger crystalline regions.[190,51,52] When comparing with literature data, it is worth noting that the impact of ceramic fillers on thermal behaviour of PEO-based electrolytes has been studied mostly in Li^+-containing systems. Compared to Li^+, the larger K-cation[292] is expected to have weaker interactions with charged surface groups, the polymer EO units, or the salt anions.[164,165] The increase of crystallinity degree in the Al_2O_3- and SiO_2-filled PEO-KTFSI samples can be seen as a result of local immobilization of PEO chains at the nanoparticle surface that may act as nuclei or seeds for nucleation of ordered PEO structures. Noteworthy, higher T_ms and crystallinity benefited mechanical strength of the PEO-based composites. Thus, all the investigated filled composites not only displayed higher G' and G'' moduli as compared to the filler-free PEO_{12}-$KTFSI_1$ but more importantly manifested the change of liquid-like to solid-like properties. In **Figure 21**, the dependencies of G' and G'' on oscillation stress of the exemplary AlOx-8 are shown in comparison with the filler-free samples. As stated above, the gain of mechanical rigidity can be attributed to the increase of crystallinity degree in the Al_2O_3- and SiO_2-filled samples due to specific nanoparticles-ion-polymer Lewis acid-base interactions.[51,52,53,54] Noteworthy, the increase of mechanical integrity came at the expense of PEO segmental mobility, which was reflected in the elevated T_g of the filled composites (**Table 5**).

In contrast to the previously examined semi-crystalline PEO_x-$KTFSI_y$ ($4:1 < x:y < 20:1$) and nano-Al_2O_3-/SiO_2-filled PEO_{12}-$KTFSI_1$ composites, BPE_{15}- and BPE_{10}-$KTFSI_1$ revealed fully amorphous nature, which can potentially improve their room temperature ionic conductivity. Therefore, the BPE-KTFSI might be advantageous in terms of ionic conductivity over the corresponding polymer electrolytes based solely on PEO at temperatures below T_m. Despite a

fully amorphous nature, BPE_{15}-$KTFSI_1$ manifested solid-like properties (G' > G'') at 25-55 °C, which contrasted with predominantly amorphous PEO-KTFSI compositions (i.e. PEO_{16}-$KTFSI_1$ and PEO_{12}-$KTFSI_1$) that revealed liquid-like properties (G'' > G') at given conditions. Moreover, as demonstrated in **Figure 21**, enhanced shear moduli of the the BPE_{15}-$KTFSI_1$ sample corresponded to oscillation stress values of 1200-1750 Pa. The combination of following advantages: (1) mobile segmental motion through PEO amorphous regions and (2) mechanical stiffness due to the formation of a rigid microphase-separated PS phase proved BPE-KTFSI to be promising candidates for SPEs application, especially at near-ambient temperatures.

6.2. Ion Transport in PEO-based SPEs

6.2.1. Total Ionic Conductivity

Temperature-dependent EIS measurements in the frequency range from 1 MHz to 500 mHz were conducted at temperatures from 15 to 85 °C (in 10 °C steps) for (1) the PEO_x-$KTFSI_1$ (x = 20, 16, 12, 8, 4) series, (2) the Al_2O_3- and SiO_2-filled PEO_{12}-$KTFSI_1$-based composites with 2-15 wt.% of nanofillers, (3) the BPE_x-$KTFSI_1$ (x = 20, 15, 10) compositions to determine their total ionic conductivities (**Figure A4**).

6.2.1.1. PEO-KTFSI SPEs

The conductivity dependencies on EO:K molar ratio in the PEO-KTFSI SPEs at 25 and 55 °C (below and above their T_m, respectively) are presented in **Figure 22a.** At first, the increase of ionic conductivity can be seen as the EO:K molar ratio changes from 20:1 to 16:1 due to the simultaneous decrease of crystallinity and increase of charge carriers number. PEO_{16}-$KTFSI_1$ demonstrated the highest values of ionic conductivity over the investigated temperature range as compared to other PEO-KTFSI SPEs. As given in the appendix **Table A4,** PEO_{16}-$KTFSI_1$ possessed 3.56×10^{-5} S cm^{-1} at 25 °C. It is noteworthy that a literature reference of PEO-LiTFSI system with molar ratio of EO:Li = 15:1 featured comparatively similar ionic conductivity of 3.54×10^{-5} S cm^{-1} at ambient temperature.[235] Following the results of DSC measurements of the PEO_x-$KTFSI_y$ series (**Figure 15** and **Table A1**), the highest ionic conductivity should be expected for PEO_{12}-$KTFSI_1$ since this composition showed the lowest crystallinity degree in combination with comparatively low T_g. However, in practice this did not appear to be the case as the highest ionic conductivity was found for the PEO_{16}-$KTFSI_1$ sample. As the KTFSI content increased from the 16:1 to 4:1 ratio, the ionic conductivity decreased continuously (**Figure 22a**).

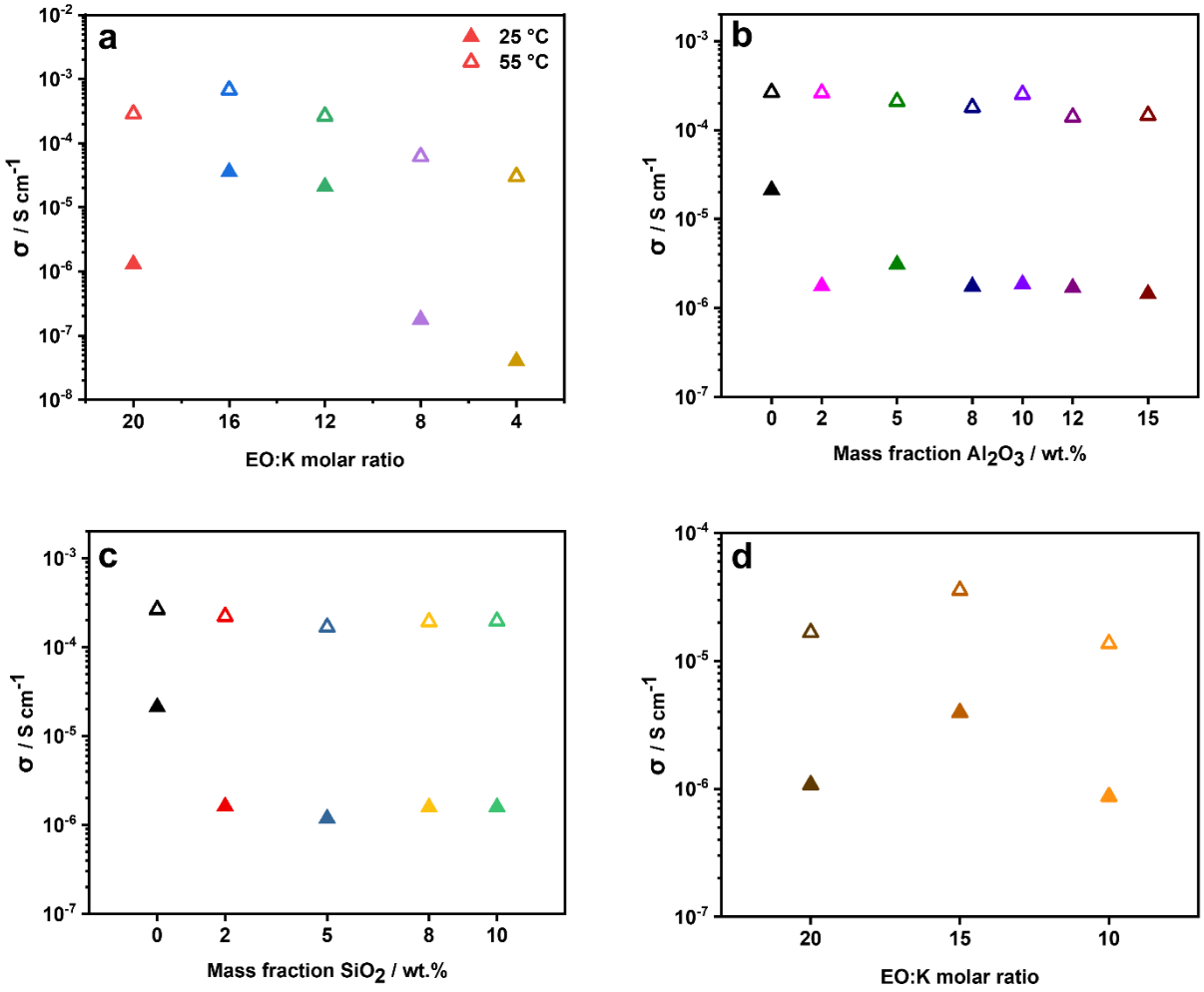

Figure 22. The dependence of ionic conductivity (derived from EIS measurements conducted in the frequency range from 1 MHz to 500 mHz) of **(a)** PEO-KTFSI SPEs on EO:K molar ratio, PEO_{12}-$KTFSI_1$-based SPEs on mass fraction of **(b)** Al_2O_3 and **(c)** SiO_2, and **(d)** BPE-KTFSI SPEs on EO:K molar ratio at 25 and 55 °C.

As the concentration of potassium ions increases, an increasing number of oxygen atoms in the PEO chain is coordinated to potassium ions. This alters both dynamic segmental motion as well as the availability of coordination sites. To the extent of available research, for PEO-K^+ system coordination geometry has been studied in the work of Bruce *et al.*,[163] who investigated PEO-based complexes incorporating Li, Na, K, and Rb cations. Their results demonstrated that the total coordination number increased in the raw PEO-$LiCF_3SO_3$ < PEO-$NaClO_4$ < PEO-K(Rb)SCN, corresponding to the increasing ionic radii of the cations. Specifically, total coordination numbers of 5, 6, and 7 were reported for Li^+, Na^+, and K^+(Rb^+), respectively. Moreover, as the coordination number increased, the strength of the coordinate bonds weakened due to the polymer adjusting its conformation to accommodate the larger cations.

However, different coordination geometry and binding strength can have a strong impact. For the series of PEO-KTFSI this specifically means that the lower ionic conductivity of the PEO_{12}-$KTFSI_1$ blend is presumably related to an increasing number of occupied coordination sites, thus slowing down the hopping mechanism. For the blends with a higher salt content (PEO_8-$KTFSI_1$ and PEO_4-$KTFSI_1$), not only a large degree of occupied hopping sites, but also the presence of crystalline intermediate compounds, i.e. a high number of physical cross-links[179,180,25] resulted in a significant drop of ionic conductivity. As can be seen in **Figure 22a**, the described trends are less pronounced at temperatures above the melting point of PEO-KTFSI SPEs due to the absence of crystalline regions. In contrast to other compositions, PEO_{16}-$KTFSI_1$ and PEO_{12}-$KTFSI_1$ possessed already a low degree of crystallinity and consequently did not exhibit an equally dramatic change of ionic conductivity over up to 3 orders of magnitude at elevated temperatures (**Figure 22a**).

6.2.1.2. Al_2O_3- and SiO_2-filled PEO-KTFSI SPEs

When examining the total ionic conductivity of the Al_2O_3- and SiO_2-filled PEO_{12}-$KTFSI_1$ composites (**Figure A4b & 4c**), no change in total ionic conductivity was observed with respect to the filler-free PEO_{12}-$KTFSI_1$ at temperatures above T_m. Compared to the filler-free PEO_{12}-$KTFSI_1$, the samples containing Al_2O_3 or SiO_2 showed one order of magnitude lower σ at 25 °C (2.1×10^{-5} vs. 1.2-3.1×10^{-6} S cm^{-1}, respectively, given in **Table A4**). When the temperature approached 45 °C (close to the T_ms of the filled SPEs, see **Table A2**), the difference in ionic conductivities became negligible (the same order of magnitude for the filler-free and modified PEO_{12}-$KTFSI_1$, around 1.0×10^{-4} S cm^{-1}). Upon further increase of the experimental temperature, the σ deviation remains the same (55-85 °C). At 55 °C, the samples demonstrated σ of 1.4-2.6×10^{-4} S cm^{-1} (**Figure 22b & 22c**). Similar findings of the ion transport dependency on temperature were manifested for the SiO_2-containing PEO_{12}-$KTFSI_1$ samples.

As previously highlighted, nanofiller-PEO and nanofiller-salt interactions can result in structural reorganisation of the polymer chains around the particles that can promote crystalline phase formation through immobilization of the polymer segments in proximity to the particle interface. As shown in the previous subsection, the addition of either Al_2O_3 or SiO_2 fillers to the PEO_{12}-$KTFSI_1$ matrix resulted in higher degrees of crystallinities of the resulting composites (**Table A2**). Consequently, the overall ion transport properties were adversely affected in the presence of more crystalline domains and locally restricted chains motion, since ion transport occurs predominantly in the amorphous phase. Hence, as the crystalline domains melted above T_m the ionic conductivities of the filler-containing samples approached similar

values as the filler-free PEO_{12}-$KTFSI_1$ formulation (**Figure 22b & 22c**). Conversely, below T_m ion transport was hindered in the samples with nanofillers.

6.2.1.3. BPE-KTFSI SPEs

Further, EIS measurements were implemented to evaluate the total ionic conductivities σ of the BPE_{20}-$KTFSI_1$, BPE_{15}-$KTFSI_1$ and BPE_{10}-$KTFSI_1$ SPEs (**Figure A4d, Figure 22d**). As already highlighted in the discussion of thermal properties, the largest σ values were expected for the amorphous BPE_{15}-$KTFSI_1$ due to its lower T_g (PEO phase) value. Supporting thermal characterization, a peak ionic conductivity was found at EO:K molar ratio of 15:1 (e.g. 1.07×10^{-6} vs. 3.95×10^{-6} and 8.73×10^{-7} S cm^{-1}, for EO:K = 20:1, 15:1 and 10:1, respectively, at 25 °C, summary given in **Table A4**). For the BPE_{20}-$KTFSI_1$, suppressed ion transport was probably caused by two effects: (1) semi-crystalline nature and (2) a lower concentration of K^+ charge carriers. Surpassing T_m of this blend (~30 °C, see **Table A3**), a significant increase of σ was observed (**Figure A4d**) as a result of the melting of any remaining crystalline regions.[25,194] However, even above T_m of the BPE_{20}-$KTFSI_1$, the ionic conductivity of the SPE with EO:K = 15:1 could not be reached, probably due to the lower KTFSI concentration (i.e. lower number of charge carriers) in the 20:1 electrolyte formulation. Conversely, the SPE with EO:K = 10:1 possessed the largest content of charge carriers but still restrained ion transport was observed (**Figure 22d**) compared to the 15:1 SPE. This can be explained by the higher T_g (PEO phase) of BPE_{10}-$KTFSI_1$ and probably more ionic cross-linking as a result of the higher cation concentration.[25,181,212]

In **Figure 23** the temperature dependencies of ionic conductivity in the SPEs based on solely PEO and block copolymer PVBmPEO-*b*-PS, BP, (as PEO_{20}-$KTFSI_1$ and BPE_{15}-$KTFSI_1$, respectively) are presented. The PEO_{20}-$KTFSI_1$ sample was chosen as an example of semi-crystalline PEO-based SPE (**Table A1**). As has been highlighted above, at ambient temperature the ion transport was expected to be advanced in BPE-based compositions due to their amorphous state enabled by the sophisticated architecture, in contrast to the semi-crystalline nature of pure PEO-based samples. As seen in **Figure 23**, compared to semi-crystalline PEO-based sample, amorphous BPE_{15}-$KTFSI_1$ revealed higher total ionic conductivities at temperatures below 35 °C. However, when approaching T_m of PEO_{20}-$KTFSI_1$ (melting point of 37 °C, see **Table A1**), the difference in ionic conductivities disappeared as crystalline domains of PEO phase started to melt. Up to 55 °C the ionic conductivity of PEO_{20}-$KTFSI_1$ enhanced rapidly (1.20×10^{-5} vs. 2.86×10^{-4} S cm^{-1} at 35 and 55 °C, respectively), exceeding ionic conductivities of BPE_{15}-$KTFSI_1$ of around one order of magnitude (**Figure 23**). This could

result from lower PEO domain fractions in block copolymers as compared to SPEs based solely on PEO (due to the additional PS phase). Therefore, at higher temperatures BPE-based SPEs possessed relatively modest ionic conductivities, while the mechanical stability was significantly improved.[58]

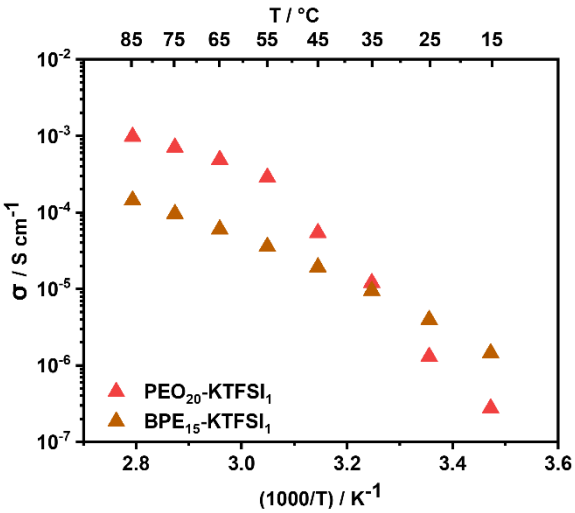

Figure 23. Temperature-dependent ionic conductivity (derived from EIS measurements conducted in the frequency range from 1 MHz to 500 mHz in the temperature range from 15 to 85 °C) of PEO_{20}-$KTFSI_1$ and BPE_{15}-$KTFSI_1$ SPEs.

6.2.2. Transference Number Measurements

The ionic conductivities obtained from the EIS measurements provide only the total ionic conductivities of the SPEs, including contributions from both cations and anions. While SPEs containing the same electrolyte salt but different polymer host material may exhibit similar total ionic conductivities, the mobility of cations (involved in electrochemical redox processes) may differ. This can be associated with different polymer chain dynamics due to a lower or higher degree of interchain links, i.e. ionic cross-links, and/or different coordination strength between cations and polymer. Therefore, in the following subsection the transference number, T_{K^+}, was measured using the commonly employed Bruce-Vincent method,[198] combination of potentiostatic polarization and EIS in symmetrical K/PEO_{20}-$KTFSI_1$/K and K/BPE_{15}-$KTFSI_1$/K cells, shortened to Sym-PEO- and Sym-BPE-cells, respectively (**Figure 24, Table 6**).

First, the experiment was carried out in the symmetrical Sym-PEO-cell at elevated temperature of 55 °C and ΔV of 30 mV. A constant dc bias potential in this experiment was set to 30 mV, as it should be low enough to obtain linear response of the system, yet high enough to receive reasonable current values. In **Figure 24** dependency of the current density (*j* mA cm^{-2}) on time as well as area specific resistance (ASR, Ohm cm^2) derived from EIS spectra (before and after

potentiostatic polarization) are plotted. Summary of the obtained characteristics is given in **Table 6**.

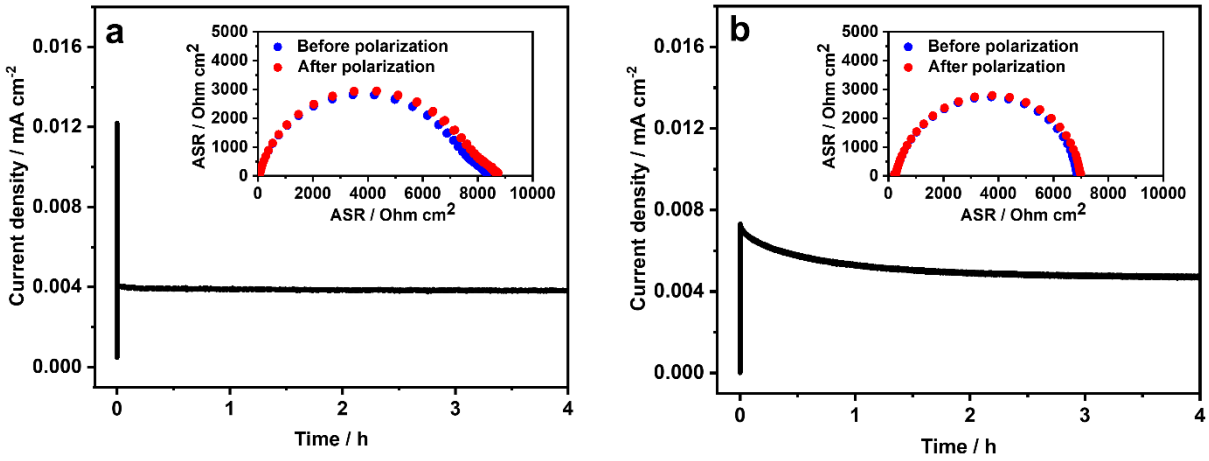

Figure 24. Chronoamperometry and area specific resistance (ASR) derived from EIS spectra (before and after potentiostatic polarization) of **(a)** K/PEO_{20}-$KTFSI_1$/K cell at ΔV of 30 mV and 55 °C, EIS recorded in the frequency range from 200 kHz to 10 mHz, and **(b)** K/BPE_{15}-$KTFSI_1$/K cell at ΔV of 50 mV and 55 °C, EIS recorded in the frequency range from 1 MHz to 100 mHz.

Table 6. Characteristics derived from potentiostatic polarization and EIS (before and after polarization) of symmetrical K/PEO_{20}-$KTFSI_1$/K and K/BPE_{15}-$KTFSI_1$/K cells.

SPE in symmetrical K-cell	Resistance initial R_0, Ohm	Resistance steady-state R_s, Ohm	Current initial I_{0exp}, mA	Current initial I_{0theor}, mA	Current steady-state I_s, mA	I_s/I_{0exp}	T_{K^+}
PEO_{20}-$KTFSI_1$	4130	4330	0.024	0.007	0.008	0.33	5.0
BPE_{15}-$KTFSI_1$	3290	3351	0.015	0.014	0.009	0.60	0.02

As indicated in **Table 6**, for the Sym-PEO-cell initial resistance R_0 of 4130 Ohm was derived from the Nyquist plot (EIS recorded before polarization). Furthermore, the cell exhibited initial current value I_0 of 0.024 mA (j = 0.012 mA cm^{-2}), followed by a steady-state value I_s of 0.008 mA (j = 0.004 mA cm^{-2}), resulting in I_s/I_0 ratio of 0.33. After polarization, the Sym-PEO-cell showed resistance increase ΔR of 200 Ohm. According to **Equation 15**, T_{K^+} of PEO_{20}-$KTFSI_1$ was calculated to be 5.0, which is larger than theoretical T_{K^+} maximum ($T_{K^+} \leq 1$). Moreover, the obtained experimental initial current I_{0exp} of 0.024 mA is not in line with theoretical I_{0theor} (0.007 mA, calculated through Ohm´s law, **Equation 16**), which

contradicts reliability of the measurement. Such inconsistency can be caused by the high reactivity of potassium metal, resulting in a large resistance at K-metal/PEO_{20}-$KTFSI_1$ interface, reflected in a high overpotential.

Further, T_K^+ was measured for BPE_{15}-$KTFSI_1$ in the symmetrical K-cell at 55 °C. As compared to the Sym-PEO-cell, the BPE-based one showed close values of initial ASR (**Figure 24**) but smaller R change after polarization (ΔR = 200 vs. 61 Ohm for the Sym-PEO- and Sym-BPE-cells, respectively, **Table 6**). In contrast to the Sym-PEO-cell, I_{0exp} value is in line with the theoretically calculated I_0 (**Table 6**) for the Sym-BPE-cell. Furthermore, the ratio of steady-state to experimental initial current I_s/I_{0exp} is higher for the Sym-BPE-cell, indicating a smaller current decay in this system. In a setup with non-blocking, yet inert, electrodes, an increase in the I_s/I_0 ratio can be interpreted as a sign of higher ionic mobility. However, potassium electrodes are well known for their high reactivity towards electrolyte components[284,293,294] and thus may also exhibit a leaking current from recurrent degradation reactions. On the other hand, the impedance measurements before and after polarization suggested that, although the interfacial resistance was large, the cell impedance did not change significantly. However, the calculated transference number T_K^+ for the K/BPE_{15}-$KTFSI_1$/K cell is 0.02, which contradicts the galvanostatic cycling results of this electrolyte in the half cell configuration (discussed further in **Section 6.3.2.3**), where BPE_{15}-$KTFSI_1$ conducted K^+ ions to a decent extent.

As stated in this subsection, the interfacial resistances at the K-metal/SPE interfaces were large. With the transport across the electrode-electrolyte interface being a determining factor, no meaningful parameters could be obtained. Although, the Bruce-Vincent method is the most used technique to determine the T_A^+ (especially for traditional Li-based systems), similar observations have been reported in literature for Na- and K-cells, indicating that the Bruce-Vincent method is difficult to adapt to post-Li systems due to their large interfacial resistances.[206,207,293,295] Such alternative methods as Watanabe method,[208] Sørensen and Jacobsen approach,[209] also utilize metallic non-blocking cell configurations. While suitable for symmetrical Li-based cells, their reliability in Na- and K-based systems is uncertain due to high overpotentials and metal passivation, which can distort measurements. PFG-NMR[210] has also been proposed for determining T_A^+, however, its application in post-Li systems is limited by the short spin relaxation times of the relevant NMR-active isotopes. Moreover, mentioned above methods remain valid in dilute systems where ion-ion interactions are negligible, while in concentrated electrolyte solutions, ion pair diffusion leads to an overestimation of T_A^+. Recent studies have combined electrophoretic NMR with EIS to determine T_{Li}^+, T_{Na}^+, T_K^+ in PEO- and PCL-based electrolytes.[65] Although, the authors highlighted a distinct correlation

between strong coordination and a low T_{A^+}, yet similar values were found for all three alkali metals (~0.2 in PEO and ~0.5 in PCL). This is in contrast to findings of the theoretical work of Fortuin *et al*. who investigated PEO-LiTFSI, -NaTFSI, -KTFSI complexes and found higher transference numbers for larger cations.[236]

Given the challenges in accurately determining cation transference numbers in post-Li systems, a more practical approach suggests measuring the limiting current density in symmetrical cells, representing the maximum sustainable cationic current.[147]

6.3. Electrochemical Performance

6.3.1. Potassium Plating and Stripping Experiments

To evaluate the interfacial stability of PEO-based SPEs against K-metal, overpotentials originating from plating and stripping in symmetrical K/SPE/K cells were determined at current densities (*j*) of 0.01-0.1 mA cm^{-2} (increasing current density each 10 cycles, 1 h per semi cycle with an OCV step, see details in the experimental section, **Section 4**). The temperature of the experiment was elevated to 55 °C to improve ionic conductivity of the PEO-based SPEs and reduce the contribution of SPE bulk resistance to the overall cell resistance.

PEO- and BPE-KTFSI SPEs. For potassium plating and stripping experiments, PEO_{20}-$KTFSI_1$ was tested because this formulation provided the highest ionic conductivity among the compositions maintaining mechanical integrity at elevated temperatures. As already discussed, amorphous nature of PEO_{12}-$KTFSI_1$ and PEO_{16}-$KTFSI_1$ blends adversely affected their mechanical stability, and therefore free-standing films based on these compositions could not be obtained, which was a prerequisite for the practical application in solid-state potassium batteries. As for the BPE-based group, BPE_{15}-$KTFSI_1$ was chosen as a representative since it fulfilled the requirements of sufficient ionic conductivity as well as mechanical stiffness at elevated temperatures.

In **Figure 25**, a reversible K-metal deposition can be seen in symmetrical K/PEO_{20}-$KTFSI_1$/K (Sym-PEO-) and K/BPE_{15}-$KTFSI_1$/K (Sym-BPE-) cells at 55 °C with *j* of 0.01, 0.02, 0.05 and 0.01 mA cm^{-2}. At an initial current density of 0.01 mA cm^{-2}, a maximum overpotential of 100 mV was detected for the Sym-PEO-cell, followed by further increase at higher current densities (**Figure 25a**). Thus, maximum overpotentials of 180 and 350 mV were observed at *j* of 0.02 and 0.05 mA cm^{-2}, respectively. When decreasing the current density (from 0.05 to 0.01 mA cm^{-2}, the last sequence in **Figure 25a**), the K/PEO_{20}-$KTFSI_1$/K cell exhibited neither

voltage noise nor following short circuit, showing a slight increase of overpotentials during 10 cycles (~80-100 mV).

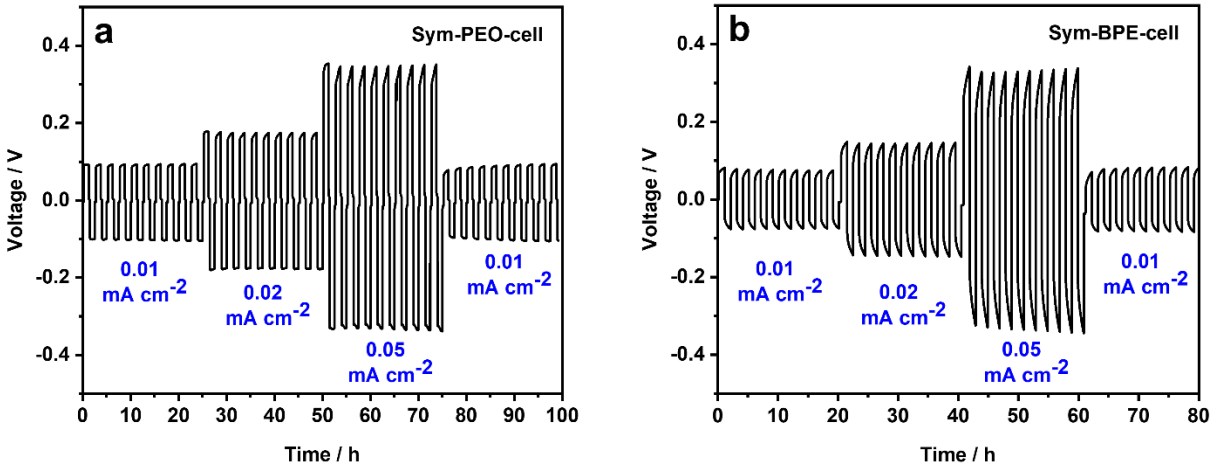

Figure 25. Plating/stripping experiments in symmetrical K/SPE/K cells at 55 °C with current densities (*j*) of 0.01, 0.02, 0.05 and 0.01 mA cm^{-2} (for 10 cycles at each current density and 1 h per semi cycle) where SPE = **(a)** PEO_{20}-$KTFSI_1$ and **(b)** BPE_{15}-$KTFSI_1$.

As displayed in **Figure 25b**, the Sym-BPE-cell showed similar stripping and plating behaviour but slightly lower values of overpotentials as compared to the Sym-PEO-cell (±20-30 mV). Since a precise measurement of the T_{K^+} was not possible, it is hard to estimate the actual influence of host material on the ion transport through the polymer electrolytes. For comparison, lower overpotentials (even at higher current densities) are commonly observed during lithium plating and stripping experiments in SPE-based symmetrical cells.[269,296] Higher potentials in the case of K-metal can be attributed to a larger cell resistance, which originates presumably from the resistance of the electrolyte, thicker and/or poorer ion-conducting SEI, as well as the charge-transfer.[297]

Al_2O_3- and SiO_2-filled PEO-KTFSI SPEs. As previously shown in **Figure A3**, all tested Al_2O_3- and SiO_2-filled PEO_{12}-$KTFSI_1$ SPEs displayed solid-like properties. However, in practice some samples did not yield processable free-standing films. Therefore, in this subsection the compositions containing 8 wt.% of filler were chosen for a first evaluation of cell resistances in plating and stripping experiments in symmetrical K/AlOx-8/K (Sym-AlOx-8-) and K/SiOx-8/K (Sym-SiOx-8-) cells at 55 °C (**Figure 26a & 26b**, respectively). Unlike the previous potassium plating/stripping experiments, the cells were cycled at higher current densities, gradually increasing *j* of 0.01, 0.02, 0.05, 0.075 and 0.1 mA cm^{-2}.

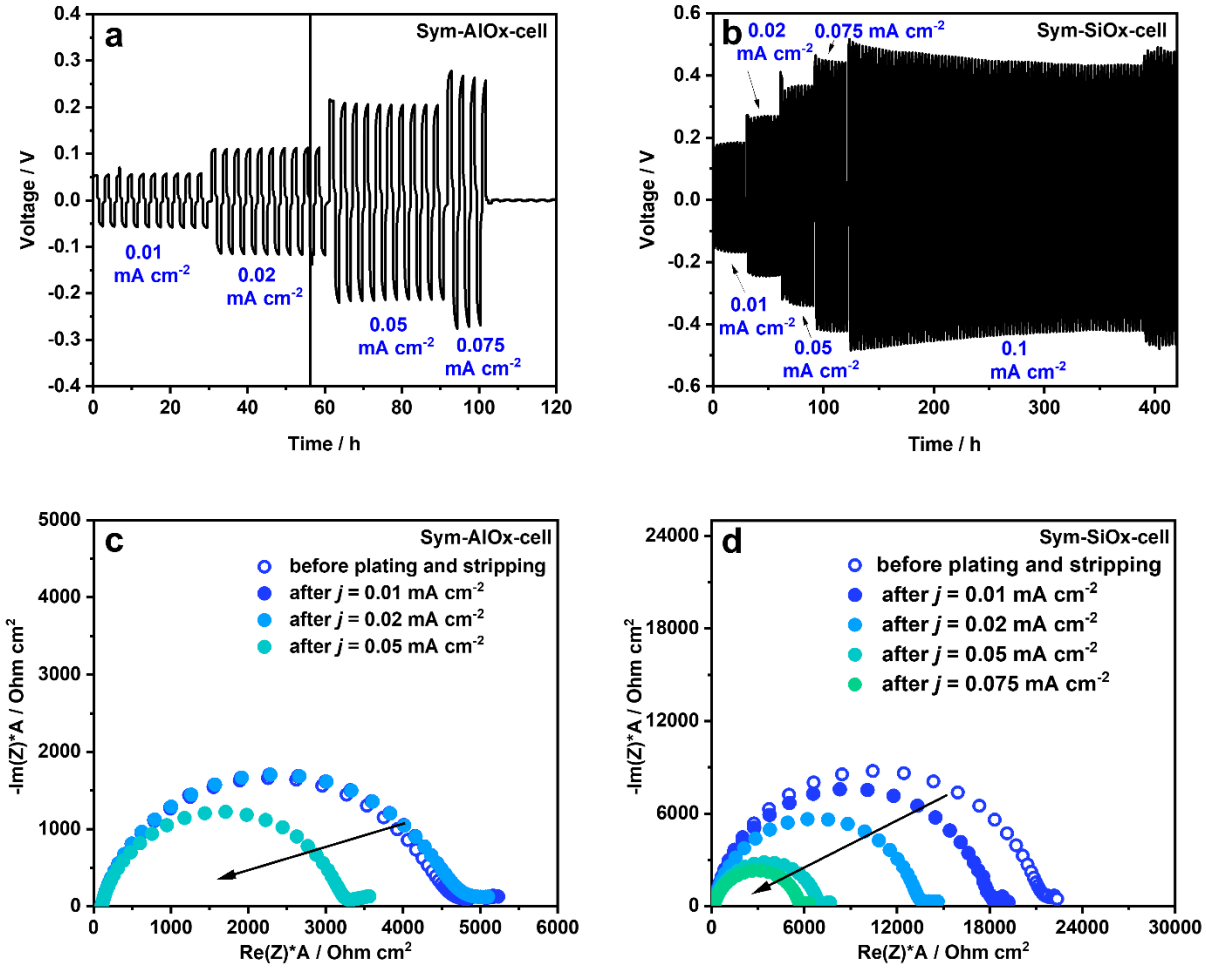

Figure 26. Plating/stripping experiments in symmetrical K/SPE/K cells at 55 °C with current densities (*j*) of 0.01, 0.02, 0.05, 0.075 and 0.1 mA cm^{-2} where SPE = **(a)** AlOx-8, **(b)** SiOx-8. EIS conducted in the frequency range from 200 kHz to 10 mHz after every *j* increase in K/SPE/K cells where SPE = **(c)** AlOx-8, **(d)** SiOx-8.

As seen in **Figure 26a**, the symmetrical K-cell with AlOx-8 SPE demonstrated a reversible metal deposition at *j* of 0.01, 0.02, 0.05 mA cm^{-2}. At the lowest current density, i.e. *j* = 0.01 mA cm^{-2}, the cell showed overpotentials of ~60 mV. In the 3rd cycle, voltage fluctuations were observed (see inset in **Figure 26a**), possibly associated with surface processes.[228] At higher *j* of 0.02 mA cm^{-2}, overpotentials almost doubled and corresponded to ~110 mV. At *j* = 0.05 mA cm^{-2}, Sym-AlOx-8-cell enabled cell cycling only under substantial overpotential of ≤220 mV. Thus, in first approximation, the plating and stripping overpotentials scale linearly with *j*. Further, a short circuit occurred in the following sequence at 0.075 mA cm^{-2}. This is most likely associated with K-metal dendrite growth, adversary affecting the cell performance in plating and stripping experiments.[28,226]

For Sym-SiOx-8-cell (**Figure 26b**), notably higher overpotentials were observed when plating and stripping at the same current densities as in the case of symmetrical cell with AlOx-8. Thus, overpotentials of ~180 mV corresponded to j=0.01 mA cm^{-2}, followed by increase to ~260 mV at 0.02 mA cm^{-2}, and further to ~360 mV at 0.05 mA cm^{-2}. Contrary to the AlOx-8 electrolyte, neither fluctuating voltages nor short circuit were noted. Moreover, the cell with SiO_2-filled sample completed the sequence at 0.075 mA cm^{-2} with initial overpotentials of ~520 mV. The overpotential decreased with increasing number of cycles to 430 mV, which is still quite substantial. Overall, the cell could be operated for over 250 h at a current density of 0.1 mA cm^{-2} and thus showed considerably better cycling stability than the Al_2O_3 composite.

For comparison, under the same experimental conditions Sym-BPE-cell, previously discussed in current subsection, displayed overpotentials of 330 mV at 0.05 mA cm^{-2}, which is in the same range as the SiO_2 composite but about 110 mV higher than the Al_2O_3. However, analogous symmetrical Li-cells typically demonstrate ca. 10 times lower overpotentials at given current densities.[2] As mentioned, higher overpotentials in the case of K-metal are attributed to larger cell resistance, due to formation of a resistive SEI layer.[297]

For this reason, in this experiment EIS spectra were recorded at the end of each cycling segment, i.e. before the next higher current density was applied. **Figure 26** shows the evolution of the cell impedance after every 10 cycles (each cycling segment) for Sym-AlOx-8-cell (**Figure 26c**) and Sym-SiOx-8-cell (**Figure 26d**). At least two discernible processes with different time constants contributed to the impedance spectrum before plating and stripping, while different electrode processes in the spectra of the cycled cells could not be properly distinguished. Considering a high reactivity of potassium, contributions of both the charge-transfer reaction and the surface layer were expected.[297] In addition, the electrolyte resistance and a dielectric contribution from the polymer electrolyte might add to the frequency arcs that may be interpreted as a single electrode process, i.e. a single semicircle. Comparing the diameter of the frequency arcs (using data points at the same frequency), it is seen that the impedance in the system decreased with increasing current density. This finding is in contrast with the expectation that a reactive K-metal electrode should show increasing impedance as cycling (and thus aging) progresses. It is an indication, however, that the plating and stripping process removes some of the charge-transfer inhibiting compounds from the surface (or fresh K-metal is plated on the surface). Noteworthy, increase of the electrode surface, e.g., by growth of dendrites or formation of more porous morphologies may reduce the impedance that is normalized to the geometric electrode area. At the same time, based on the EIS results, the SEI

layer growth does not appear to be critical at this stage of the cycling process (but might become more significant as the cell ages).

Evidently, SiO_2-based polymer electrolytes showed higher areal resistance (by a factor of 5) compared to Al_2O_3 composites at the beginning of the first cycling sequence. Interestingly, over the course of 30 cycles at three different current densities, the impedance of the cell containing SiOx-8 decreased considerably and approached similar values than the cell containing AlOx-8. Although the impedances equilibrate to similar values, the overpotentials during cycling remained larger for the SiO_2 composite, indicating that practically K^+-ion transport is slower (higher polarization) in this formulation.

6.3.2. Capacity Retention in Galvanostatic Cycling Experiments

In this last subsection, the investigated PEO-based SPEs were tested in potassium half cells with K-metal/electrolyte/cathode configurations comprising the Prussian blue analogue $K_{2-x}Fe[Fe(CN)_6]$, KFF, as the positive electrode and K-metal as negative electrode. As cathode material, KFF was chosen for its widespread use in post-Li applications, i.e. in Na- and K-based batteries, and high cycling stability reported for both liquid and solid-state polymer electrolytes.[11,79,298] In addition, the material purely iron-based and free of critical heavy metals like cobalt or nickel, rendering this material more sustainable. Herein, KFF was synthesized by the precipitation method.[11] Using the combination of TGA and ICP-OES analyses, the resulting stoichiometry of the compound was calculated to $K_{1.90}Fe[Fe(CN)_6]_{0.98}\times 1.0H_2O$ that would correspond to a theoretical capacity of ~141 mAh g^{-1}.

6.3.2.1. Liquid vs. Solid with PEO-KTFSI as an Example

Capacity retention of PEO_x-$KTFSI_y$ SPEs with $x:y$ = 4:1, 8:1, 20:1 (the samples with solid-like properties) was compared to that of a liquid electrolyte, LE, the reference system, comprising a solution of KPF_6 in a mixture of EC and PC with a fluorine-containing additive (see in the experimental section, **Section 4**) to suppress electrode-electrolyte side reactions. The EC:PC solvent mixture has been reported as a particularly stable combination towards oxidation in the high voltage region.[299] Furthermore, KTFSI was avoided as electrolyte salt, as it may induce corrosion processes at the Al current collector.[11] Because of the comparatively low ionic conductivity at room temperature, galvanostatic cycling of SPE-based cells was carried out at 55 °C while the reference LE-based cell was tested at ambient temperature (25 °C) (**Figure A5**). In both cases the cycling rate was C/25 with a voltage window of 2.5-4.3 V vs. K^+/K. In **Figure A5a** only 7 cycles can be seen for the cell employing PEO_4-$KTFSI_1$ due to its failure afterwards,

while the cell with PEO_8-$KTFSI_1$ SPE failed after 45 cycles (**Figure A5b**). Both experiments were not repeated due to the observed high polarization resulting in low capacities.

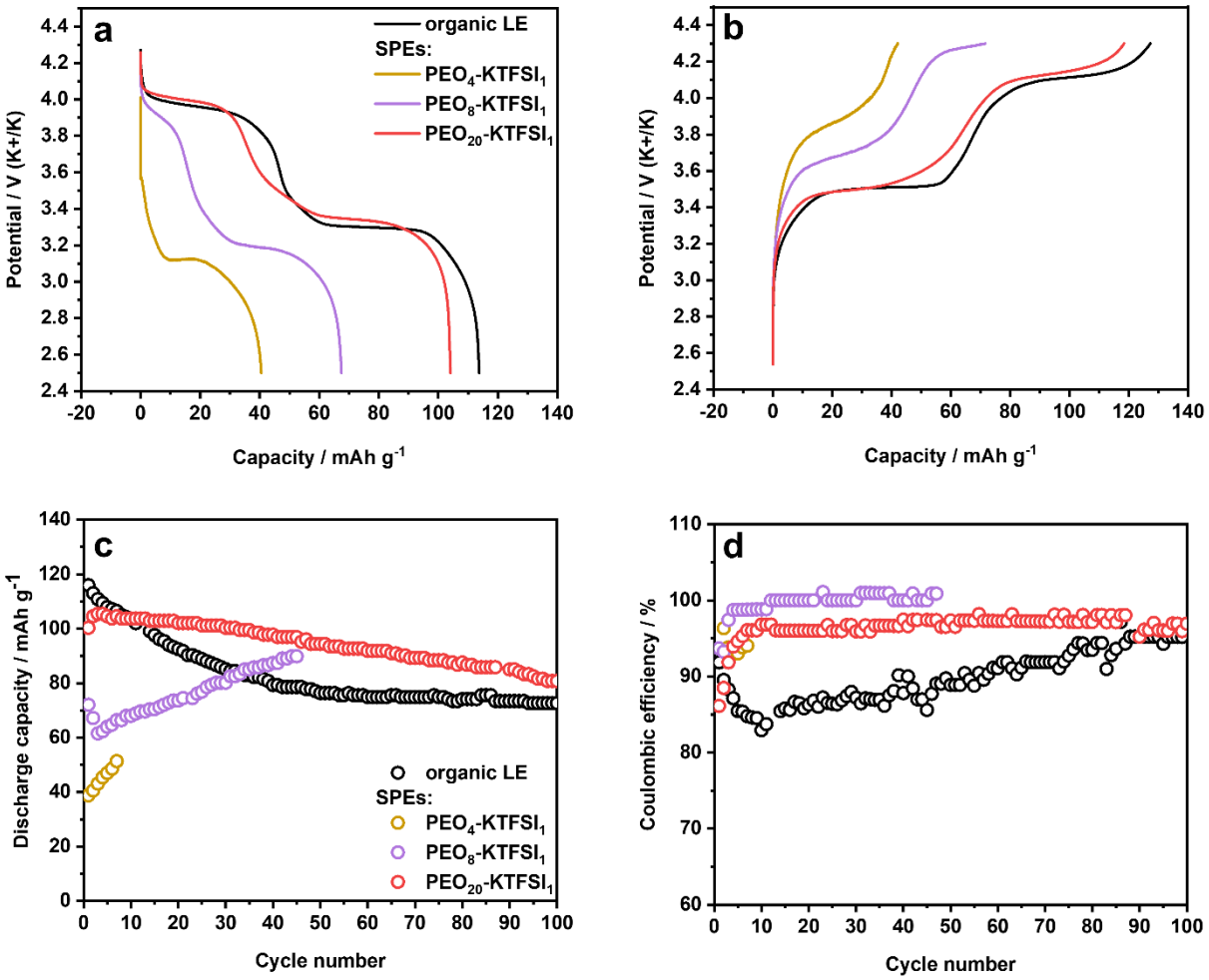

Figure 27. Comparison of K-metal/electrolyte/KFF cells with different electrolyte systems: **(a)** galvanostatic discharge profiles in the 2nd cycle, **(b)** galvanostatic charge profiles in the 2nd cycle. **(c)** Capacity retention and **(d)** corresponding Coulombic efficiencies.

In **Figure 27**, the cycling results of the tested electrolytes are shown. The galvanostatic profiles of the electrolytes in the 1st cycle correspond to the conditioning process and are not discussed herein, while the discharge and charge profiles in the 2nd cycle are presented in **Figure 27a & 27b**. As can be seen in **Figure 27a**, a practical capacity of 104.6 mAh g^{-1} was delivered in the 2nd cycle of the discharge process of the cell with the PEO_{20}-$KTFSI_1$ electrolyte, which is ~74 % of the theoretical capacity of $K_{1.90}Fe[Fe(CN)_6]_{0.98}\times 1.0H_2O$ and only 7 % lower than that of the reference cell (113.1 mAh g^{-1}) with LE. Significantly lower discharge capacities were obtained in the 2nd cycle of the cells employing PEO_8-$KTFSI_1$ and PEO_4-$KTFSI_1$ SPEs (67.2 mAh g^{-1} and 40.5 mAh g^{-1} respectively). In **Figure 27a & 27b** two distinct voltage

plateaus can be observed for PEO_{20}-$KTFSI_1$ and LE, and only a negligible polarization effect is seen in the case of PEO_{20}-$KTFSI_1$ (changes in redox potentials $\Delta V < 0.06$ V), which indicates sufficient ionic conductivity at the chosen cycling rate and good interfacial compatibility with the cathode material. In contrast, the galvanostatic profiles of the cells employing PEO_8-$KTFSI_1$ and PEO_4-$KTFSI_1$ electrolytes exhibited significant polarization ($\Delta V \approx 0.2$-0.4 V) compared to the sample with LE. Therefore, the PEO_4-$KTFSI_1$ cell did not show the second voltage plateau in the charge profile before the upper voltage cut-off (4.3 V) was reached. The PEO_8-$KTFSI_1$ cell showed the onset of the second plateau before the cycling was stopped at 4.3 V. This generally reflects well the differences of ionic conductivity depending on the KTFSI content (see **Table A4**).

As highlighted in **Figure 27c**, the benefit of using a solid electrolyte rather than a liquid electrolyte is the significantly improved capacity retention. Thus, the PEO_{20}-$KTFSI_1$ cell reached a capacity retention of 90 % over the first 50 cycles, while the reference LE-based system retained only 66 % of its initial capacity over the same cycle number interval (i.e. 36 % improvement in capacity retention). By the 100^{th} cycle, the improvement of capacity retention in the SPE-based cell remained (14 %). In general, higher capacity retention indicates lower degrees of side reactions and therefore improved electrochemical stability of SPE in comparison to LE. This is further reflected in the Coulombic efficiency, shown in **Figure 27d**, which will be discussed further. Higher electrochemical stability is strongly linked to the interface processes between electrode and electrolyte. In a battery, the SEI acts as a protective layer supressing excessive electrolyte consumption. However, the nature and quality of the SEI may vary strongly in different electrolytes.[284]

As can be seen in **Figure 27c**, the PEO_{20}-$KTFSI_1$ cell showed an increasing discharge capacity (Q_{disch}) from the 1^{st} to the following cycles. Thus, the highest Q_{disch} was detected in the 3^{rd} cycle (105.4 mAh g^{-1}, about 5 % higher compared to the 1^{st} cycle). This behaviour was more pronounced in the PEO_4-$KTFSI_1$ cell (**Figure A5a**) that exhibited a considerably smaller initial discharge capacity, but the capacity continued to increase over the following cycles. A similar behaviour was observed for the cell employing PEO_8-$KTFSI_1$ (**Figure A5b)**. This behaviour is generally attributed to the excluded electrode domains from the ion-conducting SPE due to the insufficient electrode-electrolyte surface contact and uncompleted penetration of SPE into the remaining cathode void space during the first cycles. Over time polymer electrolytes creep further into the porous network of the cathode, involving more active material particles.[146] It can be seen that the creeping process took longer for PEO_4-$KTFSI_1$ and PEO_8-$KTFSI_1$ SPEs,

which can be attributed to their significant morphology change due to a gradual fade of crystalline intermediate ionic associates over time.

The analysis of Coulombic efficiency is a measure of the degree of irreversible processes at the electrode-electrolyte interface during charge and discharge and is presented for the tested cells in **Figure 27d**. The CE data reveals significant difference in both the SEI formation process in the first cycles and the long-term CE. In the 1st cycle the cell based on PEO_{20}-$KTFSI_1$ demonstrated a CE of around 85 %, which is 7 % lower than that of LE-based cell (92 %). This can be addressed to a higher degree of irreversible reactions at the reactive potassium-SPE interface in the beginning of the experiment due to the elevated test temperature (55 °C instead of 25 °C for the LE). In the setup with conventional LE a significant drop of CE was observed on subsequent cycles (from 92 % in the 1st cycle to 83 % in the 10th cycle) indicating the gradual increase of side reactions typical for carbon-based electrolyte/K-metal setups,[10,11] leading to recurrent electrolyte consumption and capacity fade. Meanwhile, the systems with the PEO_{20}-$KTFSI_1$ polymer electrolyte displayed CE increase and remained stable throughout subsequent cycles, approaching 97 % in the 100th cycle. Although the observed CE correspond to a relatively high value of 97 %, it still indicates a significant degree of irreversible reactions consuming K, which can be mitigated by the presence of excess potassium due to the potassium metal anode.

6.3.2.2. Inorganic Fillers in PEO-KTFSI: Toward Better Capacity Retention

The SPEs based on PEO_{12}-$KTFSI_1$ with Al_2O_3 and SiO_2 nanofillers were tested in potassium half cells, comprising KFF as the positive electrode and K-metal as the negative electrode. Previously, the Al_2O_3- and SiO_2-filled SPEs showed improved mechanical stability with respect to the pristine PEO-KTFSI composition, and therefore, better electrochemical stability, i.e. higher capacity retention, could be expected.

For galvanostatic cycling tests of Al_2O_3-SPEs, three compositions were chosen with 8, 10, and 12 wt.% of nano-Al_2O_3, (AlOx-8, AlOx-10, AlOx-12, respectively). The cells were cycled at a C-rate of C/15 with a voltage window of 2.5-4.3 V vs. K^+/K at elevated temperature of 55 °C. Capacity retentions and corresponding Coulombic efficiencies, CE, are provided in **Figure 28a-c**. The voltage profiles for selected cycles can be found in **Figure A6a-c**.

The AlOx-8 cell demonstrated Q_{disch} of 82.5 mAh g^{-1} in the 1st cycle, approaching the maximum of 99.4 mAh g^{-1} in the 13th cycle. As seen in **Figure 28a**, the cell demonstrated a slight capacity decline over 60 cycles (from 99.4 to 98.2 mAh g^{-1}, ~1 %), followed by a recovery back to 99.0 mAh g^{-1}. This can be associated with electrode-electrolyte contact changes over time.[146]

Upon further cycling, the cell reached a notably high capacity retention over the first 100 cycles. Specifically, with respect to the maximum of Q_{disch} in the 13th cycle, the capacity loss on following cycles was ca. 1% up to the 100th cycle.

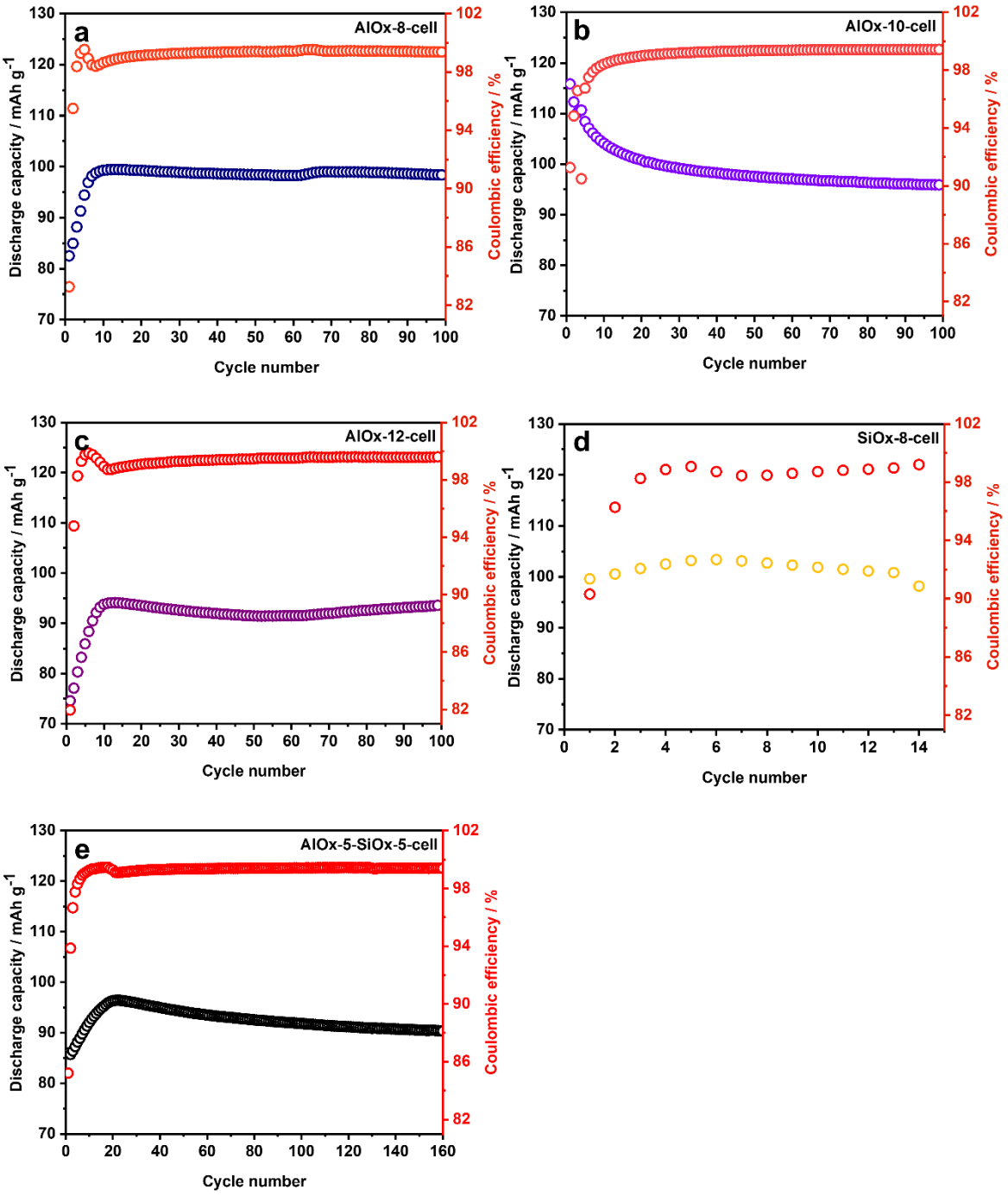

Figure 28. Capacity retention and corresponding Coulombic efficiencies of K-metal/SPE/KFF cells with different SPE composites: **(a)** AlOx-8, **(b)** AlOx-10, **(c)** AlOx-12, **(d)** SiOx-8 (failed after 14 cycles), **(e)** AlOx-5-SiOx-5.

The cell with AlOx-12 SPE showed a similar behaviour to that employing AlOx-8, i.e. increasing capacities in the conditioning phase in combination with a peak in CE after a few cycles **Figure 28c**). The maximum Q_{disch} of 94.1 mAh g^{-1} was obtained in the 13th cycle, and the CE values varied between 99.0 and 99.6 % until the 100th cycle. The capacity dropped between the 13th and 50th cycle by ca. 3 % before it started to increase slightly again. As a result, the capacity retention was 99 % after 100 cycles. It is worth noting that both AlOx-8 and AlOx-12 showed reversible discharge capacities around 100 mAh g^{-1}, while in the previous subsection a higher initial specific discharge capacity of 115 mAh g^{-1} was found in reference measurement with an organic carbon-based liquid electrolyte.

Contrary to the previously observed tendency of increasing initial discharge capacities in the conditioning phase, the AlOx-10 cell reached its maximum Q_{disch} of 115.9 mAh g^{-1} in the 1st cycle (**Figure 28b**), which is in the same range as for a corresponding LE cell (see in **6.3.2.1**). A continuous capacity decay was observed, that was most pronounced from the 1st to 20th cycle and resulted in a total capacity retention of 83 % after 100 cycles. The initial CE of 91.3 % increased to above 99.0 % after the 20th cycle and reached 99.4 % in the 100th cycle. In the series of Al_2O_3-composition SPEs, AlOx-10 was an exception. However, this not only applies to the electrochemical test but is also in agreement with its thermal and rheological properties, where AlOx-10 deviated from the other compositions. For instance, its rheological properties (G' ≈ G'' at low angular frequencies at 55 °C; **Figure 18a)**, could potentially facilitate the SPE penetration into the cathode coating layer.

Further, the PEO_{12}-$KTFSI_1$ SPE employing 8 wt.% of SiO_2 nanofillers was tested in the same cell configuration (K-metal/SPE/KFF) under the same cycling conditions (**Figure A6d**). As can be seen in the voltage profiles in **Figure A6d**, the cell only enabled 13 cycles before showing voltage noise in the 14th cycle, which marked the onset of the cell failure. The effect of voltage fluctuations during the charge/discharge process is often observed for the PEO-based SPEs in lithium metal cells[226,228] and is attributed to metallic dendrite growth.[28] As presented in **Figure 28d**, the cell achieved 4 mAh g^{-1} higher Q_{disch} maximum compared to the analogous K-metal/SPE/KFF cell with 8 wt.% of Al_2O_3 (**Figure 28a**).

A «hybrid» PEO_{12}-$KTFSI_1$ SPE filled with 5 wt.% each of Al_2O_3 and SiO_2 (i.e. 10 wt.% of the nanofillers in total) was further tested, attempting to merge a stable long-term cycling and a higher capacity (**Figure A6e**). Capacity retention and corresponding Coulombic efficiencies of the cell employing the «hybrid» SPE are shown in **Figure 28e**. In the 1st cycle, the cell demonstrated a modest Q_{disch} of 86.0 mAh g^{-1} that drastically increased over the conditioning phase, resulting in the maximum of 96.4 mAh g^{-1} in the 20th cycle. The corresponding CE in

the first cycles increased from 85.2 to 99.2 % (from the 1st to the 20th cycle, respectively) most likely due to the improvement of the electrode-electrolyte interface. After reaching the maximum Q_{disch}, the cell exhibited a slight but continuous capacity decay, eventually showing capacity retention of 95 % after 100 cycles, and 94 % after 160 cycles. Furthermore, the cell with this «hybrid» formulation quickly approached CEs >99 % (featuring 99.4 % CE in the 160th cycle) and displayed the stable long-term cycling behaviour. In fact, for other composites, testing beyond 100 cycles has not been conducted, so their long-term performance remains unknown.

6.3.2.3. Block Copolymer Design: Prospects of SPE Applications

Galvanostatic cycling of a K-metal/BPE_{15}-$KTFSI_1$/KFF cell was conducted at the chosen conditions, i.e. at a C-rate of C/15 and a voltage window of 2.5-4.3 V vs. K^+/K at 55 °C (**Figure A7**). **Figure 29** presents capacity retention and corresponding CE that are discussed in the following.

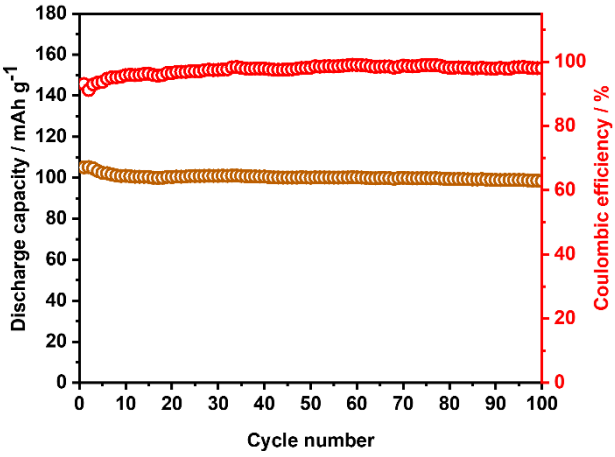

Figure 29. Capacity retention and corresponding Coulombic efficiencies of K-metal/BPE_{15}-$KTFSI_1$/KFF cell.

As can be seen in **Figure 29**, the K-metal/BPE_{15}-$KTFSI_1$/KFF cell enabled stable cycling over 100 cycles. A discharge capacity of 105 mAh g^{-1} was obtained in the 1st cycle followed by a slight increase in the 2nd cycle (105.2 mAh g^{-1}), which is ~75 % of theoretical capacity of the synthesized KFF (141 mAh g^{-1}) and about 90 % of the achievable capacity in the same cell configuration with a liquid electrolyte. Interestingly, the maximum of Q_{disch} was achieved in the first cycles, indicating a good interfacial compatibility, likely resulting in a good wetting of the active material of the porous cathode. The most notable capacity decay was observed from the

2nd to the 17th cycle, corresponding to a capacity loss of ~5 %. This was also reflected in the evolution of the CE, which increased from 91.2 to ~97 % over the same cycle interval, indicating a higher degree of irreversible reactions in the first cycles that attenuated in the subsequent cycles (**Figure 29**). Notably, after the interfaces were formed, both discharge capacity and CE remained stable over following cycles, resulting in a total capacity retention of 94 % and CE of ~98 % over 100 cycles.

6.4. PEO-based SPEs Comparison

In conclusion, different PEO-based electrolyte compositions were investigated for SPE application in potassium metal batteries. The first group of electrolytes was based on solely PEO as a host material and was considered as a reference experiment. As alternative strategies, the addition of Al_2O_3/SiO_2 inorganic nanofillers (composite materials approach), and the utilization of a copolymer with both a rigid (high T_g) PS block and an amorphous (low T_g) PEO block (block copolymer approach) were made. All host materials were tested with KTFSI salt, thus giving PEO_x-$KTFSI_y$, AlOx-PEO_x-$KTFSI_y$, SiOx-PEO_x-$KTFSI_y$ and BPE_x-$KTFSI_y$. Since all the experiments described above were conducted under similar conditions, differences in performance can be related to the electrolyte formulations. The previous subsections have discussed differences in the electrochemical characteristics of SPEs within the same group, but no overall comparison has been made so far. This section discusses the advantageous and shortcomings of different material approaches and traces the relationship between the rheological properties and ionic conductivities of different SPEs and their performance in potassium metal cells. **Table 7** summarizes the maximum Q_{disch}, capacity retention after 100 cycles and CE of the electrolytes studied in **Chapter 6**. A comparison of the galvanostatic cycling results of selected samples is shown in **Figure 30**.

Table 7. Characteristics (maximum of discharge capacity, Q_{disch}, capacity retention over 100 cycles and Coulombic efficiency, CE) derived from galvanostatic cycling experiments of K-metal/SPE/KFF cells with different SPEs.

Sample	Maximum of Q_{disch}, mAh g^{-1}	Capacity retention (over 100 cycles), %	CE (at the 100th cycle), %
PEO_{20}-$KTFSI_1$	105.4	77	97
AlOx-8	99.4	99	>99
AlOx-10	115.9	83	
AlOx-12	94.1	99	
AlOx-5-SiOx-5	96.4	95	
BPE_{15}-$KTFSI_1$	105.2	94	98

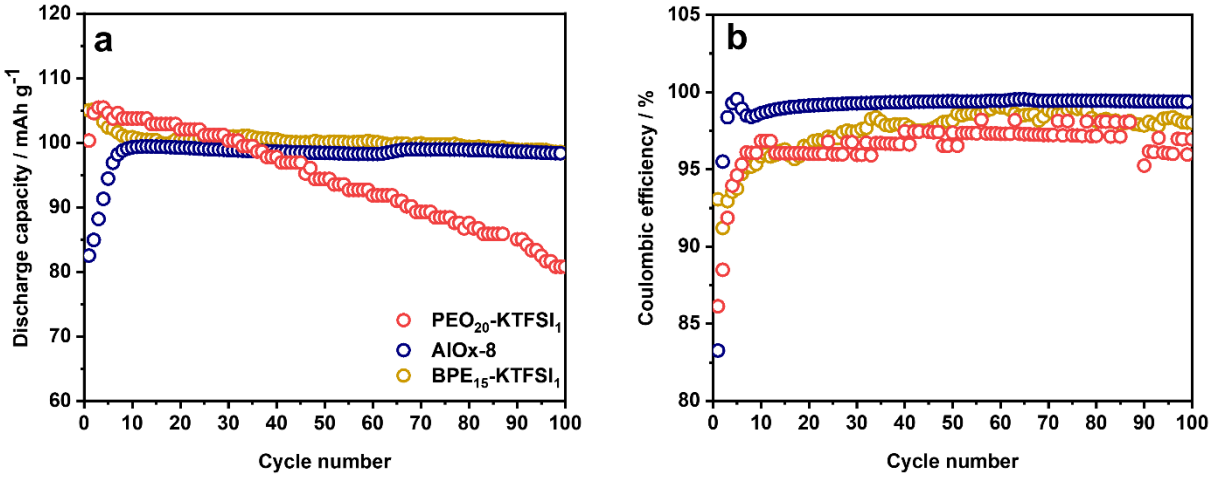

Figure 30. Comparison of **(a)** capacity retention and **(b)** corresponding Coulombic efficiencies of K-metal/SPE/KFF cells with different SPE systems representing different material approaches: PEO_{20}-$KTFSI_1$ (homopolymer)**,** AlOx-8 filled PEO_{12}-$KTFSI_1$ (composite), BPE_{15}-$KTFSI_1$ (block copolymer).

The composite strategy, specifically the incorporation of Al_2O_3 and SiO_2 nanoparticles into the PEO-KTFSI matrix in this thesis, led to the formation of specific nanoparticle-ion-polymer Lewis acid-base interactions that increased the T_g values of the filled samples. As the polymer free volume decreased, lower total ionic conductivities were observed at near-ambient temperatures. Although the direct evaluation of cationic conductivity was not possible (due to the challenges associated with the measurement of T_{K^+}), higher T_{K^+} can be expected for composite electrolytes with respect to their filler-free counterparts.[46,252,53] In this thesis, higher cationic conductivity can be evidenced by the means of galvanostatic cycling as AlOx-/SiOx-based SPEs showed an improvement in capacity retention up to 99 % and CE above 99 % in the 100th cycle (**Table 7**). Importantly, the composite approach effectively transformed liquid-like properties into solid-like properties. Thus, the Lewis acid-base interactions provided mechanical reinforcement that contributed to the suppression of dendrite growth, thereby improving cycling stability.

The block copolymer approach effectively suppressed the inherent crystallinity of PEO, resulting in fully amorphous BPE-based electrolytes while maintaining solid-like properties. The amorphous nature contributed to enhanced total ionic conductivity at near-ambient temperatures, whereas microphase separation played a crucial role in mitigating dendrite formation. This structural optimization led to improved capacity retention as compared to the electrolyte based of pure PEO (**Table 7**). Specifically, with respect to the PEO_{20}-$KTFSI_1$-based cell, the BPE_{15}-$KTFSI_1$-based one demonstrated the same initial discharge capacity

(105 mAh g^{-1}) but the capacity retention improvement of 17 % over 100 cycles. Both SPEs (based on either PEO or BP) approached Coulombic efficiencies of 97-98 % in the 100th cycle, indicating that there was still a significant degree of side reactions.

To summarize, although at 55 °C the PEO_{20}-$KTFSI_1$ (homopolymer approach) revealed the highest shear moduli and total ionic conductivity with respect to all examined AlOx-/SiOx-, BPE-based SPEs (**Figure 21**, **Table A4**), the latter showed an improvement of capacity retention and CE over 100 cycles. It should be noted that a C-rate of C/15 allowed shorter times in the high potential region, as PEO reaches its stability limit in the voltage region between 4.1 to 4.3 V vs. K^+/K,[29,222] but the improved capacity retention was mainly ascribed to the impact of the inorganic fillers and/or the advanced microphase-separated architecture of the BPE-based SPE.[45,190]

7. Polycarbonate-based SPEs: as Beyond PEO

The previous section revealed the main bottleneck of the PEO-based SPEs, i.e. low ionic conductivity, especially at near-ambient temperatures, which imposed limitations on the cell cycling conditions (requiring conditions such as elevated temperature and low cycling rate). Alternatively to the polyether-based materials, polycarbonates – the polymeric analogues to the liquid carbonate solvents, like EC or PC used in this thesis for the reference cell operated with liquid electrolyte, – have shown favorable solvation of electrolyte salts.[65,186] In contrast to the ether unit of PEO, the carbonyl-containing group demonstrated a relatively weak coordination strength of A^+,[62,186] which may be a key towards higher cationic conductivity and thus lower cell polarization, which is crucial for stable cycle life. The parent material for polycarbonates is PTMC, that typically features a predominantly amorphous nature, while the presence of crystalline domains can restrict its ionic conductivity at ambient temperature.[276] By varying the polymer architecture *via* random co-polymerization with ε-caprolactone, CL, units, a fully amorphous copolymer P(CL_m-TMC_n) with increased ionic conductivity (up to 10^{-5} S cm^{-1} at ambient temperature)[192,278] can be synthesized that is of a high interest due to the feasibility of room temperature operating cell.

For this thesis, polycarbonate-based polymers were synthesized using previously reported route (**Scheme 2**).[276,282] P(CL_m-TMC_n) with molar ratio *m:n* of 80:20 was chosen because it offered the best trade-off between mechanical strength and ionic conductivity, when tested with Li- and Na-containing salts.[192,278]

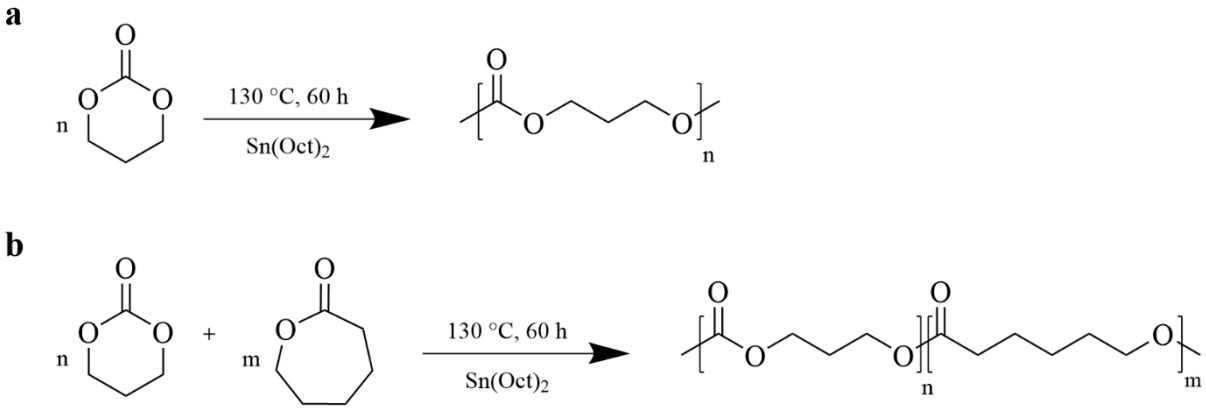

Scheme 2. Synthesis of **(a)** poly(trimethylene carbonate) PTMC and **(b)** poly(caprolactone-*co*-trimethylene carbonate) P(CL_m-TMC_n) through ring-opening (co)polymerization of corresponding (co)monomers (catalyzed by $Sn(Oct)_2$).

Using ^{1}H NMR and ^{13}C NMR spectroscopy, the chemical structures of the polymers and the desired molar ratio of CL and TMC blocks of P(CL_{80}-TMC_{20}) were confirmed. The polymers featured an average M_n of around 140.000 g mol^{-1} and 310.000 g mol^{-1} for PTMC and P(CL_{80}-TMC_{20}), respectively (determined by gel permeation chromatography, GPC).

7.1. Thermal Properties

Firstly, DSC was performed on the synthesized polymeric materials, PTMC and P(CL_{80}-TMC_{20}), to characterize their thermal properties. As shown in **Figure A8**, the T_g of the pristine PTMC was determined to be -16 °C, while the P(CL_{80}-TMC_{20}) exhibited T_g of -57 °C, both in agreement with reported T_g values for these materials.[147] Consistent with the literature for high molecular weight PTMC,[192] no endothermic peaks were observed in the thermogram, indicating its amorphous structure. In contrast, semi-crystalline P(CL_{80}-TMC_{20}) displayed a broad endothermic peak, corresponding to a melting temperature of 15 °C (**Table A5**).

Further, polycarbonate-based SPEs with a broad concentration range of KTFSI (1 < [TMC]/[CL_{80}-TMC_{20}]:K < 24) were prepared and their thermal properties were investigated by DSC (**Figure A8**). While increasing the content of amorphous phase is a desired outcome for the SPEs, the PTMC-KTFSI blends appeared to be fully amorphous at the KTFSI concentration range of 4 < [TMC]:K < 24. In contrast, for P(CL_{80}-TMC_{20})-based SPEs, the compositions with [CL_{80}-TMC_{20}]:K = 24:1, 16:1 featured T_m of around 13-15 °C (**Figure A8**, **Table A5**), most likely indicating the mixed-phase systems, where T_m can be assigned to K-depleted (polymer-rich) phases. Interestingly, mixed-phase systems were also observed for both PTMC- and P(CL_{80}-TMC_{20})-based compositions with high KTFSI fraction (i.e. 2:1 and 1:1 blends) that exhibited broad endothermic peaks at high temperature range (~125-170 °C, **Figure A8**, **Table A5**). As for the previously investigated PEO_4-$KTFSI_1$ (**Figure A1**, **Table A1**), these additional endothermic peaks can be attributed to intermediate crystalline K-rich phases, that occurred when surpassing the saturation limit of KTFSI in polymers, thus changing to polymer-in-salt regime.

Dependency of the T_g values of the polycarbonate-based electrolytes on KTFSI concentration can be seen in **Figure 31**. As for the previously investigated PEO-based electrolytes, T_g shifted to higher values with increasing salt concentration due to ionic cross-linking effect. A more gradual increase of T_g can be seen for the PTMC-KTFSI compositions with 1 < [TMC]:K < 8, with an overall T_g increase of ~20 °C (in the whole range of KTFSI concentration). Meanwhile, for P(CL_{80}-TMC_{20})-KTFSI blends, a more rapid increase of T_g was observed over the examined range of salt concentration (with several points being inconsistent with general trend),

exhibiting a total increase of T_g of ~27 °C. Most likely, CL-units coordinate stronger to potassium cations as compared to TMC-units, restricting segmental motion of the copolymer chains to a higher extent. This is in contrast to findings of Andersson and co-authors,[64] who reported that Na^+ preferably coordinated to the carbonyl group of TMC than that of CL. Similarly to the results obtained herein, stronger ion-polymer interactions to CL units as compared to carbonate groups of TMC were reported for the Li^+ systems.[62–64]

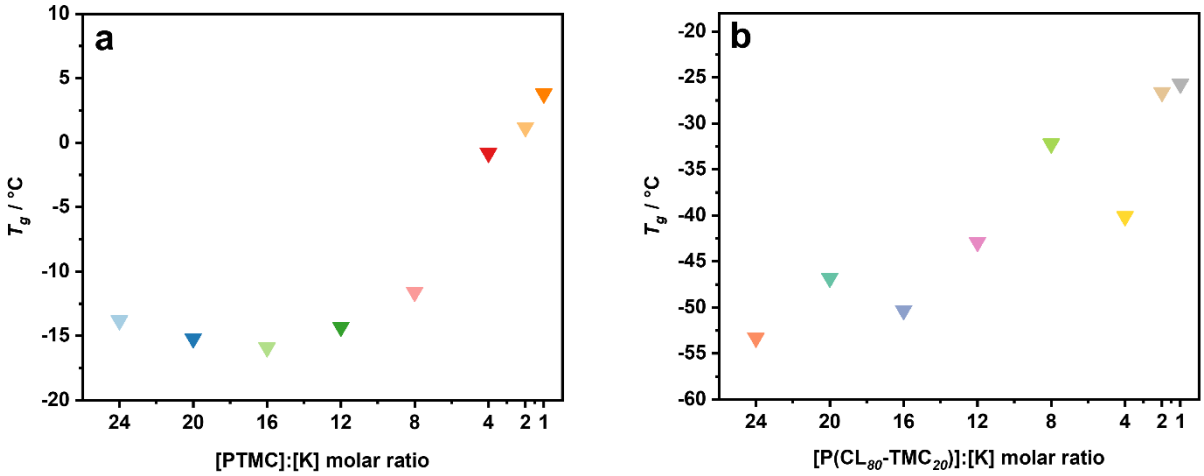

Figure 31. The dependence of glass transition temperature T_g on the [TMC]/[CL_{80}-TMC_{20}]:K molar ratios in **(a)** PTMC-KTFSI and **(b)** P(CL_{80}-TMC_{20})-KTFSI SPEs.

7.2. Total Ionic Conductivity

Further, total ionic conductivities of PTMC- and P(CL_{80}-TMC_{20})-based SPEs containing various concentrations of KTFSI were evaluated using EIS in the frequency range from 10 MHz to 1 Hz at the temperature range of 25-85 °C (in 10 °C steps) (**Figure A9**). Based on the DSC results, higher ionic conductivities were expected for the P(CL_{80}-TMC_{20})-KTFSI blends because these demonstrated lower values of T_g, indicating a higher degree of amorphous phase (preferable for the ion transport mechanism *coupled* to segmental motion). As seen in **Figure A9** and **Figure 32**, this hypothesis was confirmed by the results of the EIS measurements. At low temperature region (near-ambient temperatures), the σ values of the copolymer P(CL_{80}-TMC_{20}) were found to be 2-3 orders of magnitude higher as compared to that of the homopolymer. As the temperature of the EIS measurement increased, variance of σ values obtained for the homopolymer and the copolymer decreased (i.e. one order of magnitude at 55 °C, **Figure 32**), which can be assigned to the larger change of polymer free volume in homopolymer PTMC. For the P(CL_{80}-TMC_{20})-based SPEs, the highest ionic conductivity was demonstrated by the sample with 12:1 molar ratio of [CL_{80}-TMC_{20}]:K (6.1×10^{-6} S cm^{-1},

9.5×10^{-5} S cm^{-1} at 25 and 55 °C, respectively). Meanwhile, among the PTMC-KTFSI electrolytes, the highest σ was observed for the blend with [TMC]:K = 16:1 (2.9×10^{-8} S cm^{-1}, 3.2×10^{-6} S cm^{-1} at 25 and 55 °C, respectively).

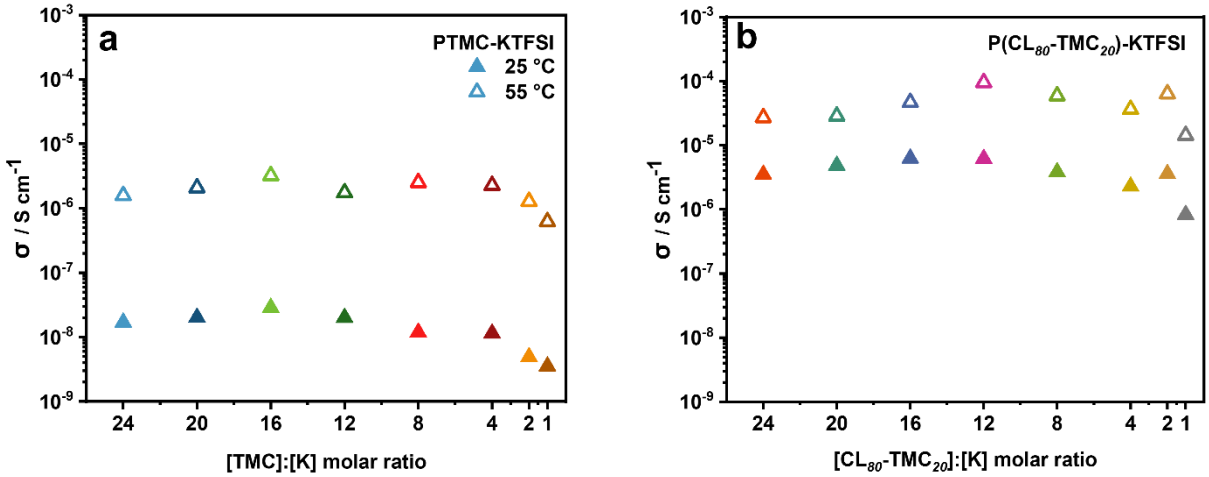

Figure 32. The dependence of ionic conductivity (derived from EIS measurements conducted in the frequency range from 10 MHz to 1 Hz) of **(a)** PTMC-KTFSI and **(b)** P(CL$_{80}$-TMC$_{20}$)-KTFSI SPEs on [TMC]/[CL$_{80}$-TMC$_{20}$]:K molar ratios at 25 and 55 °C.

In both systems, at first ionic conductivity enhanced with increasing KTFSI fraction (from 24:1 to 16/12:1 [TMC]/[CL$_{80}$-TMC$_{20}$]:K molar ratios) due to increase of the number of charge carriers, K^+. When further increasing concentration of KTFSI, higher degree of occupied coordination sites unfavourably effected the ionic conductivity (i.e. lowered free volume of the polymers). Following the results of DSC, the samples with the highest KTFSI content (2:1, 1:1 [TMC]/[CL$_{80}$-TMC$_{20}$]:K molar ratio) contained crystalline intermediate compounds that showed endothermic effects at high temperatures (**Figure A8**), and therefore exhibited relatively low σ values at examined temperatures. Noteworthy, this is inconsistent with the data reported for PTMC-NaTFSI and -NaFSI electrolytes[185,277] that exhibited high ionic conductivities at extreme salt concentrations due to *percolation* ion transport mechanism. Instead, the pattern of σ dependency on [polymer unit]:K molar ratio appeared to be consistent with the previously observed results for the investigated PEO-based SPEs.

When comparing to polyether-based SPEs (specifically semi-crystalline PEO$_{20}$-KTFSI$_1$ and amorphous BPE$_{15}$-KTFSI$_1$ previously discussed), P(CL$_{80}$-TMC$_{20}$)-KTFSI with 12:1 [CL$_{80}$-TMC$_{20}$]:K molar ratio presented higher ionic conductivities at low temperature region (**Table A4** and **Figure 33**). Moreover, following literature data,[192,186] P(CL$_{80}$-TMC$_{20}$)-based SPEs with electrolyte salts possess higher transference number as compared to electrolytes based on PEO,

and presumably might benefit a K-cell in terms of lower cell polarization. Another advantage of polycarbonate-based SPEs might be better compatibility with the components of K-ion cell. These points should be of a great focus of further K-research.

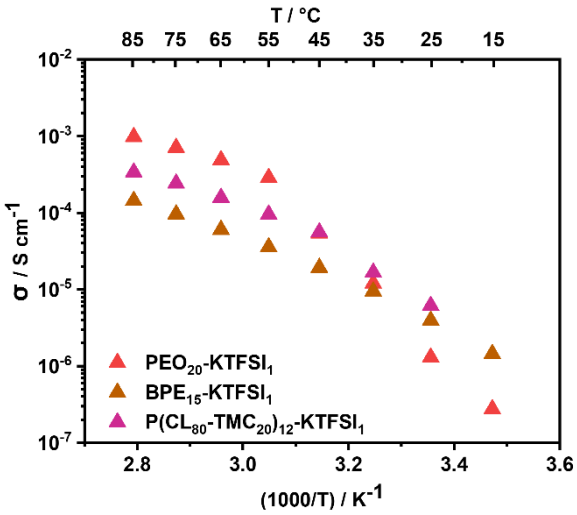

Figure 33. Comparison of temperature-dependent ionic conductivity of PEO-based (PEO_{20}-$KTFSI_1$, BPE_{15}-$KTFSI_1$) and polycarbonate-based ($P(CL_{80}$-$TMC_{20})_{12}$-$KTFSI_1$) SPEs.

8. Conclusion and Outlook

The pursuit of high-energy battery technologies to complement lithium-ion batteries has driven increasing research into post-Li systems, particularly potassium-ion batteries, KIBs. To achieve volumetric and gravimetric capacities comparable to that of LIBs, the integration of high-voltage cathode materials is essential. When combined with a metallic anode, this strategy enables the maximization of cell voltage. However, the progression of KIB technology remains hindered by several critical challenges, mostly associated with the high reactivity of potassium, leading to low CE and rapid cell failure due to dendrite growth, which compromises electrolyte stability. Given these limitations, the development of more stable electrolytes is crucial, making the solid polymer electrolyte, SPE, approach particularly relevant for potassium metal batteries. Despite a few recent studies,[18,146] research on SPEs for all-solid potassium batteries remains limited.

Therefore, the goal of this thesis was to identify K^+-SPEs that possess sufficient ion transport in combination with mechanical strength and electrochemical stability, while demonstrating their feasibility in potassium metal batteries. To do so, the following approaches were employed: analysis of SPEs physical properties to evaluate polymer chain dynamics and mechanical stability (DSC, SAOS), examination of ion transport (EIS), a complex of electrochemical analyses to study the electrode processes. Three key objectives were the focus of this thesis. The primary objective was to investigate how different material approaches – namely (1) homopolymer, (2) composite, (3) block copolymer with the example of PEO as the state-of-the-art host material – affect the key physical properties and ion transport of SPEs. Secondly, to explore the solid-state diffusion kinetics of K^+ within the alternative polymer hosts, such as polycarbonates and polyesters. The third objective was to demonstrate the feasibility of selected materials as SPEs in potassium metal battery prototypes.

As the material selection began with the most commonly used polymer host, PEO, a comprehensive investigation was conducted on a series of PEO_x-$KTFSI_y$ electrolytes across a broad range of salt concentration ($4 < x:y < 20$). The results revealed the critical role of K^+-salts in shaping the physical properties of PEO-based electrolytes. Since bulk anions acted as plasticizers, the addition of KTFSI reduced the crystallinity of PEO, mitigating the restricted ion mobility at near-ambient temperatures. However, cations demonstrated a dual effect: increasing K^+-species provided a higher number of charge carriers but also resulted in strong Lewis acid-base interactions with EO units, leading to ionic cross-linking and reduced chain mobility, as evidenced by a 13 °C T_g increase along with rising KTFSI content. The mechanical integrity of PEO_x-$KTFSI_y$ was governed by crystalline domains and/or ionic cross-links, both

restricting ion transport *coupled* to segmental motion. The highest conductivities at 25 °C were observed in predominantly amorphous samples, but their liquid-like rheological behaviour rendered them unsuitable as SPEs. In contrast, blends with higher salt content exhibited solid-like properties, but suffered a three order of magnitude drop in conductivity at 25 °C. These findings underscored the necessity of optimizing material design to achieve a balance between ionic conductivity and mechanical integrity, motivating further exploration of composite strategy and alternative polymer architectures.

The composite approach involved the incorporation of Al_2O_3 and SiO_2 nanoparticles (at mass fractions of 2-15 wt.%), which transformed the liquid-like state PEO-KTFSI into a solid-like state electrolyte, fulfilling a critical SPE requirement for suppressing dendrite growth in potassium batteries. This transition was driven by specific Lewis acid-base interactions between the nanofillers, KTFSI, and PEO. While ceramic fillers effectively modified the rheological properties, they did not improve the ionic conductivities at near-ambient temperatures. However, above the melting point at ~45 °C, the difference in conductivity between the samples with and without ceramics disappeared.

The block copolymer strategy utilizing PVBmPEO-*b*-PS (denoted as BP) successfully suppressed the intrinsic crystallinity of PEO, yielding fully amorphous electrolytes. Unlike the electrolytes based on solely PEO, BPE-KTFSI exhibited solid-like properties due to the formation of a microphase-separated structure that enabled efficient ion transport through the PEO phase while maintaining mechanical strength through the PS domains. This resulted in improved ionic conductivity at low temperatures, with values approximately half an order of magnitude higher than those of the PEO-KTFSI electrolytes. These findings highlight block copolymerization as a promising approach to balancing ion transport and mechanical integrity in potassium-ion SPEs.

Another class of polymer materials – polycarbonate-based PTMC and P(CL_{80}-TMC_{20}) – was introduced for the first time as host materials for K^+. Owing to high molecular weight of the polymer materials, the investigated SPEs demonstrated sufficient mechanical strength in the whole range of KTFSI concentration. Notably, the observed trend of dependency of T_g and total ionic conductivity on the [polymer unit]:K molar ratio appeared to be consistent with the previously discussed results for the PEO-based SPEs. The P(CL_{80}-TMC_{20})-KTFSI electrolytes showed temperature-dependent ionic conductivities comparable to those of the reference PEO-based SPEs. Moreover, higher cationic conductivity can be expected for this class of polymer host materials,[65] however, evaluating T_{K^+} appeared to be a challenging task in this thesis. Analysis of the processes at the electrode-electrolyte interfaces revealed large impedances and

overpotentials, presumably due to the large interfacial resistances in the symmetrical K-metal cells, for all examined PEO-based SPEs. This contributed unreliability into the plating and stripping experiments as well as the determination of the transference number and emphasized the need to develop novel techniques and methods for the characterization of transport parameters in K^+-containing SPEs.

Within this thesis, the feasibility of the SPE applications in potassium metal batteries was demonstrated. Thus, selected PEO-based SPEs were integrated into solid-state potassium batteries with a Prussian blue analogue $K_{2-x}Fe[Fe(CN)_6]$ positive electrode and a K-metal negative electrode with an average cell voltage of 3.6 V. In particular, this thesis revealed how the architecture of the polymer host materials influences the electrochemical characteristics of the corresponding SPE-based K-cells. Both the filler-containing and BPE-based SPEs exhibited higher capacity retention over the same cycles number with respect to the unmodified PEO-KTFSI. This was attributed to the significant improvement in mechanical stability of the SPEs architectures. The Coulombic efficiencies in the tested cells were about 98-99 % at the 100th cycle, which clearly shows that at elevated temperatures and in contact with reactive alkali metals as negative electrode, side reactions occur to a considerable extent.

This work highlights key strategies for advancing SPE architectures for long-term cycling KIBs and provides valuable insights into overcoming key challenges such as large crystallization degree and the trade-off between mechanical stability and ionic conductivity. The results contribute to the development of more robust K^+-SPEs, paving the way for improved performance in potassium metal batteries. Interfacial stability remains a major challenge, with large resistances and overpotentials, underlying the need for advanced characterization methods to better understand cation transport in post-Li systems. This thesis offers the foundation for further research towards the high-performance, sustainable solid-state potassium batteries.

References

(1) Khudyshkina, A. D.; Morozova, P. A.; Butzelaar, A. J.; Hoffmann, M.; Wilhelm, M.; Theato, P.; Fedotov, S. S.; Jeschull, F. Poly(Ethylene Oxide)-Based Electrolytes for Solid-State Potassium Metal Batteries with a Prussian Blue Positive Electrode. *ACS Appl. Polym. Mater.* **2022**, *4* (4), 2734–2746. https://doi.org/https://doi.org/10.1021/acsapm.2c00014.

(2) Khudyshkina, A. D.; Butzelaar, A. J.; Guo, Y.; Hoffmann, M.; Bergfeldt, T.; Schaller, M.; Indris, S.; Wilhelm, M.; Théato, P.; Jeschull, F. From Lithium to Potassium: Comparison of Cations in Poly(Ethylene Oxide)-Based Block Copolymer Electrolytes for Solid-State Alkali Metal Batteries. *Electrochim. Acta* **2023**, *454*, 142421. https://doi.org/10.1016/J.ELECTACTA.2023.142421.

(3) Khudyshkina, A. D.; Rauska, U.-C.; Butzelaar, A. J.; Hoffmann, M.; Wilhelm, M.; Theato, P.; Jeschull, F. Impact of Nano-Sized Inorganic Fillers on PEO-Based Electrolytes for Potassium Batteries. *Batter. Supercaps* **2023**, *7* (1), e202300404. https://doi.org/10.1002/batt.202300404.

(4) Nitta, N.; Wu, F.; Lee, J. T.; Yushin, G. Li-Ion Battery Materials: Present and Future. *Mater. Today* **2015**, *18* (5), 252–264. https://doi.org/10.1016/J.MATTOD.2014.10.040.

(5) Zubi, G.; Dufo-López, R.; Carvalho, M.; Pasaoglu, G. The Lithium-Ion Battery: State of the Art and Future Perspectives. *Renew. Sustain. Energy Rev.* **2018**, *89*, 292–308. https://doi.org/10.1016/J.RSER.2018.03.002.

(6) Li, Y.; Zhao, P. C.; Shen, B. A Review of New Technologies for Lithium-Ion Battery Treatment. *Sci. Total Environ.* **2024**, *951*, 175459. https://doi.org/10.1016/J.SCITOTENV.2024.175459.

(7) Nayak, P. K.; Yang, L.; Brehm, W.; Adelhelm, P. From Lithium-Ion to Sodium-Ion Batteries: Advantages, Challenges, and Surprises. *Angew. Chemie - Int. Ed.* **2018**, *57* (1), 102–120. https://doi.org/10.1002/ANIE.201703772.

(8) Grey, C. P.; Hall, D. S. Prospects for Lithium-Ion Batteries and beyond-a 2030 Vision. *Nat. Commun.* **2020**, *11* (6279). https://doi.org/10.1038/S41467-020-19991-4.

(9) Elbinger, L.; Enke, M.; Ziegenbalg, N.; Brendel, J. C.; Schubert, U. S. Beyond Lithium-Ion Batteries: Recent Developments in Polymer-Based Electrolytes for Alternative Metal-Ion-Batteries. *Energy Storage Mater.* **2024**, *65*, 103063. https://doi.org/10.1016/J.ENSM.2023.103063.

(10) Kubota, K.; Dahbi, M.; Hosaka, T.; Kumakura, S.; Komaba, S. Towards K-Ion and Na-Ion Batteries as “Beyond Li-Ion.” *Chem. Rec.* **2018**, *18* (4), 459–479.

https://doi.org/10.1002/TCR.201700057.

(11) Bie, X.; Kubota, K.; Hosaka, T.; Chihara, K.; Komaba, S. A Novel K-Ion Battery: Hexacyanoferrate(Ii)/Graphite Cell. *J. Mater. Chem. A* **2017**, *5* (9), 4325–4330. https://doi.org/10.1039/c7ta00220c.

(12) Yang, Z.; Zhang, J.; Kintner-Meyer, M. C. W.; Lu, X.; Choi, D.; Lemmon, J. P.; Liu, J. Electrochemical Energy Storage for Green Grid. *Chem. Rev.* **2011**, *111* (5), 3577–3613. https://doi.org/10.1021/cr100290v.

(13) Fedotov, S. S.; Khasanova, N. R.; Samarin, A. S.; Drozhzhin, O. A.; Batuk, D.; Karakulina, O. M.; Hadermann, J.; Abakumov, A. M.; Antipov, E. V. AVPO4F (A = Li, K): A 4 V Cathode Material for High-Power Rechargeable Batteries. *Chem. Mater.* **2016**, *28* (2), 411–415. https://doi.org/10.1021/acs.chemmater.5b04065.

(14) Xu, Y. S.; Duan, S. Y.; Sun, Y. G.; Bin, D. S.; Tao, X. Sen; Zhang, D.; Liu, Y.; Cao, A. M.; Wan, L. J. Recent Developments in Electrode Materials for Potassium-Ion Batteries. *J. Mater. Chem. A* **2019**, *7* (9), 4334–4352. https://doi.org/10.1039/c8ta10953b.

(15) Ahmed, S. M.; Suo, G.; Wang, W. A.; Xi, K.; Iqbal, S. Bin. Improvement in Potassium Ion Batteries Electrodes: Recent Developments and Efficient Approaches. *J. Energy Chem.* **2021**, *62*, 307–337. https://doi.org/10.1016/j.jechem.2021.03.032.

(16) Morozova, P. A.; Trussov, I. A.; Rupasov, D. P.; Nikitina, V. A.; Abakumov, A. M.; Fedotov, S. S. Exploring the Role of Crystal Water in Potassium Manganese Hexacyanoferrate as a Cathode Material for Potassium-Ion Batteries. *Crystals* **2021**, *11* (8), 895. https://doi.org/10.3390/cryst11080895.

(17) Zhu, Y. H.; Yin, Y. Bin; Yang, X.; Sun, T.; Wang, S.; Jiang, Y. S.; Yan, J. M.; Zhang, X. B. Transformation of Rusty Stainless-Steel Meshes into Stable, Low-Cost, and Binder-Free Cathodes for High-Performance Potassium-Ion Batteries. *Angew. Chemie - Int. Ed.* **2017**, *56* (27), 7881–7885. https://doi.org/10.1002/anie.201702711.

(18) Fei, H.; Liu, Y.; An, Y.; Xu, X.; Zeng, G.; Tian, Y.; Ci, L.; Xi, B.; Xiong, S.; Feng, J. Stable All-Solid-State Potassium Battery Operating at Room Temperature with a Composite Polymer Electrolyte and a Sustainable Organic Cathode. *J. Power Sources* **2018**, *399*, 294–298. https://doi.org/10.1016/j.jpowsour.2018.07.124.

(19) Hofmann, A.; Müller, F.; Schöner, S.; Jeschull, F. Revealing the Formation of Dialkyl Dioxahexane Dioate Products from Ethylene Carbonate Based Electrolytes on Lithium and Potassium Surfaces. *Batter. Supercaps* **2023**, *6* (12), e202300325. https://doi.org/10.1002/BATT.202300325.

(20) Panasenko, I.; Wildersinn, L.; Jeschull, F. How Relevant Are SEI Studies from Half Cell Samples to Understand Aging Mechanisms in Potassium Batteries? An in-Depth Photoelectron Spectroscopy Study. *ECS Meet. Abstr.* **2023**, *MA2023-02* (A05), 884. https://doi.org/10.1149/MA2023-025884MTGABS.

(21) Wildersinn, L.; Stottmeister, D.; Jeschull, F.; Groß, A.; Hofmann, A. Decomposition of Binary Mixtures of DMC/EC, EMC/EC, and DEC/EC on Potassium Surfaces; GC, XPS, and Calculation. *ACS Appl. Mater. Interfaces* **2025**, *17* (6), 10055–10072. https://doi.org/10.1021/ACSAMI.4C17461.

(22) Boaretto, N.; Meabe, L.; Martinez-Ibañez, M.; Armand, M.; Zhang, H. Review—Polymer Electrolytes for Rechargeable Batteries: From Nanocomposite to Nanohybrid. *J. Electrochem. Soc.* **2020**, *167* (7), 070524. https://doi.org/10.1149/1945-7111/ab7221.

(23) Yue, L.; Ma, J.; Zhang, J.; Zhao, J.; Dong, S.; Liu, Z.; Cui, G.; Chen, L. All Solid-State Polymer Electrolytes for High-Performance Lithium Ion Batteries. *Energy Storage Mater.* **2016**, *5*, 139–164. https://doi.org/10.1016/j.ensm.2016.07.003.

(24) Yao, P.; Yu, H.; Ding, Z.; Liu, Y.; Lu, J.; Lavorgna, M.; Wu, J.; Liu, X. Review on Polymer-Based Composite Electrolytes for Lithium Batteries. *Front. Chem.* **2019**, *7*, 522. https://doi.org/10.3389/fchem.2019.00522.

(25) Mindemark, J.; Lacey, M. J.; Bowden, T.; Brandell, D. Beyond PEO—Alternative Host Materials for Li+-Conducting Solid Polymer Electrolytes. *Prog. Polym. Sci.* **2018**, *81*, 114–143. https://doi.org/10.1016/j.progpolymsci.2017.12.004.

(26) Wright, P. V. Electrical Conductivity in Ionic Complexes of Poly(Ethylene Oxide). *Br. Polym. J.* **1975**, *7* (5), 319–327. https://doi.org/10.1002/pi.4980070505.

(27) Nair, J. R.; Imholt, L.; Brunklaus, G.; Winter, M. Lithium Metal Polymer Electrolyte Batteries: Opportunities and Challenges. *Electrochem. Soc. Interface* **2019**, *28* (2), 55–61. https://doi.org/10.1149/2.F05192if.

(28) Homann, G.; Stolz, L.; Winter, M.; Kasnatscheew, J. Elimination of "Voltage Noise" of Poly (Ethylene Oxide)-Based Solid Electrolytes in High-Voltage Lithium Batteries: Linear versus Network Polymers. *iScience* **2020**, *23* (6), 101225. https://doi.org/10.1016/J.ISCI.2020.101225.

(29) Seidl, L.; Grissa, R.; Zhang, L.; Trabesinger, S.; Battaglia, C. Unraveling the Voltage-Dependent Oxidation Mechanisms of Poly(Ethylene Oxide)-Based Solid Electrolytes for Solid-State Batteries. *Adv. Mater. Interfaces* **2021**, *9* (8), 2100704. https://doi.org/10.1002/ADMI.202100704.

(30) White, R. P.; Lipson, J. E. G. Polymer Free Volume and Its Connection to the Glass

Transition. *Macromolecules* **2016**, *49* (11), 3987–4007. https://doi.org/10.1021/acs.macromol.6b00215.

(31) Das, S.; Ghosh, A. Ionic Conductivity and Dielectric Permittivity of PEO-LiClO4 Solid Polymer Electrolyte Plasticized with Propylene Carbonate. *AIP Adv.* **2015**, *5* (2), 27125. https://doi.org/10.1063/1.4913320/21103.

(32) He, R.; Kyu, T. Effect of Plasticization on Ionic Conductivity Enhancement in Relation to Glass Transition Temperature of Crosslinked Polymer Electrolyte Membranes. *Macromolecules* **2016**, *49* (15), 5637–5648. https://doi.org/10.1021/ACS.MACROMOL.6B00918.

(33) Banitaba, S. N.; Semnani, D.; Heydari-Soureshjani, E.; Rezaei, B.; Ensafi, A. A. The Effect of Concentration and Ratio of Ethylene Carbonate and Propylene Carbonate Plasticizers on Characteristics of the Electrospun PEO-Based Electrolytes Applicable in Lithium-Ion Batteries. *Solid State Ionics* **2020**, *347*, 115252. https://doi.org/10.1016/J.SSI.2020.115252.

(34) Dreezen, G.; Koch, M. H. J.; Reynaers, H.; Groeninckx, G. Miscible Binary Blends of Poly(Ethylene Oxide) and an Amorphous Aromatic Polyamide (Aramide 34I): Crystallization, Melting Behavior and Semi-Crystalline Morphology. *Polymer (Guildf).* **1999**, *40* (23), 6451–6463. https://doi.org/10.1016/S0032-3861(98)00849-0.

(35) Lisowski, M. S.; Liu, Q.; Cho, J.; Runt, J.; Yeh, F.; Hsiao, B. S. Crystallization Behavior of Poly(Ethylene Oxide) and Its Blends Using Time-Resolved Wide-and Small-Angle X-Ray Scattering. *Macromolecules* **2000**, *33* (13), 4842–4849. https://doi.org/10.1021/ma000207c.

(36) Higa, M.; Yaguchi, K.; Kitani, R. All Solid-State Polymer Electrolytes Prepared from a Graft Copolymer Consisting of a Polyimide Main Chain and Poly(Ethylene Oxide) Based Side Chains. *Electrochim. Acta* **2010**, *55* (4), 1380–1384. https://doi.org/10.1016/J.ELECTACTA.2009.07.046.

(37) Shim, J.; Kim, D. G.; Lee, J. H.; Baik, J. H.; Lee, J. C. Synthesis and Properties of Organic/Inorganic Hybrid Branched-Graft Copolymers and Their Application to Solid-State Electrolytes for High-Temperature Lithium-Ion Batteries. *Polym. Chem.* **2014**, *5* (10), 3432–3442. https://doi.org/10.1039/c4py00123k.

(38) Rosenbach, D.; Mödl, N.; Hahn, M.; Petry, J.; Danzer, M. A.; Thelakkat, M. Synthesis and Comparative Studies of Solvent-Free Brush Polymer Electrolytes for Lithium Batteries. *ACS Appl. Energy Mater.* **2019**, *2* (5), 3373–3388. https://doi.org/10.1021/acsaem.9b00211.

(39) Xue, Z.; He, D.; Xie, X. Poly(Ethylene Oxide)-Based Electrolytes for Lithium-Ion Batteries. *J. Mater. Chem. A* **2015**, *3* (38), 19218–19253. https://doi.org/10.1039/C5TA03471J.

(40) Arya, A.; Sharma, A. L. Polymer Electrolytes for Lithium Ion Batteries: A Critical Study. *Ionics (Kiel).* **2017**, *23* (3), 497–540. https://doi.org/10.1007/s11581-016-1908-6.

(41) Wu, M.; Li, M.; Jin, Y.; Chang, X.; Zhao, X.; Gu, Z.; Liu, G.; Yao, X. In Situ Formed LiF-Li3N Interface Layer Enables Ultra-Stable Sulfide Electrolyte-Based All-Solid-State Lithium Batteries. *J. Energy Chem.* **2023**, *79*, 272–278. https://doi.org/10.1016/j.jechem.2023.01.007.

(42) Kim, M. S.; Zhang, Z.; Wang, J.; Oyakhire, S. T.; Kim, S. C.; Yu, Z.; Chen, Y.; Boyle, D. T.; Ye, Y.; Huang, Z.; Zhang, W.; Xu, R.; Sayavong, P.; Bent, S. F.; Qin, J.; Bao, Z.; Cui, Y. Revealing the Multifunctions of Li3N in the Suspension Electrolyte for Lithium Metal Batteries. *ACS Nano* **2023**, *17* (3), 3168–3180. https://doi.org/10.1021/acsnano.2c12470.

(43) Kalyana Sundaram, N. T.; Subramania, A. Nano-Size LiAlO2 Ceramic Filler Incorporated Porous PVDF-Co-HFP Electrolyte for Lithium-Ion Battery Applications. *Electrochim. Acta* **2007**, *52* (15), 4987–4993. https://doi.org/10.1016/j.electacta.2007.01.066.

(44) Chauhan, A. K.; Mishra, K.; Kumar, D.; Singh, A. Enhancing Sodium Ion Transport in a PEO-Based Solid Polymer Electrolyte System with NaAlO2 Active Fillers. *J. Electron. Mater.* **2021**, *50* (9), 5122–5133. https://doi.org/10.1007/s11664-021-09051-y.

(45) Kim, K. W.; Kim, H. W.; Kim, Y.; Kim, J. K. Composite Gel Polymer Electrolyte with Ceramic Particles for LiNi1/3Mn1/3Co1/3O2-Li4Ti5O12 Lithium Ion Batteries. *Electrochim. Acta* **2017**, *236*, 394–398. https://doi.org/10.1016/j.electacta.2017.03.176.

(46) Park, C. H.; Kim, D. W.; Prakash, J.; Sun, Y. K. Electrochemical Stability and Conductivity Enhancement of Composite Polymer Electrolytes. *Solid State Ionics* **2003**, *159* (1–2), 111–119. https://doi.org/10.1016/S0167-2738(03)00025-0.

(47) Sun, P.; Liao, Y.; Luo, X.; Li, Z.; Chen, T.; Xing, L.; Li, W. The Improved Effect of Co-Doping with Nano-SiO2 and Nano-Al2O3 on the Performance of Poly(Methyl Methacrylate-Acrylonitrile-Ethyl Acrylate) Based Gel Polymer Electrolyte for Lithium Ion Batteries. *RSC Adv.* **2015**, *5* (79), 64368–64377. https://doi.org/10.1039/C5RA10409B.

(48) Liang, B.; Tang, S.; Jiang, Q.; Chen, C.; Chen, X.; Li, S.; Yan, X. Preparation and Characterization of PEO-PMMA Polymer Composite Electrolytes Doped with Nano-Al2O3. *Electrochim. Acta* **2015**, *169*, 334–341. https://doi.org/10.1016/j.electacta.2015.04.039.

(49) Das, S.; Ghosh, A. Ion Conduction and Relaxation in PEO-LiTFSI-Al2O3 Polymer Nanocomposite Electrolytes. *J. Appl. Phys.* **2015**, *117* (17), 174103. https://doi.org/10.1063/1.4919721.

(50) Moreno, J. S.; Armand, M.; Berman, M. B.; Greenbaum, S. G.; Scrosati, B.; Panero, S. Composite PEOn:NaTFSI Polymer Electrolyte: Preparation, Thermal and Electrochemical Characterization. *J. Power Sources* **2014**, *248*, 695–702. https://doi.org/10.1016/J.JPOWSOUR.2013.09.137.

(51) Feng, J.; Wang, L.; Chen, Y.; Wang, P.; Zhang, H.; He, X. PEO Based Polymer-Ceramic Hybrid Solid Electrolytes: A Review. *Nano Converg.* **2021**, *8* (2), 1–12. https://doi.org/10.1186/S40580-020-00252-5.

(52) Croce, F.; Persi, L. L.; Scrosati, B.; Serraino-Fiory, F.; Plichta, E.; Hendrickson, M. A. Role of the Ceramic Fillers in Enhancing the Transport Properties of Composite Polymer Electrolytes. *Electrochim. Acta* **2001**, *46* (16), 2457–2461. https://doi.org/10.1016/S0013-4686(01)00458-3.

(53) Croce, F.; Appetecchi, G. B.; Persi, L.; Scrosati, B.; Croce, F.; Appetecchi, G. B.; Persi, L.; Scrosati, B. Nanocomposite Polymer Electrolytes for Lithium Batteries. *Nature* **1998**, *394* (6692), 456–458. https://doi.org/10.1038/28818.

(54) Tambelli, C. C.; Bloise, A. C.; Rosário, A. V.; Pereira, E. C.; Magon, C. J.; Donoso, J. P. Characterisation of PEO-Al2O3 Composite Polymer Electrolytes. *Electrochim. Acta* **2002**, *47* (11), 1677–1682. https://doi.org/10.1016/S0013-4686(01)00900-8.

(55) Keddie, J. L.; Jones, R. A. L.; Cory, R. A. Interface and Surface Effects on the Glass-Transition Temperature in Thin Polymer Films. *Faraday Discuss.* **1994**, *98*, 219–230. https://doi.org/10.1039/FD9949800219.

(56) Rittigstein, P.; Priestley, R. D.; Broadbelt, L. J.; Torkelson, J. M. Model Polymer Nanocomposites Provide an Understanding of Confinement Effects in Real Nanocomposites. *Nat. Mater.* **2007**, *6* (4), 278–282. https://doi.org/10.1038/nmat1870.

(57) Choi, B. K.; Shin, K. H. Effects of SiC Fillers on the Electrical and Mechanical Properties of (PEO)16LiClO4 Electrolytes. *Solid State Ionics* **1996**, *86–88* (PART 1), 303–306. https://doi.org/10.1016/0167-2738(96)00134-8.

(58) Butzelaar, A. J.; Röring, P.; Mach, T. P.; Hoffmann, M.; Jeschull, F.; Wilhelm, M.;

Winter, M.; Brunklaus, G.; Théato, P. Styrene-Based Poly(Ethylene Oxide) Side-Chain Block Copolymers as Solid Polymer Electrolytes for High-Voltage Lithium-Metal Batteries. *ACS Appl. Mater. Interfaces* **2021**, *13* (33), 39257–39270. https://doi.org/10.1021/ACSAMI.1C08841.

(59) Cao, X. H.; Li, J. H.; Yang, M. J.; Yang, J. L.; Wang, R. Y.; Zhang, X. H.; Xu, J. T. Simultaneous Improvement of Ionic Conductivity and Mechanical Strength in Block Copolymer Electrolytes with Double Conductive Nanophases. *Macromol. Rapid Commun.* **2020**, *41* (7), 1900622. https://doi.org/10.1002/marc.201900622.

(60) Huang, J.; Wang, R. Y.; Tong, Z. Z.; Xu, J. T.; Fan, Z. Q. Influence of Ionic Species on the Microphase Separation Behavior of PCL-b-PEO/Salt Hybrids. *Macromolecules* **2014**, *47* (23), 8359–8367. https://doi.org/10.1021/ma502057q.

(61) Cao, X. H.; Yang, J. L.; Wang, R. Y.; Zhang, X. H.; Xu, J. T. Microphase Separation of Poly(Propylene Monothiocarbonate)-b-Poly(Ethylene Oxide) Block Copolymers Induced by Differential Interactions with Salt. *Polymer (Guildf).* **2019**, *180*, 121745. https://doi.org/10.1016/J.POLYMER.2019.121745.

(62) Sun, B.; Mindemark, J.; Morozov, E. V.; Costa, L. T.; Bergman, M.; Johansson, P.; Fang, Y.; Furó, I.; Brandell, D. Ion Transport in Polycarbonate Based Solid Polymer Electrolytes: Experimental and Computational Investigations. *Phys. Chem. Chem. Phys.* **2016**, *18* (14), 9504–9513. https://doi.org/10.1039/C6CP00757K.

(63) Eriksson, T.; Mace, A.; Mindemark, J.; Brandell, D. The Role of Coordination Strength in Solid Polymer Electrolytes: Compositional Dependence of Transference Numbers in the Poly(ϵ-Caprolactone)-Poly(Trimethylene Carbonate) System. *Phys. Chem. Chem. Phys.* **2021**, *23* (45), 25550–25557. https://doi.org/10.1039/d1cp03929f.

(64) Andersson, R.; Hernández, G.; Mindemark, J. Quantifying the Ion Coordination Strength in Polymer Electrolytes. *Phys. Chem. Chem. Phys.* **2022**, *24* (26), 16343–16352. https://doi.org/10.1039/d2cp01904c.

(65) Andersson, R.; Mönich, C.; Hernández, G.; Schönhoff, M.; Mindemark, J. Transference Numbers and Ion Coordination Strength for Mg2+, Na+, and K+ in Solid Polymer Electrolytes. *J. Phys. Chem. C* **2024**, *128* (39), 16393–16399. https://doi.org/10.1021/acs.jpcc.4c04632.

(66) Lotfabad, E. M.; Ding, J.; Cui, K.; Kohandehghan, A.; Kalisvaart, W. P.; Hazelton, M.; Mitlin, D. High-Density Sodium and Lithium Ion Battery Anodes from Banana Peels. *ACS Nano* **2014**, *8* (7), 7115–7129. https://doi.org/10.1021/nn502045y.

(67) Komaba, S.; Hasegawa, T.; Dahbi, M.; Kubota, K. Potassium Intercalation into

Graphite to Realize High-Voltage/High-Power Potassium-Ion Batteries and Potassium-Ion Capacitors. *Electrochem. commun.* **2015**, *60*, 172–175. https://doi.org/10.1016/J.ELECOM.2015.09.002.

(68) Hosaka, T.; Kubota, K.; Hameed, A. S.; Komaba, S. Research Development on K-Ion Batteries. *Chem. Rev.* **2020**, *120* (14), 6358–6466. https://doi.org/10.1021/acs.chemrev.9b00463.

(69) Moshkovich, M.; Gofer, Y.; Aurbach, D. Investigation of the Electrochemical Windows of Aprotic Alkali Metal (Li, Na, K) Salt Solutions. *J. Electrochem. Soc.* **2001**, *148* (4), E155. https://doi.org/10.1149/1.1357316.

(70) Wu, X.; Leonard, D. P.; Ji, X. Emerging Non-Aqueous Potassium-Ion Batteries: Challenges and Opportunities. *Chem. Mater.* **2017**, *29* (12), 5031–5042. https://doi.org/10.1021/acs.chemmater.7b01764.

(71) Li, W.; Yao, H.; Yan, K.; Zheng, G.; Liang, Z.; Chiang, Y. M.; Cui, Y. The Synergetic Effect of Lithium Polysulfide and Lithium Nitrate to Prevent Lithium Dendrite Growth. *Nat. Commun.* **2015**, *6* (1), 1–8. https://doi.org/10.1038/ncomms8436.

(72) Xie, J.; Lu, Y. C. A Retrospective on Lithium-Ion Batteries. *Nat. Commun.* **2020**, *11* (1), 1–4. https://doi.org/10.1038/s41467-020-16259-9.

(73) Xu, Z.; Song, K.; Chang, X.; Li, L.; Zhang, W.; Xue, Y.; Zhang, J.; Lin, D.; Liu, Z.; Wang, Q.; Yu, Y.; Yang, C.; Zheyuan Liu, C. Layered Oxide Cathodes: A Comprehensive Review of Characteristics, Research, and Development in Lithium and Sodium Ion Batteries. *Carbon Neutralization* **2024**, *3* (5), 832–856. https://doi.org/10.1002/CNL2.162.

(74) Yang, Q.; Wang, P. F.; Guo, J. Z.; Chen, Z. M.; Pang, W. L.; Huang, K. C.; Guo, Y. G.; Wu, X. L.; Zhang, J. P. Advanced P2-Na2/3Ni1/3Mn7/12Fe1/12O2 Cathode Material with Suppressed P2-O2 Phase Transition toward High-Performance Sodium-Ion Battery. *ACS Appl. Mater. Interfaces* **2018**, *10* (40), 34272–34282. https://doi.org/10.1021/acsami.8b12204.

(75) Meng, X.; Wang, J.; Li, L. Layered-Oxide Cathode Materials for Fast-Charging Lithium-Ion Batteries: A Review. *Molecules* **2023**, *28* (10), 4007. https://doi.org/10.3390/MOLECULES28104007.

(76) Zhang, X.; Wei, Z.; Ngoc Dinh, K.; Chen, N.; Chen, G.; Du, F.; Yan, Q.; Zhang, X.; Wei, Z.; Chen, N.; Chen, G.; Du, F.; Dinh, K. N.; Yan, Q. Layered Oxide Cathode for Potassium-Ion Battery: Recent Progress and Prospective. *Small* **2020**, *16* (38), 2002700. https://doi.org/10.1002/SMLL.202002700.

(77) Pramudita, J. C.; Sehrawat, D.; Goonetilleke, D.; Sharma, N.; Pramudita, J. C.; Sehrawat, D.; Goonetilleke, D.; Sharma, N. An Initial Review of the Status of Electrode Materials for Potassium-Ion Batteries. *Adv. Energy Mater.* **2017**, *7* (24), 1602911. https://doi.org/10.1002/AENM.201602911.

(78) Toriyama, M. Y.; Kaufman, J. L.; Van Der Ven, A. Potassium Ordering and Structural Phase Stability in Layered KxCoO2. *ACS Appl. Energy Mater.* **2019**, *2* (4), 2629–2636. https://doi.org/10.1021/acsaem.8b02238.

(79) Kim, H.; Ji, H.; Wang, J.; Ceder, G. Next-Generation Cathode Materials for Non-Aqueous Potassium-Ion Batteries. *Trends Chem.* **2019**, *1* (7), 682–692. https://doi.org/10.1016/j.trechm.2019.04.007.

(80) Hironaka, Y.; Kubota, K.; Komaba, S. P2- and P3-KxCoO2 as an Electrochemical Potassium Intercalation Host. *Chem. Commun.* **2017**, *53* (26), 3693–3696. https://doi.org/10.1039/C7CC00806F.

(81) Wang, X.; Xu, X.; Niu, C.; Meng, J.; Huang, M.; Liu, X.; Liu, Z.; Mai, L. Earth Abundant Fe/Mn-Based Layered Oxide Interconnected Nanowires for Advanced K-Ion Full Batteries. *Nano Lett.* **2017**, *17* (1), 544–550. https://doi.org/10.1021/acs.nanolett.6b04611.

(82) Zhang, X.; Yang, Y.; Qu, X.; Wei, Z.; Sun, G.; Zheng, K.; Yu, H.; Du, F. Layered P2-Type K0.44Ni0.22Mn0.78O2 as a High-Performance Cathode for Potassium-Ion Batteries. *Adv. Funct. Mater.* **2019**, *29* (49), 1905679. https://doi.org/10.1002/ADFM.201905679.

(83) Vaalma, C.; Buchholz, D.; Passerini, S. Non-Aqueous Potassium-Ion Batteries: A Review. *Curr. Opin. Electrochem.* **2018**, *9*, 41–48. https://doi.org/10.1016/j.coelec.2018.03.031.

(84) Huang, W.; Zhu, Z.; Wang, L.; Wang, S.; Li, H.; Tao, Z.; Shi, J.; Guan, L.; Chen, J. Quasi-Solid-State Rechargeable Lithium-Ion Batteries with a Calix[4]Quinone Cathode and Gel Polymer Electrolyte. *Angew. Chem. Int. Ed. Engl.* **2013**, *52* (35), 9162–9166. https://doi.org/10.1002/ANIE.201302586.

(85) Hong, J.; Lee, M.; Lee, B.; Seo, D. H.; Park, C. B.; Kang, K. Biologically Inspired Pteridine Redox Centres for Rechargeable Batteries. *Nat. Commun.* **2014**, *5* (1), 1–9. https://doi.org/10.1038/ncomms6335.

(86) Pan, Q.; Zheng, Y.; Tong, Z.; Shi, L.; Tang, Y. Novel Lamellar Tetrapotassium Pyromellitic Organic for Robust High-Capacity Potassium Storage. *Angew. Chemie Int. Ed.* **2021**, *60* (21), 11835–11840. https://doi.org/10.1002/ANIE.202103052.

(87) Hu, Y.; Tang, W.; Yu, Q.; Wang, X.; Liu, W.; Hu, J.; Fan, C. Novel Insoluble Organic Cathodes for Advanced Organic K-Ion Batteries. *Adv. Funct. Mater.* **2020**, *30* (17), 2000675. https://doi.org/10.1002/ADFM.202000675.

(88) Obrezkov, F. A.; Ramezankhani, V.; Zhidkov, I.; Traven, V. F.; Kurmaev, E. Z.; Stevenson, K. J.; Troshin, P. A. High-Energy and High-Power-Density Potassium Ion Batteries Using Dihydrophenazine-Based Polymer as Active Cathode Material. *J. Phys. Chem. Lett.* **2019**, *10* (18), 5440–5445. https://doi.org/10.1021/acs.jpclett.9b02039.

(89) Chen, Y.; Luo, W.; Carter, M.; Zhou, L.; Dai, J.; Fu, K.; Lacey, S.; Li, T.; Wan, J.; Han, X.; Bao, Y.; Hu, L. Organic Electrode for Non-Aqueous Potassium-Ion Batteries. *Nano Energy* **2015**, *18*, 205–211. https://doi.org/10.1016/J.NANOEN.2015.10.015.

(90) Ma, J.; Zhou, E.; Fan, C.; Wu, B.; Li, C.; Lu, Z. H.; Li, J. Endowing CuTCNQ with a New Role: A High-Capacity Cathode for K-Ion Batteries. *Chem. Commun.* **2018**, *54* (44), 5578–5581. https://doi.org/10.1039/C8CC00802G.

(91) Tian, B.; Zheng, J.; Zhao, C.; Liu, C.; Su, C.; Tang, W.; Li, X.; Ning, G. H. Carbonyl-Based Polyimide and Polyquinoneimide for Potassium-Ion Batteries. *J. Mater. Chem. A* **2019**, *7* (16), 9997–10003. https://doi.org/10.1039/C9TA00647H.

(92) Jian, Z.; Liang, Y.; Pérez, I. A. R.; Yao, Y.; Ji, X. Poly(Anthraquinonyl Sulfide) Cathode for Potassium-Ion Batteries. *Electrochem. commun.* **2016**, *71*, 5–8. https://doi.org/10.1016/J.ELECOM.2016.07.011.

(93) Zhang, W.; Huang, W.; Zhang, Q. Organic Materials as Electrodes in Potassium-Ion Batteries. *Chem. – A Eur. J.* **2021**, *27* (20), 6131–6144. https://doi.org/10.1002/CHEM.202005259.

(94) Recham, N.; Chotard, J. N.; Dupont, L.; Delacourt, C.; Walker, W.; Armand, M.; Tarascon, J. M. A 3.6 V Lithium-Based Fluorosulphate Insertion Positive Electrode for Lithium-Ion Batteries. *Nat. Mater.* **2009**, *9* (1), 68–74. https://doi.org/10.1038/nmat2590.

(95) Manthiram, A.; Goodenough, J. B. Lithium Insertion into Fe2(SO4)3 Frameworks. *J. Power Sources* **1989**, *26* (3–4), 403–408. https://doi.org/10.1016/0378-7753(89)80153-3.

(96) Gutierrez, A.; Benedek, N. A.; Manthiram, A. Crystal-Chemical Guide for Understanding Redox Energy Variations of M 2+/3+ Couples in Polyanion Cathodes for Lithium-Ion Batteries. *Chem. Mater.* **2013**, *25* (20), 4010–4016. https://doi.org/10.1021/cm401949n.

(97) Voronina, N.; Jo, J. H.; Konarov, A.; Kim, J.; Myung, S. T. KTi2(PO4)3 Electrode

with a Long Cycling Stability for Potassium-Ion Batteries. *Small* **2020**, *16* (20), 2001090. https://doi.org/10.1002/SMLL.202001090.

(98) Wernert, R.; Nguyen, L. H. B.; Petit, E.; Camacho, P. S.; Iadecola, A.; Longo, A.; Fauth, F.; Stievano, L.; Monconduit, L.; Carlier, D.; Croguennec, L. Controlling the Cathodic Potential of KVPO4F through Oxygen Substitution. *Chem. Mater.* **2022**, *34* (10), 4523–4535. https://doi.org/10.1021/acs.chemmater.2c00295.

(99) Liao, J.; Hu, Q.; He, X.; Mu, J.; Wang, J.; Chen, C. A Long Lifespan Potassium-Ion Full Battery Based on KVPO4F Cathode and VPO4 Anode. *J. Power Sources* **2020**, *451*, 227739. https://doi.org/10.1016/J.JPOWSOUR.2020.227739.

(100) Fedotov, S. S.; Samarin, A. S.; Antipov, E. V. KTiOPO4-Structured Electrode Materials for Metal-Ion Batteries: A Review. *J. Power Sources* **2020**, *480*, 228840. https://doi.org/10.1016/J.JPOWSOUR.2020.228840.

(101) Petranikova, M.; Tkaczyk, A. H.; Bartl, A.; Amato, A.; Lapkovskis, V.; Tunsu, C. Vanadium Sustainability in the Context of Innovative Recycling and Sourcing Development. *Waste Manag.* **2020**, *113*, 521–544. https://doi.org/10.1016/J.WASMAN.2020.04.007.

(102) Zhu, Y. H.; Yang, X.; Sun, T.; Wang, S.; Zhao, Y. L.; Yan, J. M.; Zhang, X. B. Recent Progresses and Prospects of Cathode Materials for Non-Aqueous Potassium-Ion Batteries. *Electrochem. Energy Rev.* **2018**, *1* (4), 548–566. https://doi.org/10.1007/s41918-018-0019-7.

(103) Lu, Y.; Wang, L.; Cheng, J.; Goodenough, J. B. Prussian Blue: A New Framework of Electrode Materials for Sodium Batteries. *Chem. Commun.* **2012**, *48* (52), 6544–6546. https://doi.org/10.1039/C2CC31777J.

(104) Qian, J.; Wu, C.; Cao, Y.; Ma, Z.; Huang, Y.; Ai, X.; Yang, H. Prussian Blue Cathode Materials for Sodium-Ion Batteries and Other Ion Batteries. *Adv. Energy Mater.* **2018**, *8* (17), 1702619. https://doi.org/10.1002/AENM.201702619.

(105) Xu, Y.; Titirici, M.; Chen, J.; Cora, F.; Cullen, P. L.; Edge, J. S.; Fan, K.; Fan, L.; Feng, J.; Hosaka, T.; Hu, J.; Ryan, K. M.; Sankar, G.; Scanlon, D. O.; Shi, T.; Stievano, L. 2023 Roadmap for Potassium-Ion Batteries. *J. Phys. Energy* **2023**, *5* (2), 021502. https://doi.org/10.1088/2515-7655/acbf76.

(106) Xue, L.; Li, Y.; Gao, H.; Zhou, W.; Lü, X.; Kaveevivitchai, W.; Manthiram, A.; Goodenough, J. B. Low-Cost High-Energy Potassium Cathode. *J. Am. Chem. Soc.* **2017**, *139* (6), 2164–2167. https://doi.org/10.1021/jacs.6b12598.

(107) Liao, J.; Hu, Q.; Yu, Y.; Wang, H.; Tang, Z.; Wen, Z.; Chen, C. A Potassium-Rich Iron

Hexacyanoferrate/Dipotassium Terephthalate@carbon Nanotube Composite Used for K-Ion Full-Cells with an Optimized Electrolyte. *J. Mater. Chem. A* **2017**, *5* (36), 19017–19024. https://doi.org/10.1039/C7TA05460B.

(108) Deng, L.; Qu, J.; Niu, X.; Liu, J.; Zhang, J.; Hong, Y.; Feng, M.; Wang, J.; Hu, M.; Zeng, L.; Zhang, Q.; Guo, L.; Zhu, Y. Defect-Free Potassium Manganese Hexacyanoferrate Cathode Material for High-Performance Potassium-Ion Batteries. *Nat. Commun.* **2021**, *12* (1), 1–9. https://doi.org/10.1038/s41467-021-22499-0.

(109) Li, C.; Wang, X.; Deng, W.; Liu, C.; Chen, J.; Li, R.; Xue, M. Size Engineering and Crystallinity Control Enable High-Capacity Aqueous Potassium-Ion Storage of Prussian White Analogues. *ChemElectroChem* **2018**, *5* (24), 3887–3892. https://doi.org/10.1002/CELC.201801277.

(110) Franklin, R. Crystallite Growth in Graphitizing and Non-Graphitizing Carbons. *Proc. R. Soc. Lond. A. Math. Phys. Sci.* **1951**, *209* (1097), 196–218. https://doi.org/10.1098/RSPA.1951.0197.

(111) Mizutani, Y.; Abe, T.; Ikeda, K.; Ihara, E.; Asano, M.; Harada, T.; Inaba, M.; Ogumi, Z. Graphite Intercalation Compounds Prepared in Solutions of Alkali Metals in 2-Methyltetrahydrofuran and 2,5-Dimethyltetrahydrofuran. *Carbon N. Y.* **1997**, *35* (1), 61–65. https://doi.org/10.1016/S0008-6223(96)00127-3.

(112) Ma, M.; Chong, S.; Yao, K.; Liu, H. K.; Dou, S. X.; Huang, W. Advanced Anode Materials for Potassium Batteries: Sorting out Opportunities and Challenges by Potassium Storage Mechanisms. *Matter* **2023**, *6* (10), 3220–3273. https://doi.org/10.1016/J.MATT.2023.07.009.

(113) Jian, Z.; Luo, W.; Ji, X. Carbon Electrodes for K-Ion Batteries. *J. Am. Chem. Soc.* **2015**, *137* (36), 11566–11569. https://doi.org/10.1021/jacs.5b06809.

(114) Xu, Z.; Lv, X.; Chen, J.; Jiang, L.; Lai, Y.; Li, J. Dispersion-Corrected DFT Investigation on Defect Chemistry and Potassium Migration in Potassium-Graphite Intercalation Compounds for Potassium Ion Batteries Anode Materials. *Carbon N. Y.* **2016**, *107*, 885–894. https://doi.org/10.1016/J.CARBON.2016.06.101.

(115) Luo, W.; Wan, J.; Ozdemir, B.; Bao, W.; Chen, Y.; Dai, J.; Lin, H.; Xu, Y.; Gu, F.; Barone, V.; Hu, L. Potassium Ion Batteries with Graphitic Materials. *Nano Lett.* **2015**, *15* (11), 7671–7677. https://doi.org/10.1021/ACS.NANOLETT.5B03667.

(116) Share, K.; Cohn, A. P.; Carter, R.; Rogers, B.; Pint, C. L. Role of Nitrogen-Doped Graphene for Improved High-Capacity Potassium Ion Battery Anodes. *ACS Nano* **2016**, *10* (10), 9738–9744. https://doi.org/10.1021/ACSNANO.6B05998.

(117) Stevens, D. A.; Dahn, J. R. The Mechanisms of Lithium and Sodium Insertion in Carbon Materials. *J. Electrochem. Soc.* **2001**, *148* (8), A803. https://doi.org/10.1149/1.1379565.

(118) Wang, W.; Zhou, J.; Wang, Z.; Zhao, L.; Li, P.; Yang, Y.; Yang, C.; Huang, H.; Guo, S.; Wang, W.; Zhou, J.; Zhao, L.; Li, P.; Yang, Y.; Yang, C.; Huang, H.; Guo, S.; Wang, Z. Short-Range Order in Mesoporous Carbon Boosts Potassium-Ion Battery Performance. *Adv. Energy Mater.* **2018**, *8* (5), 1701648. https://doi.org/10.1002/AENM.201701648.

(119) Jian, Z.; Hwang, S.; Li, Z.; Hernandez, A. S.; Wang, X.; Xing, Z.; Su, D.; Ji, X. Hard–Soft Composite Carbon as a Long-Cycling and High-Rate Anode for Potassium-Ion Batteries. *Adv. Funct. Mater.* **2017**, *27* (26), 1700324. https://doi.org/10.1002/ADFM.201700324.

(120) Jian, Z.; Xing, Z.; Bommier, C.; Li, Z.; Ji, X. Hard Carbon Microspheres: Potassium-Ion Anode Versus Sodium-Ion Anode. *Adv. Energy Mater.* **2016**, *6* (3), 1501874. https://doi.org/10.1002/AENM.201501874.

(121) David, L.; Bhandavat, R.; Singh, G. MoS2/Graphene Composite Paper for Sodium-Ion Battery Electrodes. *ACS Nano* **2014**, *8* (2), 1759–1770. https://doi.org/10.1021/nn406156b.

(122) Soares, D. M.; Mukherjee, S.; Singh, G. TMDs beyond MoS2 for Electrochemical Energy Storage. *Chem. – A Eur. J.* **2020**, *26* (29), 6320–6341. https://doi.org/10.1002/CHEM.202000147.

(123) Sultana, I.; Rahman, M. M.; Chen, Y.; Glushenkov, A. M. Potassium-Ion Battery Anode Materials Operating through the Alloying–Dealloying Reaction Mechanism. *Adv. Funct. Mater.* **2018**, *28* (5), 1703857. https://doi.org/10.1002/ADFM.201703857.

(124) Wang, Q.; Zhao, X.; Ni, C.; Tian, H.; Li, J.; Zhang, Z.; Mao, S. X.; Wang, J.; Xu, Y. Reaction and Capacity-Fading Mechanisms of Tin Nanoparticles in Potassium-Ion Batteries. *J. Phys. Chem. C* **2017**, *121* (23), 12652–12657. https://doi.org/10.1021/acs.jpcc.7b03837.

(125) Kim, H.; Kim, J. C.; Bianchini, M.; Seo, D.-H.; Rodriguez-Garcia, J.; Ceder, G.; Kim, H.; Kim, J. C.; Bianchini, M.; Ceder, G.; Seo, D.-H.; Rodriguez-Garcia, J. Recent Progress and Perspective in Electrode Materials for K-Ion Batteries. *Adv. Energy Mater.* **2018**, *8* (9), 1702384. https://doi.org/10.1002/AENM.201702384.

(126) Huang, X.; Sui, X.; Ji, W.; Wang, Y.; Qu, D.; Chen, J. From Phosphorus Nanorods/C to Yolk–Shell P@hollow C for Potassium-Ion Batteries: High Capacity with Stable

Cycling Performance. *J. Mater. Chem. A* **2020**, *8* (16), 7641–7646. https://doi.org/10.1039/D0TA01576H.

(127) Madec, L.; Gabaudan, V.; Gachot, G.; Stievano, L.; Monconduit, L.; Martinez, H. Paving the Way for K-Ion Batteries: Role of Electrolyte Reactivity through the Example of Sb-Based Electrodes. *ACS Appl. Mater. Interfaces* **2018**, *10* (40), 34116–34122. https://doi.org/10.1021/acsami.8b08902.

(128) Wang, A.; Hong, W.; Yang, L.; Tian, Y.; Qiu, X.; Zou, G.; Hou, H.; Ji Wang, X. A.; Hong, W.; Yang, L.; Tian, Y.; Qiu, X.; Zou, G.; Hou, H.; Ji, X. Bi-Based Electrode Materials for Alkali Metal-Ion Batteries. *Small* **2020**, *16* (48), 2004022. https://doi.org/10.1002/SMLL.202004022.

(129) Deng, W.; Qian, J.; Cao, Y.; Ai, X.; Yang, H. Graphene-Wrapped Na2C12H6O4 Nanoflowers as High Performance Anodes for Sodium-Ion Batteries. *Small* **2016**, *12* (5), 583–587. https://doi.org/10.1002/SMLL.201502278.

(130) Li, Z.; Peng, Z.; Sun, R.; Qin, Z.; Liu, X.; Wang, C.; Fan, H.; Lu, S. Super Na+ Half/Full Batteries and Ultrafast Na+ Diffusion Kinetics of Cobalt-Nickel Selenide from Assembling Co0.5Ni0.5Se2@NC Nanosheets into Cross-Stacked Architecture. *Chinese J. Chem.* **2021**, *39* (9), 2599–2606. https://doi.org/10.1002/CJOC.202100192.

(131) Sun, T.; Xie, J.; Guo, W.; Li, D.-S.; Zhang, Q.; Sun, T.; Xie, J.; Zhang, Q.; Guo, W.; Li, -S D. Covalent–Organic Frameworks: Advanced Organic Electrode Materials for Rechargeable Batteries. *Adv. Energy Mater.* **2020**, *10* (19), 1904199. https://doi.org/10.1002/AENM.201904199.

(132) Shea, J. J.; Luo, C. Organic Electrode Materials for Metal Ion Batteries. *ACS Appl. Mater. Interfaces* **2020**, *12* (5), 5361–5380. https://doi.org/10.1021/acsami.9b20384.

(133) Deng, J.; Zhang, Q.; Wu, Y.; Zhu, X.; Ali, R. N.; Song, M.; Tang, Y.; Fan, Z. Recent Advances in Polymers for Potassium Ion Batteries. *Polymers (Basel).* **2022**, *14* (24), 5538. https://doi.org/10.3390/polym14245538.

(134) Deng, Q.; Pei, J.; Fan, C.; Ma, J.; Cao, B.; Li, C.; Jin, Y.; Wang, L.; Li, J. Potassium Salts of Para-Aromatic Dicarboxylates as the Highly Efficient Organic Anodes for Low-Cost K-Ion Batteries. *Nano Energy* **2017**, *33*, 350–355. https://doi.org/10.1016/J.NANOEN.2017.01.016.

(135) Li, H.; Wu, J.; Li, H.; Xu, Y.; Zheng, J.; Shi, Q.; Kang, H.; Zhao, S.; Zhang, L.; Wang, R.; Xin, S.; Zhou, T.; Zhang, C. Designing π-Conjugated Polypyrene Nanoflowers Formed with Meso- and Microporous Nanosheets for High-Performance Anode of Potassium Ion Batteries. *Chem. Eng. J.* **2022**, *430*, 132704.

https://doi.org/10.1016/J.CEJ.2021.132704.

(136) Xiang, J.; Yang, L.; Yuan, L.; Yuan, K.; Zhang, Y.; Huang, Y.; Lin, J.; Pan, F.; Huang, Y. Alkali-Metal Anodes: From Lab to Market. *Joule* **2019**, *3* (10), 2334–2363. https://doi.org/10.1016/J.JOULE.2019.07.027.

(137) Liu, H.; Cheng, X. B.; Jin, Z.; Zhang, R.; Wang, G.; Chen, L. Q.; Liu, Q. B.; Huang, J. Q.; Zhang, Q. Recent Advances in Understanding Dendrite Growth on Alkali Metal Anodes. *EnergyChem* **2019**, *1* (1), 100003. https://doi.org/10.1016/J.ENCHEM.2019.100003.

(138) Liu, P.; Wang, Y.; Gu, Q.; Nanda, J.; Watt, J.; Mitlin, D.; Liu, P.; Wang, Y.; Mitlin, D.; Gu, Q.; Nanda, J.; Watt, J. Dendrite-Free Potassium Metal Anodes in a Carbonate Electrolyte. *Adv. Mater.* **2020**, *32* (7), 1906735. https://doi.org/10.1002/ADMA.201906735.

(139) Qin, L.; Lei, Y.; Wang, H.; Dong, J.; Wu, Y.; Zhai, D.; Kang, F.; Tao, Y.; Yang, Q. H. Capillary Encapsulation of Metallic Potassium in Aligned Carbon Nanotubes for Use as Stable Potassium Metal Anodes. *Adv. Energy Mater.* **2019**, *9* (29), 1901427. https://doi.org/10.1002/AENM.201901427.

(140) Ye, M.; Hwang, J. Y.; Sun, Y. K. A 4 V Class Potassium Metal Battery with Extremely Low Overpotential. *ACS Nano* **2019**, *13* (8), 9306–9314. https://doi.org/10.1021/acsnano.9b03915.

(141) Xiao, N.; Zheng, J.; Gourdin, G.; Schkeryantz, L.; Wu, Y. Anchoring an Artificial Protective Layer to Stabilize Potassium Metal Anode in Rechargeable K-O2 Batteries. *ACS Appl. Mater. Interfaces* **2019**, *11* (18), 16571–16577. https://doi.org/10.1021/acsami.9b02116.

(142) Duan, B.; Wang, W.; Zhao, H.; Wang, A.; Wang, M.; Yuan, K.; Yu, Z.; Yanga, Y. Li-B Alloy as Anode Material for Lithium/Sulfur Battery. *ECS Electrochem. Lett.* **2013**, *2* (6), A47. https://doi.org/10.1149/2.005306eel.

(143) Zhang, X.; Wang, W.; Wang, A.; Huang, Y.; Yuan, K.; Yu, Z.; Qiu, J.; Yang, Y. Improved Cycle Stability and High Security of Li-B Alloy Anode for Lithium–Sulfur Battery. *J. Mater. Chem. A* **2014**, *2* (30), 11660–11665. https://doi.org/10.1039/C4TA01709A.

(144) Xia, S.; Wu, X.; Zhang, Z.; Cui, Y.; Liu, W. Practical Challenges and Future Perspectives of All-Solid-State Lithium-Metal Batteries. *Chem* **2019**, *5* (4), 753–785. https://doi.org/10.1016/J.CHEMPR.2018.11.013.

(145) Wei, C.; Tao, Y.; Fei, H.; An, Y.; Tian, Y.; Feng, J.; Qian, Y. Recent Advances and

Perspectives in Stable and Dendrite-Free Potassium Metal Anodes. *Energy Storage Mater.* **2020**, *30*, 206–227. https://doi.org/10.1016/j.ensm.2020.05.018.

(146) Fei, H.; Liu, Y.; An, Y.; Xu, X.; Zhang, J.; Xi, B.; Xiong, S.; Feng, J. Safe All-Solid-State Potassium Batteries with Three Dimentional, Flexible and Binder-Free Metal Sulfide Array Electrode. *J. Power Sources* **2019**, *433*, 226697. https://doi.org/10.1016/j.jpowsour.2019.226697.

(147) Brandell, D.; Mindemark, J.; Hernández, G. *Polymer-Based Solid State Batteries*; Boston: De Gruyter: Berlin, 2021. https://doi.org/10.1515/9781501521140.

(148) Stolz, L.; Röser, S.; Homann, G.; Winter, M.; Kasnatscheew, J. Pragmatic Approaches to Correlate between the Physicochemical Properties of a Linear Poly(Ethylene Oxide)-Based Solid Polymer Electrolyte and the Performance in a High-Voltage Li-Metal Battery. *J. Phys. Chem. C* **2021**, *125*, 18089–18097. https://doi.org/10.1021/ACS.JPCC.1C03614.

(149) Monroe, C.; Newman, J. The Impact of Elastic Deformation on Deposition Kinetics at Lithium/Polymer Interfaces. *J. Electrochem. Soc.* **2005**, *152* (2), A396. https://doi.org/10.1149/1.1850854.

(150) Frenck, L.; Sethi, G. K.; Maslyn, J. A.; Balsara, N. P. Factors That Control the Formation of Dendrites and Other Morphologies on Lithium Metal Anodes. *Front. Energy Res.* **2019**, *7*, 115. https://doi.org/10.3389/FENRG.2019.00115.

(151) Cao, D.; Sun, X.; Li, Q.; Natan, A.; Xiang, P.; Zhu, H. Lithium Dendrite in All-Solid-State Batteries: Growth Mechanisms, Suppression Strategies, and Characterizations. *Matter* **2020**, *3* (1), 57–94. https://doi.org/10.1016/J.MATT.2020.03.015.

(152) Yang, H.; Wu, N. Ionic Conductivity and Ion Transport Mechanisms of Solid-State Lithium-Ion Battery Electrolytes: A Review. *Energy Sci. Eng.* **2022**, *10* (5), 1643–1671. https://doi.org/10.1002/ESE3.1163.

(153) Stolz, L.; Homann, G.; Winter, M.; Kasnatscheew, J. The Sand Equation and Its Enormous Practical Relevance for Solid-State Lithium Metal Batteries. *Mater. Today* **2021**, *44*, 9–14. https://doi.org/10.1016/J.MATTOD.2020.11.025.

(154) Stolz, L.; Homann, G.; Winter, M.; Kasnatscheew, J. Kinetical Threshold Limits in Solid-State Lithium Batteries: Data on Practical Relevance of Sand Equation. *Data Br.* **2021**, *34*, 106688. https://doi.org/10.1016/J.DIB.2020.106688.

(155) Wu, F.; Zhang, K.; Liu, Y.; Gao, H.; Bai, Y.; Wang, X.; Wu, C. Polymer Electrolytes and Interfaces toward Solid-State Batteries: Recent Advances and Prospects. *Energy Storage Mater.* **2020**, *33*, 26–54. https://doi.org/10.1016/j.ensm.2020.08.002.

(156) Gutmann, V. Empirical Parameters for Donor and Acceptor Properties of Solvents. *Electrochim. Acta* **1976**, *21* (9), 661–670. https://doi.org/10.1016/0013-4686(76)85034-7.

(157) Qiao, L.; Judez, X.; Armand, M.; Zhang, H. Review—Polymer Electrolytes for Sodium Batteries. *J. Electrochem. Soc.* **2020**, *167*, 070534. https://doi.org/10.1149/1945-7111/ab7aa0.

(158) Wang, P.; Wang, L.; Liang, X.; You, Y.; Li, Z.; Liu, Y.; Liu, B.; Sun, Z.; Hu, W. Single-Ion Gel Polymer Electrolyte Based on In-Situ UV Irradiation Cross-Linked Polyimide Complexed with PEO for Lithium-Ion Batteries. *Macromol. Rapid Commun.* **2023**, *44* (10), 2200865. https://doi.org/10.1002/MARC.202200865.

(159) Kolesnikov, T. I.; Voll, D.; Jeschull, F.; Theato, P. Synthesis of Polyimide-PEO Copolymers: Toward Thermally Stable Solid Polymer Electrolytes for Lithium-Metal Batteries. *Eur. Polym. J.* **2024**, *217*, 113315. https://doi.org/10.1016/J.EURPOLYMJ.2024.113315.

(160) Wang, H.; Wang, Q.; Cao, X.; He, Y.; Wu, K.; Yang, J.; Zhou, H.; Liu, W.; Sun, X.; Wang, H.; Cao, X.; He, Y.; Yang, J.; Liu, W.; Sun, X.; Wang, Q.; Wu, K.; Zhou, H. Thiol-Branched Solid Polymer Electrolyte Featuring High Strength, Toughness, and Lithium Ionic Conductivity for Lithium-Metal Batteries. *Adv. Mater.* **2020**, *32* (37), 2001259. https://doi.org/10.1002/ADMA.202001259.

(161) Oteo, U.; Martinez-Ibañez, M.; Aldalur, I.; Sanchez-Diez, E.; Carrasco, J.; Armand, M.; Zhang, H. Improvement of the Cationic Transport in Polymer Electrolytes with (Difluoromethanesulfonyl)(Trifluoromethanesulfonyl)Imide Salts. *ChemElectroChem* **2019**, *6* (4), 1019–1022. https://doi.org/10.1002/CELC.201801472.

(162) Perrier, M.; Besner, S.; Paquette, C.; Vallée, A.; Lascaud, S.; Prud'homme, J. Mixed-Alkali Effect and Short-Range Interactions in Amorphous Poly(Ethylene Oxide) Electrolytes. *Electrochim. Acta* **1995**, *40* (13–14), 2123–2129. https://doi.org/10.1016/0013-4686(95)00151-4.

(163) Thomson, J. B.; Lightfoot, P.; Bruce, P. G. Structure of Polymer Electrolytes: The Crystal Structure of Poly(Ethylene Oxide)4:RbSCN. *Solid State Ionics* **1996**, *85* (1–4), 203–208. https://doi.org/10.1016/0167-2738(96)00060-4.

(164) Memboeuf, A.; Vékey, K.; Lendvay, G. Structure and Energetics of Poly(Ethylene Glycol) Cationized by Li+, Na+, K+ and Cs+: A First-Principles Study: *Eur. J. Mass Spectrom.* **2011**, *17* (1), 33–46. https://doi.org/10.1255/EJMS.1107.

(165) Poudel, L.; Podgornik, R.; Ching, W. Y. The Hydration Effect and Selectivity of Alkali

Metal Ions on Poly(Ethylene Glycol) Models in Cyclic and Linear Topology. *J. Phys. Chem. A* **2017**, *121* (24), 4721–4731. https://doi.org/10.1021/ACS.JPCA.7B04061.

(166) Zhang, B.; Tan, R.; Yang, L.; Zheng, J.; Zhang, K.; Mo, S.; Lin, Z.; Pan, F. Mechanisms and Properties of Ion-Transport in Inorganic Solid Electrolytes. *Energy Storage Mater.* **2017**, *10*, 139–159. https://doi.org/10.1016/j.ensm.2017.08.015.

(167) Ravi, M.; Pavani, Y.; Bhavani, S.; Sharma, A. K.; Narasimha Rao, V. V. R. Investigations on Structural and Electrical Properties of KClO4 Complexed PVP Polymer Electrolyte Films. *Int. J. Polym. Mater. Polym. Biomater.* **2012**, *61* (5), 309–322. https://doi.org/10.1080/00914037.2011.584225.

(168) Baskaran, R.; Selvasekarapandian, S.; Kuwata, N.; Kawamura, J.; Hattori, T. Structure, Thermal and Transport Properties of PVAc-LiClO4 Solid Polymer Electrolytes. *J. Phys. Chem. Solids* **2007**, *68* (3), 407–412. https://doi.org/10.1016/J.JPCS.2006.12.001.

(169) Kadir, M. F. Z.; Majid, S. R.; Arof, A. K. Plasticized Chitosan-PVA Blend Polymer Electrolyte Based Proton Battery. *Electrochim. Acta* **2010**, *55* (4), 1475–1482. https://doi.org/10.1016/J.ELECTACTA.2009.05.011.

(170) Gadjourova, Z.; Andreev, Y. G.; Tunstall, D. P.; Bruce, P. G. Ionic Conductivity in Crystalline Polymer Electrolytes. *Nature* **2001**, *412* (6846), 520–523. https://doi.org/10.1038/35087538.

(171) Stoeva, Z.; Martin-Litas, I.; Staunton, E.; Andreev, Y. G.; Bruce, P. G. Ionic Conductivity in the Crystalline Polymer Electrolytes PEO6:LiXF6, X = P, As, Sb. *J. Am. Chem. Soc.* **2003**, *125* (15), 4619–4626. https://doi.org/10.1021/JA029326T.

(172) Christie, A. M.; Lilley, S. J.; Staunton, E.; Andreev, Y. G.; Bruce, P. G. Increasing the Conductivity of Crystalline Polymer Electrolytes. *Nature* **2005**, *433* (7021), 50–53. https://doi.org/10.1038/NATURE03186.

(173) Zhang, C.; Gamble, S.; Ainsworth, D.; Slawin, A. M. Z.; Andreev, Y. G.; Bruce, P. G. Alkali Metal Crystalline Polymer Electrolytes. *Nat. Mater.* **2009**, *8* (7), 580–584. https://doi.org/10.1038/NMAT2474.

(174) Meyer, W. H. Polymer Electrolytes for Lithium-Ion Batteries. *Adv Mater.* **1998**, *10* (6), 439–448. https://doi.org/10.1002/(SICI)1521-4095(199804)10:6<439::AID-ADMA439>3.0.CO;2-I.

(175) Vogel, H. The Temperature Dependence Law of the Viscosity of Fluids. *Phys. Zeitschrift* **1921**, *22*, 645–646.

(176) Fulcher, G. S. ANALYSIS OF RECENT MEASUREMENTS OF THE VISCOSITY

OF GLASSES. *J. Am. Ceram. Soc.* **1925**, *8* (6), 339–355. https://doi.org/10.1111/J.1151-2916.1925.TB16731.X.

(177) Tammann, G.; Hesse, W. Die Abhängigkeit Der Viscosität von Der Temperatur Bie Unterkühlten Flüssigkeiten. *Zeitschrift für Anorg. und Allg. Chemie* **1926**, *156* (1), 245–257. https://doi.org/10.1002/ZAAC.19261560121.

(178) Maurel, A.; Armand, M.; Grugeon, S.; Fleutot, B.; Davoisne, C.; Tortajada, H.; Courty, M.; Panier, S.; Dupont, L. Poly(Ethylene Oxide)−LiTFSI Solid Polymer Electrolyte Filaments for Fused Deposition Modeling Three-Dimensional Printing. *J. Electrochem. Soc.* **2020**, *167* (7), 070536. https://doi.org/10.1149/1945-7111/AB7C38.

(179) Le Nest, J. F.; Gandini, A.; Cheradame, H.; Cohen-Addad, J. P. Influence of LiCLO4 on the Properties of Polyether Networks: Specific Volume and Glass Transition Temperature. *Macromolecules* **1988**, *21* (4), 1117–1120. https://doi.org/10.1021/ma00182a044.

(180) Mao, G.; Perea, R. F.; Howells, W. S.; Price, D. L.; Saboungi, M. L. Relaxation in Polymer Electrolytes on the Nanosecond Timescale. *Nature* **2000**, *405* (6783), 163–165. https://doi.org/10.1038/35012032.

(181) Butzelaar, A. J.; Liu, K. L.; Röring, P.; Brunklaus, G.; Winter, M.; Theato, P. A Systematic Study of Vinyl Ether-Based Poly(Ethylene Oxide) Side-Chain Polymer Electrolytes. *ACS Appl. Polym. Mater.* **2021**, *3* (3), 1573–1582. https://doi.org/10.1021/acsapm.0c01398.

(182) Mishra, R.; Baskaran, N.; Ramakrishnan, P. A.; Rao, K. J. Lithium Ion Conduction in Extreme Polymer in Salt Regime. *Solid State Ionics* **1998**, *112* (3–4), 261–273. https://doi.org/10.1016/S0167-2738(98)00209-4.

(183) Forsyth, M.; Jiazeng, S.; MacFarlane, D. R. Novel High Salt Content Polymer Electrolytes Based on High Tg Polymers. *Electrochim. Acta* **2000**, *45* (8), 1249–1254. https://doi.org/10.1016/S0013-4686(99)00328-X.

(184) Forsyth, M.; Sun, J.; Macfarlane, D. R.; Hill, A. J. Compositional Dependence of Free Volume in PAN/LiCF3SO3 Polymer-in-Salt Electrolytes and the Effect on Ionic Conductivity. *J Polym Sci Part B Polym Phys.* **2000**, *38* (2), 341–350. https://doi.org/10.1002/(SICI)1099-0488(20000115)38:2<341::AID-POLB6>3.0.CO;2-S.

(185) Sångeland, C.; Mogensen, R.; Brandell, D.; Mindemark, J. Stable Cycling of Sodium Metal All-Solid-State Batteries with Polycarbonate-Based Polymer Electrolytes. *ACS Appl. Polym. Mater.* **2019**, *1* (4), 825–832. https://doi.org/10.1021/ACSAPM.9B00068.

(186) Rosenwinkel, M. P.; Andersson, R.; Mindemark, J.; Schönhoff, M. Coordination Effects in Polymer Electrolytes: Fast Li+ Transport by Weak Ion Binding. *J. Phys. Chem. C* **2020**, *124* (43), 23588–23596. https://doi.org/10.1021/acs.jpcc.0c08369.

(187) Zhang, Y.; Lu, W.; Cong, L.; Liu, J.; Sun, L.; Mauger, A.; Julien, C. M.; Xie, H.; Liu, J. Cross-Linking Network Based on Poly(Ethylene Oxide): Solid Polymer Electrolyte for Room Temperature Lithium Battery. *J. Power Sources* **2019**, *420*, 63–72. https://doi.org/10.1016/J.JPOWSOUR.2019.02.090.

(188) Paranjape, N.; Mandadapu, P. C.; Wu, G.; Lin, H. Highly-Branched Cross-Linked Poly(Ethylene Oxide) with Enhanced Ionic Conductivity. *Polymer (Guildf).* **2017**, *111*, 1–8. https://doi.org/10.1016/j.polymer.2017.01.014.

(189) Xu, L.; Li, J.; Deng, W.; Li, L.; Zou, G.; Hou, H.; Huang, L.; Ji, X. Boosting the Ionic Conductivity of PEO Electrolytes by Waste Eggshell-Derived Fillers for High-Performance Solid Lithium/Sodium Batteries. *Mater. Chem. Front.* **2021**, *5* (3), 1315–1323. https://doi.org/10.1039/D0QM00541J.

(190) Huy, V. P. H.; So, S.; Hur, J. Inorganic Fillers in Composite Gel Polymer Electrolytes for High-Performance Lithium and Non-Lithium Polymer Batteries. *Nanomaterials* **2021**, *11* (3), 614. https://doi.org/10.3390/nano11030614.

(191) Ng, B. C.; Wong, H. Y.; Chew, K. W.; Osman, Z. Development and Characterization of Poly-ε-Caprolactone-Based Polymer Electrolyte for Lithium Rechargeable Battery. *Int. J. Electrochem. Sci.* **2011**, *6* (9), 4355–4364. https://doi.org/10.1016/S1452-3981(23)18333-7.

(192) Mindemark, J.; Sun, B.; Törmä, E.; Brandell, D. High-Performance Solid Polymer Electrolytes for Lithium Batteries Operational at Ambient Temperature. *J. Power Sources* **2015**, *298*, 166–170. https://doi.org/10.1016/J.JPOWSOUR.2015.08.035.

(193) Choudalakis, G.; Gotsis, A. D. Free Volume and Mass Transport in Polymer Nanocomposites. *Curr. Opin. Colloid Interface Sci.* **2012**, *17* (3), 132–140. https://doi.org/10.1016/j.cocis.2012.01.004.

(194) Kim, Y. W.; Lee, W.; Choi, B. K. Relation between Glass Transition and Melting of PEO-Salt Complexes. *Electrochim. Acta* **2000**, *45* (8), 1473–1477. https://doi.org/10.1016/S0013-4686(99)00362-X.

(195) Brooks, D. J.; Merinov, B. V.; William A. Goddard, I.; Kozinsky, B.; Mailoa, J. Atomistic Description of Ionic Diffusion in PEO–LiTFSI: Effect of Temperature, Molecular Weight, and Ionic Concentration. *Macromolecules* **2018**, *51* (21), 8987–8995. https://doi.org/10.1021/ACS.MACROMOL.8B01753.

(196) Lascaud, S.; Perrier, M.; Vallée, A.; Besner, S.; Prud'homme, J.; Armand, M. Phase Diagrams and Conductivity Behavior of Poly(Ethylene Oxide)-Molten Salt Rubbery Electrolytes. *Macromolecules* **1994**, *27* (25), 7469–7477. https://doi.org/10.1021/ma00103a034.

(197) Marzantowicz, M.; Dygas, J. R.; Krok, F.; Nowiński, J. L.; Tomaszewska, A.; Florjańczyk, Z.; Zygadło-Monikowska, E. Crystalline Phases, Morphology and Conductivity of PEO:LiTFSI Electrolytes in the Eutectic Region. *J. Power Sources* **2006**, *159* (1), 420–430. https://doi.org/10.1016/J.JPOWSOUR.2006.02.044.

(198) Evans, J.; Vincent, C. A.; Bruce, P. G. Electrochemical Measurement of Transference Numbers in Polymer Electrolytes. *Polymer (Guildf).* **1987**, *28* (13), 2324–2328. https://doi.org/10.1016/0032-3861(87)90394-6.

(199) Xu, K. Navigating the Minefield of Battery Literature. *Commun. Mater.* **2022**, *3* (1), 1–7. https://doi.org/10.1038/s43246-022-00251-5.

(200) Newman, J. S.; Doyle, M.; Fuller, T.; Newman, J. S. The Importance of the Lithium Ion Transference Number in Lithium Polymer Cells. *Electrochim. Acta* **1994**, *39* (13), 2073–2081. https://doi.org/10.1016/0013-4686(94)85091-7.

(201) Chazalviel, J. N. Electrochemical Aspects of the Generation of Ramified Metallic Electrodeposits. *Phys. Rev. A* **1990**, *42* (12), 7355–7367. https://doi.org/10.1103/PHYSREVA.42.7355.

(202) Monroe, C.; Newman, J. Dendrite Growth in Lithium/Polymer Systems : A Propagation Model for Liquid Electrolytes under Galvanostatic Conditions. *J. Electrochem. Soc.* **2003**, *150* (10), A1377. https://doi.org/10.1149/1.1606686.

(203) Li, Z.; Fu, J.; Zhou, X.; Gui, S.; Wei, L.; Yang, H.; Li, H.; Guo, X. Ionic Conduction in Polymer-Based Solid Electrolytes. *Adv. Sci.* **2023**, *10* (10), 2201718. https://doi.org/10.1002/ADVS.202201718.

(204) Yang, X.; Liu, J.; Pei, N.; Chen, Z.; Li, R.; Fu, L.; Zhang, P.; Zhao, J. The Critical Role of Fillers in Composite Polymer Electrolytes for Lithium Battery. *Nano-Micro Lett.* **2023**, *15*, 74. https://doi.org/10.1007/s40820-023-01051-3.

(205) Bruce, P. G.; Vincent, C. A. Steady State Current Flow in Solid Binary Electrolyte Cells. *J. Electroanal. Chem. Interfacial Electrochem.* **1987**, *225* (1–2), 1–17. https://doi.org/10.1016/0022-0728(87)80001-3.

(206) Dugas, R.; Forero-Saboya, J. D.; Ponrouch, A. Methods and Protocols for Reliable Electrochemical Testing in Post-Li Batteries (Na, K, Mg, and Ca). *Chem. Mater.* **2019**, *31* (21), 8613–8628. https://doi.org/10.1021/ACS.CHEMMATER.9B02776.

(207) Boschin, A.; Abdelhamid, M. E.; Johansson, P. On the Feasibility of Sodium Metal as Pseudo-Reference Electrode in Solid State Electrochemical Cells. *ChemElectroChem* **2017**, *4* (10), 2717–2721. https://doi.org/10.1002/CELC.201700273.

(208) Watanabe, M.; Nagano, S.; Sanui, K.; Ogata, N. Estimation of Li+ Transport Number in Polymer Electrolytes by the Combination of Complex Impedance and Potentiostatic Polarization Measurements. *Solid State Ionics* **1988**, *28–30* (PART 2), 911–917. https://doi.org/10.1016/0167-2738(88)90303-7.

(209) Ravn Sørensen, P.; Jacobsen, T. Conductivity, Charge Transfer and Transport Number—an Ac-Investigation of the Polymer Electrolyte LiSCN-Poly(Ethyleneoxide). *Electrochim. Acta* **1982**, *27* (12), 1671–1675. https://doi.org/10.1016/0013-4686(82)80162-X.

(210) Boden, N.; Leng, S. A.; Ward, I. M. Ionic Conductivity and Diffusivity in Polyethylene Oxode/Electrolyte Solutions as Models for Polymer Electrolytes. *Solid State Ionics* **1991**, *45* (3–4), 261–270. https://doi.org/10.1016/0167-2738(91)90160-D.

(211) Khurana, R.; Schaefer, J. L.; Archer, L. A.; Coates, G. W. Suppression of Lithium Dendrite Growth Using Cross-Linked Polyethylene/Poly(Ethylene Oxide) Electrolytes: A New Approach for Practical Lithium-Metal Polymer Batteries. *J. Am. Chem. Soc.* **2014**, *136* (20), 7395–7402. https://doi.org/10.1021/JA502133J.

(212) Butzelaar, A. J.; Röring, P.; Hoffmann, M.; Atik, J.; Paillard, E.; Wilhelm, M.; Winter, M.; Brunklaus, G.; Theato, P. Advanced Block Copolymer Design for Polymer Electrolytes: Prospects of Microphase Separation. *Macromolecules* **2021**, *54* (23), 11101–11112. https://doi.org/10.1021/ACS.MACROMOL.1C02147.

(213) Bergman, M.; Bergfelt, A.; Sun, B.; Bowden, T.; Brandell, D.; Johansson, P. Graft Copolymer Electrolytes for High Temperature Li-Battery Applications, Using Poly(Methyl Methacrylate) Grafted Poly(Ethylene Glycol)Methyl Ether Methacrylate and Lithium Bis(Trifluoromethanesulfonimide). *Electrochim. Acta* **2015**, *175*, 96–103. https://doi.org/10.1016/j.electacta.2015.01.226.

(214) Lin, Z.; Guo, X.; Yang, Y.; Tang, M.; Wei, Q.; Yu, H. Block Copolymer Electrolyte with Adjustable Functional Units for Solid Polymer Lithium Metal Battery. *J. Energy Chem.* **2021**, *52*, 67–74. https://doi.org/10.1016/j.jechem.2020.04.052.

(215) Harun, F.; Chan, C. H.; Guo, Q. Rheology and Microscopic Heterogeneity of Poly(Ethylene Oxide) Solid Polymer Electrolytes. *Macromol. Symp.* **2017**, *376* (1), 1700040. https://doi.org/10.1002/masy.201700040.

(216) Lopez, J.; Mackanic, D. G.; Cui, Y.; Bao, Z. Designing Polymers for Advanced Battery

Chemistries. *Nat. Rev. Mater.* **2019**, *4* (5), 312–330. https://doi.org/10.1038/s41578-019-0103-6.

(217) Zhao, Q.; Liu, X.; Stalin, S.; Archer, L. In-Built Polymer-in-Solvent and Solvent-in-Polymer Electrolytes for High-Voltage Lithium Metal Batteries. *Cell Reports Phys. Sci.* **2020**, *1* (8), 100146. https://doi.org/10.1016/j.xcrp.2020.100146.

(218) Huo, S.; Sheng, L.; Xue, W.; Wang, L.; Xu, H.; Zhang, H.; He, X. Challenges of Polymer Electrolyte with Wide Electrochemical Window for High Energy Solid-State Lithium Batteries. *InfoMat* **2023**, *5* (3), e12394. https://doi.org/10.1002/inf2.12394.

(219) Chen, L.; Venkatram, S.; Kim, C.; Batra, R.; Chandrasekaran, A.; Ramprasad, R. Electrochemical Stability Window of Polymeric Electrolytes. *Chem. Mater.* **2019**, *31* (12), 4598–4604. https://doi.org/10.1021/acs.chemmater.9b01553.

(220) Peljo, P.; Girault, H. H. Electrochemical Potential Window of Battery Electrolytes: The HOMO–LUMO Misconception. *Energy Environ. Sci.* **2018**, *11* (9), 2306–2309. https://doi.org/10.1039/C8EE01286E.

(221) Méry, A.; Rousselot, S.; Lepage, D.; Dollé, M. A Critical Review for an Accurate Electrochemical Stability Window Measurement of Solid Polymer and Composite Electrolytes. *Materials (Basel).* **2021**, *14* (14), 3840. https://doi.org/10.3390/MA14143840.

(222) Hernández, G.; Johansson, I. L.; Mathew, A.; Sångeland, C.; Brandell, D.; Mindemark, J. Going Beyond Sweep Voltammetry: Alternative Approaches in Search of the Elusive Electrochemical Stability of Polymer Electrolytes. *J. Electrochem. Soc.* **2021**, *168* (10), 100523. https://doi.org/10.1149/1945-7111/AC2D8B.

(223) Qiu, J.; Liu, X.; Chen, R.; Li, Q.; Wang, Y.; Chen, P.; Gan, L.; Lee, S. J.; Nordlund, D.; Liu, Y.; Yu, X.; Bai, X.; Li, H.; Chen, L. Enabling Stable Cycling of 4.2 V High-Voltage All-Solid-State Batteries with PEO-Based Solid Electrolyte. *Adv. Funct. Mater.* **2020**, *30* (22), 1909392. https://doi.org/10.1002/ADFM.201909392.

(224) Homann, G.; Stolz, L.; Nair, J.; Laskovic, I. C.; Winter, M.; Kasnatscheew, J. Poly(Ethylene Oxide)-Based Electrolyte for Solid-State-Lithium-Batteries with High Voltage Positive Electrodes: Evaluating the Role of Electrolyte Oxidation in Rapid Cell Failure. *Sci. Rep.* **2020**, *10* (1), 1–9. https://doi.org/10.1038/s41598-020-61373-9.

(225) Dewald, G. F.; Ohno, S.; Kraft, M. A.; Koerver, R.; Till, P.; Vargas-Barbosa, N. M.; Janek, J.; Zeier, W. G. Experimental Assessment of the Practical Oxidative Stability of Lithium Thiophosphate Solid Electrolytes. *Chem. Mater.* **2019**, *31* (20), 8328–8337. https://doi.org/10.1021/ACS.CHEMMATER.9B01550.

(226) Homann, G.; Stolz, L.; Neuhaus, K.; Winter, M.; Kasnatscheew, J. Effective Optimization of High Voltage Solid-State Lithium Batteries by Using Poly(Ethylene Oxide)-Based Polymer Electrolyte with Semi-Interpenetrating Network. *Adv. Funct. Mater.* **2020**, *30* (46), 2006289. https://doi.org/10.1002/ADFM.202006289.

(227) Mohamed, F.; Hameed, T. A.; Abdelghany, A. M.; Turky, G. Structure–Dynamic Properties Relationships in Poly(Ethylene Oxide)/Silicon Dioxide Nanocomposites: Dielectric Relaxation Study. *Polym. Bull.* **2021**, *78* (9), 5205–5223. https://doi.org/10.1007/s00289-020-03368-0.

(228) Homann, G.; Stolz, L.; Nair, J.; Laskovic, I. C.; Winter, M.; Kasnatscheew, J. Poly(Ethylene Oxide)-Based Electrolyte for Solid-State-Lithium-Batteries with High Voltage Positive Electrodes: Evaluating the Role of Electrolyte Oxidation in Rapid Cell Failure. *Sci. Rep.* **2020**, *10* (1), 1–9. https://doi.org/10.1038/s41598-020-61373-9.

(229) El Bellihi, A. A.; Bayoumy, W. A.; Masoud, E. M.; Mousa, M. A. Preparation, Characterizations and Conductivity of Composite Polymer Electrolytes Based on PEO-LiClO4 and Nano ZnO Filler. *Bull. Korean Chem. Soc.* **2012**, *33* (9), 2949–2954. https://doi.org/10.5012/bkcs.2012.33.9.2949.

(230) Schulz, M.; Schäfer, M.; Saalwächter, K.; Thurn-Albrecht, T. Competition between Crystal Growth and Intracrystalline Chain Diffusion Determines the Lamellar Thickness in Semicrystalline Polymers. *Nat. Commun.* **2022**, *13* (119), 1–10. https://doi.org/10.1038/s41467-021-27752-0.

(231) Takahashi, Y.; Tadokoro, H. Structural Studies of Polyethers, (–(CH2)m–O–)n. X. Crystal Structure of Poly(Ethylene Oxide). *Macromolecules* **1973**, *6* (5), 672–675. https://doi.org/10.1021/ma60035a005.

(232) St-Onge, V.; Rochon, S.; Daigle, J. C.; Soldera, A.; Claverie, J. P. The Unusual Conductivity of Na+ in PEO-Based Statistical Copolymer Solid Electrolytes: When Less Means More. *Angew. Chemie Int. Ed.* **2021**, *60* (49), 25897–25904. https://doi.org/10.1002/ANIE.202109709.

(233) Chandra, A. Hot Pressed K+ Ion Conducting Solid Polymer Electrolytes: Synthesis, Ion Conduction and Polymeric Battery Fabrication. *Indian J. Phys.* **2016**, *90* (7), 759–765. https://doi.org/10.1007/s12648-015-0805-6.

(234) Chandra, A.; Dhundhel, R. S.; Chandra, A. Electrical Properties of a Newly Synthesized Potassium Ion Conducting Solid Polymer Electrolytes. *Mater. Today Proc.* **2022**, *57* (Part 4), 1473–1476. https://doi.org/10.1016/j.matpr.2021.11.479.

(235) Hashim, N. H. A. M.; Subban, R. H. Y. Studies on Conductivity, Structural and

Thermal Properties of PEO-LiTFSI Polymer Electrolytes Doped with EMImTFSI Ionic Liquid. *J. Chem. Phys.* **2031**, *143*, 24904. https://doi.org/10.1063/1.5066977.

(236) Fortuin, B. A.; Otegi, J.; López del Amo, J. M.; Peña, S. R.; Meabe, L.; Manzano, H.; Martínez-Ibañez, M.; Carrasco, J. Synergistic Theoretical and Experimental Study on the Ion Dynamics of Bis(Trifluoromethanesulfonyl)Imide-Based Alkali Metal Salts for Solid Polymer Electrolytes. *Phys. Chem. Chem. Phys.* **2023**, *25* (36), 25038–25054. https://doi.org/10.1039/D3CP02989A.

(237) Armand, M. Polymer Solid Electrolytes - an Overview. *Solid State Ionics* **1983**, *9–10* (PART 2), 745–754. https://doi.org/10.1016/0167-2738(83)90083-8.

(238) Zhao, E.; Guo, Y.; Xin, Y.; Xu, G. Facile Synthesis and Performance of NASICON Li1+xAlxGe2-x(PO4)3 Electrolytes for All Solid State Lithium-Ion Battery. *Solid State Ionics* **2020**, *356*, 115454. https://doi.org/10.1016/j.ssi.2020.115454.

(239) Pfalzgraf, D.; Mutter, D.; Urban, D. F. Atomistic Analysis of Li Migration in Li1+xAlxTi2−x(PO4)3 (LATP) Solid Electrolytes. *Solid State Ionics* **2021**, *359*, 115521. https://doi.org/10.1016/j.ssi.2020.115521.

(240) Kim, K. M.; Shin, D. O.; Lee, Y. G. Effects of Preparation Conditions on the Ionic Conductivity of Hydrothermally Synthesized Li1+xAlxTi2-x(PO4)3 Solid Electrolytes. *Electrochim. Acta* **2015**, *176*, 1364–1373. https://doi.org/10.1016/j.electacta.2015.07.170.

(241) Zhang, Z.; Wenzel, S.; Zhu, Y.; Sann, J.; Shen, L.; Yang, J.; Yao, X.; Hu, Y. S.; Wolverton, C.; Li, H.; Chen, L.; Janek, J. Na3Zr2Si2PO12: A Stable Na+-Ion Solid Electrolyte for Solid-State Batteries. *ACS Appl. Energy Mater.* **2020**, *3* (8), 7427–7437. https://doi.org/10.1021/acsaem.0c00820.

(242) Chen, J.; Wang, C.; Wang, G.; Zhou, D.; Fan, L.-Z. An Interpenetrating Network Polycarbonate-Based Composite Electrolyte for High-Voltage All-Solid-State Lithium-Metal Batteries. *Energy Mater.* **2022**, *2* (3), 200023. https://doi.org/10.20517/ENERGYMATER.2022.25.

(243) Il'ina, E. Recent Strategies for Lithium-Ion Conductivity Improvement in Li7La3Zr2O12 Solid Electrolytes. *Int. J. Mol. Sci.* **2023**, *24* (16), 12905. https://doi.org/10.3390/ijms241612905.

(244) He, X.; Zhu, Y.; Mo, Y. Origin of Fast Ion Diffusion in Super-Ionic Conductors. *Nat. Commun.* **2017**, *8*, 15893. https://doi.org/10.1038/ncomms15893.

(245) Kang, O. L.; Ahmad, A.; Hassan, N. H.; Rana, U. A. [MG49-LiClO4]:[TiO2-SiO2] Polymer Electrolytes: In Situ Preparation and Characterization. *Int. J. Polym. Sci.* **2016**,

9838067. https://doi.org/10.1155/2016/9838067.

(246) Shen, Z.; Zhong, J.; Chen, J.; Xie, W.; Yang, K.; Lin, Y.; Chen, J.; Shi, Z. SiO2 Nanofiber Composite Gel Polymer Electrolyte by In-Situ Polymerization for Stable Li Metal Batteries. *Chinese Chem. Lett.* **2023**, *34* (3), 107370. https://doi.org/10.1016/j.cclet.2022.03.093.

(247) Suarez, S.; Abbrent, S.; Greenbaum, S. G.; Shin, J. H.; Passerini, S. Effect of Nanosized SiO2 on the Transport Properties of Solventless P(EO)20LIBETI Polymer Electrolytes: A Solid-State NMR Study. *Solid State Ionics* **2004**, *166* (3–4), 407–415. https://doi.org/10.1016/j.ssi.2003.11.009.

(248) Patriarchi, A.; Darjazi, H.; Minnetti, L.; Sbrascini, L.; Elia, G. A.; Castorani, V.; Muñoz-Márquez, M. Á.; Nobili, F. All-Solid-State Li-Metal Cell Using Nanocomposite TiO2/Polymer Electrolyte and Self-Standing LiFePO4 Cathode. *Batteries* **2024**, *10* (1). https://doi.org/10.3390/batteries10010011.

(249) Dyartanti, E. R.; Widiasa, I. N.; Purwanto, A.; Susanto, H. Nanocomposite Polymer Electrolytes in PVDF/ZnO Membranes Modified with PVP for Use in LiFePO4 Batteries. *Evergreen* **2018**, *5* (2), 19–25. https://doi.org/10.5109/1936213.

(250) D'Epifanio, A.; Fiory, F. S.; Licoccia, S.; Traversa, E.; Scrosati, B.; Croce, F. Metallic-Lithium, LiFePO4-Based Polymer Battery Using PEO-ZrO2 Nanocomposite Polymer Electrolyte. *J. Appl. Electrochem.* **2004**, *34* (4). https://doi.org/10.1023/B:JACH.0000016623.42147.68.

(251) Lee, T. K.; Andersson, R.; Dzulkurnain, N. A.; Hernández, G.; Mindemark, J.; Brandell, D. Polyester-ZrO2 Nanocomposite Electrolytes with High Li Transference Numbers for Ambient Temperature All-Solid-State Lithium Batteries. *Batter. Supercaps* **2021**, *4* (4), 653–662. https://doi.org/10.1002/batt.202000254.

(252) Huo, H.; Wu, B.; Zhang, T.; Zheng, X.; Ge, L.; Xu, T.; Guo, X.; Sun, X. Anion-Immobilized Polymer Electrolyte Achieved by Cationic Metal-Organic Framework Filler for Dendrite-Free Solid-State Batteries. *Energy Storage Mater.* **2019**, *18*, 59–67. https://doi.org/10.1016/j.ensm.2019.01.007.

(253) Wang, Y.; Wu, L.; Lin, Z.; Tang, M.; Ding, P.; Guo, X.; Zhang, Z.; Liu, S.; Wang, B.; Yin, X.; Chen, Z.; Amine, K.; Yu, H. Hydrogen Bonds Enhanced Composite Polymer Electrolyte for High-Voltage Cathode of Solid-State Lithium Battery. *Nano Energy* **2022**, *96*, 107105. https://doi.org/10.1016/j.nanoen.2022.107105.

(254) Gao, L.; Wu, N.; Deng, N.; Li, Z.; Li, J.; Che, Y.; Cheng, B.; Kang, W.; Liu, R.; Li, Y. Optimized CeO2 Nanowires with Rich Surface Oxygen Vacancies Enable Fast Li-Ion

Conduction in Composite Polymer Electrolytes. *Energy Environ. Mater.* **2023**, *6* (1), e12272. https://doi.org/10.1002/eem2.12272.

(255) Ai, S.; Mazumdar, S.; Li, H.; Cao, Y.; Li, T. Nano-Silica Doped Composite Polymer Chitosan/Poly(Ethylene Oxide)-Based Electrolyte with High Electrochemical Stability Suitable for Quasi Solid-State Lithium Metal Batteries. *J. Electroanal. Chem.* **2021**, *895*, 115464. https://doi.org/10.1016/j.jelechem.2021.115464.

(256) Wang, Q.; Wu, J. F.; Yu, Z. Y.; Guo, X. Composite Polymer Electrolytes Reinforced by Two-Dimensional Layer-Double-Hydroxide Nanosheets for Dendrite-Free Lithium Batteries. *Solid State Ionics* **2020**, *347*, 115275. https://doi.org/10.1016/j.ssi.2020.115275.

(257) Zhao, E.; Guo, Y.; Liu, Y.; Liu, S.; Xu, G. Nanostructured Zeolitic Imidazolate Framework-67 Reinforced Poly(Ethylene Oxide) Composite Electrolytes for All Solid State Lithium Ion Batteries. *Appl. Surf. Sci.* **2022**, *573*, 151489. https://doi.org/10.1016/j.apsusc.2021.151489.

(258) Bao, W.; Zhao, L.; Zhao, H.; Su, L.; Cai, X.; Yi, B.; Zhang, Y.; Xie, J. Vapor Phase Infiltration of ZnO Quantum Dots for All-Solid-State PEO-Based Lithium Batteries. *Energy Storage Mater.* **2021**, *43*, 258–265. https://doi.org/10.1016/j.ensm.2021.09.010.

(259) Phan, T. N. T.; Issa, S.; Gigmes, D. Poly(Ethylene Oxide)-Based Block Copolymer Electrolytes for Lithium Metal Batteries. *Polym. Int.* **2019**, *68* (1), 7–13. https://doi.org/10.1002/pi.5677.

(260) Wang, T.; Zhong, L.; Xiao, M.; Han, D.; Wang, S.; Huang, Z.; Huang, S.; Sun, L.; Meng, Y. Block Copolymer Electrolytes for Lithium Metal Batteries: Strategies to Boost Both Ionic Conductivity and Mechanical Strength. *Prog. Polym. Sci.* **2023**, *146*, 101743. https://doi.org/10.1016/j.progpolymsci.2023.101743.

(261) Rollo-Walker, G.; Malic, N.; Wang, X.; Chiefari, J.; Forsyth, M. Development and Progression of Polymer Electrolytes for Batteries: Influence of Structure and Chemistry. *Polymers (Basel).* **2021**, *13* (23), 4127. https://doi.org/10.3390/polym13234127.

(262) Itoh, T.; Fujita, K.; Uno, T.; Kubo, M. Polymer Electrolytes Based on Vinyl Ethers with Various EO Chain Length and Their Polymer Electrolytes Cross-Linked by Electron Beam Irradiation. *Ionics (Kiel).* **2017**, *23* (2), 257–264. https://doi.org/10.1007/s11581-016-1815-x.

(263) Rolland, J.; Brassinne, J.; Bourgeois, J. P.; Poggi, E.; Vlad, A.; Gohy, J. F. Chemically Anchored Liquid-PEO Based Block Copolymer Electrolytes for Solid-State Lithium-

Ion Batteries. *J. Mater. Chem. A* **2014**, *2* (30), 11839–11846. https://doi.org/10.1039/c4ta02327g.

(264) Itoh, T.; Fujita, K.; Inoue, K.; Iwama, H.; Kondoh, K.; Uno, T.; Kubo, M. Solid Polymer Electrolytes Based on Alternating Copolymers of Vinyl Ethers with Methoxy Oligo(Ethyleneoxy)Ethyl Groups and Vinylene Carbonate. *Electrochim. Acta* **2013**, *112*, 221–229. https://doi.org/10.1016/j.electacta.2013.08.124.

(265) St-Onge, V.; Cui, M.; Rochon, S.; Daigle, J. C.; Claverie, J. P. Reducing Crystallinity in Solid Polymer Electrolytes for Lithium-Metal Batteries via Statistical Copolymerization. *Commun. Mater.* **2021**, *2* (83). https://doi.org/10.1038/s43246-021-00187-2.

(266) Wang, C.; Sakai, T.; Watanabe, O.; Hirahara, K.; Nakanishi, T. All Solid-State Lithium-Polymer Battery Using a Self-Cross-Linking Polymer Electrolyte. *J. Electrochem. Soc.* **2003**, *150* (9), A1166. https://doi.org/10.1149/1.1593652.

(267) Singh, M.; Odusanya, O.; Wilmes, G. M.; Eitouni, H. B.; Gomez, E. D.; Patel, A. J.; Chen, V. L.; Park, M. J.; Fragouli, P.; Iatrou, H.; Hadjichristidis, N.; Cookson, D.; Balsara, N. P. Effect of Molecular Weight on the Mechanical and Electrical Properties of Block Copolymer Electrolytes. *Macromolecules* **2007**, *40* (13), 4578–4585. https://doi.org/10.1021/MA0629541.

(268) Worzakowska, M. Thermal and Mechanical Properties of Polystyrene Modified with Esters Derivatives of 3-Phenylprop-2-En-1-Ol. *J. Therm. Anal. Calorim.* **2015**, *121* (1), 235–243. https://doi.org/10.1007/S10973-015-4547-7.

(269) Zhang, B.; Zhang, Y.; Zhang, N.; Liu, J.; Cong, L.; Liu, J.; Sun, L.; Mauger, A.; Julien, C. M.; Xie, H.; Pan, X. Synthesis and Interface Stability of Polystyrene-Poly(Ethylene Glycol)-Polystyrene Triblock Copolymer as Solid-State Electrolyte for Lithium-Metal Batteries. *J. Power Sources* **2019**, *428*, 93–104. https://doi.org/10.1016/J.JPOWSOUR.2019.04.033.

(270) Tomita, H.; Sanda, F.; Endo, T. Reactivity Comparison of Five- and Six-Membered Cyclic Carbonates with Amines: Basic Evaluation for Synthesis of Poly(Hydroxyurethane). *J. Polym. Sci. Part A Polym. Chem.* **2001**, *39* (1), 162–168. https://doi.org/10.1002/1099-0518(20010101)39:1<162::AID-POLA180>3.0.CO;2-O.

(271) Xu, J.; Feng, E.; Song, J. Renaissance of Aliphatic Polycarbonates: New Techniques and Biomedical Applications. *J. Appl. Polym. Sci.* **2014**, *131* (5), 39822. https://doi.org/10.1002/APP.39822.

(272) Tominaga, Y.; Nanthana, V.; Tohyama, D. Ionic Conduction in Poly(Ethylene

Carbonate)-Based Rubbery Electrolytes Including Lithium Salts. *Polym. J.* **2012**, *44* (12), 1155–1158. https://doi.org/10.1038/pj.2012.97.

(273) Tominaga, Y.; Yamazaki, K. Fast Li-Ion Conduction in Poly(Ethylene Carbonate)-Based Electrolytes and Composites Filled with TiO2 Nanoparticles. *Chem. Commun.* **2014**, *50* (34), 4448–4450. https://doi.org/10.1039/C3CC49588D.

(274) Li, Y.; Ding, F.; Xu, Z.; Sang, L.; Ren, L.; Ni, W.; Liu, X. Ambient Temperature Solid-State Li-Battery Based on High-Salt-Concentrated Solid Polymeric Electrolyte. *J. Power Sources* **2018**, *397*, 95–101. https://doi.org/10.1016/J.JPOWSOUR.2018.05.050.

(275) Wang, C.; Zhang, H.; Li, J.; Chai, J.; Dong, S.; Cui, G. The Interfacial Evolution between Polycarbonate-Based Polymer Electrolyte and Li-Metal Anode. *J. Power Sources* **2018**, *397*, 157–161. https://doi.org/10.1016/J.JPOWSOUR.2018.07.008.

(276) Sun, B.; Mindemark, J.; Edström, K.; Brandell, D. Polycarbonate-Based Solid Polymer Electrolytes for Li-Ion Batteries. *Solid State Ionics* **2014**, *262*, 738–742. https://doi.org/10.1016/j.ssi.2013.08.014.

(277) Mindemark, J.; Mogensen, R.; Smith, M. J.; Silva, M. M.; Brandell, D. Polycarbonates as Alternative Electrolyte Host Materials for Solid-State Sodium Batteries. *Electrochem. Commun.* **2017**, *77*, 58–61. https://doi.org/10.1016/j.elecom.2017.02.013.

(278) Sångeland, C.; Younesi, R.; Mindemark, J.; Brandell, D. Towards Room Temperature Operation of All-Solid-State Na-Ion Batteries through Polyester–Polycarbonate-Based Polymer Electrolytes. *Energy Storage Mater.* **2019**, *19*, 31–38. https://doi.org/10.1016/J.ENSM.2019.03.022.

(279) Berg, H. *Batteries for Electric Vehicles*; Cambridge University Press, 2015.

(280) Stuve, E. M. Overpotentials in Electrochemical Cells. In *Encyclopedia of Applied Electrochemistry*; Springer New York, 2014; pp 1445–1453. https://doi.org/10.1007/978-1-4419-6996-5_330.

(281) Huang, Y.; Lai, X.; Han, X.; Yuan, Y.; Ren, D.; Qiao, D.; Zhu, J.; Zheng, Y.; Lu, L.; Ouyang, M. Mechanism of Lithium Plating and Stripping in Lithium-Ion Batteries Induced by Overhang Failure Defects. *Cell Reports Phys. Sci.* **2024**, *5* (12), 102299. https://doi.org/10.1016/J.XCRP.2024.102299.

(282) Puchkov, A. A.; Sedush, N. G.; Buzin, A. I.; Bozin, T. N.; Bakirov, A. V.; Borisov, R. S.; Chvalun, S. N. Synthesis and Characterization of Well-Defined Star-Shaped Poly(L-Lactides). *Polymer (Guildf).* **2023**, *264*, 125573. https://doi.org/10.1016/j.polymer.2022.125573.

(283) Jeschull, F. Bat2dat_v1.0.1. 2022. https://doi.org/10.5281/zenodo.7439377.

(284) Allgayer, F.; Maibach, J.; Jeschull, F. Comparing the Solid Electrolyte Interphases on Graphite Electrodes in K and Li Half Cells. *ACS Appl. Energy Mater.* **2022**, *5* (1), 1136–1148. https://doi.org/10.1021/ACSAEM.1C03491.

(285) Caracciolo, L.; Madec, L.; Martinez, H. XPS Analysis of K-Based Reference Compounds to Allow Reliable Studies of Solid Electrolyte Interphase in K-Ion Batteries. *ACS Appl. Energy Mater.* **2021**, *4* (10), 11693–11699. https://doi.org/10.1021/acsaem.1c02400.

(286) Jeschull, F.; Maibach, J. Inactive Materials Matter: How Binder Amounts Affect the Cycle Life of Graphite Electrodes in Potassium-Ion Batteries. *Electrochem. Commun.* **2020**, *121*, 106874. https://doi.org/10.1016/j.elecom.2020.106874.

(287) Shin, J. H.; Henderson, W. A.; Passerini, S. Ionic Liquids to the Rescue? Overcoming the Ionic Conductivity Limitations of Polymer Electrolytes. *Electrochem. commun.* **2003**, *5* (12), 1016–1020. https://doi.org/10.1016/j.elecom.2003.09.017.

(288) Angell, C. A.; Liu, C.; Sanchez, E. Rubbery Solid Electrolytes with Dominant Cationic Transport and High Ambient Conductivity. *Nature* **1993**, *362* (6416), 137–139. https://doi.org/10.1038/362137a0.

(289) Yi, C.; Liu, W.; Li, L.; Dong, H.; Liu, J. Polymer-in-Salt Solid Electrolytes for Lithium-Ion Batteries. *Funct. Mater. Lett.* **2019**, *12* (6), 1930006. https://doi.org/10.1142/S1793604719300068.

(290) Edman, L.; Ferry, A.; Doeff, M. M. Slow Recrystallization in the Polymer Electrolyte System Poly(Ethylene Oxide)n–LiN(CF3SO2)2. *J. Mater. Res.* **2000**, *15* (9), 1950–1954. https://doi.org/10.1557/JMR.2000.0281.

(291) Marzantowicz, M.; Dygas, J. R.; Krok, F.; Łasińska, A.; Florjańczyk, Z.; Zygadło-Monikowska, E.; Affek, A. Crystallization and Melting of PEO:LiTFSI Polymer Electrolytes Investigated Simultaneously by Impedance Spectroscopy and Polarizing Microscopy. *Electrochim. Acta* **2005**, *50* (19), 3969–3977. https://doi.org/10.1016/J.ELECTACTA.2005.02.053.

(292) Shannon, R. D. Revised Effective Ionic Radii and Systematic Studies of Interatomic Distances in Halides and Chalcogenides. *Acta Cryst.* **1976**, *32* (5), 751–767. https://doi.org/10.1107/S0567739476001551.

(293) Wang, H.; Yu, D.; Kuang, C.; Cheng, L.; Li, W.; Feng, X.; Zhang, Z.; Zhang, X.; Zhang, Y. Alkali Metal Anodes for Rechargeable Batteries. *Chem* **2019**, *5* (2), 313–338. https://doi.org/10.1016/J.CHEMPR.2018.11.005.

(294) Xing, S.; Khudyshkina, A.; Rauska, U.-C.; Butzelaar, A. J.; Voll, D.; Theato, P.; Tübke, J.; Jeschull, F. Degradation of Styrene-Poly(Ethylene Oxide)-Based Block Copolymer Electrolytes at the Na and K Negative Electrode Studied by Microcalorimetry and Impedance Spectroscopy. *J. Electrochem. Soc.* **2024**, *171* (4), 040516. https://doi.org/10.1149/1945-7111/AD3B72.

(295) Park, J.; Lee, J.; Alfaruqi, M. H.; Kwak, W.-J.; Kim, J.; Hwang, J.-Y. Initial Investigation and Evaluation of Potassium Metal as an Anode for Rechargeable Potassium Batteries. *J. Mater. Chem. A* **2020**, *8* (33), 16718–16737. https://doi.org/10.1039/D0TA03562A.

(296) Wan, J.; Xie, J.; Kong, X.; Liu, Z.; Liu, K.; Shi, F.; Pei, A.; Chen, H.; Chen, W.; Chen, J.; Zhang, X.; Zong, L.; Wang, J.; Chen, L. Q.; Qin, J.; Cui, Y. Ultrathin, Flexible, Solid Polymer Composite Electrolyte Enabled with Aligned Nanoporous Host for Lithium Batteries. *Nat. Nanotechnol.* **2019**, *14* (7), 705–711. https://doi.org/10.1038/s41565-019-0465-3.

(297) Wang, H.; Zhai, D.; Kang, F. Solid Electrolyte Interphase (SEI) in Potassium Ion Batteries. *Energy Environ. Sci.* **2020**, *13* (12), 4583–4608. https://doi.org/10.1039/D0EE01638A.

(298) Huang, T.; Du, G.; Qi, Y.; Li, J.; Zhong, W.; Yang, Q.; Zhang, X.; Xu, M. A Prussian Blue Analogue as a Long-Life Cathode for Liquid-State and Solid-State Sodium-Ion Batteries. *Inorg. Chem. Front.* **2020**, *7* (20), 3938–3944. https://doi.org/10.1039/D0QI00872A.

(299) Kim, H.; Tian, Y.; Ceder, G. Origin of Capacity Degradation of High-Voltage KVPO4F Cathode. *J. Electrochem. Soc.* **2020**, *167* (11), 110555. https://doi.org/10.1149/1945-7111/aba54e.

Appendix

Table A1. Thermal quantities (T_g, T_m, ΔH_m and degree of crystallinity X_C) of PEO-KTFSI-based polymer electrolytes with different molar ratio of EO:K.

Entry	EO:K molar ratio	T_g, °C	T_m, °C	ΔH_m, J g^{-1}	Crystallinity X_C*, %
1	100:0	-59.8	69.2	126.2**	64.3**
2	20:1	-48.1	53.0/37.0	68.1	34.7
3	16:1	-46.9	48.8	27.5	14.0
4	12:1	-47.7	39.5	11.1	5.7
5	8:1	-40.6	54.6	30.2	15.4
6	4:1	-35.2	51.3/135.2	38.5	19.6

* For PEO-KTFSI compositions, crystallinity was calculated relatively to theoretical ΔH_m of PEO = 196.4 J g^{-1},[34] according to **Equation 7.** ** Pre-dried molten and thus not completely recrystallized PEO was used, and its crystallinity was calculated relatively to the theoretical ΔH_m of PEO as well as for all PEO-KTFSI SPEs.

Table A2. Thermal quantities (T_g, T_m, ΔH_m, and degree of crystallinity X_C) of Al_2O_3/SiO_2-filled PEO_{12}-$KTFSI_1$ samples with different mass fraction of the nanofillers.

Sample	Nanofiller	Nanofiller mass fraction, wt.%	T_g, °C	T_m, °C	ΔH_m, J g^{-1}	Crystallinity X_C***, %
AlOx-2	Al_2O_3	2	-43.5	50.1	47.5	24.7
AlOx-5		5	-38.7	43.2/59.0	54.4	29.2
AlOx-8		8	-41.5	48.8	43.6	24.1
AlOx-10		10	-43.2	56.3	52.7	29.8
AlOx-12		12	-38.1	45.0	40.7	23.5
AlOx-15		15	-42.6	46.6	38.1	22.8
SiOx-2	SiO_2	2	-46.5	45.5	46.1	24.0
SiOx-5		5	-45.4	46.5	42.4	22.7
SiOx-8		8	-43.7	47.7	46.2	25.6
SiOx-10		10	-43.1	51.4	41.4	23.4

*** For the samples with the nanofillers the total amount of the additives, ϕ_{add}, was accounted according to **Equation 7.**

Table A3. Thermal quantities (T_g, T_m, ΔH_m and degree of crystallinity X_C) of the BPE-KTFSI polymer electrolytes with different molar ratio of EO:K.

EO:K molar ratio in BPE-KTFSI	**T_g (PEO phase), °C**	**T_g (PS phase), °C**	**T_m (PEO phase), °C**	**ΔH_m (PEO phase), J g^{-1}**	**Crystallinity X_C**** (PEO phase), %**
20:1	-56.5	100.6	29.6	11.9	12.1
15:1	-49.9	102.2	–	–	–
10:1	-46.5	100.1	–	–	–

**** Calculated relative to theoretical ΔH_m of PEO, 196.4 J g^{-1} [34], according to **Equation 7**, and divided by two, 98.2 J g^{-1} (since BPE blocks were matched to ~ 50:50 weight ratio).

Table A4. Total ionic conductivity σ (derived from EIS measurements carried out in the frequency range from 1 MHz to 500 mHz) of the PEO-based SPEs at 25 and 55 °C.

SPE	**EO:K molar ratio**	**σ (25 °C), S cm^{-1}**	**σ (55 °C), S cm^{-1}**
PEO-KTFSI	20:1	1.30×10^{-6}	2.86×10^{-4}
	16:1	3.56×10^{-5}	6.77×10^{-4}
	12:1	2.11×10^{-5}	2.65×10^{-4}
	8:1	1.79×10^{-7}	6.18×10^{-5}
	4:1	4.01×10^{-8}	3.03×10^{-5}
AlOx-2	12:1	1.75×10^{-6}	2.61×10^{-4}
AlOx-5	12:1	3.07×10^{-6}	2.09×10^{-4}
AlOx-8	12:1	1.74×10^{-6}	1.80×10^{-4}
AlOx-10	12:1	1.85×10^{-6}	2.52×10^{-4}
AlOx-12	12:1	1.68×10^{-6}	1.40×10^{-4}
AlOx-15	12:1	1.43×10^{-6}	1.46×10^{-4}
SiOx-2	12:1	1.61×10^{-6}	2.22×10^{-4}
SiOx-5	12:1	1.18×10^{-6}	1.68×10^{-4}
SiOx-8	12:1	1.58×10^{-6}	1.93×10^{-4}
SiOx-10	12:1	1.59×10^{-6}	1.96×10^{-4}
BPE-KTFSI	20:1	1.07×10^{-6}	1.67×10^{-5}
	15:1	3.95×10^{-6}	3.57×10^{-5}
	10:1	8.73×10^{-7}	1.37×10^{-5}

Table A5. Thermal quantities (T_g, T_m) of the PTMC-KTFSI and P(CL_{80}-TMC_{20})-KTFSI polymer electrolytes with different molar ratios of [TMC]:K, [CL_{80}-TMC_{20}]:K.

Polycarbonate-based host material					
PTMC			**P(CL_{80}-TMC_{20})**		
[TMC]:K molar ratio	**T_g, °C**	**T_m, °C**	**[CL_{80}-TMC_{20}]:K molar ratio**	**T_g, °C**	**T_m, °C**
100:0	-15.6	–	100:0	-57.2	14.7
24:1	-13.8	–	24:1	-53.3	13.5
20:1	-15.2	–	20:1	-46.8	–
16:1	-15.9	–	16:1	-50.3	15.6
12:1	-14.3	–	12:1	-42.9	–
8:1	-11.6	–	8:1	-32.2	–
4:1	-0.8	–	4:1	-40.1	–
2:1	1.2	125.0	2:1	-26.6	145.6
1:1	3.8	170.9	1:1	-25.7	167.9

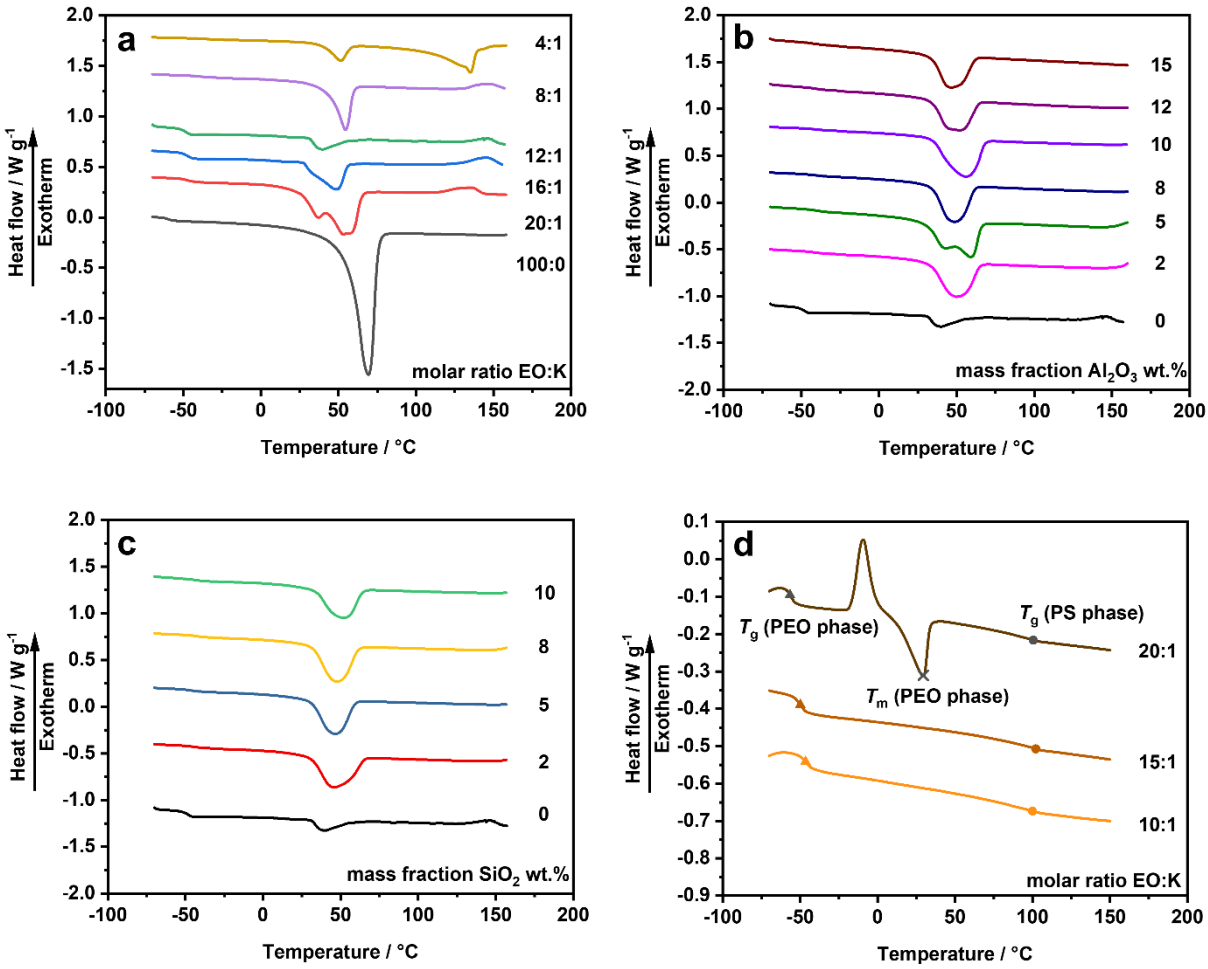

Figure A1. DSC thermograms of SPEs: **(a)** PEO-KTFSI with different molar ratio of EO:K and pure PEO (EO:K = 100:0); PEO_{12}-$KTFSI_1$ with different mass fraction of nano-sized **(b)** Al_2O_3 and **(c)** SiO_2; **(d)** BPE-KTFSI with different molar ratio of EO:K. DSC thermograms were recorded at heating rate of 10 K min^{-1} for the determination of glass transition T_g and melting T_m temperatures.

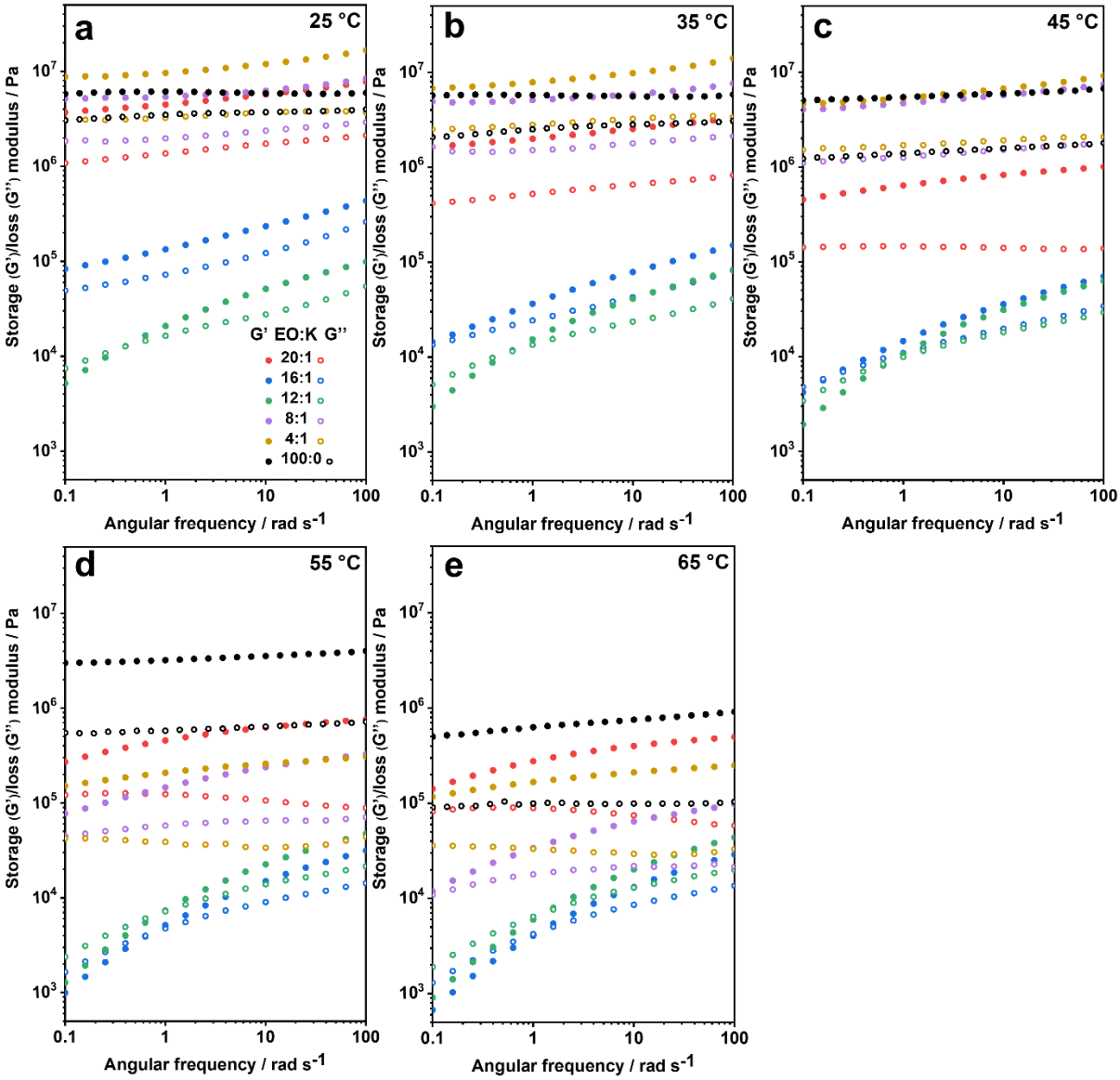

Figure A2. The dependence of storage (G') and loss (G'') moduli of PEO-KTFSI SPEs with different molar ratio of EO:K on angular frequency at **(a)** 25 ℃, **(b)** 35 ℃, **(c)** 45 ℃, **(d)** 55 ℃, **(e)** 65 ℃.

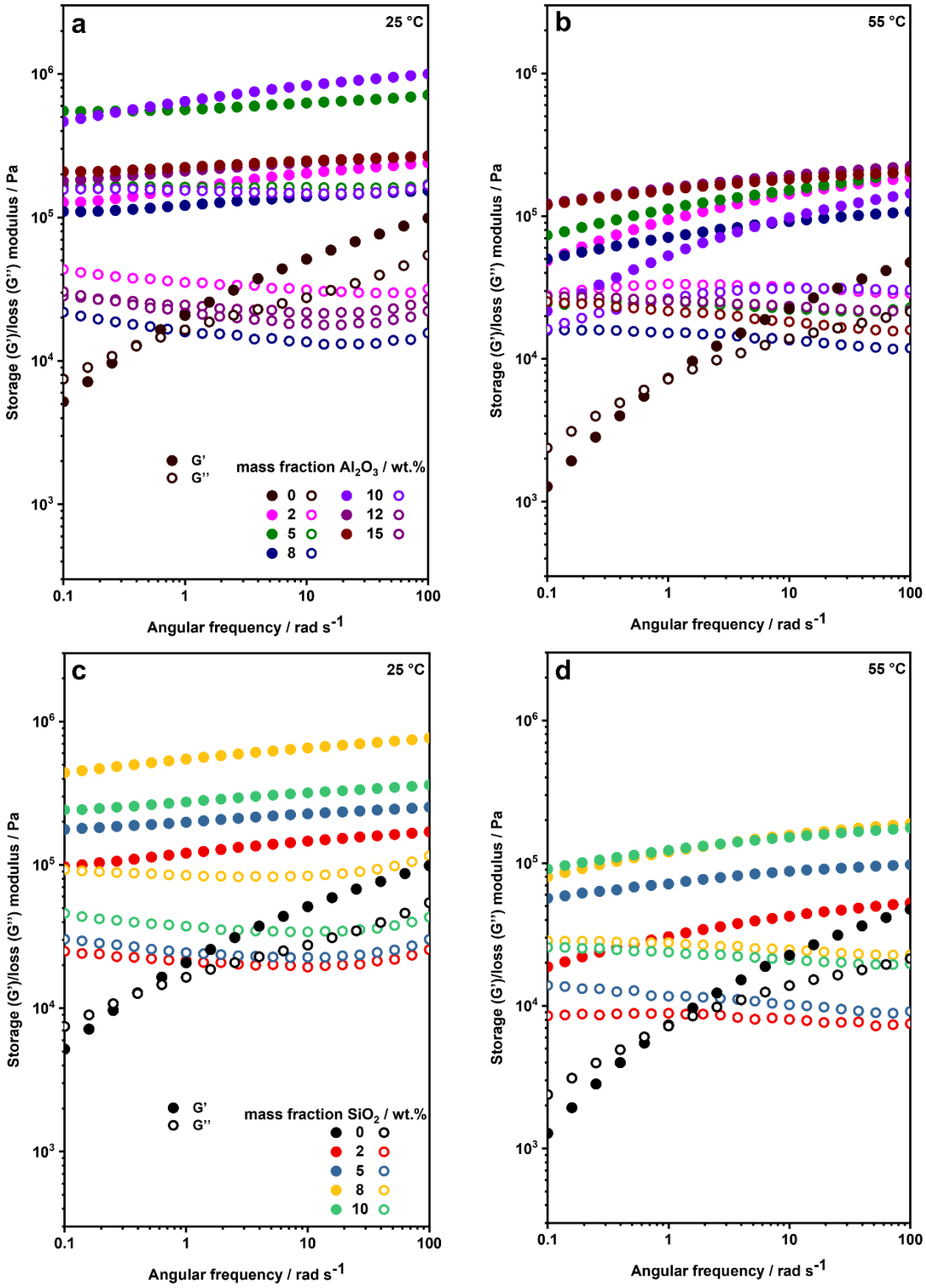

Figure A3. The dependence of storage (G') and loss (G'') moduli on angular frequency of PEO_{12}-$KTFSI_1$-based SPEs with different mass fraction of Al_2O_3 at **(a)** 25 °C and **(b)** 55 °C, and SiO_2 at **(c)** 25 °C and **(d)** 55 °C.

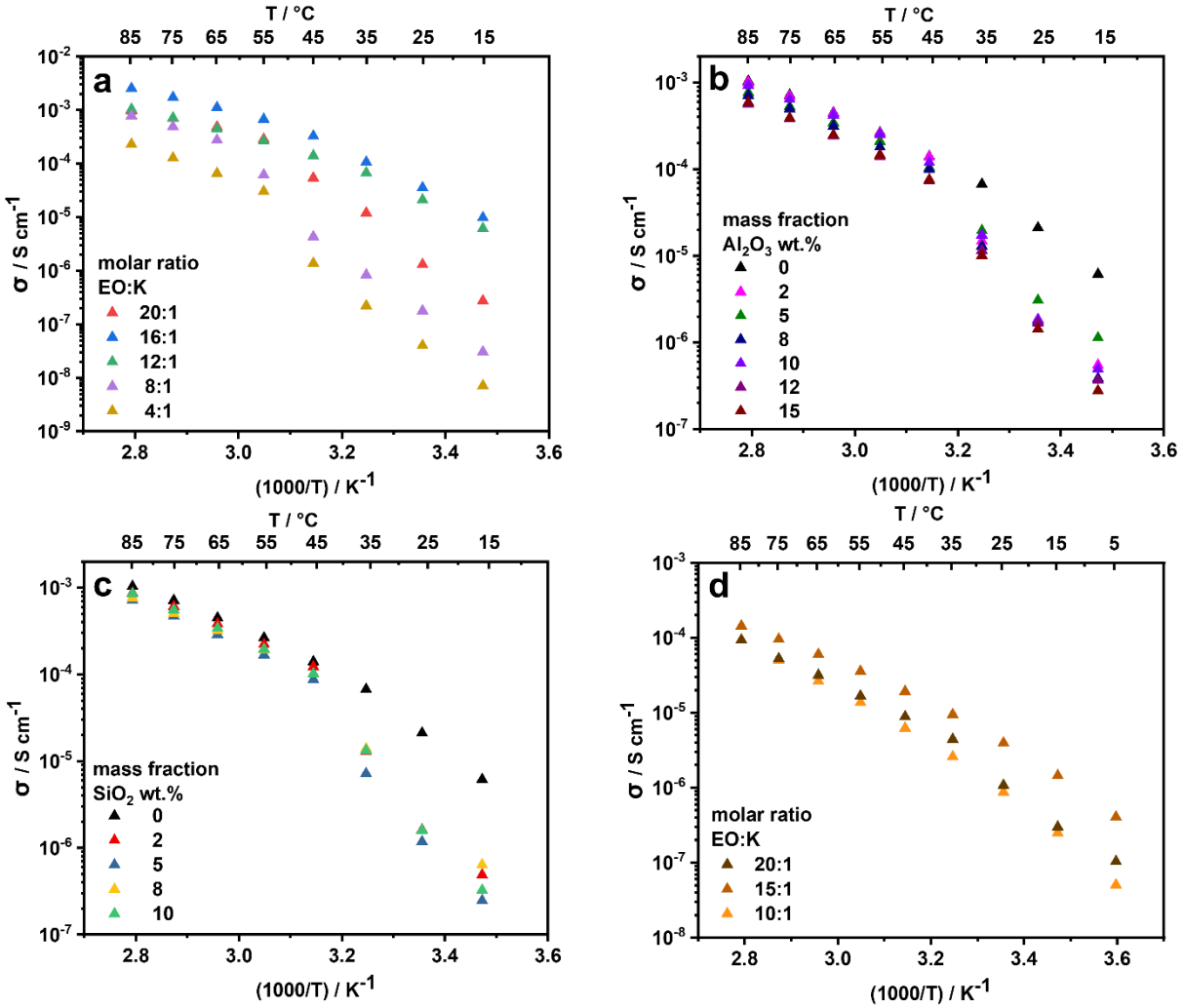

Figure A4. Temperature-dependent ionic conductivity (derived from EIS measurements conducted in the frequency range from 1 MHz to 500 mHz in the temperature range from 15 to 85 °C) of **(a)** PEO-KTFSI SPEs with different molar ratio of EO:K; PEO_{12}-$KTFSI_1$-based SPEs with different mass fraction of **(b)** Al_2O_3 and **(c)** SiO_2; and **(d)** BPE-KTFSI SPEs with different molar ratio of EO:K.

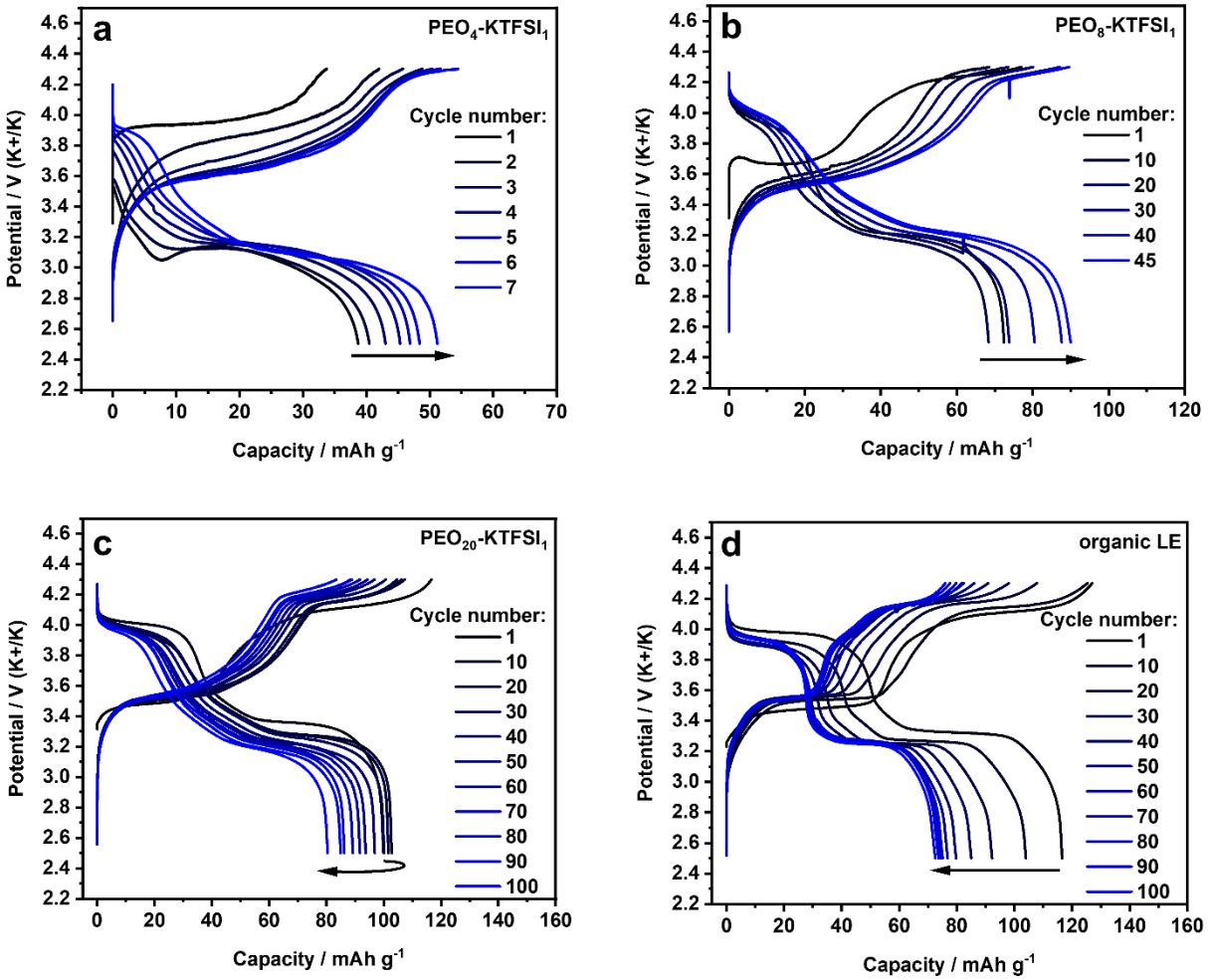

Figure A5. Galvanostatic charge-discharge profiles of K-metal/electrolyte/KFF cells with different electrolyte systems at C/25 (at 25 °C for liquid electrolyte (LE)-based system, and at 55 °C for the systems with SPEs): **(a)** PEO_4-$KTFSI_1$, **(b)** PEO_8-$KTFSI_1$, **(c)** PEO_{20}-$KTFSI_1$, **(d)** organic LE.

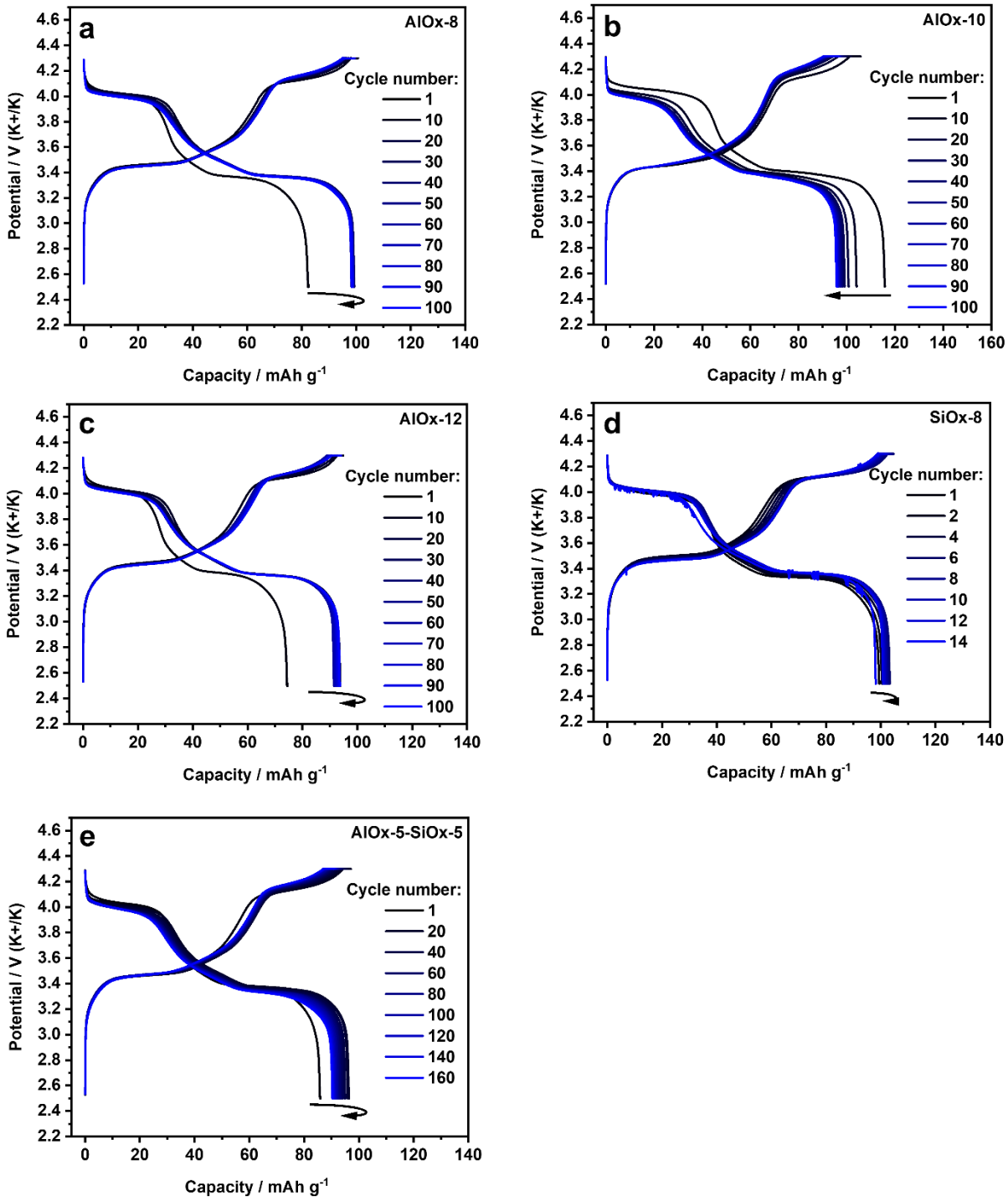

Figure A6. Galvanostatic charge-discharge profiles of K-metal/SPE/KFF cells with different SPE composites: **(a)** AlOx-8, **(b)** AlOx-10, **(c)** AlOx-12, **(d)** SiOx-8 (failed after 14 cycles), **(e)** AlOx-5-SiOx-5.

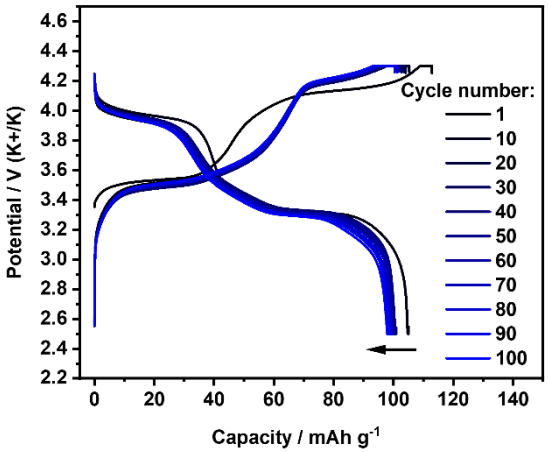

Figure A7. Galvanostatic charge-discharge profiles of K-metal/BPE_{15}-$KTFSI_1$/KFF cell.

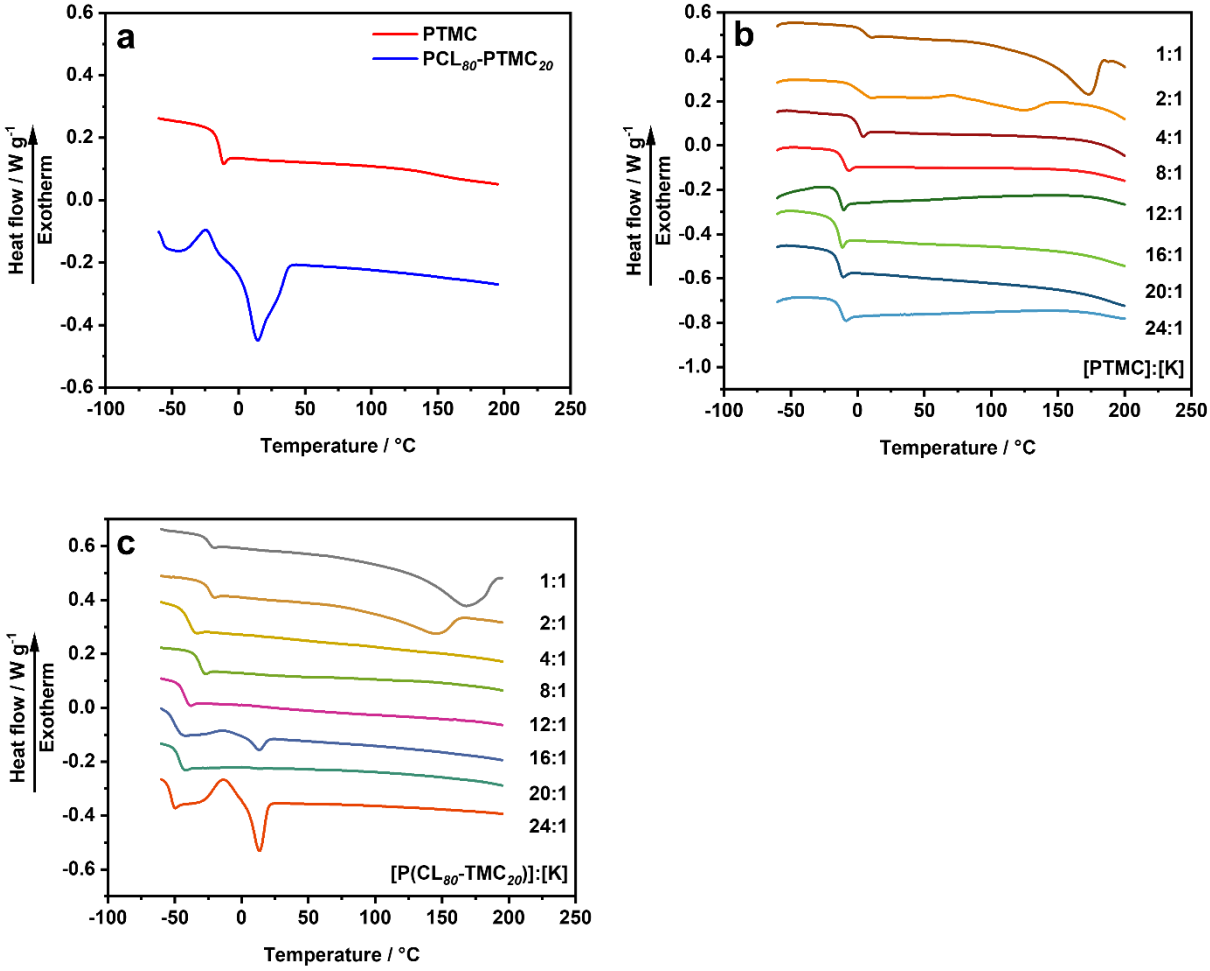

Figure A8. DSC thermograms of **(a)** pristine homopolymer PTMC and copolymer P(CL_{80}-TMC_{20}); SPEs based on **(b)** PTMC and **(c)** P(CL_{80}-TMC_{20}) with different [TMC]/[CL_{80}-TMC_{20}]:K molar ratios. DSC thermograms were recorded at heating rate of 10 K min^{-1} for the determination of glass transition T_g and melting T_m temperatures.

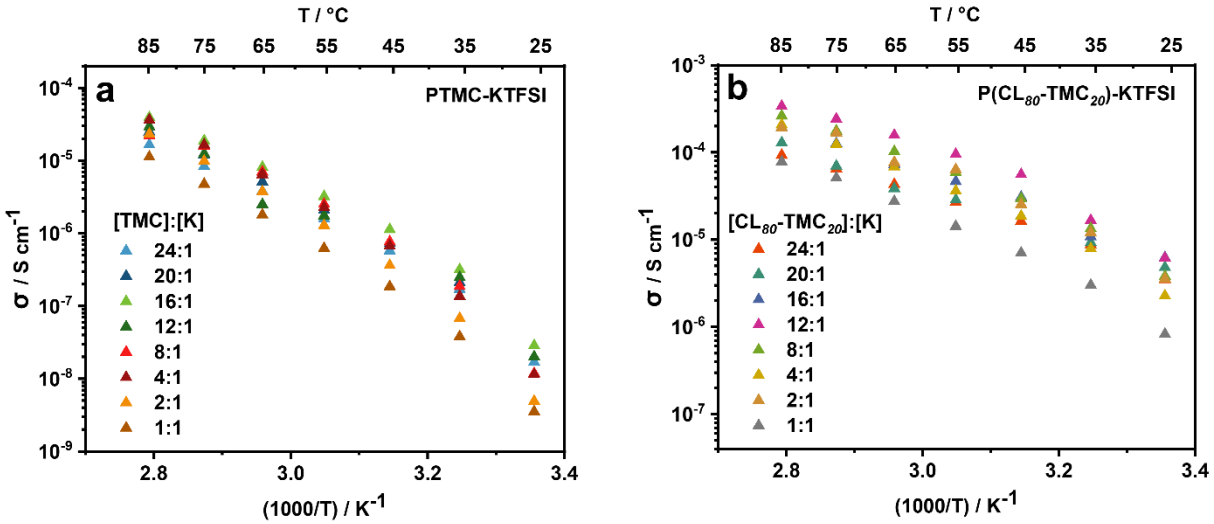

Figure A9. Temperature-dependent ionic conductivity (derived from EIS measurements conducted in the frequency range from 1 Hz to 10 MHz in the temperature range from 25 to 85 °C) of **(a)** PTMC-KTFSI and **(b)** P(CL_{80}-TMC_{20})-KTFSI SPEs with different [TMC]/[CL_{80}-TMC_{20}]:K molar ratios.